Dissertation

Czech
Technical
University
in Prague

Faculty of Nuclear Sciences and Physical Engineering

Lasers Generating Radiation in the Mid-infrared Region of the Electromagnetic Spectrum

Ing. Adam Říha

Supervisor: Prof. Ing. Helena Jelínková, DrSc.
Supervisor–specialist: Ing. Michal Němec, Ph.D.
Field of study: Physical Engineering
Subfield: Applications of Natural Sciences
September 14, 2023

Bibliographic Entry

Author:	**Ing. Adam Říha** Czech Technical University in Prague Faculty of Nuclear Sciences and Physical Engineering Department of Physical Electronics
Title of Dissertation:	Lasers Generating Radiation in the Mid-infrared Region of the Electromagnetic Spectrum
Degree Program:	Applications of Natural Sciences
Field of study:	Physical Engineering
Supervisor:	**Prof. Ing. Helena Jelínková, DrSc.** Czech Technical University in Prague Faculty of Nuclear Sciences and Physical Engineering Department of Physical Electronics
Supervisor–specialist:	**Ing. Michal Němec, Ph.D.** Czech Technical University in Prague Faculty of Nuclear Sciences and Physical Engineering Department of Physical Electronics
Academic year:	2022/2023
Number of pages:	161
Keywords:	Solid-state Laser, Mid-infrared Laser, Cr:ZnSe, Cr:ZnMnSe, Cr:ZnMgSe, Cr,Fe:ZnMnSe, Cr,Fe:ZnMgSe, Fe:ZnSe, Fe:ZnMnTe, Fe:CdMnTe

Bibliografický záznam

Autor:	**Ing. Adam Říha** České vysoké učení technické v Praze Fakulta jaderná a fyzikálně inženýrská Katedra fyzikální elektroniky
Název práce:	Lasery generující záření ve střední infračervené oblasti elektromagnetického spektra
Studijní program:	Aplikace přírodních věd
Studijní obor:	Fyzikální inženýrství
Školitel:	**Prof. Ing. Helena Jelínková, DrSc.** České vysoké učení technické v Praze Fakulta jaderná a fyzikálně inženýrská Katedra fyzikální elektroniky
Školitel–specialista:	**Ing. Michal Němec, Ph.D.** České vysoké učení technické v Praze Fakulta jaderná a fyzikálně inženýrská Katedra fyzikální elektroniky
Akademický rok:	2022/2023
Počet stran:	161
Klíčová slova:	Pevnolátkový laser, střední infračervená spektrální oblast, Cr:ZnSe, Cr:ZnMnSe, Cr:ZnMgSe, Cr,Fe:ZnMnSe, Cr,Fe:ZnMgSe, Fe:ZnSe, Fe:ZnMnTe, Fe:CdMnTe

Funding

The author would like to acknowledge the following funding resources of the research:

Funding agency	Grant number
Czech Science Foundation, MEYS	15-05360S
Czech Science Foundation, MEYS	18-11954S
Students Grant Competition, CTU in Prague	SGS16/247/OHK4/3T/14
Students Grant Competition, CTU in Prague	SGS19/191/OHK4/3T/14
Students Grant Competition, CTU in Prague	SGS22/191/OHK4/3T/14
Center for Advanced Applied Sciences, Team LASE-A	CZ.02.1.01/0.0/0.0/16_019/0000778

Financování

Autor by tímto rád poděkoval za následující zdroje financování výzkumu:

Financující agentura	Číslo grantu
Grantová agentura České republiky, MŠMT	15-05360S
Grantová agentura České republiky, MŠMT	18-11954S
Studentská grantová soutěž, ČVUT v Praze	SGS16/247/OHK4/3T/14
Studentská grantová soutěž, ČVUT v Praze	SGS19/191/OHK4/3T/14
Studentská grantová soutěž, ČVUT v Praze	SGS22/191/OHK4/3T/14
Centrum pokročilých aplikovaných přírodních věd, podprogram LASE-A	CZ.02.1.01/0.0/0.0/16_019/0000778

Acknowledgements

I would like to thank my supervisors prof. Ing. Helena Jelínková, DrSc. and Ing. Michal Němec, Ph.D. for useful notes and corrections of the dissertation thesis and their professional approach in conducting experiments. Also, discussion about the scientific content of this thesis as well as suggestions addressing the formal structure and consistency of the text were an asset during the writing. Furthermore, I would like to thank them for their important comments during the preparation of papers and presentations or posters presented at scientific conferences in the course of my studies. Professor Helena Jelínková introduced me to the world of lasers and was supporting me for more than ten years during my whole university studies. Doctor Michal Němec successfully supervised my bachelor and master theses, and introduced me to the experimental measurements of important laser systems parameters.

Acknowledgement also go to the Czech Science Foundation (GAČR), the Center for Advanced Applied Sciences (CAAS) and the Student Grant Competition of the Czech Technical University in Prague (SGS), from which the research was co-financed.

Many thanks to my closest colleagues Jan Šulc, Michal Jelínek, David Vyhlídal, Karel Veselský, Richard Švejkar, Jan Kratochvíl and Martin Fibrich, for their help and inspiring environment.

I would like to thank my parents Jitka and Vladimír for their love and support through my whole live including my studies and to the rest of my family.

Declaration

I declare that I have prepared the submitted work independently and that I have listed all the literature used. I also declare that except where specific reference is made to the work of others, the contents of this dissertation are original and have not been submitted in whole or in part for consideration for any other degree or qualification in this, or any other university.

In Prague, September 14, 2023

.....
Ing. Adam Říha

Abstract

In the submitted work the properties of novel chalcogenide laser active materials based on divalent transition metal ions, specifically Cr^{2+} and Fe^{2+}, generating coherent radiation in mid-infrared (mid-IR) part of the electromagnetic spectrum are investigated. This radiation is widely used in medical diagnostics, spectroscopy, free space optical communications and other fields. The Cr^{2+}:ZnSe and Fe^{2+}:ZnSe lasers are a relatively new class of solid-state laser gain media and they are a source of widely tunable laser radiation. For these reasons, the Cr/Fe:ZnSe media are considered as analogues of the Ti^{3+}:sapphire laser in the mid-IR part of the spectrum.

In the introductory part of the thesis, a text summarizing the state-of-the-art results of the ZnSe lasers doped with Cr^{2+} and Fe^{2+} ions is presented. The analysis is subdivided according to different operating modes: pulsed (Q-switched or mode-locked mode) and continuous wave regime of generation. The detailed overview of the development of these lasers, including their properties are mentioned.

After the motivational part of this work summarising the applications of mid-IR laser radiation, the performed experiments with the aim of characterisation of novel laser active materials singly doped by Cr^{2+}or Fe^{2+}, and or co-doped by both Cr^{2+},Fe^{2+} ions in different host materials ($Zn_{1-x}Mn_xSe$, $Zn_{1-x}Mg_xSe$, $Zn_{1-x}Mn_xTe$, and $Cd_{1-x}Mn_xTe$) are described. Several laboratory-built laser oscillators generating radiation in the mid-IR region based on novel laser active media were designed. Their fundamental spectroscopic and laser output parameters were subsequently characterised and compared – the absorption and fluorescence spectra, fluorescence decay time, generated wavelength, pulse duration, energy/power and spatial beam profile of generated laser radiation including temperature dependences, different excitation wavelengths and host material composition. The obtained laser radiation covered a wide spectral range of ∼2.1–2.7 µm (Cr^{2+}-doped lasers) and ∼3.95–6.05 µm (Fe^{2+}-doped or Cr^{2+},Fe^{2+} co-doped lasers). In particular, the achieved laser radiation with a wavelength of ∼6 µm generated using the Fe:CdMnTe laser was also significant.

Laser radiation in the mid-IR spectral region of 4–5 µm is usually obtained from Fe^{2+} ions pumped by another mostly solid-state laser (Er:YAG). Based on previous theoretical studies, successful $Cr^{2+} \rightarrow Fe^{2+}$ inter-ionic energy transfer was experimentally achieved, described and published for the first time for different sources of optical excitation of Cr^{2+} ions, at various set of chosen active media temperatures and for different wavelengths of pumping radiation in chosen host materials.

For the optical excitation of Cr^{2+} ions, the effective, commercially available pump lasers, especially laser diodes or thulium-doped fiber lasers, already exist. In our experiments, this novel excitation concept was confirmed, allowing to obtain mid-IR laser radiation in the spectral region of 4–5 µm.

Overall, these findings are an important initial step towards developing compact, cost-effective, efficient, directly pumped broadband laser sources and amplifiers of radiation in mid-IR spectral region based on Fe^{2+} ions.

Keywords: Solid-state Laser, Mid-infrared Laser, Cr:ZnSe, Cr:ZnMnSe, Cr:ZnMgSe, Cr,Fe:ZnMnSe, Cr,Fe:ZnMgSe, Fe:ZnSe, Fe:ZnMnTe, Fe:CdMnTe

Abstrakt

V předložené práci jsou studovány vlastnosti nových chalkogenidových laserových aktivních materiálů dopovaných dvojmocnými ionty přechodných kovů, konkrétně Cr^{2+} a Fe^{2+}, generujících koherentní záření ve střední infračervené (IČ) části elektromagnetického spektra. Toto záření je široce využíváno v lékařské diagnostice, spektroskopii, optických komunikacích a dalších oborech. Cr^{2+}:ZnSe a Fe^{2+}:ZnSe lasery jsou poměrně nová pevnolátková laserová prostředí a jsou taktéž zdrojem záření, jehož vlnovou délku lze přeladovat v širokém rozsahu. Z těchto důvodů jsou tyto materiály považovány za obdobu titan-safírového laseru ve střední IČ oblasti spektra.

V úvodní části práce byla provedena rešerše shrnující dosavadní výsledky výzkumu vlastností ZnSe laserů dopovaných ionty Cr^{2+} a Fe^{2+}. Studie byla rozdělená do podsekcí podle různých provozních režimů: pulzní (Q-spínaný režim nebo režim synchronizace módů) a kontinuální režim generace. V práci je podrobně uveden přehled vývoje těchto laserů včetně jejich vlastností.

Po motivační části shrnující aplikace středního IČ záření generovaného těmito lasery jsou popsány experimenty, jejichž cílem byla charakterizace nových laserových aktivních prostředí dopovaných pouze ionty Cr^{2+} nebo Fe^{2+} a nebo kodopovaných oběma ionty Cr^{2+} i Fe^{2+} v různých hostitelských matricích $Zn_{1-x}Mn_xSe$, $Zn_{1-x}Mg_xSe$, $Zn_{1-x}Mn_xTe$ a $Cd_{1-x}Mn_xTe$. Bylo sestaveno několik laboratorních laserových oscilátorů generujících záření ve střední IČ oblasti založených na těchto nových laserových aktivních prostředích a následně byly charakterizovány a porovnávány jejich základní spektroskopické a laserové výstupní parametry – spektra absorpce a fluorescence, doba doznívání fluorescence, vlnová délka, délka pulzu, energie/výkon a prostorová struktura svazku generovaného laserového záření včetně jejich závislostí na teplotě, typu čerpání a složení matrice. Získané záření generované těmito systémy pokrývalo široké spektrum 2,1–2,7 μm (lasery dopované ionty Cr^{2+}) a 3,95–6,05 μm (lasery dopované ionty Fe^{2+} nebo kodopované oběma ionty Cr^{2+},Fe^{2+}). Zvláště významné bylo dosažené generované laserové záření s vlnovou délkou ∼6 μm pomocí Fe^{2+}:CdMnTe laseru.

Laserové záření ve střední IČ spektrální oblasti 4–5 μm je obvykle získáváno z iontů Fe^{2+} čerpaných jiným většinou pevnolátkovým laserem (Er:YAG). Na základě předchozích teoretických studií byl poprvé experimentálně dosažen, popsán a publikován úspěšný přenos energie mezi aktivními ionty $Cr^{2+} \rightarrow Fe^{2+}$ pro různé zdroje optické excitace iontů Cr^{2+}, při různých vybraných teplotách aktivních prostředí a pro různé vlnové délky čerpacího záření ve vybraných hostitelských materiálech.

Pro optické buzení iontů Cr^{2+} dnes již existují efektivní, komerčně dostupné čerpací lasery, zejména laserové diody nebo thuliové vláknové lasery. V našich experimentech byla ověřena nová koncepce buzení umožňující získat střední IČ laserové záření ve spektrální oblasti 4–5 μm.

Tato zjištění jsou důležitým počátečním krokem k vývoji kompaktních, rentabilních, účinných, přímo čerpaných širokopásmových laserových zdrojů a zesilovačů záření ve střední IČ oblasti založených na iontech Fe^{2+}.

Klíčová slova: Pevnolátkový laser, střední infračervená spektrální oblast, Cr:ZnSe, Cr:ZnMnSe, Cr:ZnMgSe, Cr,Fe:ZnMnSe, Cr,Fe:ZnMgSe, Fe:ZnSe, Fe:ZnMnTe, Fe:CdMnTe

Contents

List of figures

List of tables

Part I

State-of-the-art and Motivation

Introduction

We have entered the seventh decade of lasers, which, as is well known, originated from the work of Theodore Harold Maiman, who built the world's first operable solid-state laser based on a synthetic ruby crystal (Cr^{3+}:Al_2O_3) in 1960 [1].

The current development of lasers generating coherent radiation in the mid-infrared (mid-IR) part of the electromagnetic spectrum of about 2–6 µm is given by the growing interest in their practical applications. The solid-state lasers based on divalent transition metal ions belonging to this region also have many favourable spectroscopic properties such as high gain and a widely tunable wavelength range of the generated laser radiation. A basic research of novel laser active media generally contributes to the future development of these laser systems construction and their subsequent applications.

The aim of this dissertation is to investigate properties of novel laser active materials based on divalent transition metal ions (TM^{2+}) with emphasis on Cr^{2+} and Fe^{2+} laser active ions. The excitation of these laser active media by coherent radiation sources such as laser diodes (LD) or other solid-state lasers increases the efficiency of laser generation and reduces the overall energy consumption of the resulting laser systems. To characterise these materials several laboratory-built mid-IR laser oscillators based on novel chalcogenide laser active media were constructed and their fundamental spectroscopic and laser output characteristics were measured. To be specific, the following properties of developed laser systems including temperature dependences, where it was appropriate, were measured: absorption and fluorescence spectra, fluorescence decay times, laser output energy/power characteristics, laser beam spatial profiles, pulse duration, and generated oscillation spectra. In cases of interest the tunability of generated radiation wavelength was also studied. To evaluate the results obtained a comparison of measured properties with such well-known lasers as Cr^{2+}:ZnSe and Fe^{2+}:ZnSe is included.

The research Part I begins with the Chapter 1 dealing with the characterisation of mid-IR solid-state lasers doped with divalent transition metal ions (TM^{2+}). The introduction is devoted to the general properties of these ions and subsequently to Cr^{2+} and Fe^{2+} ions in detail. It is followed by the properties of typically used II–VI chalcogenide host materials with a tabular overview of their properties, brief description of their production methods, and doping techniques of activator ions. The chapter is concluded by a brief summary of laser active materials doped with V^{2+}, Mn^{2+}, Co^{2+}, and Ni^{2+} from the same row of periodic table as Cr^{2+} and Fe^{2+} ions.

Chapter 2 is devoted to state-of-the-art of the Cr^{2+}:ZnSe and Fe^{2+}:ZnSe lasers based on the active media mentioned in the first chapter. It starts with the overview of coherent optical sources suitable and frequently used for their excitation. The laser results of both

systems are described in more details to prepare a good background knowledge about these systems for future comparison with our experimental results obtained with novel crystal samples. Except the firstly mentioned laser generation from Cr:ZnSe and Fe:ZnSe laser systems, the state-of-the-art laser output properties are divided into subsections according to different modes of generation – pulsed Q-switched mode and mode-locking mode (generating of (ultra)short pulses), and continuous wave (CW) regime of operation.

Chapter 3 concludes the first part and describes the motivation of this research and acquaints the reader with applications of the mid-IR laser radiation in the wavelength range from 2 up to 6 µm generated by these lasers. This radiation is widely used in (bio)medical diagnostics and medical treatment, spectroscopy – trace gases detection, material processing, remote sensing, metrology, LIDAR systems, free space optical communications, optical switching, and many other fields. These lasers can also serve as a coherent pumping sources of other laser active or non-linear materials such as optical parametric oscillators (OPOs). Selected applications, for which this part of electromagnetic radiation is useful, are described in detail in appropriate subsections.

Second Part II, with the Chapters 4 and 5, summarizes the objectives of this work and the description of the elaboration methods, respectively. Instrumentations used and their characteristics are listed and properties, experimental procedures including schematic figures of measurement setups, description of pumping laser systems and overview of investigated crystal samples properties are included as well.

The experimental Part III, beginning with Chapter 6, describes the results of performed experiments with references to relevant author's published peer-reviewed publications and conference proceedings. Peer reviewed papers are marked in the text as [P#] and conferences contributions as [C#]. The characterisation of some important individual laser systems built divided into six sections according to the host materials and their dopants can be found there. These sections are further subdivided according to the pumping wavelength used or due to the direct or indirect excitation of laser active ions.

The work concludes with Part IV containing discussion and conclusions being described in Chapter 7 comparing the results obtained with the novel laser active materials. A brief summary of the contribution for practice and further development of science of this work is also included. More details can be then found in appropriate referenced papers and conference proceedings which are listed in the bibliography and are included in the appendices 1–3. The dissertation is also supplemented with the list of all author works related to this dissertation in the bibliography.

Chapter 1

Transition metal ions doped mid-infrared laser gain media

Solid-state lasers (SSL) are usable in many diverse applications. The choice of a suitable SSL active medium for a specific application depends on its performance capabilities, such as available oscillation wavelengths, tuning range, efficiency, reliability, repetition rate, and generated pulse duration. These performance capabilities are closely related to the spectroscopic properties of SSL gain materials that are often unique among other laser types (gas, liquid (dye), chemical, metal-vapour, semiconductor, free-electron lasers, and others).

For practical applications, the laser system has to be usable outside the laboratory. Therefore, a compact, maintenance-friendly, break-resistant system is required. SSL generally fulfil these criteria better than the other types of lasers named above. A novel generations of SSL systems (fiber, diode-pumped, slab and thin-disc lasers) have introduced a new era in the research and development of their usage in many applications due to their reduction in size and less consumption of energy. [2]

SSL can be simply subdivided into two basic categories according to laser active ions based on: (i) *transition metal ions* lasers – active ions come from the 4^{th} period in the periodic table of the elements, and (ii) *rare-earth-doped (lanthanide)* lasers – active ions from the 6^{th} period. Although many properties of these two categories are similar, spectral absorption and emission characteristics, and thus tunable range, are significantly different. Transition metal ions doped solid-state host materials are usually broad laser gain media tunable over a wide spectral range, whereas the lanthanide series lasers tuning range is partially limited. [3]

Considering the given work concerns the generation of laser radiation in the mid-infrared (mid-IR) region of the optical spectrum, this chapter concentrates to general properties of transition metal ions and II–VI host materials. The growth techniques and active ions doping technology of such laser gain media is included. A brief general overview of these laser active media properties as a promising source of tunable broadband mid-IR radiation capable to ultrashort pulses generation is presented in the end of this chapter. Comparison and more specific details about state-of-the-art laser action results of these materials, especially of Cr:ZnSe and Fe:ZnSe, whose modification was the subject of research in the experimental Part III, can be found in Chapter 2.

1.1 Transition metal ions (TM^{2+}) properties

Transition metal (TM) is a chemical element whose atom has a partially filled d subshell, or which can give rise to cations with an incomplete d subshell [4]. From the point of possibility of stimulated emission radiation amplification, only several transition metal ions are interesting – according to the order in the third period of the periodic table *titanium* (Ti), *vanadium* (V), *chromium* (Cr), *manganese* (Mn), *iron* (Fe), *cobalt* (Co), and *nickel* (Ni). Divalent transition metal ions are generally referred as TM^{2+}. When TM^{2+} ions are doped into II–VI chalcogenide crystals, such materials dispose with strong and ultra-broad absorption and emission bands in the mid-IR spectra. It is worth noting that only these divalent ions among TM emit in this spectral region. Laser active TM^{2+} ions are basically always used in crystalline host media rather than in glasses, since crystals offer a higher thermal conductivity and the additional inhomogeneous broadening in glass matrices would hardly be useful [5].

$3d$ electrons of the TM^{2+} ions are strongly influenced by the crystalline electric field. One of the very first studies of the effects of crystal fields on the properties of TM^{2+} ions was published in 1952 in [6]. These effects giving a rise to strong splitting of the laser active medium energy levels and to strong vibronic side-bands [7]. Thanks to stronger interaction between the laser-active electron shells and the host lattice vibrations (i.e. with phonons), TM^{2+}-doped laser media typically have a larger gain bandwidth in comparison with rare-earth-doped media. This interaction leads to a strong homogeneous broadening of the transition, and thus to a large gain bandwidth. Optical transitions can also involve the absorption of phonons. Typically, not only a photon is emitted, but also one or several phonons. For that reason, such lasers are sometimes called *vibronic* (vibrational-electronic) or *phonon-terminated* lasers [7, 8].

The main subject of the investigation of the experimental part of this work are novel laser active media doped by Cr^{2+} and Fe^{2+} ions. Therefore, more details about properties of these ions are discussed in two following subsections 1.1.1 and 1.1.2, respectively.

1.1.1 Properties of Cr^{2+} ions

Chromium is the 24^{th} element of the periodic table, the third member of transition metals group. The atomic mass of chromium is $m_{\text{Cr}} = 51.996\,\text{amu}$, melting point of $t_{\text{m}} = 1907\,^{\circ}\text{C}$, boiling point of $t_{\text{b}} = 2672\,^{\circ}\text{C}$ and volumetric density $\rho = 7.19\,\text{g}\cdot\text{cm}^{-3}$ [9].

It is a hard silvery grey/white, brittle, non-corrosive metal. Different compounds and minerals of chromium show various colours such as red, green or yellow, which gave the name to this element coming from the Greek words "χρῶμα" (*chroma*) or "χρομοσ" (*chromos*) which means colour [9]. Pure chromium was firstly isolated from an oxide in 1797 by the French chemist *Louis-Nicolas Vauquelin* while studying some of the minerals collected in Siberia. Pure metal structure of chromium does not occur in nature. Major part of chromium oxides is found in a mixture with other metals, such as iron, magnesium or aluminium [9, 10].

Physical and chemical properties of chromium are similar to that of previous two elements from the d group of 4^{th} period (vanadium and titanium). Electron configuration of chromium in the neutral state can be written in abbreviated form as $[\text{Ar}]4s^1 3d^5$ and in the divalent excited state of Cr^{2+} ion then as $[\text{Ar}]3d^4$, where [Ar] represents the electron

configuration of argon, the previous closest noble gas. Cr^{2+} ions form high spin complexes only for crystal fields with an energy of less than 2000 cm^{-1} [11]. The ground and excited states in an octahedral crystal field are ^5E_g and $^5T_{2g}$, respectively. The $3d^4$ electron is susceptible to Jahn-Teller distortion effect causing vibrational levels to shift, split and mix. Therefore, compounds containing Cr^{2+} ions are usually of only low symmetry. Hence, the excited quintet state of Cr^{2+} splits into three levels and the ground level quintet state ^5D splits into two sublevels ^5E and $^5T_2$. The energy levels of the Cr^{2+} ion are further divided into sublevels $^5\overline{A}_1$, $^5\overline{B}_1$, $^5\overline{E}$, and $^5\overline{B}_2$ under the influence of the crystal field due to the Jahn-Teller effect. Excitation of Cr^{2+} ions takes place at the $^5\overline{B}_2 \rightarrow {}^5\overline{A}_1$ junction and stimulated laser emission between the $^5\overline{B}_1 \rightarrow {}^5\overline{E}$ levels. Therefore, lasers based on Cr^{2+} ions belong to group of four-level laser systems. For instance, in Cr^{2+}:ZnSe lie all listed energy levels within the forbidden band gap of the ZnSe semiconductor (band gap energy: $E_g = 2.7$ eV; band gap wavelength: $\lambda_g = 0.46$ µm) [12, 13]. The schematic diagram of Cr^{2+} ions energy levels in a ZnSe host is shown in Fig. 1.1 [9, 11, 12].

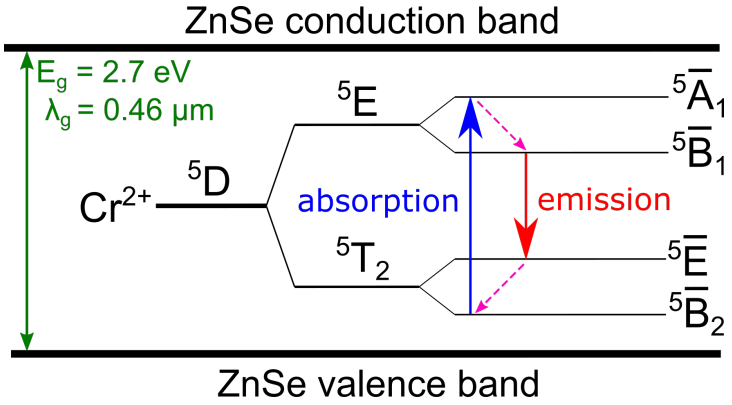

Figure 1.1: Simplified schematic diagram of Cr^{2+} ions energy levels in a ZnSe host material. E_g – band gap energy; λ_g – band gap wavelength.

Further details about Cr^{2+} ions spectroscopic properties in specific host materials were published in: ZnS [14–17], ZnSe [16, 18], ZnS_xSe_{1-x} [19], ZnTe [20], $Zn_{1-x}Mg_xSe$ [21], CdSe [22], and $CdSe_xS_{1-x}$ [23], and more general details can be found in [11, 24].

Due to the large number of available oxidation states of chromium ions (±I, ±II, +III, ±IV, +V, +VI), there exist a possible presence of other (Cr^{1+}, Cr^{3+}) than effective dominant valence states (Cr^{2+}) in different positions of the host material crystal lattice. These differences in charge states lead to a reduction in the number of effective luminescence centres and may eventually lead to undesired energy transfer between these differently charged states, which further reduces the luminescence efficiency. Moreover, any valence states of chromium, other than Cr^{2+}, may require charge compensation, which could increase the number of defects associated with this phenomenon, which impairs the optical quality or luminescence properties due to unexpected absorption or emission. $Cr^{2+}$and other charge states in chalcogenides II–VI [25], including Cr^{1+} and Cr^{3+}, have been studied, for example, by electron spin resonance (ESR) or electron paramagnetic resonance (EPR) in [25, 26].

For example, in the lattice of ZnSe and ZnS host materials, chromium ions substitute and occupy Zn^{2+} cation sites with the dominant charge state of +II (Cr^{2+}). Almost all the contained chromium (> 95 %) is present in the form of the Cr^{2+} ion (with electronic

configuration of $3d^4$) [27].

Active media doped with Cr^{2+} ions usually possesses a strong absorption band centred near ∼1.8 µm. Typically used optical coherent pumping sources lie in the wavelength range of 1.5–2.1 µm (Er-doped lasers, Tm- or Tm,Ho-doped lasers, laser diodes, fiber lasers, etc.) which produces a broad, strong emission band with the lasser oscillation tunable in the wide range of 1.88–3.1 µm [28]. Despite a large emission bandwidth, they dispose with reasonably low pumping power threshold. They can also be operated in passive mode-locking regime with a pulse duration less than 50 fs [12, 29].

More details about Cr^{2+}:ZnSe laser properties, historical milestones and state-of-the-art will follow in Sec. 2.2.

1.1.2 Properties of Fe^{2+} ions

Iron is the 26$^{\text{th}}$ chemical element of the periodic table, the fifth member of transition metals group. Atomic mass of iron is $m_{\text{Fe}} = 55.847$ amu, melting point of $t_{\text{m}} = 1535\,^{\circ}\text{C}$, boiling point of $t_{\text{b}} = 2750\,^{\circ}\text{C}$, and volumetric density of $\rho = 7.87\,\text{g}\cdot\text{cm}^{-3}$ [9].

An iron is a silvery-white, hard, brittle non-corrosive metal. The name *iron* comes from Anglo-Saxon, and the symbol Fe and words such as *ferrous* derive from the Latin word "*ferrum*" – iron [9]. Pure iron is reactive and can form many compounds with other elements. Iron conducts the electricity and heat well, and is easily magnetized. However, its magnetic properties disappear at higher temperatures. Iron is the only metal that can be tempered (hardened by heating, then quenching in water or oil). [9, 10]

The most common oxidation states of iron are +II (Fe^{2+}) and +III (Fe^{3+}). Electron configuration of iron in the neutral state can be written in abbreviated form as $[\text{Ar}]4s^2 3d^6$ and in the divalent excited state of Fe^{2+} ion then as $[\text{Ar}]3d^6$. In this divalent state d^6, the free ground term is ^{5}D and the excited terms are triplet states ^{3}H, ^{3}P, ^{3}F, ^{3}G, ^{3}D and singlet states ^{1}I, ^{1}D. The transitions from the excited triplet states are spin-forbidden. In an octahedral field, the ^{5}D term splits into an upper $^5\text{E}_\text{g}$ level and a lower $^5\text{T}_{2\text{g}}$ level which forms the ground state. The only allowed transition is $^5\text{T}_{2\text{g}} \rightarrow {}^5\text{E}_\text{g}$ that results in an intense broad absorption band in mid-IR spectral region. This band splits into two bands due to Jahn-Teller effect similarly like for Cr^{2+} ions [30]. [11]

The second order spin-orbit coupling results in splitting of the ^{5}E ground state to five equidistant levels: Γ_1-singlet, Γ_2-singlet, Γ_3-doublet, Γ_4-triplet, and Γ_5-triplet. Energy splitting of these levels is $\text{K} = \frac{6\lambda^2}{\Delta} = 10\text{–}20\,\text{cm}^{-1}$ ($\lambda \approx 100\,\text{cm}^{-1}$, $\Delta \approx 3000\,\text{cm}^{-1}$). The experimental results in most cases shown that Fe^{2+}-doped II–VI crystals are best fitted for a $\text{K} \approx 15\,\text{cm}^{-1}$ [31, 32]. Due to spin-orbit interaction predictions, the triplet $^5\text{T}_2$ level is split by first order spin-orbit interactions into three multiplets separated with an energy gap of 2λ and 3λ. Second order spin-orbit interaction further splits these levels. According to the selection rules, transitions between ground level Γ_1 and upper levels Γ_5 are allowed by electric-dipole interactions. Therefore, according to crystal field theory there should exist two narrow lines separated by $5\lambda \sim 500\,\text{cm}^{-1}$ (20 µm) in the absorption spectrum at low temperatures. The first strong narrow absorption line is observed in all chalcogenides, but a second line has never been observed in II–VI materials. Therefore, the mechanism responsible for the $^5\text{T}_2$ level splitting is considered due to most of the theories as the Jahn-Teller effect. A detailed study about Fe^{2+} ions energetic levels in II–VI semiconductors can be found in [33]. [13]

The schematic energy diagram of Cr^{2+} (octahedral coordination) and Fe^{2+} ions (tetrahedral coordination) in a ZnSe host is shown in Fig. 1.2. As it can be seen from this figure, absorption as well as emission transitions of both ions take place between ^5E and $^5T_2$ levels which are split into several sublevels. Therefore, Cr^{2+} ions fluorescence spectrum partially overlap with the Fe^{2+} ions absorption band. Thus, there may exist some Cr^{2+} emission transitions with the same energy as the Fe^{2+} absorption transition. When both ions are co-doped into one chalcogenide material, the $Cr^{2+} \rightarrow Fe^{2+}$ ions energy transfer (indicated by orange dotted double arrow in Fig. 1.2) may occur.

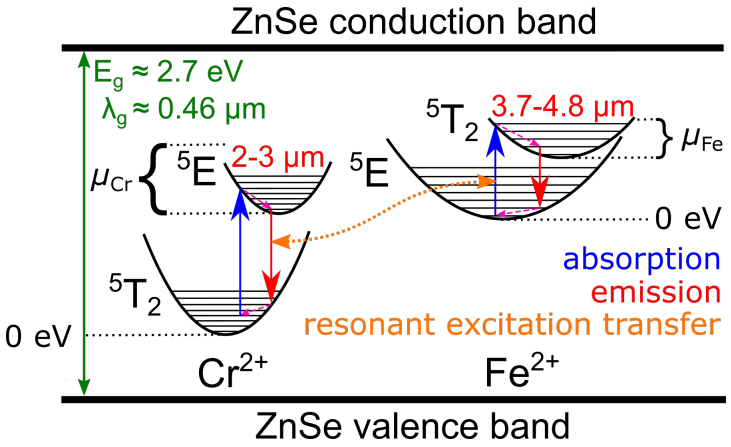

Figure 1.2: Schematic energy diagram of Cr^{2+} (octahedral coordination) and Fe^{2+} ions (tetrahedral coordination) in a ZnSe host material. Vibronic substates are spaced by the longitudinal optical (LO) phonon energy of 31 meV. μ_{Cr}, μ_{Fe} – thermal activation energy of Cr^{2+} and Fe^{2+} ions according to the semi-classical model. [16,34,35]

A small disadvantage of Fe^{2+}-doped lasers from the point of spectroscopic properties may be the shortening of Fe^{2+} ions metastable-level lifetimes with temperature rising above 100–110 K because the nonradiative relaxation rates are increased [36,37], which also increases the laser threshold [38]. On the other hand, this is the reason why a cryogenic cooling of Fe^{2+}-doped laser active media improves efficiency of such laser system. Low temperature also greatly reduce thermo-optic effects at a given power level. Moreover, at liquid nitrogen (LN_2) temperature there is significantly higher thermal conductivity than at room temperature (RT) and the thermal expansion coefficient of chalcogenides decreases significantly too. It results to smaller temperature coefficient of refractive index $\frac{dn}{dT}$, and thus in improvement of power scalability at cryogenic temperature as compared with RT. [38]

The unusual temperature dependence of the Fe^{2+} ions luminescence lifetime in the Fe:ZnSe laser active crystal may be explained by two different processes. The first stage in very low temperature range up to 100–110 K is characteristic for the luminescence lifetime increase from 33 µs at 12 K up to 105 µs at 110 K [37] due to the thermal population of levels with smaller oscillator strength. By low temperature absorption measurements performed in [30], there was shown that transitions from these levels feature of smaller oscillator strength, e.g. longer radiative lifetime than that found between the lowest levels. Therefore, the population of these levels should result in an increase of the luminescence lifetime. The second stage for temperatures above 110–120 K is characteristic for decreasing luminescence lifetime mainly due to thermally activated

nonradiative decay. The quantum efficiency of Fe:ZnSe luminescence at RT is too small for efficient CW pumping. However, the luminescence lifetime at RT is still longer than the typical Q-switched laser pulses duration (~1–100 ns). Therefore, it is possible to operate Fe:ZnSe laser at RT in a gain-switched mode with pumping pulses shorter than ~300 ns. [13]

More details about optical spectroscopic properties of Fe^{2+} ions in ZnSe can be found, for instance, in [39]. State-of-the-art of the Fe^{2+}:ZnSe laser systems operated in different regimes are described further in the Sec. 2.3.

1.2 Properties of II–VI chalcogenide hosts

A relatively new class of solid-state laser gain media are TM^{2+}-doped chalcogenide semiconductor crystals. For the first time, the mid-IR laser radiation generation in a TM^{2+} ions doped wide band gap II–VI semiconductor crystals was demonstrated in Lawrence Livermore National Laboratory in 1996 [40]. These II–VI compounds, such as ZnSe, ZnS, CdSe, ZnTe, etc., are transparent in a wide spectral range from near-IR up to far-IR. These materials also combine a unique versatility of the ion-doped solid-state lasers with the semiconductor lasers engineering capabilities. [41]

From other fluoride- and oxide-host based laser crystals, II–VI chalcogenides distinguish themselves in the following features. The heavier anions in the crystals (e.g. Se^{-2}, S^{-2}, Te^{-2}) provide a very low energy optical phonon cut-off that makes them transparent in a wide spectral region and decreases the efficiency of nonradiative decay. It results in a high fluorescence yield at RT. II–VI chalcogenides tend to crystallize in tetrahedral coordination [42] in which the energy field is splits and strong electron-phonon interactions result in the formation of a broad absorption and emission bands shifted further into the mid-IR part of optical spectrum. In terms of spectroscopic and laser output characteristics, these media are considered as mid-IR analogues of the titanium-doped sapphire (Ti:sapphire) laser in near-IR part. [5, 43–45]

Methods of such TM^{2+}-doped II–VI crystals growth and doping techniques are described in the following Sec. 1.3.

1.3 TM^{2+} ions doped II–VI crystal growth

Melting points of wide-bandgap II–VI compound semiconductors are higher due to the overheating phenomenon when they are heated to their melting point because of ionic bondings strength. Therefore, it is difficult to grow bulk crystals from melt owing to the higher vapour pressures at their melting points. On the other hand, it is easier to grow bulk crystals from the vapour phase. [46]

There exist two principal methods of the II–VI crystal growth: epitaxial or bulk crystal growth. The first approach is mainly carried out using liquid-phase epitaxy (LPE), or vapour-phase epitaxy (VPE). VPE includes several techniques, such as hot-wall epitaxy (HWE), metal-organic chemical vapour deposition (MOCVD) or metal-organic vapour phase epitaxy (MOVPE), molecular-beam epitaxy (MBE), metal-organic molecular-beam epitaxy (MOMBE), atomic-layer epitaxy (ALE), and others. [46]

Due to problems with sufficiently good optical quality related to a growth of bulk Cr:ZnSe crystals Cr^{2+}-related mid-IR lasers were not commercialized yet in 2005. Crystal samples prepared using Bridgman-Stockbarger method, used to demonstrate laser generation, contained too large densities of dislocations and of parasitic deep centres (Zn^{2+} vacancies). Moreover, there were often inhomogeneous concentration of Cr^{2+} ions and also crystal locations containing chromium precipitates. As the consequence, it was difficult to grow a Cr:ZnSe crystal with repeatable and stable laser parameters. [47]

Since then, the growth methods of Cr:ZnSe crystals were improved. Next part is focused on the bulk crystal growth, especially the Bridgman method, because crystal samples investigated in the experimental Part III (in Chapter 6) were prepared using this growth technique. More general information and also specific details about all growth techniques mentioned above can be found in [46].

1.3.1 Bulk crystal growth

Three main techniques are employed for growing bulk ZnSe crystals: i) chemical vapour deposition (CVD), ii) physical vapour transport (PVT) method, and iii) the Bridgman method involving growth from a melt. Each of these methods has its own strengths and weaknesses. CVD allows for the production of large polycrystalline crystals with diameters reaching hundreds of centimetres and heights under 10 cm. The PVT method enables the creation of high-quality single crystals, although the rate of deposition is relatively slow, making it primarily suitable for experimental growth purposes. Striking a balance between quality and practicality, the growth from a melt method is being usually utilized. [48]

Growing of high quality bulk crystals is the important subject studied in recent decades due to their importance of electronic and laser systems design. There exist many growth methods and significant improvements have been made with regard to uniformity, impurity, dopant and diameter control, reproducibility, and thermal stability. According to the phase balance, crystals can be grown from vapour, liquid (melt), and solid phase. Basic method is the crystal growth from vapour phase which can be performed at lower temperatures that prevents from phase transition and unfavourable contamination. It can be divided into two similar methods: chemical vapour transport (CVT) and physical vapour transport (PVT). CVT is based on chemical transport reactions and PVT technique is based on the dissociative sublimation of compounds. The difference is that transport agent (usually hydrogen H_2; halogens I_2, Br_2, Cl_2; or halides HCl, HBr) is not used in CVT. A schematic diagram of a CVT system is shown in Fig. 1.3. The typical CVT growth temperature for ZnS is 1073–1173 K, for ZnSe 1023–1073 K and growth rates are around ∼2 mm/h. PVT method was developed by the Piper and Polich in 1961 [49] and was improved by Prior adding a reservoir to control the deviation from stoichiometry in the same year [50]. However, there are still problems including impurities ($\sim 10^{16}$ cm^{-3}), voids, high dislocation densities, and mixed polymorphism. [46]

In both cases the material for crystal growth is transported in a closed ampoule typically placed in a furnace with a temperature gradient over the length of the ampoule. Therefore, the polycrystalline source materials sublime at one end with the higher temperature. Second end of the ampoule where the crystal is expected to be grown is then maintained at a lower temperature. Thanks to the temperature difference the supersaturation

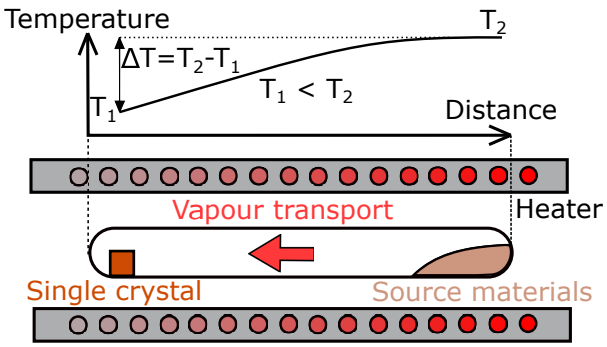

Figure 1.3: Schematic diagram of a chemical vapour transport system.

occurs, and vaporized molecules from source materials eventually deposit at the cooler end. In order to control the deviation from stoichiometry, a reservoir containing one of the constituent elements is often used. By selecting the proper growth conditions, the rate of deposition can be optimized leading to growth of high-quality crystals. [46]

However, from the point of industrial production view, for obtaining large single crystals the most useful is the growth from melt although it is challenging. Crystal size and productivity is limited by VPE technique. The typical crystal growth method from melt is the Bridgman method [51] which can be simply described in terms of a molten charge that slowly passes through a temperature gradient and solidifies when the temperature is below the melting point of the material. Second method is called (vertical) gradient freezing (GF) and is based on stationary ampoule and furnace. The temperature is gradually reduced by keeping the temperature gradient at the interface constant. Single crystals can be grown using either seeded or unseeded ampoules or crucibles in both methods. The Bridgman growth method and technology are relatively simple and require little supervision. Dimensions of the crystal can be easily controlled and the growth rate is relatively high: in the range of 0.1–30 mm/h. Either the furnace or the crucible can be moved to achieve movement of the freezing isotherm, and both horizontal and vertical orientations are used. [46]

Crystalline ingots grown by the Bridgman method consist of sizeable single crystal blocks and exhibit satisfactory optical and structural characteristics. However, the growth from melt technique entails certain technical challenges, such as composition dissociation at temperatures lower than the melting point, differing vapour pressures of composition components, and high-temperature phase transitions. On the other hand these unique aspects can result in unfavourable outcomes, such as disruption of melt stoichiometry, substantial material evaporation during the growth process, and the emergence of structural defects like "twins". [48]

The high pressure Bridgman method (HPBM) [52,53] allows the growth of large uniform crystals. A high pressure of ∼100 atm. is used. The melt growth of TM^{2+} ions doped II–VI materials by solidification from melted mixture is one of widely used methods. A given amount of dopant (a powder of the separated TM^{2+} ions or a transition metal oxides) is firstly mixed with the host material, and the final doped samples are then pulled from the molten mixture. It has been previously shown that melt-grown chalcogenide crystal samples suffer from being polycrystalline and contain defects such as voids and inclusions [40]. In addition, it is very difficult to control the final impurity concentration

because the actual dopant concentration in the final sample is not necessarily the same as its initial value in the molten mixture. In samples prepared by this method the concentration gradients thus were observed. In [54], inter alia, the possibility of uncontrolled contamination during the melting process leading to undesirable passive losses has been highlighted. [12]

1.3.2 Doping techniques of II–VI crystals by TM^{2+} ions

Various techniques can be used for TM^{2+} ions doping into II–VI chalcogenide matrices, either during the crystal growth or even after the pure II–VI host has been grown. TM^{2+}-ions occupy low crystalline field tetrahedral sites coordinated by the heavy selenide (Se^{-2}), telluride (Te^{-2}) or sulphide (S^{-2}) anions. Techniques containing chromium ions already during growth include melt growth, physical or chemical vapour deposition (PVD or CVD) [55], pulsed laser deposition, or molecular beam epitaxy (MBE) [56]. The most widespread TM^{2+} ions post-growth doping technique of pure crystals is carried out by a thermal diffusion process. An overview of the listed production methods and their comparison can be found in [12, 19].

Zhang et al. studied the doping non-uniformity influence on the electrical and optical properties of Cr^{2+}:ZnSe in 2020 [57]. Based on their calculations, it has been established that dopants exert localization effects with significant repercussions on the Cr:ZnSe structure, electrical and optical characteristics. The creation of non-uniformly doped Cr:ZnSe structures during sample preparation is more common. Due to the crystal field's asymmetry within such non-uniformly doped configurations, optical anisotropy is introduced into various aspects, including the complex dielectric function, absorption, reflectance, extinction, and refractive index spectra. These outcomes hold the potential to enhance the optical performance of Cr:ZnSe. Furthermore, these findings offer an alternative perspective for comprehending the underlying physical mechanisms governing Cr^{2+} ions doping processes. [57]

1.4 Overview of mid-IR TM^{2+} ions doped II–VI host materials

TM^{2+} ions doped II–VI lasers dispose with a great variety of possible oscillation regimes. Moreover, laser systems based on Cr^{2+}-doped ZnS, ZnSe, CdSe, and $Cd_{1-x}Mn_xTe$ crystals working with efficiency of over 70 % in CW, can be operated in free-running, Q-switched and mode-locked regimes as well as being tunable over the 2–3.5 μm spectral range. [5, 43]

A typical prototype of wide band gap II–VI chalcogenides is a zinc selenide (ZnSe). It crystallizes in the zinc-blende cubic structure (similarly like ZnS), although it is also possible to grow ZnSe crystal in hexagonal wurtzite form [42]. ZnSe has a band gap of energy of size $E_g = 2.67\,eV$ and phonon energy $E_{pn} = 250\,cm^{-1}$. Pure bulk ZnSe crystal is transparent in the wide spectral range from 0.5 up to 22 μm. In contrast, Cr^{2+}-doped ZnSe crystal has a strong absorption band centred around the wavelength of 1.8 μm. The interaction between electronic transitions in the TM^{2+} ions used for the laser generation and the lattice vibrations in the host crystals is robust, causing notable uniform spreading of frequencies, frequently reaching ∼30 % or more of the central frequency. Chalcogenide hosts like ZnSe and ZnS are especially fitting for this purpose, as they facilitate this type of vibronic broadening. Therefore, the Cr^{2+} ions conventional optical

excitation by a pumping source in the wavelength range of 1.5–2.1 µm creates a wide mid-IR emission band between 2 and 3 µm. Despite this, undesired non-radiative multi-phonon relaxation is effectively controlled, even under RT conditions, owing to the limited energy of their highest phonon modes. [58]

Table 1.1: Material properties of selected II–VI host matrix compounds. Structure: ZB – zinc-blende (cubic), WZ – wurtzite (hexagonal). [45, 46]

Material property	ZnS	ZnSe	ZnTe	CdS	CdSe	CdTe
Melting point [K]	2038	1797	1513	2023	1623	1370
Structure	ZB/WZ	ZB/WZ	ZB	WZ	WZ	ZB
Energy gap E_g at 300 K (ZB/WZ) [eV]	3.68/3.91	2.7/3.4	2.39	2.5/2.5	–/1.75	1.47
Lattice constant at 300 K (ZB) a_0 [nm]	0.541	0.567	0.610	0.582	0.608	0.648
Lattice constant at 300 K (WZ) $a_0 = b_0$ [nm]	0.381	0.398	0.427	0.413	0.430	–
(WZ) c_0 [nm]	0.623	0.653	0.699	0.675	0.702	–
Knoop hardness [N/cm^2]	0.18	0.15	0.13	–	–	0.1
Thermal conductivity [W/cm·K]	0.27	0.19	0.18	0.20	0.09	0.01
Refractive index (ZB/WZ)	2.37/2.38	2.5/–	2.72/–	–/53	2.5/–	2.72/–
Absorption coefficient at 10.6 µm [cm^{-1}]	$\leqslant 0.15$	1-2·10^{-3}	–	$\leqslant 0.007$	$\leqslant 0.0015$	$\leqslant 0.003$
Average phonon energy (ZB/WZ) [meV]	16.1/17.1	15.1/–	10.8/–	–/13.9	18.9/25.4	5.8/–

1.5 Properties of TM^{2+} ions based lasers

The Fig. 1.4 shows that the spin of the first excited and ground states of Cr^{2+} and Fe^{2+} ions are the same. Moreover, the energy gap for these levels corresponds to the mid-IR part of the optical spectrum. In the following subsections 1.5.1–1.5.4, there can be found a brief description of results achieved with lasers doped by V^{2+}, Mn^{2+}, Co^{2+}, and Ni^{2+} ions laying at the same row of the periodic table as $Cr^{2+}$and Fe^{2+} ions. More details about these tunable solid-state lasers can be found in [59]. The properties and state-of-the-art results obtained with Cr^{2+} and Fe^{2+} ions doped lasers are described in following Chapter 2.

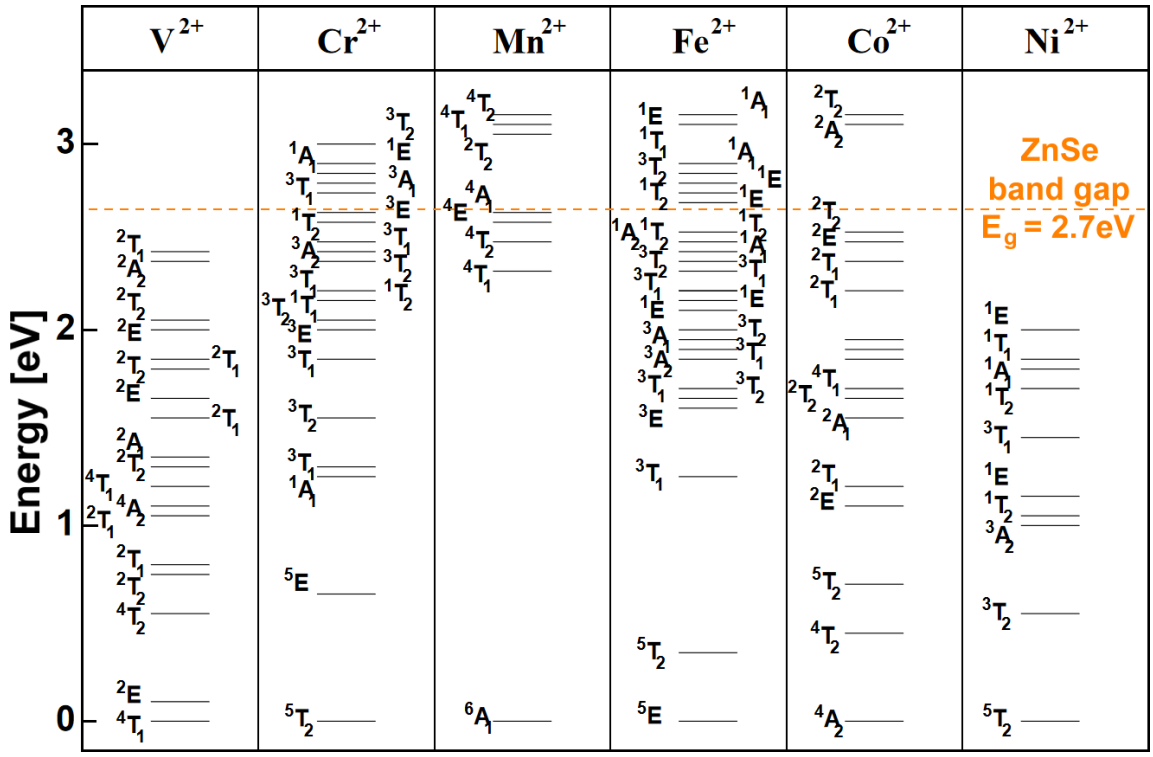

Figure 1.4: Energy level diagram and crystal field splitting in a ZnSe host material – calculated multiplet structure of various TM^{2+} ions ($3d$ impurities). [60]

1.5.1 V^{2+}-doped lasers

V^{2+} ions are iso-structural with Cr^{3+} ions. Therefore, their spectroscopic properties and the structure of their energy levels are similar. The difference is included in the crystal-field splitting parameter Dq which is always less for divalent $3d^3$ ions. [61]

$^4T_2 \rightarrow {}^4A_2$ laser transition of V^{2+} ions was firstly reported with two fluoride crystals. The first pulsed operating V^{2+} ions based laser was a V^{2+}:MgF_2 published by Johnson et al. in 1967 [62]. The investigation of this system continued thanks to its potential as an efficient xenon flash-lamp pumped laser generating radiation at the wavelength of ~1.1 μm. Tunable V^{2+}:MgF_2 laser operation was reported below 200 K in the near-IR range between 1.06–1.16 μm. [62]

The V^{2+} ions laser oscillations were reported also in different host materials. The tunable CW laser operation in a cubic fluoride single crystal with perovskite structure V^{2+}:$CsCaF_3$ was reported in [63]. This system partly overlaps the gap between the tuning range of Co^{2+}- and Cr^{3+}-doped perovskite laser active materials of 1.24–1.33 μm. [63]

V^{2+}-doped halide crystals and their potential as the near-IR laser source were investigated by Knierim et al. [64]. $KMgF_3$, $KMnF_3$, $RbMnF_3$, $CsCaF_3$, $CsCdCl_3$, and NaCl showed broadband emission covering the spectral range between 0.9 and 1.9 μm. All these materials were reported as a suitable for tunable pulsed- or CW-laser operation at RT except the V^{2+}:NaCl from which the laser emission may be expected only for low temperatures below 200 K [64].

1.5.2 Mn^{2+}-doped lasers

The first study about spectroscopic properties of Mn^{2+}-doped $MgAl_2O_4$ was published in [65]. This material is suitable for the laser generation in visible range (fluorescence maximum of 652 nm at 77 K and 550 nm at 300 K) is predicted in the conclusions. Two main absorption peaks at around 423 and 497 nm were observed. However, a limiting factor of excited state absorption (ESA) in this host material due to its crystal field was reported, thus the laser generation was not observed [66]. Since then a lot of various host materials were studied but only luminescence or fluorescence properties were reported [67–69]. Therefore, up to date no direct Mn^{2+}-ions based solid-state laser generation was experimentally confirmed.

1.5.3 Co^{2+}-doped lasers

The $3d^7$ electronic configuration of Co^{2+} ions means that three electrons are required to fill up the $3d$ subshell. Therefore, due to this electron–hole symmetry the structure of the terms of $3d^7$ and $3d^3$ ions is identical, however, the sequence of energy levels is reversed [61]. The first investigated ions among transition metals potentially useful for tunable solid-state laser generation were Co^{2+} and Ni^{2+} already investigated since 1963 by Johnson et al. [70–72].

One of the promising composition, a Co^{2+}:MgF_2, with its tunable range of output oscillation covering the entire fluorescence spectrum (1.63–2.08 μm) was investigated by Moulton et al. [73]. To obtain a broad tuning range, the ESA has to be very low. However, with increasing temperature grow also a number of nonradiative transitions which reduce the quantum yield. This parameter steadily deteriorates by approximately two orders of magnitude from 4 K up to RT. This phenomenon limits the practical use of this laser for temperatures above ∼80 K and ∼225 K in CW and pulsed operation mode, respectively. Different modes of generation such as Q-switched and mode-locking modes have also been explored in Co:MgF_2 [74–77]. A CW mode of Co:MgF_2 laser operation at cryogenic temperatures was also realized [78]. The continuously tunable laser oscillation in the range of 1.6–2.1 μm, with output power of 1–2 W was obtained.

Another investigated material was a Co^{2+}:$KZnF_3$ which also requires a cryogenic cooling due to similar rapid decrease of quantum efficiency with rising temperature as Co:MgF_2 [79]. The laser operation is based on Co^{2+} ions transition of $^4T_2 \rightarrow {}^4T_1$. The laser system operated at single-frequency could be tuned in broad range (i.e. low ESA) of 1.75–2.15 μm with maximum output power of 48 mW (or 55 mW in multimode) while the crystal absorbed about 1.7 W argon ion laser pump radiation in the blue and green visible range. Thanks to double-passing excitation radiation throughout the crystal in the laser cavity, the absorption of pumping energy as high as 80 % was reached. [79]

1.5.4 Ni^{2+}-doped lasers

Since CW Nd:YAG lasers were used for excitation of Ni^{2+}- and Co^{2+}-doped laser active media, their output characteristics were improved in late 1970's [73, 80–82]. However, all host materials doped with these ions require cryogenic cooling. On the other hand, the crystal thermal conductivity increases when it is cooled. Moreover, cooling also greatly reduces thermally induced optical distortion. [83]

Ni:MgF_2 and Co:MgF_2 lasers has been studied extensively in [73,81]. The Ni:MgF_2 laser output power of almost ∼2 W at CW operation mode and continuously tunable oscillation wavelength were obtained with a 28 % optical-to-optical slope efficiency (relative to the crystal absorbed power) at temperature of 77 K. The efficiency was about half than was predicted from resonator loss due to excited state absorption (ESA) phenomenon. [83]

Although its production is difficult, one of the most suitable host material is MgO. One major advantage of Ni:MgO crystal over Ni:MgF_2 is that its absorption band is shifted to be possibly pumped by major and more efficient 1.06 μm Nd:YAG oscillation wavelength than that of 1.32 μm. Moreover, at cryogenic temperatures around ∼80 K, where the thermal conductivity is very high, the average output power of 10 W has been demonstrated by Moulton et al. in [84]. The tunable range of output oscillation was separated into two regions around ∼1.32 μm and ∼1.41 μm corresponding to its fluorescence spectrum peaks. [83]

Other Ni^{2+}-doped laser active materials were also investigated in the matrices of $KMgF_3$ [85], MgF_2, MnF_2 [86], $Ca_2Y_2Mg_2Ge_3O_{12}$ [87], and $Gd_3Ga_5O_{12}$ [88].

Chapter 2

Cr^{2+} and Fe^{2+} doped ZnSe lasers: State-of-the-art

This chapter describes properties of Cr:ZnSe and Fe:ZnSe lasers, their milestones and current state-of-the-art results. The first Sec. 2.1 is devoted to the excitation methods of both crystals where the summary of usually used coherent sources of pumping radiation can be found. Two following sections 2.2 and 2.3 content the historical milestones in the development of the best results obtained with the Cr:ZnSe and Fe:ZnSe lasers in different modes of generation, respectively.

2.1 Cr:ZnSe and Fe:ZnSe excitation methods

Sources for optical pumping of Cr:ZnSe and Fe:ZnSe laser active media are dependent on their spectral characteristics, especially absorption. Therefore, main spectroscopic data of typical Cr:ZnSe and Fe:ZnSe crystals are listed in Tab. 2.1. In following two subsections 2.1.1 and 2.1.2 are summarized several possible coherent sources being used for direct optical pumping of the Cr:ZnSe and Fe:ZnSe lasers, respectively. Moreover, the results of Cr^{2+} and Fe^{2+} ions photo-ionization excitation in visible range are described in subsection 2.1.3 as well as the current research about novel concept of indirect Fe^{2+} ions excitation via the intra-ionic energy transfer which can be found in subsection 2.1.4.

Table 2.1: Main spectroscopic properties of Cr:ZnSe and Fe:ZnSe crystals. [89]

Parametres/Crystal	Cr:ZnSe	Fe:ZnSe
Absorption peak at RT [μm]	1.78	3.10 [44]
Absorption bandwidth at RT [nm]	355 (FWHM)	1360 (FWHM)
Peak absorption cross-section	$87{\cdot}10^{-20}$ cm^2 [40]	$97{\cdot}10^{-20}$ cm^2 [36]
Gain peak at RT [μm]	2.40–2.45	4.35 [44]
Gain bandwidth at RT [nm]	1220 (FWHM) [28]	1550 (FWHM) [35]
Peak emission cross-section	$90–130{\cdot}10^{-20}$ cm^2 [40]	$24{\cdot}10^{-19}$ cm^2 [90]
Saturation intensity [kW/ cm^2]	11	- - -
Luminescence lifetime at 78 K	5.7 μs [44]	57 μs [44]
Luminescence lifetime at RT	4.8 μs	370 ± 25 ns [91]

2.1.1 Sources for direct optical excitation of Cr:ZnSe laser active medium

The overview of several possible sources of coherent optical radiation used for the excitation of Cr:ZnSe lasers is listed in Tab. 2.2. Due to the broad availability of high-brightness fiber lasers, the most attractive are the eye-safe solid-state laser systems for the optical

pumping [45]. The broad absorption band of Cr^{2+} ions in the II–VI chalcogenides spanning over the spectral range of 1.4–2.2 µm, with its absorption maximum at ~1775 nm, allows to possibly use a variety of coherent optical sources for the pumping. Typical absorption spectrum of Cr:ZnSe crystal at room temperature (RT) together with the central laser oscillation lines of several coherent laser systems frequently being used for its pumping (from Tab. 2.2) are presented in Fig. 2.1.

Table 2.2: Overview of different coherent sources typically being used for the optical excitation of Cr:ZnSe lasers.

Laser	Wavelength	Reference
Er:glass	1.53 µm	[92]
Er-fiber laser	1.55 µm	[93, 94]
$Ba(NO_3)_2$ Raman laser	1.60 µm	[95]
InP laser diode	1.65 µm	[96]
Er:YAP	1.66 µm	[97]
InGaAsP laser diode	~1.73 µm/1.92 µm	[98]
Er:YLF	1.73 µm	[99]
Co:MgF_2	1.86 µm	[40]
GaSb laser diode	~1.9 µm/2.0 µm	[100]
Tm-fiber laser	1.90 µm	[101]
Tm:YAP	1.94 µm	[102, 103]
Tm:YAG	2.01 µm	[104]
Cr,Tm,Ho:YAG	2.09 µm	[105]
Ho:YAG	2.09 µm	[44]

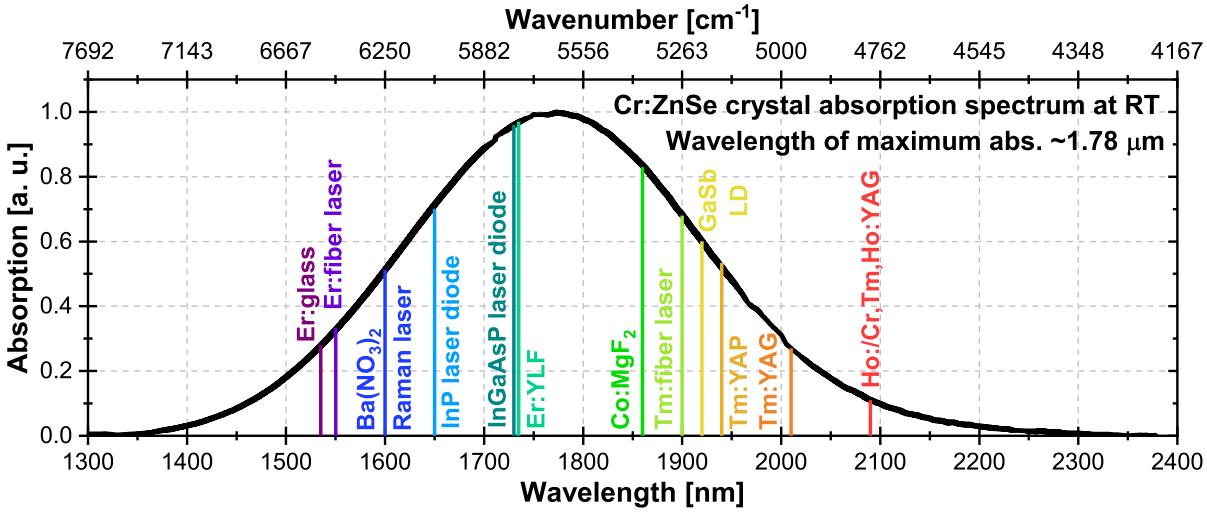

Figure 2.1: Typical absorption spectrum of Cr:ZnSe crystal at RT together with central laser oscillation lines frequently used for its optical pumping.

2.1.2 Sources for direct optical excitation of Fe:ZnSe laser active medium

Similarly like in the case of Cr:ZnSe crystal, the broad absorption band of Fe^{2+} ions in the II–VI host materials spanning over the wide spectral range of 2.2–5.1 µm with its absorption maxima at ~3.1 µm and ~3.7 µm which allows to utilize a wide range of lasers for the pumping. Unfortunately, due to the multi-phonon quenching, the photolumines-

cence (PL) lifetime of Fe^{2+} ions in ZnSe at RT is quite low (less than 300 ns) [91]. Thus the pump sources that are required for Fe:ZnSe laser action need to have pulse durations shorter than the Fe^{2+} ions luminescence lifetime when operating at RT. This obstacle is gradually being overcome thanks to the development of short-pulse, high-intensity pump sources during last years [106]. However, the availability of such short-pulse pump sources at the spectral position of Fe^{2+} ions absorption band of around ~2.50–4.25 μm is still limited. The second option how to extend the Fe^{2+} ions lifetime is to cool the active element down to cryogenic temperature. During the cooling, the amount of phonon transitions is being reduced and the laser oscillation spectrum shifts to the shorter wavelengths. The overview of several possible sources of coherent optical radiation usually used for the excitation of Fe:ZnSe lasers are listed in Tab. 2.3. Typical absorption spectrum of Fe:ZnSe crystal at RT together with the spectral lines of coherent sources possible for its excitation from Tab. 2.3 are presented in Fig. 2.2.

Table 2.3: Overview of different coherent sources being typically used for the optical excitation of Fe:ZnSe lasers.

Laser	Wavelength	Reference
HF electric-discharge laser	2.6–3.1 μm	[107–112]
Er:YLF	2.66 μm	[113]
Cr:ZnSe	2.70 μm	[114]
Er:YAG	2.70 μm	[37]
Er:Y_2O_3	2.74 μm	[115]
Er:YSSG	2.79 μm	[116]
Er:ZrF_4 fiber laser	2.79 μm	[117]
Er,Cr:YAG; Er,Cr:YSGG	2.80 μm	[36, 118]
Er:ZBLAN fiber laser	2.80 μm	[119, 120]
Nd:YAG	2.92 μm	[90]
Er:YAG	2.94 μm	[35, 114, 121–123]
Ho,Pr:$LiLuF_4$	2.95 μm	[124]
Cr:CdSe	2.97 μm	[125, 126]
Fe:ZnSe	4.05 μm	[127]

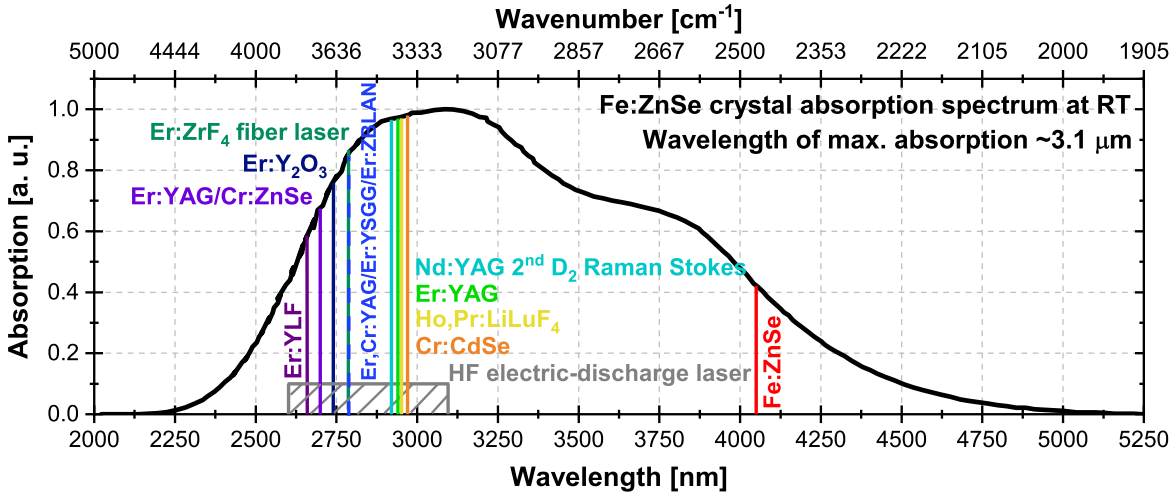

Figure 2.2: Typical absorption spectrum of Fe:ZnSe single crystal at RT together with central laser oscillation lines of realized optical pumping.

Another possible sources for the Fe:ZnSe crystal excitation may be Dy^{3+}-doped solid-state lasers generating radiation close to the maximum of the Fe^{2+} absorption of ~3.2 μm [128, 129]. However, such pumping was not realized yet. There exists another possibility of Fe^{2+} ions excitation by a liquid nitrogen cooled (LN_2-cooled) Fe:ZnSe laser operated at around ~4.05 μm. Although this may at first glance seems impractical, it was shown in [127] that it is possible to pump Fe^{2+} ions to different upper energetic states at around this wavelength. As a result of this excitation the laser oscillations at longer mid-IR wavelengths are generated (in comparison with conventional ~2.9 μm pumping). Moreover, lower nonradiative losses at RT can decrease the oscillation threshold for Fe^{2+} centres at the ~4.05 μm radiation excitation.

Another approach may be, for example, to use the inter-ionic energy transfer from other ions to create inversion of Fe^{2+} ions. Such energy transfer could be realized between Ni^{2+} [130], Co^{2+} [131–133] or Cr^{2+} ions [134] in Fe^{2+} co-doped materials. The advantage of such laser systems is the availability of simpler pumping sources of co-doped ions and the overall compactness of the resulting system. The investigation of Cr^{2+},Fe^{2+} ions co-doped novel laser active materials is an important part of this research described in Chapter 6.

2.1.3 Excitation of Cr^{2+} or Fe^{2+} ions in visible range via photo-ionization

Cr^{2+} and Fe^{2+} mid-IR luminescence in Cr^{2+}- or Fe^{2+}-doped ZnSe crystals can be also obtained under excitation at visible part of the optical spectrum, specifically at 532 nm ≈ 2.33 eV. The energy of this radiation is smaller than the ZnSe bandgap of 2.7 eV ≈ 460 nm [47]. The luminescence is induced by photo-ionization excitation these ions in ZnSe. Mechanisms of Cr^{2+} ions ionization under 532 nm or excitation leading to a strong mid-IR emission were described in [47, 135–138]. The excitation of intra-shell emission of Cr^{2+} or Fe^{2+} ions can be achieved up on processes changing the charge state of Cr^{2+}or Fe^{2+} ions. For example, irradiation of Fe^{2+} ions in the ground state at wavelength of 532 nm leads to their ionization to Fe^{3+} which then recombines with previously released electron from the conduction band. As a result, there is the $(Fe^{2+})^*$ ion in an excited state $^5T_2$ with the same properties as through the direct intra-shell optical excitation [139].

The first demonstration of Cr:ZnSe mid-IR laser oscillation at RT obtained under pumping by the radiation at the wavelength of 532 nm followed by a successful intra-shell emission was published in 2005 by Gallian et al. [47]. This indirect pumping process related to $Cr^{2+} \rightarrow Cr^{1+}$ photo-ionization is realized due to a subsequent hole re-trapping from the valence band proceeding via one of Cr^{2+} intra-shell states. Photo-ionization bands of TM^{2+} ions are typically characterized by large oscillator strengths. Therefore, this type of pumping can be more efficient than ordinary intra-shell excitation and can result in a much more efficient optical pumping. Moreover, this process opens the possibility of laser emission upon direct carrier injection (free electrons and holes), but as well, a construction of compact mid-IR laser system pumped by available and efficient lasers in visible range such as green or blue colour laser diodes or by high harmonic generation (HHG) of near-IR lasers. [47]

Another noteworthy findings by Kernal et al. in 2005 [90] was the identification of mid-IR emission between 3.5 and 5 μm, originating from ionization transitions

($Fe^{2+} \rightarrow Fe^{3+} \rightarrow (Fe^{2+})^*$) of Fe^{2+} ions in the Fe:ZnSe crystal under 532 nm radiation excitation. This discovery holds vital implications for the use of common and efficient visible lasers to optically pump Fe:ZnSe, and it particularly paves the way for achieving broadband mid-IR laser emissions in Fe:ZnSe by the direct introduction of free electrons and holes. [90]

In 2010, Jaeck et al. [138] have presented compelling evidence that infrared photoluminescence, triggered by excitation through a charge-transfer band at 532 nm, can be significantly amplified by introducing an extra electric field to a Cr:ZnSe single crystal. Their findings showcased a notable sixfold amplification of the mid-infrared emission, particularly in the vicinity of the cathode, when an average applied intensity of electric field of 30 kV/cm was employed. This enhanced emission is linked to the heightened concentration of positive charge carriers (holes) near the cathode, which fluctuates with the applied electrical voltage. [138]

2.1.4 Indirect excitation of Fe^{2+} via the intra-ions energy transfer

Pumping sources mentioned in previous subsections can be used for the Fe^{2+} ions excitation, but they are not simple solutions. One approach to make pumping easier is to combine Fe^{2+} ions with various transitional metals (co-dopants) within the same active medium and utilize an energy transfer process between them. This kind of energy transfer mechanism can be effectively employed for indirect pumping of mid-IR laser operations using Fe^{2+} ions. This opens up possibilities for broadband laser action and amplification in the 4–5 μm wavelength range using commercially available pump sources around 1.6–2.1 μm wavelength range.

Previous efforts have been made to achieve Fe^{2+} ions excitation through energy transfer from Ni^{2+} [130], Co^{2+} [132] or Cr^{2+} ions [140, 141]. The first experimental confirmation of laser generation via this transfer only for self-lasing at ~3.9 μm from the Co^{2+},Fe^{2+}:ZnSe and Co^{2+},Fe^{2+}:ZnS at temperatures below ~24 K was reported in 2012 and 2013 by Peppers and Myoung et al. [131, 132]. The study involved the $Co^{2+} \rightarrow Fe^{2+}$ energy transfer via the $^4A_2(F) \rightarrow {}^4T_1(F)$ and $^4A_2(F) \rightarrow {}^4T_1(P)$ transitions at excitation wavelengths of ~1.56 μm and ~0.7 μm in the Co,Fe:ZnSe and the Co,Fe:ZnS materials. The laser oscillations were successfully demonstrated at wavelengths of ~3.6 μm (achieved at temperature range of 14–21 K) in Co,Fe:ZnS under ~1.56 μm excitation, and at ~3.9 μm (at 14 K) in Co,Fe:ZnSe under ~760 nm excitation. [132]

As for energy transfer from Cr^{2+} ions, the research of Kernal et al. [90] from 2005 documented the unprecedented occurrence of energy transfer from Cr^{2+} ions (^5E level) to Fe^{2+} ions ($^5T_2$ level) under excitation at ~1.56 μm. This phenomenon resulted in simultaneous spontaneous emission from the Cr,Fe:ZnSe crystal at RT, spanning an exceptionally broad fluorescence spectral range of 2–3 and 3.5–5 μm. [90]

Another evidence of the possibility of $Cr^{2+} \rightarrow Fe^{2+}$ energy transfer was provided by Wang et al. [142, 143] in 2016/2017. The fluorescence spectra of Fe^{2+} ions under Cr^{2+} ions excitation of Cr,Fe:ZnSe and Cr,Fe:ZnS polycrystalline materials at RT were demonstrated. Their analysis revealed two absorption bands of co-doped samples at ~1.67 and ~4.0 μm, corresponding to the $^5E \rightarrow {}^5T_2$ transition of Cr^{2+} and $^5E(D) \rightarrow {}^5T_2$ (D) transition of Fe^{2+} ions, respectively (see Fig. 1.2). Both Cr^{2+} and Fe^{2+} ions were found to be in the divalent state within the ZnS or ZnSe host materials. The fluorescence spectrum

indicated the presence of energy transfer between Cr^{2+} and Fe^{2+} ions in the tetrahedral ZnS crystal under ∼1.56 µm excitation. The fast and efficient energy transition, facilitated by the favourable overlap of absorption and emission bands of Fe^{2+} and Cr^{2+} ions, allows for the creation of population inversion and laser emission of Fe^{2+} ions under Cr^{2+} excitation at ∼1.56 µm. [143]

The kinetics of the Cr,Fe:ZnSe sample at RT were also studied and published in 2019 by Fedorov et al. [144]. When excited to Cr^{2+} absorption band at the wavelength of ∼1.56 µm, a rapid energy transfer in Cr-Fe centres taking only about ∼290 ns was revealed. This transfer rate closely matches the nonradiative relaxation rate of Fe^{2+} ions in this particular host material at low temperature (78 K). By optimizing the concentrations of Cr^{2+} and Fe^{2+} ions in the ZnSe crystal, an efficient $Cr^{2+} \rightarrow Fe^{2+}$ energy transfer is enabled. This suggests that the efficient pumping of Cr^{2+}-based lasers using Er: or Tm:fiber lasers could also be applicable for Fe^{2+} laser systems generation in future. Moreover, cooling the Cr,Fe:ZnSe crystal significantly suppresses the nonradiative decay of Fe^{2+} ions and results in better overlap between the absorption band of Fe^{2+} and the emission band of Cr^{2+} ions. [144]

The research conducted in 2019 by Antonov et al. [134] verifies the occurrence of rapid energy transfer from Cr^{2+} to Fe^{2+} ions in Cr,Fe:ZnSe polycrystals when excited within the absorption band of divalent chromium. A comparison of Fe:ZnSe and Cr,Fe:ZnSe laser outputs under hydrogen-fluoride (HF) laser pumping shows that the co-doped active element exhibits a twofold increase in the generation threshold (when excited directly in the iron absorption band). However, the authors express doubt about the feasibility of achieving efficient lasing in the 4–5 µm range using the $Cr^{2+} \rightarrow Fe^{2+}$ energy transfer mechanism. [134]

However, one of the latest experimental investigations to this topic provided by Steinmeyer et al. [141] from 2023 has revealed RT rates of excitation via inter-ionic energy transfer in Cr,Fe:ZnSe that are ∼5× higher than what is predicted by elementary Förster transfer theory. This unexpected enhancement greatly boosts the potential energy transfer efficiency. They attributed this enhancement to a prominent contribution of (multi)phonon-assisted excitation transfer, which leads to the observed faster transfer rates. As a proof, in experiments even at RT, maximum transfer efficiencies above 80 % for Fe^{2+} doping densities in the range of $\sim 6 \cdot 10^{18}\,cm^{-1}$ were observed. However, despite this high transfer efficiency, the overall photoluminescence (PL) efficiency remains relatively poor, below 5 %. Despite previous attempts to improve this efficiency by using higher doping levels, this approach faces limitations due to concentration quenching effects. [141]

They proposed that instead of increasing doping concentrations further, the key to efficient utilization of the Förster transfer process lies in operating Cr,Fe:ZnSe in low temperature range from ∼170–190 K (corresponding to -80 °C to -100 °C). In this temperature range, nonradiative losses of the Fe^{2+} ions are significantly suppressed, and the transfer efficiency only reduces by 10 % to 20 % compared to that at RT. With careful temperature control, overall efficiencies above 50 % seem feasible. By considering even higher doping levels than those used in this study, overall efficiencies larger than 80 % could be expected. [141]

Tomm et al. conducted a study [140] published in 2023 to analyse the transfer efficiency in both Cr^{2+} ions or Fe^{2+} ions singly-doped and six Cr^{2+},Fe^{2+} co-doped ZnSe crystals using the time-resolved photoluminescence (PL) spectroscopy. A key focus was comparing

the intensities of the PLs emitted by Cr^{2+} and Fe^{2+} ions. The kinetics of Cr^{2+} and Fe^{2+} emissions in the different crystals exhibited a consistent pattern. Specifically, when the co-doped samples in the Cr^{2+} absorption band were resonantly excited, clear proof of efficient $Cr^{2+} \rightarrow Fe^{2+}$ excitation transfer emerged. This evidence included a rapid initial rise time of ~60 ns for the transient, a peak occurring ~200 ns after the peak of the excitation laser, and a prolonged Fe^{2+} photoluminescence decay time of ~1 µs. The long decay time for Fe^{2+} PL, despite the short ~380 ns lifetimes of Fe^{2+} ions, indicates replenishment via the $Cr^{2+} \rightarrow Fe^{2+}$ transfer process. [140]

This analysis of the PL measurements revealed a surprising finding corresponding to [141]. The observed $Cr^{2+} \rightarrow Fe^{2+}$ transfer is much more efficient (with efficiencies $\geqslant 80\,\%$) than it was theoretically expected. Even accounting for nonradiative losses of Fe^{2+} ions, the overall efficiency remains significantly higher than the estimation by Fedorov et al. in [144]. Furthermore, they suggested that excessive nonradiative losses of the Fe^{2+} ions could potentially be mitigated through carefully adapted cooling of the co-doped laser crystals. If this challenge will be addressed successfully, the $Cr^{2+} \rightarrow Fe^{2+}$ transfer could lead to a useful pumping scheme for short-pulse compact mid-IR laser sources. [140]

As can be seen from above mentioned results, all published works related to the topic of intra-ionic energy transfer to Fe^{2+} ions were predominately spectroscopically based studies and the $Cr^{2+} \rightarrow Fe^{2+}$ energy transfer leading to the successful Fe^{2+} ions laser oscillations was not reported yet up to this work. The successful $Cr^{2+} \rightarrow Fe^{2+}$ inter-ionic energy transfer obtained under specific conditions in the Cr^{2+},Fe^{2+}:$Zn_{1-x}Mn_xSe$ and Cr^{2+},Fe^{2+}:$Zn_{1-x}Mg_xSe$ single crystals resulting in generation of the Fe^{2+} ions laser oscillations was described and published as part of this work in several papers and presented at international conferences, to the best of our knowledge, for the first time. In the experimental Part III in Chapter 6 of this thesis, the measurements and their results obtained with these single crystals at low temperatures (78–220 K) under different pumping wavelengths (~1.71, ~1.73, and ~1.94 µm) and pump pulse durations (~hundred of nanoseconds and units of milliseconds) are described.

2.2 State-of-the-art: Cr:ZnSe lasers

Cr^{2+} laser active ion is suitable for generation of coherent radiation in mid-infrared (mid-IR) part of optical spectrum in range of 1.9–3.4 µm, when doped into various zinc-chalcogenide hosts such as ZnS or ZnSe. The most famous among these Cr^{2+} ions doped II–VI compounds is the Cr^{2+}:ZnSe laser active medium.

The first demonstration of lasing at RT has been successfully achieved using Cr:ZnS and Cr:ZnSe crystals in 1996 by DeLoach et al. [40]. A Co:MgF_2 laser operating at 1.86 µm, served as the pump source for the Cr^{2+} ions excitation. Slope efficiencies of up to 20 % were recorded for both Cr:ZnS and Cr:ZnSe laser systems, which were tested within a confocal laser resonator cavity featuring output coupler with transmission of $T_{OC} \approx 7.5\,\%$. The potential for a compact system that can be pumped by laser diodes and generates tunable mid-IR laser radiation underscored the importance of continual research of these novel materials that begun since this paper has been published. [40]

Cr:ZnSe exhibits a broad absorption band centred around ~1.8 µm and can be pumped by various pump sources including Tm-doped lasers emitting at ~1.9 µm [101], Er:fiber laser at ~1.55 µm [94], infrared laser diodes [98, 145] (the first LD pumping of Cr:ZnSe

in a side-pumped configuration was demonstrated in 1997), and since these materials are semiconductors, they could be also pumped electrically according to [138, 146]. The tetrahedral coordination of the Cr^{2+} ion in the crystal lattice resulting in a great emission cross-section of more than 10^{-18} cm^2 [38]. The small quantum defect allows an efficient RT operation of Cr^{2+}:ZnSe laser with continuous broadband oscillation wavelength tuning (1.88–3.10 μm with 4 different sets of cavity mirrors [28]). Thanks to this wide tuning range of over 1.2 μm, the Cr:ZnSe laser is often referred to as the Ti:sapphire laser of the mid-IR part of optical spectrum. The excited state absorption (ESA) transitions from the upper state are spin-forbidden. Altogether this ensures that Cr:ZnSe has the highest gain among all vibronic solid-state lasers and enables efficient broadband RT operation [147]. For instance, Cr:ZnSe with multi-watt output power and a slope efficiency of 73 % reported in [148] is very close to its quantum limit of 77 %. Moreover, due to extremely broad gain, the Cr:ZnSe is a suitable laser active medium for ultrashort pulse generation. For instance, as short as 45 fs mode-locked pulses were reported by Nagl et al. in 2019 [29]. [38, 149]

Therefore, Cr:ZnSe lasers are very interesting as affordable, compact, RT operational and broadly tunable mid-IR laser sources for use in a variety of remote sensing applications [149]. The shortest tunable oscillation wavelength of 1.88 μm was obtained in Cr:ZnSe crystal in [28] and the longest central oscillation wavelength of Cr^{2+}-doped laser at 3.6 μm was reported with the CdSe host material in [150]. A review of spectroscopic, laser and non-linear properties of II–VI host materials doped with Cr^{2+} ions is given in [19].

Except the bulk Cr:ZnSe laser materials, a novel Cr:ZnSe fiber laser was reported by Sparks et al. in 2020 [151]. Up to date, fiber lasers were usually constrained (except some special fibers such as ZBLAN) to the visible and near-IR parts of the electromagnetic spectrum due to silica's limitations in transmission (above ∼2 μm). To expand this wavelength range into the mid-IR range, crystalline II–VI optical gain materials doped with transition metals can be utilized. Unfortunately, the conventional glass drawing techniques cannot be applied to shape these materials into optical fibers. A novel method involving high-pressure chemical vapour deposition (HPCVD) was introduced for creating fiber cores made of silica-cladded ZnSe that are uniformly doped with Cr^{2+} ions. Experimental optical pumping demonstrated that these fibers exhibit a lasing threshold behaviour, effectively serving as lasers in mid-IR spectral range. Furthermore, simulations using finite element analysis indicated that the unwanted thermal effects commonly seen in bulk Cr:ZnSe crystals are greatly reduced in this fiber-based geometry. For instance, when employing a diamond cladding, the laser emission from a 15 μm core diameter made of Cr:ZnSe is projected to achieve up to ∼0.33 kW of output power. It significantly surpasses the bulk Cr:ZnSe laser gain media outputs and would be restricted primarily by the material's damage threshold. Cr:ZnSe fiber gain-switched lasing was seen to arise above 0.5 W of average pump power, or 50 μJ per pulse, and the spectral output around the wavelength of ∼2.3 μm was stable and repeatable. [151]

The overview of milestones in development of Cr:ZnSe lasers can be found in Tab. 2.4. The following subsections summarize the state-of-the-art results obtained with Cr:ZnSe laser systems up to date in various modes of operation: 2.2.1 – Q-switched mode, 2.2.2 – mode-locked regime, and 2.2.3 – continuous wave (CW) regime.

Table 2.4: Milestones in development of Cr:ZnSe lasers.

Cr:ZnSe laser milestone	Year	Parameters	Ref.
First lasing	1996	RT/$\eta \approx 20\,\%$/$\sim$2.35 µm	[40]
First diode-pumped laser	1997	side pumped; 0.3 W	[145]
First CW laser	1999	380 mW/$\eta = 63\,\%$	[102]
First active mode-locked laser	2000	82 mW/4.4 ps	[152]
First passive Kerr lens mode-locked laser	2009	300 mW/100 fs	[153]
First graphene-based SAM mode-locked laser	2013	80 mW/226 fs/77 MHz	[154]
First Cr:ZnSe fiber laser	2020	804 mW/$\sim$2.3 µm	[151]
CPA max. peak power/duration/energy	2020	115 GW/39 fs/6.2 mJ	[155]
The widest tunable range	2006	1.88–3.10 µm	[28]

2.2.1 Cr:ZnSe lasers in Q-switched/gain-switched mode

To obtain an efficient nanosecond pulsed operation of Cr:ZnSe, the pulsed pumping due to the short upper excited level lifetime of $\sim$6 µs is required. [149, 156]

The first Q-switched pulses from a Cr:ZnSe laser were demonstrated in 2003 by W. J. Alford et al. [157]. Both acousto-optic (AO) and electro-optic (EO) Q-switching was realized resulting in the $\sim$15 ns output pulses with the output energy of 70 µJ under 700 µJ of pumping. The gain-switched mode was presented as well with the output power of 12.5 W at a wavelength of $\sim$2.5 µm. For all experiments, the crystal was pumped by a Q-switched Tm:YAP (Tm:YALO, Tm:$YAlO_3$) laser with maximum output power of 30 W. [157]

By adjusting a laser cavity intended for the passive mode-locking operation with SESAM by its shortening resulted in a weaker focus on the SESAM and the passive Q-switched operation could also be obtained. In this case a 50 ns pulses with a 1 MHz repetition rate, and peak powers up to 10 W was reported in [158]. The crystal was pumped again by a Tm:YAP laser with the mean CW output power of 2.4 W. [158]

A powerful Cr:ZnSe laser pumped by the Q-switched Tm:YAP laser at 7 kHz repetition rate with average output power of 18 W at 30 W of absorbed power was presented in [103]. Moreover, a tunable radiation at up to 10 W output power in a wide range of 2.1–2.85 µm was achieved with an acousto-optical filter located inside the laser cavity. [103]

A stable Q-switched Cr:ZnSe laser realized with the graphene saturable absorber was demonstrated in 2015 for the first time by Wang et al. [159]. Under an absorbed pump power of 1.8 W, a maximum average output power of $\sim$0.25 W was obtained with an optical-to-optical conversion efficiency of 14 % and a slope efficiency of 19.6 %. It corresponds to the highest single pulse energy of 1.66 µJ. The shortest pulse width and highest pulse repetition rate were 157 ns and 169 kHz, respectively. The M^2 beam parameter of great value of $\sim$1.1 was obtained. These results shown the graphene passive Q-switching of Cr:ZnSe lasers as a simple and cheap method. [159]

2.2.2 Cr:ZnSe lasers in mode-locked regime

Femtosecond lasers operating at high repetition rates in the mid-IR spectral range are of great interest for a multitude of applications such as an ultrafast, broadband and high-resolution spectroscopy, frequency metrology, quantum optics, and the synthesis

of optical frequency combs in this spectral range. During last years there was a great demand of the developing laser system with train of ultrashort pulses in the mid-IR range at ∼2.5 µm and beyond, where organic and inorganic molecules have the strongest absorption lines associated with fundamental rotational-vibrational transitions (more details about mid-IR spectroscopy can be found in following chapter – Sec. 3.1). [160]

The first active mode-locking of the Cr:ZnSe laser operating near ∼2.5 µm was published by Carrig et al. in 2000 [152]. This laser generated 4.4 ps transform-limited Gaussian-shaped pulses with the average output power of 82 mW. Another active mode-locking of Cr:ZnSe laser with obtained 15–30 ps pulses as well as acousto-optically initiated passive mode-locking with shortening of generated pulses down to ∼4 ps (400 mW) was reported by Sorokina et al. in 2001 [161].

The passive mode-locking of Cr^{2+} ions doped II-VI lasers [162, 163] is a great alternative to generate high-repetition rate femtosecond mid-IR pulses compared to the complicated ultrafast sources based on downconversion of near-IR laser's radiation in difference frequency generation (DFG) and optical parametric oscillators (OPO) setups. The first achievement of Cr:ZnSe femtosecond pulses was presented by Sorokina et al. in 2006: a continuous-wave (CW) Cr:ZnSe laser passively mode-locked by an InAs/GaSb SESAM generated ∼106 fs pulses at up to 75 mW output power at the wavelength of ∼2.5 µm [164]. However, it was quickly overcame by the same group by 80 fs pulses (10 optical cycles) at 80 mW output power with 1.6 W pump power next year [165]. The passive Kerr lens mode-locking (KLM) in polycrystalline Cr:ZnSe has in consequence notable improvements of the output parameters in terms of pulse energy, average power, and pulse duration. More details about this method of ultrashort laser pulse generation in Cr:ZnSe materials and its further improvements can be found in [29, 153, 160, 166–170].

Cr:ZnSe Kerr lens passive mode-locking was for the first time achieved in 2009 by Sorokin et al. [153] and within the same year also by Cizmeciyan et al. [166]. It resulted in the first frequency comb generated directly from a solid-state gain-stage based oscillator in the mid-IR spectral region featuring numerous absorption lines from vibrational resonances of many molecules [171].

The first Cr:ZnSe passive mode-locking based on saturable absorption of graphene monolayer applied onto a CaF_2 substrate was published by Cizmeciyan et al. [172] in 2013. The laser system generated pulses lasting 226 fs at a repetition rate of 77 MHz, yielding an average output power of 80 mW with time-bandwidth product (TBP) of ∼0.39. [172]

Wang et al. reported in 2017 [160] a self-starting KLM Cr:ZnSe femtosecond laser pulses with a minimum duration of 47 fs operating at wavelength around ∼2.4 µm at RT. Such a short pulse duration corresponds to only 6 optical cycles which is very close to the transform-limit of ∼40 fs. The excitation was provided by the Er:fiber laser with a linearly polarized output radiation at 1.57 µm in this case. Average output power of 250 mW at repetition rate in the range from 140 to 300 MHz was demonstrated. [160]

Another group of Nagl et al. reached the Cr:ZnSe laser pulse durations of 45 fs at wavelength of 2.4 µm and a repetition rate of ∼65 MHz in 2019. KLM oscillator was directly pumped by a single InP diode at 1.65 µm. Laser generated train of pulses with an average output power of over 0.5 W. [29, 170]

However, up to date, the shortest pulses generated by Cr:ZnSe laser were reported by Wang et al. in 2022 [173]. Laser was operated at RT and employs KLM. This system generated pulses spanning four optical cycles. Notably, the laser polycrystal

has undergone hot isostatic pressing (HIP) treatment. The individual pulse duration of only 34 fs at the wavelength of 2.4 μm, with a repetition rate of 171 MHz were reported. This laser system exhibited the capability to achieve average output powers of up to 150 mW. Moreover, a comparison conducted experimentally between the treated polycrystal and an untreated counterpart underscores the advantageous impact of HIP treatment on facilitating mode-locking behaviour in this active material. [173]

More details about mid-IR femtosecond pulses generation with lasers based on Cr^{2+} ions can be found in a review paper [162] or [174].

2.2.3 Cr:ZnSe lasers in CW operation mode

The first Cr:ZnSe laser operated in CW mode at RT with the slope efficiency as high as 63 % and the output power of 380 mW pumped by Tm:YAP laser at 1.94 μm was presented by Wagner et al. in 1999 [102, 175].

The first diode-pumped crystalline CW Cr:ZnSe laser operated at RT with output power of 65 mW was presented by Sorokin et al. in 2001 [176, 177]. Since then, the Cr:ZnSe laser output power slope efficiency were improved many times. There was enormous potential of Cr:ZnSe laser for its compactness, efficiency and cost-effectivity thanks to availability of novel 1.7–2 μm laser diodes for reasonable prices. The similar Sorokin's group also reported the CW laser operation tunable over 350 nm with the mean output power up to 70 mW at 460 mW of the absorbed pump power (17.5 % slope efficiency) in 2002 [178].

Moskalev et al. [179] presented the Cr:ZnSe CW laser operation with 35 % slope-, and 24 % real optical efficiency with up to 400 mW of output power in 2010. Tunable range of 2.2–2.7 μm was also demonstrated [179].

We could observe the similar improvement in the case of CW (thulium or erbium) fiber lasers used for Cr:ZnSe excitation. A Tm:fiber-laser pumped Cr:ZnSe bulk CW laser with an output power of 6.5 W as well as a Tm:fiber laser or laser-diode-stack pumped Cr:ZnSe thin disk CW laser with almost 2 W of output powers were presented in 2012 by Renz et al. [180]. The same group improved their CW thin disk laser output power up to 5 W within the next year [181]. The group of Stites et al. was working on the optimization of Cr:ZnSe thin disk laser by increasing the pump beam diameter [182].

Up to date, the highest Cr:ZnSe CW laser output power with levels of up to 140 W near the peak gain at the wavelength of ∼2.5 μm, and 32 W at 2.94 μm with corresponding optical efficiencies of 62 % and 29 %, respectively, was reported by Moskalev et al. [183]. This novel approach employs a pioneering method involving the rapid scanning of the collinear pump beam and laser mode across the Cr:ZnSe gain medium that allowed to virtually eliminate thermal lensing effects and to obtain such high output power levels together with a very high optical-to-optical efficiency. These results suggested the potential to achieve output powers in the kW range within the spectral domain of 2–3 μm and beyond. These findings clearly indicate the maturity of Cr:ZnSe and Cr:ZnS laser systems, rendering them suitable for practical applications in material processing across medical, industrial, and cutting-edge research fields. [183]

2.3 State-of-the-art: Fe:ZnSe lasers

In contrast to Cr^{2+}:ZnSe laser, absorption and fluorescence spectra of the Fe^{2+}:ZnSe active medium are shifted farther to the mid-IR part of the optical spectrum. The shortest oscillation wavelength of Fe^{2+} ions at 3.49 μm was demonstrated with ZnS host material [184] and the longest at around ~6.8 μm was achieved in CdTe matrix [185, 186].

Unlike Cr^{2+} ions, mid-IR transitions in the Fe^{2+}:ZnSe have a strong multi-phonon quenching with increasing temperature that strongly limits lasing capabilities (Fe^{2+} ions lifetime shortening) of this material [13, 149]. The first laser oscillations at the wavelength of ~3.53 μm from a Fe^{2+}-doped n-InP semiconductor crystal at very low temperature of only ~2 K was demonstrated in 1983 by Klein et al. [139].

The first free-running spikes operation of tunable Fe:ZnSe laser system operating in a spectral range of 3.98–4.5 μm was presented in 1999 by Adams et al. [37] for temperature from 15 K up to 180 K. The first RT Fe:ZnSe laser in gain-switch operation was reported by Kernal et al. [90] in 2005 together with the spectral tunability of laser oscillation in the range of 3.9–4.8 μm.

The free-running (FR) mode of operation was also studied. For instance, Frolov et al. in 2018 [187] presented a comprehensive assessment of the Fe:ZnSe laser's performance as a highly efficient and extensively tunable laser source within the 4 μm spectral range, utilizing an electrically cooled crystal. In FR mode, they showcased an impressive 7.5 J output energy with an optical-to-optical efficiency of 30 %. However, the increase of output energy is constrained by thermal-optical effects due to a fixed pump spot diameter. Additionally, when employing an AR-uncoated crystal, one of the factors limiting the tuning range is the onset of lasing within the cavity formed just by the crystal polished facets. [187]

Similarly as in the case of the Cr:ZnSe the CW Fe:ZnSe mid-IR optical fiber laser was reported by Coco et al. in 2020 [188]. It was the first reported solid-state fiber laser with direct laser emission generated beyond 4 μm that showed a new possibility of mid-IR laser generation development. Thus it was the first demonstration, a low slope efficiency of only 0.1 % was reported. It can be explained due to multiple contributing factors. Initially, it can be attributed to the substantial difference in refractive indices between silica ($n \approx 1.38$) and ZnSe ($n \approx 2.42$), combined with the considerable fiber core diameter, which enables to optical fiber to accommodate numerous modes, reaching into the thousands. Furthermore, the presence of the central void influences the mode arrangement, preventing the support of a preferable Gaussian-mode profile. [188]

The overview of milestones in development of Fe:ZnSe lasers can be found in Tab. 2.5. The state-of-the-art results obtained with Fe:ZnSe laser systems up to date in various modes of operations are summarized in the following subsections: 2.3.1 – Q-switched mode, 2.3.2 – mode-locked regime, and 2.3.3 – continuous wave (CW) mode.

Table 2.5: Milestones in development of Fe:ZnSe lasers.

Fe:ZnSe laser milestone	Year	Parameters	Ref.
1st lasing of Fe^{2+} ions in InP	1983	T = 2 K/~3.53 μm	[139]
1st lasing of Fe^{2+} ions in II–VI host	1999	15–180 K/12 μJ/~3.98 μm	[37]
1st room temperature lasing	2005	~4.4 μm/5 ns	[90]
1st CW laser	2008	160 mW/~4.06 μm/$\eta \approx 56$ %	[125]
1st energy transfer pump ($Co^{2+} \rightarrow Fe^{2+}$)	2013	T = 14–21 K/~3.6 μm	[132]
1st mode-locked laser	2020	415 mW/732 fs/100 MHz	[120]
1st Fe:ZnSe fiber laser	2020	0.4 mW/~4.12 μm/$\eta \approx 0.1$ %	[188]
CPA based on Fe:ZnSe laser	2019	23 GW/150 fs/3.4 mJ	[189]
The widest tunable range	2019	3.60–5.15 μm	[35]

2.3.1 Fe:ZnSe lasers in Q-switched/gain-switched mode

The Fe:ZnSe lasing in a gain-switched mode at the wavelength of 4.4 μm at RT was demonstrated for the first time in 2005 by Kernal et al. in [90]. This laser generation was accomplished within a non-selective cavity setup under 2.92 μm excitation, featuring a pulse duration of 5 ns. Further experiments were performed in a Littrow mount configuration with a selective cavity, showcasing tunable oscillation of the Fe:ZnSe crystal across a spectral range of 3.9–4.8 μm while operating at RT. This research was also focused on examining the absorption and emission characteristics of Fe^{2+}-doped and Cr^{2+},Fe^{2+}-doped ZnSe crystals. These investigations were conducted at both RT and low temperatures. The emission behaviour of Fe^{2+} ions during the $^5E \rightarrow {}^5T_2$ transition was deduced from spectroscopic assessments at RT. The study is divided into three distinct excitation methods of getting mid-IR emission of Fe^{2+} in ZnSe: i) standard optical excitations (at 2.92 μm) of Fe^{2+} ions first excited state ($^5T_2$), ii) excitation through the ^5E level of the co-dopant Cr^{2+} ions (at 1.56 μm), and iii) excitation via the photo-ionization transition of Fe^{2+} ions (at 532 nm). ii) and iii) excitation methods were already mentioned in subsection 2.1.3. [90]

In 2007, Akimov et al. [190] have successfully showcased effective pulsed laser operation within a Fe:ZnSe single crystal at RT. The achieved results include an output energy of 1.42 mJ, an input energy slope efficiency of 11.3 %, and the slope efficiency with respect to the absorbed energy of 17 % (with a quantum efficiency of 25 %). The laser's spectrum can be seamlessly tuned over a wide range of 3.9–5.1 μm by utilizing a dispersive resonator using a prism. As a result, the complete continuous tuning span of the Fe:ZnSe laser, when considering the outcomes acquired during crystal cooling at 4 K, covers the spectral interval from 3.77 up to 5.1 μm. The luminescence decay time from the upper laser level was determined to be 370 ± 25 ns at a temperature of 293 K. [190]

Myoung et al. in 2011 [118] have shown that by utilizing post-growth thermal diffusion from the metal phase highly doped Fe:ZnSe gain media with excellent optical quality for mid-IR laser applications can be created. Their results brought a significant fourfold enhancement in the output energy of the gain-switched Fe:ZnSe laser compared to previous methods. When excited by the Q-switched co-doped Cr,Er:YSGG laser (at ~2.8 μm) with specific parameters (33 mJ pump energy, 0.35 J/cm^2 energy density, 20 ns pulse duration, and 6.7 Hz repetition rate), they achieved a maximum output energy of 4.7 mJ at 4.3 μm (corresponding to a maximum peak power of 0.3 MW) and 3.6 mJ at 4.37 μm

at both 236 K and 300 K temperatures, respectively. This output was primarily limited by the available pump energy. The laser's threshold remained relatively constant at ~8 mJ across the studied temperature range. Notably, the laser slope efficiencies decreased from 19 % to 16 % as the temperature increased from 236 K to 300 K. [118]

A successful demonstration of passively Q-switched laser oscillation using Fe^{2+} ions within ZnSe, achieving high average power was demonstrated by Evans et al. in 2014 [191]. To achieve Q-switching, a semiconductor saturable absorber mirror (SESAM) was employed as the passive element. Using the OC with the reflectivity of $R_{OC} \approx 60\,\%$, the laser achieved a pump-limited output power of 515 mW. The laser operated at a central oscillation wavelength of ~4.05 nm. The pulse repetition frequency (PRF) reached ~850 kHz at maximum power, yielding a minimum pulse width of 64 ns (FWHM). The resulting output pulse energy and peak power exceeded 600 nJ and 8.3 W, respectively. The average output power was primarily constrained by the available pump power and displayed a slope efficiency of 22 %, maintaining consistent efficiency without thermal roll-off. The beam quality was assessed with a value of $M^2 \leqslant 2.6$. The temporal stability of the pulsed output, revealing the significant influence of thermal effects on the PRF of the output was also studied. [191]

A very wide tunable range spanning from 3.60 μm to 5.15 μm at RT from the gain-switched Fe:ZnSe lasers was reported by Fedorov et al. in 2019 [35]. The laser was pumped by a mechanically Q-switched Er:YAG laser operating at ~2.94 μm. Notably, a maximum output energy of 5 mJ was achieved with a pump energy of 15 mJ. They also presented the effective utilization of the Q-switched oscillation regime for Fe:ZnSe lasers pumping, although it required the fabrication of large scale Fe:ZnSe gain media. This approach holds promise for the advancement of high-energy, short-pulse solid-state systems generating in the wide mid-IR spectral range. [35]

Karki et al. presented in 2020 [123] the initial achievement of RT gain-switched lasing in a Fe:ZnSe hot-pressed ceramic sample. This was accomplished through the use of ~2.94 μm radiation from a mechanically Q-switched Er:YAG laser operating at repetition rate of 3 Hz. Under quasi-collinear pumping, a maximum output energy of 41 mJ with a pulse duration of 120 ns (FWHM) was obtained. The slope efficiency, calculated in relation to absorbed energy, was found to be 25 %. Shifting to a collinear pumping setup, a maximum output energy of 8 mJ with a slope efficiency of 25 % concerning absorbed energy (limited by input mirror optical damage threshold) was achieved. [123]

The performance of a pulse Fe:ZnSe laser pumped by an Er:YAG laser with optical chopper Q-switching was studied by Xu et al. in 2023 [192]. The Fe:ZnSe laser's maximum energy per single pulse reached 10 mJ, accompanied by an 80 ns pulse width, a slope efficiency of 35 %, and a central oscillation wavelength of 4.4 μm at RT. Furthermore, the directly Q-switched Fe:ZnSe laser through optical chopper excitation was explored, utilizing a free-running Er:YAG laser for its pumping. Through this approach, a mid-IR laser output of 2.7 mJ with a pulse width of 200 ns at 80 K was achieved. These findings hold the potential to advance the progress of pulse mid-IR solid-state Fe:ZnSe lasers in future. [192]

2.3.2 Fe:ZnSe lasers in mode-locked regime

Passive mode-locking of infrared lasers is conventionally achieved through the utilization of semiconductor saturable absorber mirrors (SESAM). However, the development of such devices beyond 3 μm wavelengths has not yet been realized. Consequently, for passive mode-locking within the mid-IR range, graphene emerges as the most fitting material due to its distinctive attributes that enable it to operate as a saturable absorber across an exceptionally broad span of wavelengths. Graphene has been successfully employed in the context of Q-switching [159] and mode-locking [172] in numerous solid-state and fiber lasers. Unlike SESAM, graphene lacks spectral selectivity, which eliminates constraints on generation bandwidth and, subsequently, achievable pulse duration. The attainable output power is commonly restricted by the damage threshold of the graphene itself. In comparison to alternative techniques for generating mid-IR femtosecond radiation, such as non-linear optical conversion and carving out a portion of the supercontinuum, the mode-locked laser oscillator yields superior performance in terms of both high average power and the quality of the beam and spectrum shape. [120]

The extensive emission spectrum and the presence of high-power CW pump sources enable the potential for achieving mode-locking in the Fe:ZnSe. The first report of cryogenically cooled mode-locked laser Fe:ZnSe laser was reported by Ongstadt et al. [193] in 2018. A polycrystalline Fe:ZnSe element, positioned at a Brewster angle and cooled to 78 K, exhibited laser generation at ∼4.1 μm. Passive mode-locking was achieved, resulting in the generation of pulses with a duration of 8.9 ps. However, the available information regarding this remains limited and is not extensively documented in other publicly accessible references. [120]

The first successful demonstration of the femtosecond mode-locking of a Fe:ZnSe laser was introduced by Pushkin et al. in 2020 [120]. Utilizing a monolayer graphene saturable absorber deposited on a BaF_2 substrate, laser pulses at a repetition rate of 100 MHz, delivering an average power of 415 mW were generated. The duration of these pulses, determined through the first-order autocorrelation function, were measured as $\sim 732 \pm 76$ fs. The spectral width of the measured lasing spectrum of 42 nm, aligning well within measurement error margins and confirming the pulse width derived from the first-order autocorrelation analysis. Notably, the Kerr lensing effect within the Fe:ZnSe laser cavity was observed. This contribution effectively bridges an operational gap in the Fe:ZnSe realm, opening doors for the advancement of highly potent, ultrafast, and high-repetition-rate mid-IR sources. Moreover, the Fe:ZnSe laser pulses can be compressed into ultrashort durations following spectral broadening in chalcogenide fibers. By adopting a similar methodology based on different host materials of Fe:CdSe [194] and Fe:CdTe [185] crystals, it is conceivable to design mode-locked oscillators targeting longer wavelengths, such as 5–6 μm. [120]

2.3.3 Fe:ZnSe lasers in CW operation mode

The first CW Fe:ZnSe laser operation at RT was realized by group of Voronov et al. in 2008 [125]. A liquid-nitrogen-cooled Fe:ZnSe was pumped by a Cr:CdSe laser at 2.97 μm. The central laser oscillation wavelength was obtained at ∼4.06 μm. The maximum laser output power of 160 mW with the 56 % slope efficiency was reported. [125]

Five years later, the group of Evans et al. [195] successfully attained CW output power

of $\geqslant 840\,\mathrm{mW}$ from Fe:ZnSe laser at the wavelength of $4.14\,\mu\mathrm{m}$ longitudinally pumped by two Er:YAG lasers from opposite sides. The exceptional beam quality of $M^2 < 1.2$ was reached. The discrete tuning of the CW Fe:ZnSe central laser oscillation wavelength was demonstrated for the first time. This tuning span ranged from a minimum of $\sim 3.84\,\mu\mathrm{m}$ to a maximum of $\sim 4.34\,\mu\mathrm{m}$, showcasing nearly $\sim 500\,\mathrm{nm}$ of tunable range. This tuning could be continuously variable through the utilization of a dispersive tuning element. Notably, given that nearly $200\,\mathrm{mW}$ of output power was achieved at these wavelength extrema, it was probable that the effective tuning range for CW Fe:ZnSe extends even far beyond that range. Disregarding the impact of coupling losses, an optical efficiency of the Fe:ZnSe laser at 39 % at maximum output power was confirmed. The ultimate output power of the laser was limited by the available pump power, and no indications of thermal roll-off were observed even at maximum output levels. Furthermore, these findings demonstrated that the deterioration of laser performance due to thermally activated nonradiative quenching correlated well with obtained temperature-dependent lifetime data. [195]

As it was said, the output power of Fe:ZnSe laser was limited by the pump power of excitation laser used. Therefore, two years later, another study of the same group of Evans et al. [115] has focused on implementing a more stable resonator configuration for the Er:Y_2O_3 pumping laser to effectively manage thermal lensing effects. A CW Fe:ZnSe laser pumped by such improved excitation laser was presented. According to calculations and reported 22 % efficiency achieved in this study, it should be feasible to achieve an output power exceeding $2.25\,\mathrm{W}$ from the Fe:ZnSe laser if modifications were made to enhance the pointing stability of the Er:Y_2O_3 lasers pumping beam. This underscores the potential for a stable, high-power pump source to drive the performance of Fe:ZnSe lasers into the multi-watt range. [115]

Up to date, the highest CW output power reached with the Fe:ZnSe laser was reported by Martyshkin et al. in 2017 [196]. The active medium was cooled by liquid nitrogen, operating in a non-selective cavity configuration, with an impressive output power of $9.2\,\mathrm{W}$. The central laser oscillation wavelength of $\sim 4.15\,\mu\mathrm{m}$ was characterized by FWHM bandwidth of $\sim 100\,\mathrm{nm}$. Despite the presence of inherent losses within the laser cavity caused by AR-uncoated CaF_2 cryostat windows and uncoated CaF_2 intracavity lens leading to Fresnel reflections, the lasing threshold remained remarkably low, being observed at $\sim 200\,\mathrm{mW}$ of pump radiation. The input-output relationship exhibited a smooth linear correlation, accurately described by a slope efficiency of ~41 % with a Gaussian like beam profile structure TEM_{00}. To achieve even greater capabilities of the CW laser output power, authors suggested the mitigating inherent cavity losses, reducing pump radiation losses in the atmosphere through vacuum or nitrogen vapour tubes, or shortening the optical path, optimizing the thermal regulation of the gain element, and amplifying the pump power. [196]

In [197] a high-efficiency CW Fe:ZnSe mid-IR laser end-pumped by a self-constructed LD pumped Er:YAP laser operating at the wavelength of $2.92\,\mu\mathrm{m}$ was reported by Li et al. in 2021. The compact Er:YAP laser exhibited a steady output power of $3.6\,\mathrm{W}$, accompanied by an average slope efficiency of 36.6 %. The Fe:ZnSe laser delivered an output power of around $1\,\mathrm{W}$, accompanied by favourable beam quality ($M^2 < 1.6$) at an absorbed pump power of $2.1\,\mathrm{W}$. This corresponds to an average slope efficiency of 48 % and an optical-to-optical efficiency of 40 %. Notably, the comprehensive optical

conversion efficiency, encompassing the transition from the 976 nm LD to the ∼4 µm Fe:ZnSe laser, reached 8.8 %, marking the highest reported value up to date. [197]

Thanks to impressive performance, cost-effectiveness, and its scalability, the Er:YAP laser revealed as a useful pump source for Fe:ZnSe lasers. Furthermore, the theoretical model about CW Fe:ZnSe laser operation to anticipate optimized laser performance was prepared in [197]. The outcomes suggest considerable space for enhancing power performance by elevating the OC transmission up to ∼60 % and employing a longer Fe:ZnSe crystal to maximize the absorption of pump power. Numerical thermal analysis reveals the pivotal role of the thermal lensing effect in constraining the power scaling of the Fe:ZnSe laser and this theoretical model is proposed to serve as a preliminary guide for future studies aimed at scaling CW Fe:ZnSe laser output power levels to tens of watts. [197]

However, the group of Pushkin et al. [119] presented in 2018 a pioneering demonstration of efficient and compact Er:ZBLAN fiber pumping for a cryogenically cooled CW Fe:ZnSe crystal, achieving the 2.1 W of laser output power. A slope efficiency of 59 %, calculated concerning the absorbed pump power, was achieved. The observed Fe:ZnSe output spectra reveal the notable impact of re-absorption on the generated wavelength. At higher doping levels and output powers, the spectrum undergoes red shift, enabling continuous tunability from ∼4 up to ∼4.2 µm. [119]

This kind of pumping via Er:ZBLAN fiber laser should be usable also for alternative gain media possessing ∼3 µm absorption bands, such as Fe:CdSe [185]. Currently, output powers exceeding 40 W at ∼3 µm are attainable, with further prospects for power scaling. These high-power, stable, and excellent beam quality pump lasers play a pivotal role in fostering the development of Kerr lens mode-locked systems, utilizing the whole potential of broadband mid-IR active media. [119]

Chapter 3

Motivation – mid-infrared laser radiation applications

Following chapter brings a brief introduction to several specific applications of the mid-IR laser radiation in spectral region of 2–5 μm. The development of tunable mid-IR lasers is mainly given due to interest in their various applications in a wide range of fields from diagnosis and (bio)medical treatment, through the trace gas sensing, spectroscopic measurements, chemical and biological analysis, metrology, optical radars (LIDAR), free space optical (FSO) communication, optical switching, distance measurement, as an optical frequency standard, and also for pumping of non-linear (i.e. optical parametric oscillators – OPOs) or other laser active materials. Among other things, research of RT laser operation of Cr^{2+} ions based materials has contributed to the development of these practical and useful applications. [198]

To remind the current possibilities of the output parameters of Cr:ZnSe lasers, the best achieved results mentioned in Chapter 2 are recapitulated here. The presentation of an efficient (slope efficiency of $\eta > 70\,\%$) Cr:ZnSe laser generation at RT was followed by a great recovery in the research of these materials. It is possible to achieve an extremely wide laser tuning range (2–3.1 μm) with the CW output power of up to 140 W [183], in pulse regime up to 18 W [103], in narrow oscillation lines in the case of Cr^{2+} ions based lasers. Thanks to possibility of direct laser diode pumping and a research of novel ceramic-based hosts, the development of affordable efficient compact tunable lasers capable of generating radiation in mode-locking mode and achieving pulses as short as 45 fs with the average output power of 0.5 W [29] was enabled. Cr^{2+} ions doped laser crystals have proven to be competitive with some semiconductor lasers (interband cascade lasers [199]) or even more complex laser systems based on frequency conversion techniques in mid-IR part of the spectrum. [19]

Similar brief review of current best laser output properties of the Fe:ZnSe to know which radiation can be utilized for applications is following. The slope efficiency of Fe:ZnSe laser reaching 59 % at 78 K was presented in [119]. Moreover, a very wide laser tuning range of 3.6–5.15 μm was demonstrated in [35]. Maximum output power in CW regime of 9.2 W [196], or generated energy up to 1.43 J in pulsed regime (slope efficiency of 53 %) at ∼140 ns pulses [200] were obtained. In passive graphene mode-locking mode, pulses as short as 732 fs with the average output power of 415 mW at a repetition rate of 100 MHz were achieved in [120]. After chirped pulse and multi-pass amplification in another Fe:ZnSe crystal the output energy of 3.4 mJ in 150 fs pulses was reached in [189].

There also exist other laser sources in this region such as quantum cascade lasers (QCL) or optical parametric generators (OPG) which can be utilized. However, these systems are rather expensive, complex and bulky [201]. Following Sec. 3.1 describes the various

spectroscopic applications and for which molecules is this part of electromagnetic spectrum advantageous. Other sections in this chapter are devoted to medical applications (Sec. 3.2), laser beam machining of material (Sec. 3.3), non-linear optical generation (Sec. 3.4), remote sensing (Sec. 3.5), free-space optical communications (Sec. 3.6), and excitation of other mid- or far-IR lasers (Sec. 3.7).

3.1 Spectroscopy

All polyatomic molecules, except of homonuclear diatomic molecules (e.g. N_2, O_2, etc.), absorb the infrared radiation. A set of energy levels uniquely characterize every atom or molecule. In so called *fingerprint region* of the wide infrared part of optical spectrum (1.5–25 μm [202]) lay a numerous set of absorption and emission lines of specific chemical and biological compounds corresponding to transitions between these levels. This spectral region is characterized by the presence of strong fundamental and high harmonic vibrational and rotational-vibrational absorption lines of atmospheric components, vapours and other gases. Therefore, the infrared laser spectroscopy is one of the most reliable techniques for the detection and identification of various organic and inorganic molecules. [201]

To determine the concentration of a known gas, or gases, a trace gas detection from a measured optical absorption spectrum of the gas mixture can be used. For this purpose a good quantitative molecular spectroscopy knowledge of the gas absorption characteristics is required. Absorption or emission transitions of radiation between these levels allow us both the identification and quantification of the atoms or molecules, such as atmospheric trace gases. After exposition of the molecules or atoms to electromagnetic (laser) radiation transitions between electronic, vibrational, and rotational states occur which results in possible determination of their specific absorption spectra consisted of many discrete absorption lines. The state of molecular rotation and vibration is changed due to the absorption of such radiation. An absorption spectrum therefore depends on the physical properties of the exposed molecule such as its size and shape. This is the reason why each molecule can be characterized and precisely identified by its unique spectral signature thanks to these absorption lines with a certain shape and linewidth depending on temperature and also molecule surround. [202]

This allows the detection at the level of several or even individual molecules in the overall composition in even only single measurement. Broadband mid-IR tunable CW or pulsed lasers cover a significant part of this spectral region. For example, water vapour absorbs radiation in whole range of 2.5–3 μm with a maximum at ∼2.9 μm, carbon monoxide (CO) absorbs in the range of 2.3–2.4 μm, carbon dioxide (CO_2) at ∼2.7–2.8 μm and nitrous oxide (N_2O) has several absorption bands in the range of 2–4 μm. Therefore, this spectral area could potentially be utilized, for example, to detect small traces of environmental and toxic vapours in atmospheric and industrial applications (e.g. explosives detection, biomolecular and environmental sensing applications). The ability of broadband solid-state (or supercontinuum) lasers to spectrally cover a wide range including above mentioned molecular absorptions in a single pulse, or their rapid tunability is a major advantage of these relatively compact and user-friendly coherent sources. The primary benefit of such optical methods lies in the ability to non-intrusively detect *in situ* trace gases and their isotopologues (molecules containing isotopes). [13, 203, 204]

There exist a large number of atmospheric trace gases with concentrations in parts-per-trillion (ppt, 10^{-12}), parts-per-billion (ppb, 10^{-9}) to parts-per-million (ppm, 10^{-6}) range. On the other hand, there are also some species, as for instance water vapour, with concentrations of up to a few percent (%, 10^{-2}). This is the greatest detection hurdle because even weak presence of water vapour with its high absorption cross-section complicates the identification of interested molecule with the concentration weaker by factor of 10^{-10}. [202]

An overview of selected molecular end groups absorption wavelength regions in mid-IR region of 2.5–5 μm are presented in Tab. 3.1.

Table 3.1: Characteristic absorption wavelength regions in the 2.5–5 μm range (4000–2000 cm^{-1}) of selected molecular end groups. [205]

Molecular end group	Spectral range [nm] / [cm^{-1}]	Molecular end group	Spectral range [nm] / [cm^{-1}]
>CH_2/–CH_3	3380–3510 / 2960–2850	>P–H	4100–4260 / 2440–2350
–CHO	3450–3700 / 2900–2700	–POOH	3700–3900 / 2700–2560
>O–CH_3	3500–3560 / 2850–2810	−C≡C−	4420–4650 / 2260–2150
–O–CH_2–O	3585–3610 / 2790–2770	−C≡N	4425–4545 / 2260–2200
>N–CH_3	3545–3600 / 2820–2780	−N=C=O	4395–4445 / 2275–2250
>C=CH_2	3230–3250 / 3095–3075	–N_3	4630–4715 / 2160–2120
>C=C−H	3290–3320 / 3040–3010	−C=C=N−	4640–4695 / 2155–2130
−OH	2740–2785 / 3650–3590	>C=C=O	∼4650 / ∼2150
−C≡CH	∼3030 / ∼3300	−N=C=S	4670–5025 / 2140–1990
>NH/–NH	2860–3030 / 3500–3300	R–S–C≡N	4600–4670 / 2175–2140

Recent progress in tunable mid-IR laser sources and spectroscopic techniques together with growing optical industrial resources (e.g. optical telecommunication) has led to the development and utilization of mid-IR spectroscopic techniques to a wide range of gas sensor applications. These sensors have several favourable properties such as sensitivity, selectivity, fast response time, and compactness. They can be used for:

1. monitoring of important environmental atmospheric gases (e.g. CO, CO_2, CH_4, and CH_2O);
2. detection of toxic gases, drugs, explosives, and medically important molecules (e.g. NO, N_2O, CO, CO, NH_3, C_2H_6, and CS_2);
3. planetary atmospheric science and air-quality (e.g. H_2O, CH_4, CO, CO_2, and C_2H_2);
4. measurements of urban (e.g. traffic, power generation), industrial (e.g. gas leaks monitoring in the petrochemical industry) and agriculture emissions (e.g. greenhouses, fruit storage);
5. chemical analysis and control for manufacturing processes (e.g. in the semiconductor, pharmaceutical, and food industries). [202]

The coherent (spatial coherence $M^2 \approx 1$), highly monochromatic and tunable laser sources are required for this purpose. There is a strong demand on mid-IR lasers for the detection. Therefore, their research is nowadays one of the most active areas of solid-state lasers [44, 149]. Laser diodes and erbium (1.6–1.7 μm), thulium (1.8–2 μm),

holmium (2.05–2.2 μm) doped solid-state lasers realized in bulk, crystalline, or fibre laser technology are available on the border between near- and mid-IR wavelength region. Further in the mid-IR range of 2–3 μm and 4–5 μm are most perspective Cr^{2+}- and Fe^{2+}-doped II–VI lasers, respectively. [201]

The first spectroscopic measurements using a tunable Cr:ZnSe laser operating at RT was introduced in 2005 by Fischer et al. in [206]. The mean laser output power of 350 mW in the spectral range of 2.2–2.8 μm enabled sensitive photoacoustic measurements of trace gases with detection limits in sub-ppm concentration. They specifically presented the results of detecting the amount of methane (CH_4) and nitrous oxide (N_2O) in the ambient air. The derived detection limits were in the ppm or even sub-ppm range: CO_2 – 0.2 ppm, CH_4 – 0.8 ppm, and CO – 2.7 ppm. [206]

3.1.1 Dual-comb spectroscopy

Another example is 2D infrared spectroscopy based on time-domain interferences between two comb sources to study the behaviour of molecular structures and dynamics. This so called *dual-comb spectroscopy* is based on two frequency-stabilized pulsed laser sources providing broadband spectra composed of well-defined series of very narrow frequency lines with a regular frequency interval $\Delta\omega$ but each frequency-comb have slightly different spacing between their ridge lines. The mutual displacement of one against the other ridge shifts the measured spectrum to radio frequencies, which enables easier and precision analysis thanks to high resolution and sensitivity. For the demanding applications related to the use of optical-frequency combs based on mid-IR mode-locked femtosecond lasers, time jitter stability and spectral purity properties are particularly relevant [58]. [203]

Bernhardt et al. presented in 2010 [203] the inaugural utilization of dual-comb spectroscopy in the mid-IR range of 2–7 μm. Using a basic experimental arrangement involving two 2.4 μm Cr:ZnSe femtosecond laser oscillators, they successfully captured spectra covering a span of 150 nm in just 10 μs, achieving a resolution of 12 GHz. Despite the ongoing difficulty in achieving stable mode-locked operation with ceramic Cr:ZnSe lasers, these findings presented a straightforward and dependable instrument design capable of conducting real-time, wide-ranging absorption measurements in this spectral region. [203]

The detection of air pollutants, greenhouse gases for environmental diagnostics or even human breath spectroscopy for medical diagnostic is already performed using laser systems, which are mainly based on non-linear optical techniques including an OPO or a difference-frequency generation (DFG). OPOs are almost an ideal solution, on the other hand they are expensive and complex systems. [13]

Today, the mid-IR pulse sequences from Cr:ZnSe lasers exhibit exceptional spectral clarity and consistent pulse-to-pulse stability, primarily constrained by the pump source's intensity fluctuations [160]. Furthermore, the presence of random quasi-phase matching in the polycrystalline Cr:ZnSe active crystal enables the concurrent generation of robust second harmonic pulse sequences. These distinctive attributes make the femtosecond Cr:ZnSe lasers valuable for diverse applications such as precise molecular spectroscopy, accurate frequency measurement, and notably, the prospective creation of high-power mid-IR optical frequency combs. [160]

3.2 Medical applications

There are several advantages of using laser surgery than conventional scalpel. The laser surgery procedures usually less bleeding and decreases the risk of infection. Sealing of blood vessels and nerves reduces bleeding and the length of patient recovery period. However, there existed some limitations of previously used lasers. They did not allow the control of cutting depth, which is critical in some cases. This limitation may be removed by introducing a tunable laser in a spectral region with an exponential change of water absorption. Water is one of these molecules that exhibit a set of strong absorption lines in the mid-IR region, especially near ∼2.9 and ∼6 μm [207]. This causes strong mid-IR absorption in human tissue (which typically consists of around 70 % water), which facilitates numerous biomedical applications in laser surgery, tissue ablation, and photo dermatology. For instance, the optical depth of tissue penetration at ∼2.9 μm is about 1 μm (as water acts as an inherent chromophore in human tissue). Consequently, the region where thermal damage occurs is kept to a minimum, particularly when employing short pulses. From this point of view, the short pulse laser sources tunable in spectral region of 2–6 μm significantly overlapping with a strong water absorption, are of interest. As a reason, it is possible to control the laser cutting depth by the laser output energy and wavelength tuning at a given water absorption rate. [47, 204]

The very wide gain bands of Cr:ZnSe and Fe:ZnSe crystals allow the generation of ultra short pulses that are also unique diagnostic tools for a range of transient events at the femtosecond scale. These lasers are also attractive for optical coherence tomography (OCT). [147]

3.2.1 Mid-IR laser spectroscopy for breath analysis

A novel application of mid-IR lasers involves the analysis of exhaled breath composition in the medical context, utilizing spectroscopic methods for detecting trace gases. Exhaled breath contains trace quantities of ∼1000 volatile organic compounds. Unusual concentrations of numerous such molecules, known as biomarkers, have already been linked to specific illnesses and health conditions [208]. These encompass cardiovascular diseases, asthma, gastrointestinal problems, chronic obstructive pulmonary disease (COPD), diabetes, helicobacter pylori infection, oxidative stress, and diverse types of cancers. These correlations enable swift and non-invasive approaches to health screening across a broad spectrum of medical situations. [204]

The concentrations of biomarkers in exhaled breath exhibit significant variability. Apart from notably high levels of water (H_2O – 5 %) and carbon dioxide (CO_2 – 5 %), the usual concentration ranges are as follows: 1–100 ppm (parts-per-million by volume) for methane (CH_4), 1–5 ppm for carbon monoxide (CO), 0.3–2.5 ppm for acetone (CH_3COCH_3), 0.3–1.6 ppm for nitrous oxide (N_2O), 0.1–3 ppm for ammonia (NH_3), around 500 ppb (parts-per-billion by volume) for methanol (CH_3OH), 1–80 ppb for nitric oxide (NO), 2–20 ppb for ethane (C_2H_4), and others [204]. Therefore, the optical frequency comb spectroscopy, mentioned previously, can be used for the exhaled breath analysis as well. Measuring exhaled nitric oxide concentrations offers a novel approach to monitoring inflammatory conditions in respiratory disorders, including asthma and various pulmonary ailments. Detecting exhaled ammonia presents a potential non-invasive method for evalu-

ating liver and kidney function, as well as identifying peptic ulcer disease. Methane serves as a volatile indicator of lipid per-oxidation in organisms, which leads to oxidative stress and damage within the body. Exhaled carbon monoxide is a biomarker used to assess medical conditions like cardiovascular diseases, diabetes, nephritis, oxidative stress, and inflammation. Carbonyl sulfide (OCS) present in exhaled breath is being considered as a biomarker for both liver function failure and acute lung transplant rejection. [204]

Despite being in its early stages, clinical breath analysis provides distinct advantages to the medical field due to its non-invasive nature for a tested patient and a minimal risk to the sample collector. A great review paper to this topic can be found in [208]. [204]

3.3 Laser beam machining

Laser beam machining (LBM) technology is widely popular due to its versatility in working with a diverse array of materials like metals, plastics, ceramics, wood, paper, and glass. Nonetheless, the feasibility and effectiveness of laser applications depends on the specific attributes of the material being used. Parameters such as chemical composition, absorption, responses to laser irradiation, and material permeability are all assessed. These processes are contactless. Among the merits of lasers is the automated nature of the procedures, resulting in high-quality surface finishes without the need for subsequent treatments or final adjustments. This also contributes to cost savings by reducing the need for finishing procedures, less total waste, as well as cutting down on labour and time requirements. [209]

With a laser beam in the mid-IR region, where, for example, polymers exhibit strong absorption, it is possible to cut, weld or perform other heat treatment methods [207]. By tuning the wavelength in this spectral region, it is possible to significantly change the degree of absorption up to a fine setting for machining processes. For this reason, Cr:ZnSe and Fe:ZnSe lasers are suitable for such application due to their wide spectral tunability. Tunable output radiation could also be used for selective material machining, when the absorption in the target material is significantly higher than in the adjacent material. Up to date, these wavelengths were usually obtained with already well-developed gas lasers such as carbon monoxide CO laser (5–6 μm) or carbon dioxide CO_2 laser (9.4 and 10.6 μm) [207]. As it is presented later in the experimental Part III of this work, the wavelengths in the range from 5 up to 6 μm can already be generated directly from solid-state lasers based on novel active materials investigated in Sec. 6.5 and Sec. 6.6. Such solid-state laser based system is much simpler, more compact, and requires easier and less maintenance compared to complex gas lasers such as mentioned CO laser.

CO lasers typically have lower efficiency, which can lead to higher operating costs and usually operate in a narrow emission linewidths, while solid-state lasers, such as Fe:ZnSe laser, can cover a broad tunable spectral range, allowing for more versatility in various applications. CO lasers are generally larger and bulky, which limits their portability and ease of integration into different systems. CO lasers involve the use of toxic and potentially hazardous gases, which requires careful handling, storage, and disposal. Solid-state lasers tend to have longer lifetimes and higher reliability compared to CO lasers. Moreover, the gas mixture in CO lasers can degrade over time, affecting their performance and requiring more frequent maintenance. Moreover, CO lasers require more complex and sophisticated cooling systems due to their higher heat

generation. This can also add to the operational complexity and maintenance costs. Solid-state lasers can provide better beam quality and spatial coherence than CO lasers. This can be important for applications requiring precise focusing and accurate beam shaping as for instance in the laser micro-machining. Moreover, the solid-state lasers can achieve shorter pulse durations, making them more suitable for certain ultrafast applications, such as mentioned laser micro-machining or medical procedures. [210]

However, it is important to note that the choice between the CO or suitable solid-state lasers depends on the specific application requirements, including power, beam quality, and environmental considerations.

3.4 Non-linear optical generation

In contrast to conventional dielectric laser active media, transition metal ions doped II–VI compounds also have semiconductor properties. Such structure determines the strong non-linear optical response of these materials, which can lead to charge transport, a photorefraction-like phenomenon, a high harmonic generation (HHG), an OPO, and a self-focusing effect of various origins. This required a modification of mode-locking generation techniques and a reassessment of existing theories, which allowed the generation of ultrashort optical pulses in the mid-IR region directly from the laser oscillator from both Cr:ZnSe and Fe:ZnSe lasers. In this context, a number of important new aspects were considered at the same time, such as the cascade contribution of the 2^{nd} order of non-linearity, Raman processes of the 3^{rd} order of non-linearity, their dispersion, anisotropy and others. [19]

Cutting-edge ultrafast sources of mid-IR laser radiation rely on optical parametric amplifiers (OPA) powered by a GW-level fs-laser systems operating in the near-IR range. These laser sources are further enhanced through chirped pulse amplification (CPA) in II–VI crystals doped with Fe^{2+} ions, forming the basis for a highly promising femtosecond photonic platform that spans a wide spectrum from UV up to THz. It is possible to design an effective mid-IR OPA that operate at wavelengths beyond 4 μm by utilizing a powerful Cr:Forsterite laser system for pumping, although this technique is not yet widely adopted. Parametric sources based on both oxide crystals (such as BBO) and non-oxide crystals (like AGS and KTA) provide access to a broad range of tunable ultrashort laser pulses in the range of 1.65–6 μm. These pulses can be used as a seed for powerful CPA setups, utilizing Fe^{2+}-doped chalcogenides such as Fe:ZnSe and Fe:CdSe. [211]

Innovative and adaptable methods have been developed for precise control of the spectral and temporal characteristics (including central frequency shifts, spectrum broadening, and non-linear compression) of intense femtosecond radiation operating at powers > 10 GW in both the near- and mid-IR regions. This control is achieved through filamentation (self-guiding) in dense gas media, leveraging controlled dispersion and non-linearity. These attributes are attained by carefully selecting gas mixtures of inert and molecular gases, and adjusting pressures. This newly devised approach allows for the generation of few-cycle optical laser pulses, offering the potential to scale the initial peak power. This development presents an alternative to complex multistage laser systems based on the optical parametric chirp pulse amplification (OPCPA), and it holds considerable promise for fundamental and applied research endeavours that explore the interactions between intense laser radiation and matter. Such research areas include THz radiation,

the generation of higher optical harmonics (HHG), and investigations into the behaviour of matter under extreme conditions. [211]

3.5 Remote sensing

The radiation of mid-IR wavelengths, where the atmosphere is relatively transparent (3–5 μm and 8–12 μm), can be used for remote sensing. The principle lies in monitoring the reflected radiation from the target to obtain information about its appearance, position, speed and composition. Although this sensing was originally developed in the radio frequency domain (Radio Detection and Ranging – RADAR), the imaging resolution of this technology was greatly improved by using optical frequencies (Light Detection and Ranging – LIDAR). In the fundamental transverse mode generation, the lasers also allow excellent directivity, which increases the distance over which remote sensing can be performed. The range can be further improved by increasing the average power of the laser source. [207]

3.6 Free space optical communications

Ultrafast mid-IR lasers are also usable for free-space optical (FSO) communication operating within the 3–5 μm atmospheric transmission window. Soibel et al. assessed in 2010 [212] its performance alongside a near-IR link under varying fog conditions using an indoor communications test environment. Their study confirmed the viability of mid-IR laser sources for FSO communication links with high data rates. Furthermore, the benefits of the mid-IR FSO link in foggy conditions, attributed to its low attenuation and scintillation were showcased. [212]

3.7 Direct excitation of other mid- or far-infrared lasers

Tovey et al. [213] published in 2021 a paper where the optical excitation of a CO_2 gas laser active medium by a tunable Fe:ZnSe laser operating at 3 Hz is investigated. The study reveals through experimentation that adjusting the pump wavelength to decrease the absorption coefficient has the effect of elevating the upper limit of CO_2 pressure for lasing to 15 atm. The most favourable pump wavelength was identified at 4.4 μm, which conveniently permits the propagation of the pump radiation through the air without energy loss thanks to the minimum CO_2 atmospheric absorption at that wavelength. [213]

As it was already mentioned Fe:ZnSe laser can be also utilized for the pumping of several others Fe^{2+} ions doped materials including other Fe:ZnSe, Fe:$Zn_{1-x}Mn_xTe$, Cr,Fe:$Zn_{1-x}Mn_xSe$ or Cr,Fe:$Zn_{1-x}Mg_xSe$ [127] [P3, P7]. Despite a lower absorption, there is a positive lower quantum defect and output laser oscillations can be generated at even longer wavelengths farther in the mid-IR region compared to a convent ~3 μm pump sources. This kind of excitation and comparison between ~2.94 and ~4.05 μm pumping wavelengths is also demonstrated in the experimental part of this thesis in Chapter 6.

Part II

Objectives and Methods of Elaboration

Chapter 4

Objectives

The aim of this dissertation thesis is to prepare the research about current state of the art divalent transition metal ions doped solid-state lasers generating radiation in the mid-IR region of the electromagnetic spectrum. Following point is to design several laser systems based on novel laser active materials of Cr^{2+}:$Zn_{1-x}Mn_xSe$, and Cr^{2+}:$Zn_{1-x}Mg_xSe$, Cr^{2+},Fe^{2+}:$Zn_{1-x}Mn_xSe$, Cr^{2+},Fe^{2+}:$Zn_{1-x}Mg_xSe$, Fe^{2+}:$Zn_{1-x}Mn_xTe$, and Fe^{2+}:$Cd_{1-x}Mn_xTe$, and to measure their spectroscopic and laser output characteristics including temperature dependence. For this purpose, spectral properties of new laser active media will be investigated at first and subsequently several laser systems will be laboratory-built and an analysis of their physical properties will be carried out. Where it was useful, the temperature dependence of spectral and laser output characteristics of selected active media will also be measured. As sources of pumping radiation, an Er:glass laser at the wavelength of ∼1.53 µm, laser diode (LD) at ∼1.7 µm, Er:YLF laser at ∼1.73 µm, thulium fiber (Tm:fiber) laser at ∼1.94 µm, Er:YAG laser at ∼2.94 µm, or Fe:ZnSe laser at ∼4.05 µm are expected. The optical parametric oscillator Ekspla NT252 will be also used for some spectroscopic analysis of fluorescence spectra or decay time. Obtained results will be discussed and compared. The specific objectives are as follows:

- Implementation of Cr^{2+}:ZnSe and Cr^{2+}:$Zn_{1-x}Mn_xSe$ (Cr^{2+}:$Zn_{1-x}Mg_xSe$) laser systems resonantly pumped by radiation in different modes of generation.
- Characterisation and comparison of the Cr^{2+}:ZnSe, Cr^{2+}-only doped and Cr^{2+},Fe^{2+} co-doped $Zn_{1-x}Mn_xSe$ and $Zn_{1-x}Mg_xSe$ lasers spectral properties including temperature dependences: absorption and fluorescence spectra, and fluorescence decay time.
- Characterisation and comparison of the Cr^{2+}:ZnSe, Cr^{2+}-only doped and Cr^{2+},Fe^{2+} co-doped $Zn_{1-x}Mn_xSe$ and $Zn_{1-x}Mg_xSe$ lasers output properties including temperature dependences: output power/energy, pulse duration, beam profile structure, laser oscillation spectra (eventually spectral tunability).
- Characterisation and comparison of the Fe^{2+}-doped $Zn_{1-x}Mn_xTe$ and $Cd_{1-x}Mn_xTe$ laser materials spectral and laser output properties.

Chapter 5

Methods of elaboration

Elaboration of this dissertation thesis is based on the analysis of existing knowledge in the field of solid-state lasers generating in the mid-IR region in various modes of generation from Chapter 2. Since having collected useful informations from published papers, the various pumping sources are applied in order to investigate the influence of excitation wavelengths used. Furthermore, Cr^{2+} ions doped or Cr^{2+},Fe^{2+} ions co-doped novel host materials of $Zn_{1-x}Mn_xSe$, $Zn_{1-x}Mg_xSe$, $Zn_{1-x}Mn_xTe$, and $Cd_{1-x}Mn_xTe$ are investigated together with the influence of the amount (x) of Mn^{2+} or Mg^{2+} ions in the solid-solutions on their spectral and laser output properties. The systems are characterized in terms of output energy/power, pulse duration, laser oscillation spectra, laser beam spatial profiles, and in some cases also by the possibility of continuous output radiation wavelength tuning. The results from experimental part in Chapter 6 can be compared with spectral and laser characteristics of investigated materials with typically used Cr^{2+}:ZnSe or Fe^{2+}:ZnSe laser active media. Furthermore, the temperature dependence in the range from 78 K up to 380 K is included in appropriate cases. By changing of active media in a previously functionally set and unchanged laser resonator cavities a better comparison thanks to similar conditions is expected. Different coherent sources of pumping radiation will also contribute to the comparison of spectral and laser properties of these novel laser active media. For the Cr^{2+} ions excitation, it is assumed to use the Er:glass laser at ∼1.53 µm (in the free-running (FR) or Q-switched mode of operation), the new laser diode generating radiation at the wavelength of ∼1.7 µm with an output power exceeding 35 W, the flash-lamp pumped Er:YLF laser (in the FR or Q-switched mode) generating radiation at ∼1.73 µm, and or thulium doped fiber laser at ∼1.94 µm. Within the case of excitation of Fe^{2+} ions doped materials a flash-lamp pumped Er:YAG (in the FR or Q-switched mode), and or a laboratory-built Fe^{2+}:ZnSe laser operable for different temperatures are expected.

The next Sec. 5.1 specifies the methods, individual instruments and tools together with presented simplified experimental setups used common to all following measurements which results are described in experimental Part III of this work. Lasers used for the excitation are specified in Sec. 5.2 and the overview of investigated single crystalline materials can be found in Sec. 5.3.

More specific details can be found in related peer-reviewed author papers marked as [P#] and conference proceedings [C#]. Other publications and conference proceedings not directly related to this work but also dealing with mid-infrared laser sources or their applications are listed in the author bibliography as [O#]. Full texts of all published papers, abstracts and proceedings are enclosed in the appendices 1–3.

5.1 Instrumentation, methods and experimental setups

This section describes the instrumentation used and methods of realized measurements. For the illustration, simplified experimental setups are included where necessary. It begins with the description of spectral properties measurements such as 5.1.1 – absorption spectra, 5.1.2 – photodiodes for temporal profiles of exciting (and generated) radiation, 5.1.3 – fluorescence lifetime/decay time, 5.1.4 – fluorescence (and generated laser oscillation) spectra. The laser output characteristics measurement description of 5.1.5 – output power/energy, 5.1.6 – spectral tunability of generated laser radiation and 5.1.7 – laser beam spatial profiles measurement follow as well.

5.1.1 Absorption spectra measurement

Transmission spectra of laser active media, filters and laser cavity mirrors used in the final laser systems were measured in most cases by spectrophotometer Shimadzu (UV-3600 UV-VIS-NIR spectrophotometer, spectral range: 185–3300 nm; measurements were performed with a slit width of 2 nm and a step of 1 or 2 nm) or by spectrophotometer Nicolet (iS5 FTIR spectrometer, spectral range: 7800–350 cm^{-1}, i.e. ∼1.3–28.5 µm; spectral resolution: ∼0.8 cm^{-1} without aperture; ∼0.5 cm^{-1} using aperture).

In the case of temperature dependence measurements, the investigated crystal was held in the copper holder thermally connected by thin indium foil. Such prepared holder with the crystal sample was then placed into the variable temperature cryostat VPF-100 (Janis Research Company, LLC., temperature range: 65–500 K) with CaF_2 windows cooled using the liquid nitrogen (LN_2) to the temperature of ∼78 K. The temperature inside the cryostat was controlled by the 325 Cryogenic Temperature Controller (Lake Shore Cryotronics, Inc.). This cryostat was also used for other temperature dependence measurements such as fluorescence decay time or laser oscillation spectra measurement as well as for the investigation of laser output properties.

The calculation of the absorption coefficient α from measured transmission spectrum was based on the Lambert-Beer's law expressing the radiation intensity $I(l)$ after passing through a homogeneous medium of length l in the form of:

$$I(l) = I_0 \cdot e^{-\alpha l}, \tag{5.1}$$

where I_0 is the radiation intensity at the input to the medium where attenuation occurs. Note: This relationship is also valid in terms of incident (P_0) and output $P(l)$ power.

When pumping radiation coming from air hits the interface of another medium with different refractive index, Fresnel reflection occurs. Similarly this reflection appears at the output interface where exponentially attenuated radiation after passing through this medium of length l impacts the air-medium interface. The Fresnel reflection R_F of interface between two media with different refractive indices n_1 and n_2 is given by the relation:

$$R_F = \left(\frac{n_1 - n_2}{n_1 + n_2}\right)^2. \tag{5.2}$$

After substituting specific refractive indices of air (refractive index $n_1 = 1.00027$ at $\lambda_p = 1.7\,\mu m$) and Cr:ZnSe crystal (refractive index $n_2 \approx 2.437$ at $\lambda_p = 1.7\,\mu m$ [214]),

the reflectivity of one face comes out to be $R_F \approx 17.7\%$. The crystal transmittance T_F for one passage of pumping radiation through this interface is then $T_F = 1 - R_F \approx 82.32\%$. The total transmittance T_{tot} of the crystal after the radiation has passed through both faces is then

$$T_{tot} = T_F \cdot T_F = (1 - R_F)^2. \tag{5.3}$$

Specifically for the interface of our media – air and Cr:ZnSe crystal, this value comes out to be $T_{tot} \approx 67.76\%$. Due to this, it is necessary to modify the Lambert-Beer's law into the form of

$$I(l) = I_0 \cdot (1 - R_F)^2 \cdot e^{-\alpha l}. \tag{5.4}$$

After the introduction of the transmittance T definition relation as the ratio of the intensity of radiation leaving the medium of length l – $I(l)$ and the intensity of the input radiation – I_0:

$$T = \frac{I(l)}{I_0}, \tag{5.5}$$

the absorption coefficient α than can be expressed using the equations 5.4 and 5.5 in the form of

$$\alpha \approx \frac{2 \cdot \ln(1 - R_F) - \ln(T)}{l} \tag{5.6}$$

considering approximate Fresnel reflection losses on both interfaces. The real formula will be more complex due to the internal reflections and thus multi-pass of part of the radiation between crystal facets and thus a bit higher absorption. However, it is worth to note here that the multi-pass effect was neglected in the calculations of the absorption coefficient in this work.

The formula 5.6 could be also rewritten in the term of absorbance A defined as

$$A = \log_{10} \frac{I_0}{I(l)} \tag{5.7}$$

in the form of

$$\alpha = \frac{A - 2 \cdot \log_{10}(1 - R_F)}{l \cdot \log_{10}(e)} \approx 2.3026 \cdot \frac{A - 2 \cdot \log_{10}(1 - R_F)}{l}, \tag{5.8}$$

which can be simplified for a thin film layer of absorbing material of the thickness of l to

$$\alpha \approx \frac{2.3026 \cdot A}{l}. \tag{5.9}$$

5.1.2 Temporal profiles of pumping and generated radiation measurement

Pumping as well as generated laser oscillation pulse temporal profile were measured using several detectors differing in their spectral range and rise time: **(a)** Thorlabs PbSe fixed gain detector PDA20H-EC (spectral range: 1.5–4.8 µm; peak wavelength: 4.0 µm; rise time: 35 µs); **(b)** Thorlabs PbS fixed gain detector PDA30G-EC (spectral

range: 1.5–4.8 µm; peak wavelength: 4.0 µm; rise time: 35 µs); **(c)** Thorlabs InGaAs photodiode FGA10 (spectral range: 0.9–1.7 µm; peak wavelength: 1.55 µm; rise/fall time: 10 ns); **(d)** Roithner Lasertechnik GmbH photodiode PD36-05 (spectral range: 2.2–3.4 µm; peak wavelength: ∼2.7 µm; rise/fall time: 10 ns); **(e)** Vigo PVI-4TE-6 (spectral range: 2.5–6.5 µm; peak wavelength: 6 µm; time constant: ⩽ 50 ns); **(f)** Vigo PVI-6 (spectral range: 2.4–6.4 µm; peak wavelength: 6 µm; time constant: ⩽ 80 ns); **(g)** Teledyne-Judson Technologies cryogenic cooled photoconductive mercury-cadmium-telluride (MCT) detector J15D12 (spectral range: 2–12 µm; peak wavelength: ∼11 µm; time constant: 0.5 µs); **(h)** Electro-Optics Technology, Inc. ET-3000 InGaAs photodetector suitable for Q-switched and mode-locked lasers (spectral range: 0.9–1.7 µm; time constant: rise/fall time ⩽̃ 175 ps). The summary of photodiodes used can be found in Tab. 5.1. Fluorescence decay time was measured by fast detectors with low rise/fall time mentioned above (PD36-05 for Cr^{2+} ions and Vigo for Fe^{2+} ions).

Table 5.1: Summary of photodiodes used to measure pump and output laser pulses duration.

	Manufacturer	Model	Spectral range
(a)	Thorlabs, Inc.	PDA20H-EC	1.5–4.8 µm
(b)	Thorlabs, Inc.	PDA30G-EC	1.0–2.9 µm
(c)	Thorlabs, Inc.	FGA10	0.9–1.7 µm
(d)	Roithner Lasertechnik GmbH	PD36-05	2.2–3.4 µm
(e)	Vigo System, S.A.	PVI-4TE-6	2.5–6.5 µm
(f)	Vigo System, S.A.	PVI-6	2.4–6.4 µm
(g)	Teledyne Judson Technologies, Inc.	J15D12	2.0–12 µm
(h)	Electro-Optics Technology, Inc.	ET-3000	0.9–1.7 µm

The temporal profiles of the pump and output laser pulses (or the temporal profiles of flash-lamp pump or the current through the LD) were recorded on the oscilloscope. In the case of Q-switched or gain-switched regimes, the pulse duration was measured at full-width at half intensity maximum (FWHM). In the CW excitation by the laser diode an optical chopper (Thorlabs MC2000B, chopping frequency with various blades: 4 Hz–10 kHz) has to be used in some cases (for triggering the signal for its measurement or for shortening and selection of the pump pulse duration).

In the case of temperature dependence measurements a LN_2-cooled cryostat by Janis Research Company, LLC. (VPF-100; temperature range: 78–500 K; typical temperature stability: ±50 mK) with uncoated CaF_2 windows in combination with a cryogenic temperature controller by Lake Shore Cryotronics, Inc. (model no. 325) were used.

5.1.3 Fluorescence decay time measurement

The measurement setup of the temperature dependence of the fluorescence decay time or fluorescence spectra is shown in Fig. 5.1. The crystal sample was placed at angle of 45° perpendicular to the incident pump beam. The fluorescence decay signal from the exposed crystal face was detected by an adequate fast photodiode described in 5.1.2. We assumed that no reflected signal from the back face of the crystal causing the reabsorption effects was detected. The corresponding infrared longwave- or band-pass filters were used to avoid the pumping radiation. The overview of the most used filters is summarized

in Tab. 5.2.

Table 5.2: Summary of infrared longwave-pass and band-pass filters used to filter out any undesirable pumping radiation.

Longwave-pass filters		
Manufacturer	**Designation**	**Cut-on wavelength [nm]**
Spectrogon	LP1850	1800
Spectrogon	LP2000	2000
Spectrogon	LP3000	3000
Spectrogon	LP3750	3750
Spectrogon	LP4095	4095
Andover Co.	LWP4300	4300
Spectrogon	LP4500	4500
Spectrogon	LP4750	4750
Spectrogon	LP5000	5000
Band-pass filters		**Spectral range [nm]**
Thorlabs, Inc.	FB2250-250	2250–2750
Thorlabs, Inc.	FB2500-250	2500–3000
Thorlabs, Inc.	FB4250-250	4000–4500
Thorlabs, Inc.	FB4750-250	4500–5000
Optoelectronics Co., Ltd.	IWBP3750-5800	3750–5800
Thorlabs, Inc.	FB5750-250	5500–6000

The fluorescence spectrum was usually measured using the similar arrangement with the same fast photodetector as for the decay signal measurement. In this case, the photodiode was placed behind the monochromator (Newport Corporation/Oriel Instruments; model no. 77250; spectral range depending on diffraction gratings used: 0.18–24 µm), and thus the intensity of fluorescence decay signal at different spectral positions could be resolved (see subsection 5.1.4).

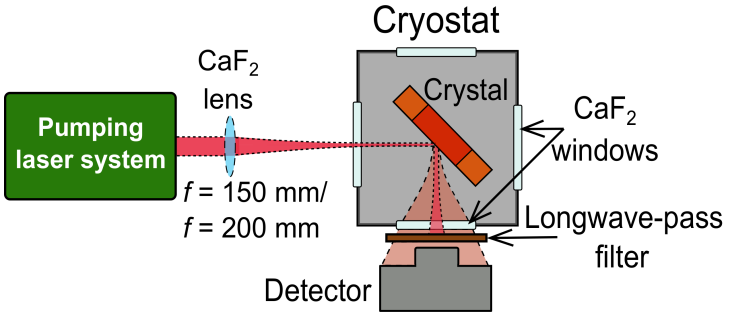

Figure 5.1: Simplified experimental setup for fluorescence spectra and decay time measurement.

One of photodiodes sensed the excitation radiation and the other collected the measured crystal fluorescence decay signal. Both probes were connected to an oscilloscope. The decay curve has to be fit with the exponential time dependence of the attenuation (quenching) of the fluorescence intensity

$$\mathrm{I}(t) = \mathrm{I}_0 \cdot \mathrm{e}^{-\frac{t}{\tau}}, \tag{5.10}$$

where I_0 is the initial fluorescence intensity (at the end of the pump pulse), t is the time and τ is the determined upper laser level fluorescence lifetime. The upper laser level occupation may also be reduced by nonradiative transitions (e.g. multiphonon transitions in solid-states). Nonradiative processes also lead to an exponential population decline with a characteristic time of τ_{nr} (nonradiative lifetime). The total lifetime of the upper laser level is thus:

$$\frac{1}{\tau} = \frac{1}{\tau_r} + \frac{1}{\tau_{nr}}. \tag{5.11}$$

Moreover, the radiative part of lifetime τ_r may have more contributions form different laser sublevels (τ_{r1}, τ_{r2}, $\cdots$, τ_{rn}) with different initial intensities (I_{01}, I_{02}, $\cdots$, I_{0n}) as for instance in the case of energy level splitting which is characteristic for Cr^{2+} and Fe^{2+}-doped ZnSe. In this case, the total time course of fluorescence intensity can be described as:

$$I(t) = I_{01} \cdot e^{-\frac{t}{\tau_{r1}}} + I_{02} \cdot e^{-\frac{t}{\tau_{r2}}} + \cdots + I_{0n} \cdot e^{-\frac{t}{\tau_{rn}}}. \tag{5.12}$$

We can easily identify between the single and multiple exponential decay time contribution using the logarithmic scale of the intensity temporal profile $\log(I(t))$. The overall radiative decay curve will then be (a) linear or (b) nonlinear in the case of (a) single decay or (b) several decay times contribution, respectively.

Since we were not able to distinguish between the individual lifetime contributions of split sublevels from the overall value, we describe our measured experimental results (in Chapter 6) as a fluorescence decay time instead of the lifetime.

5.1.4 Fluorescence and generated laser oscillation spectra measurement

Fluorescence and laser oscillation spectra were measured using monochromator with changeable ruled diffraction gratings by Newport Corporation: **(i)** model no. 77301 (dimensions: 3×3 cm; 150 grooves/mm; spectral range: 2.5–8.0 µm; peak efficiency 90 %), and **(ii)** model no. 77300 (dimensions: 3×3 cm; 300 grooves/mm; spectral range: 1.1–4.0 µm; peak efficiency 88 %). This monochromator dispose with changeable slits with different widths from 50 µm up to 3 mm. The narrower the slit, the lower the output signal, but at the same time the higher the spectral resolution. The fluorescence spectrum was also measured by ArcOptix Fourier-Transform Infrared (FTIR) spectrometer (Peltier-cooled MCT detector, spectral range: 1.5–8.5 µm, spectral resolution: 4 cm^{-1}) in the case of higher repetition rate of 1 kHz or CW mode.

The measurement of the fluorescence spectrum was carried out in a similar way to the measurement of the generated laser oscillation wavelength. The simplified setup of this measurement is shown in Fig. 5.1. However, instead of the longwave-pass filter the monochromator was placed. It was necessary to place the monochromator as close as possible behind the crystal (cryostat window) due to much lower fluorescence signal. The fluorescence spectrum of the crystal was usually averaged from 3–5 following measurements at the same spectral position selected by the monochromator.

5.1.5 Output power/energy measurement

For the output power/energy measurement several pyroelectric power probes by Coherent, Inc. or thermal power sensor head by Thorlabs, Inc. were used. Their summary can be found in Tab. 5.3. For longer pulse in free-running or CW mode: **(a)** PM3 (wavelength range: 0.3–11 µm; power range: 5 mW–2 W; noise equivalent power: 0.2 mW; response time: 2 s); **(b)** PM10 (wavelength range: 0.25–11 µm; power range: 5 mW–10 W; noise equivalent power: 0.2 mW; response time: 2 s); **(c)** PM30 (wavelength range: 0.25–11 µm; power range: 100 mW–30 W; noise equivalent power: 0.5 mW; response time: 3 s); **(d)** Thorlabs S401C (wavelength range: 0.19-20 µm; power range up to 1 W or 3 W for less than 20 seconds of irradiation), Thorlabs PM100USB power and energy meter interface. For shorter pulses of Q-switched or gain-switched generation (ns region) following probes were used: **(e)** J25LP-ERBI (wavelength: 2.94 µm; energy range: 1 mJ–5 J; maximum pulse width: 500 µs; maximum average power: 1 mJ–5 J); **(f)** J25 (wavelength range: 0.1–100 µm; maximum pulse width: 200 µs; energy range: 200 µJ–1 J; maximum average power: 5 W); **(g)** J-25MB-LE (wavelength range: 0.19–12 µm; energy range: 25 µJ–50 mJ; maximum pulse width: 17 µs; maximum average power: 5 W); **(h)** J-10MB-LE (wavelength range: 0.19–12 µm; energy range: 300 nJ–600 µJ; maximum pulse width: 17 µs; maximum average power: 4 W).

Table 5.3: Summary of detectors used to measure laser output power/energy.

	Manufacturer	Model	Power/energy range	Spectral range
(a)	Coherent, Inc.	PM3	5 mW–2 W	0.30–11 µm
(b)	Coherent, Inc.	PM10	5 mW–10 W	0.25–11 µm
(c)	Coherent, Inc.	PM30	100 mW–30 W	0.25–11 µm
(d)	Thorlabs, Inc.	S401C	10 µW–1 W	0.19–12 µm
(e)	Coherent, Inc.	J25LP-ERBI	1 mJ–5 J	2.94 µm
(f)	Coherent, Inc.	J25	200 µJ–1 J	0.30–12 µm
(g)	Coherent, Inc.	J-25MB-LE	25 µJ–50 mJ	0.19–12 µm
(h)	Coherent, Inc.	J-10MB-LE	300 nJ–600 µJ	0.19–12 µm

Power probes were connected to the digital power meter EPM 2000 (Coherent, Inc./Molectron, power range: 1 mW–10 kW; resolution: 0.1 mW – both depend on the probe), to the laser power meter FieldMate (Coherent, Inc./Molectron, power range: 100 µW–29.9 kW; accuracy: ±1 %,), or to the digital oscilloscopes DPO4104b (Tektronix, Inc., 4 channels, 1 GHz bandwidth, 5 GS/S sampling frequency and 350 ps calculated rise time) or DPO3032 (Tektronix, Inc., 2 channels, 300 MHz bandwidth, 2.5 GS/S sampling frequency and ∼1.17 ns calculated rise time).

All crystals were investigated in a very similar pumping scheme and laser cavity arrangement. The simplified experimental scheme is presneted in Fig. 5.2. Depending on the pump source used a focusing lenses of focal lengths of $f = 150$ mm or $f = 200$ mm or even without lens (depending on the quality of pumping beam). The laser cavity typically consisted of a flat pumping mirror (PM) and a curved concave output coupler (OC). Typical radii of curvature used were r = -150 mm, -200 mm, or -500 mm. For temperature dependence measurements, the mirrors were usually placed closed outside the cryostat with CaF_2 windows containing the investigated crystal in a copper holder. To improve

the heat transfer, the crystals were also surrounded by a thin indium foil. The longwave-pass filters or two dichroic mirrors highly reflecting in the generated spectral range forming a Z-line were used for elimination of unabsorbed pumping radiation.

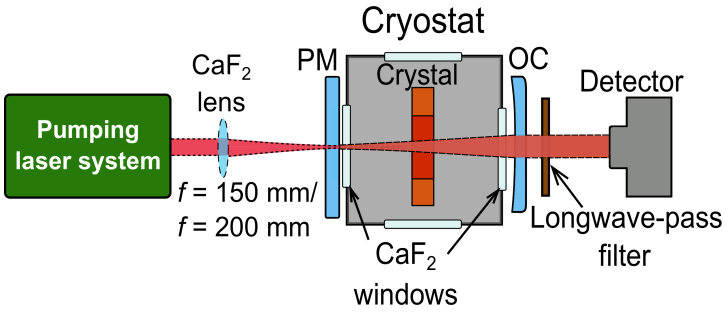

Figure 5.2: Simplified experimental laser system setup. PM – pumping mirror, OC – output coupler.

The resonator together with the crystal position and its tilt were optimally adjusted to obtain the maximum laser mean output power/energy and lowest threshold in all cases. The determination of the power/energy characteristics consisted in the calculation of pump power/energy absorbed by the crystal, then in the determination of the mean output power/energy depending on the absorbed power and subsequently in the corresponding slope efficiency η of the system.

In some cases the energy was measured instead of the mean output power. However, following derivation is in terms of power but it can be freely exchanged for energy. The absorbed power P_{abs} was determined from the measured levels of the unabsorbed pump power of the pumping radiation measured at the input of the crystal P_{in} (behind the pumping mirror), and close at the crystal output P_{unabs}. Taking into account Fresnel losses on the crystal faces (T_F – Fresnel transmittance of the air-crystal or crystal-air interface), the absorbed power was calculated according to the simplified relationship of

$$P_{abs} = P_{in} \cdot T_F - \frac{P_{unabs}}{T_F}. \tag{5.13}$$

This approach does not include the multi-reflection of pumping radiation inside the crystal between its air interfaces. However in the first approximation, this relationship is sufficient for our determination of absorbed pump power.

5.1.6 Spectral tunability of generated laser radiation measurement

In several cases, the tunable wavelength spectrum was also measured. A simplified arrangement for this measurement under laser diode excitation is shown in Fig. 5.3. For the tuning a birefringent plate (BP) from magnesium fluoride (MgF_2) or crystalline quartz (SiO_2) placed between the crystal sample and output coupler under the Brewster angle (in order to minimize reflection losses for *p*-polarization) was used. The birefringence leads to wavelength-dependent polarization changes and thus transmission losses, arising from the Fresnel reflection of *s*-polarized light at the surfaces. By rotating of this plate, the laser output oscillation wavelength is being tuned by rotating of this birefringent plate along its perpendicular axis. The induced losses vary approximately sinusoidally with the wavelength. The thicker the birefringent plate is, the smaller is the free spectral (and thus tunable) range.

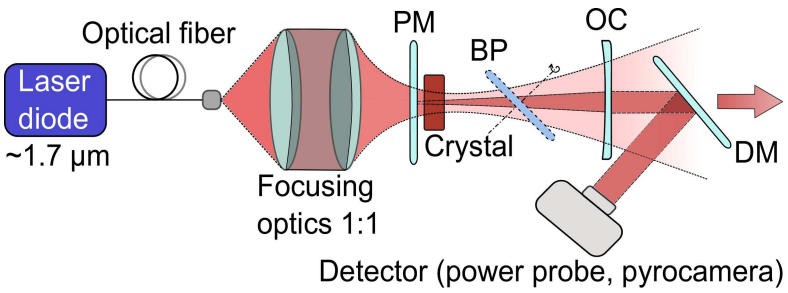

Figure 5.3: Simplified experimental arrangement for laser oscillation wavelength tuning. PM – pumping mirror, BP – birefringent plate, OC – output coupler, DM – dichroic mirror.

5.1.7 Laser beam profiles measurement

The laser beam spatial profile of generated laser beam in the pulse mode of generation in the case of low repetition rate (up to 5 Hz) was monitored by infrared sensitive pyroelectric camera Spiricon Pyrocam III (Ophir Optronics Solutions Ltd., spectral range: 13–355 nm and 1.06–3000 μm; effective pixel pitch: 80 μm; resolution: 124×124 pixels; active area: 12.8×12.8 mm; beam size range: 1600 μm–25.4 mm; dynamic range: 60 dB; frame rate at full resolution: 100 fps). In the case of higher repetition rates or in the CW mode, especially when the crystal was pumped by the laser diode at ~1.7 μm, the Spiricon Pyrocam PY-IV-C-A (Ophir Optronics Solutions Ltd., spectral range: 13–355 nm and 1.06–3000 μm; effective pixel pitch: 80 μm; resolution: 320×320 pixels; active area: 25.6×25.6 mm; dynamic range: 60 dB) was used. The pyroelectric camera has to be externally triggered by the pulse source with an adequate delay behind the pump pulse and an appropriate integration time and attenuation filters according to the intensity (energy/power) of the measured laser radiation has to be chosen. The camera was placed behind appropriate longwave-pass or band-pass filters separating the unabsorbed pumping radiation from the measured generated one. In some cases, a pair of mirrors forming the Z-line highly reflecting only the generated laser radiation served to direct the generated beam to the camera. Pictures of both cameras are shown in Fig. 5.4.

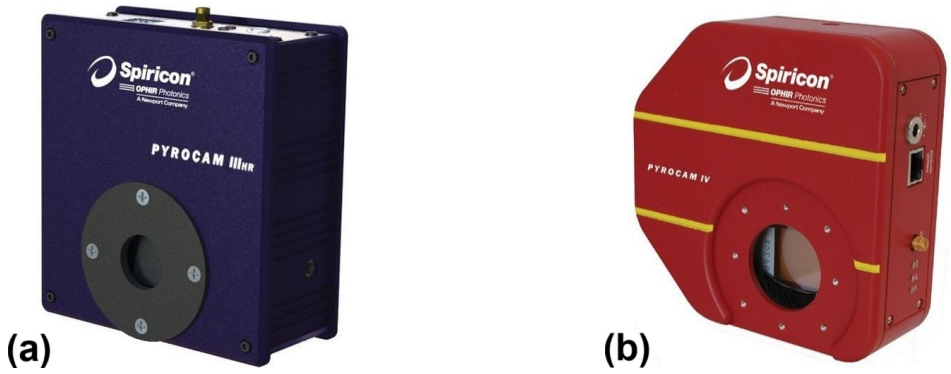

Figure 5.4: Photographs of pyrocameras used for beam spatial profile measurements. **(a)** Pyrocam III (for the pulsed mode of operation), **(b)** Pyrocam PY-IV-C-A (for the CW mode of operation).

The lasers frequently used for the optical pumping of investigated crystalline samples are described in the following section.

5.2 Pumping laser systems

The properties of novel laser active single crystals were investigated under excitation by different sources of the coherent pumping radiation. For the Cr^{2+} ions direct excitation the Er:glass, Er:YLF, laser diode (LD) or Tm:fiber laser were used. The Fe^{2+} ions were directly pumped by the Er:YAG laser or by the liquid nitrogen cooled gain-switched Fe:ZnSe laser. The Fe^{2+} ions were also excited indirectly via the $Cr^{2+} \rightarrow Fe^{2+}$ energy transfer. These sources of coherent radiation and their properties are briefly described in the following paragraphs. They are ordered according to their output laser oscillation wavelength from the shortest (~1.53 μm) up to the longest (~4.05 μm). Measured radiation spectra of all lasers used for the excitation are demonstrated in Fig. 5.5.

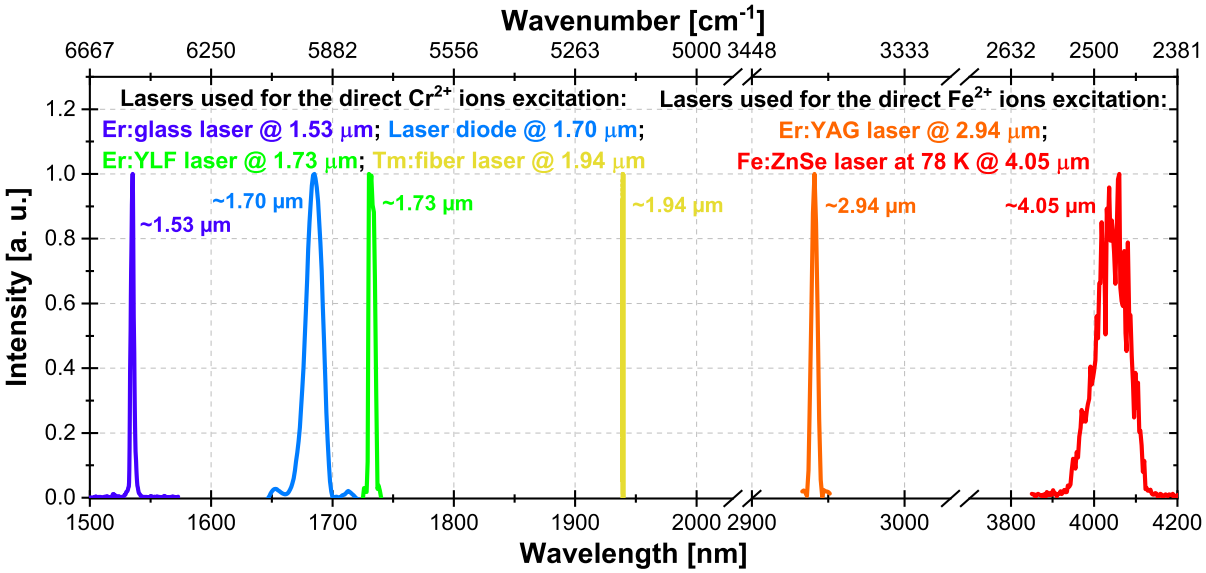

Figure 5.5: Measured radiation spectra of pumping lasers used: Er:glass – dark blue, laser diode – light blue, Er:YLF laser – light green, Tm:fiber laser – yellow, Er:YAG laser – orange, Fe:ZnSe laser operated at 78 K – red curve.

Lasers used for the Cr^{2+} ions direct excitation

Ekspla NT252 optical parametric oscillator (OPO)

This commercial diode pumped solid state laser (DPSSL) optical parametric oscillator was used only for the spectroscopic measurements with Cr^{2+} ions (e.g. fluorescence decay time). This system has a high repetition rate of 1 kHz with ultrabroad tuning range from 335 nm up to 2600 nm with the output pulse energy up to 1.1 mJ in the 1–4 ns pulse duration.

1.53 μm (Q-switched) Er:glass laser

A laboratory built flash-lamp pumped Er:glass laser generated radiation at the central wavelength of 1535 nm with the repetition rate of 0.5 Hz. It was also possible to operate this laser in the passive Q-switched mode after adding the Co^{2+}:$MgAl_2O_4$ saturable absorber between the active medium of Er:glass and the output coupler. In this case, the energy of one Q-switched pulse was ~8.5 mJ with the FWHM pulse duration of ~260 ns which corresponds to the peak output power of ~33 kW.

- **1.7 µm laser diode**

A laser diode (LD) Bright Lase Ultra - 100 (QPC Lasers, Inc.) was the compact pumping source generating up to 35 W in the CW mode and up to ~3 W in 10 ms/10 Hz pulse mode at the wavelengths of ~1.71 µm and ~1.69 µm (in a narrower spectral linewidth), respectively. The LD output radiation is coupled into the optical fiber with the diameter of $d = 400$ µm with the numerical aperture of 0.22. This fiber delivered the pumping LD radiation to the 1:1 focusing optics (AC-508-075-C, Thorlabs). This optics consists of two doublets with focal lengths of $f = 75$ mm and an anti-reflection (AR) coating in the spectral range of 1050–1700 nm.

- **1.73 µm Q-switched Er:YLF laser**

Another utilized pumping source was a laboratory built flash-lamp pumped electro-optically Q-switched Er:YLF laser. The Q-switching was supported by the lithium niobate ($LiNbO_3$) Pockels cell with the ends cut along the Brewster angle to serve as a polariser for Q-switch quarter-wave voltage $U_{\frac{\lambda}{4}}$ arrangement. The central laser oscillation wavelength of 1735 nm at the repetition rate of 1 Hz with FWHM pulse duration of ~200 ns up to ~16 mJ of the output energy were the typical output characteristics of this laser.

- **1.94 µm Tm:fiber laser**

Thulium fiber laser model TLR-50-AC-Y12 (IPG Photonics) with a central oscillation wavelength of 1939.2 nm and the maximum output power of 52.9 W was used as the fourth excitation system of the Cr^{2+} ions. The laser was operated in a CW mode and its output beam could be modulated by a mechanical chopper in order to get pulses at a repetition rate of 10 Hz and duration of ~1 ms in most of our experiments. The emission bandwidth was very narrow of $\Delta\lambda_{FWHM} \approx 1$ nm. Beam quality of this laser was also very high typically less than $M^2 \leqslant 1.1$.

Lasers used for the Fe^{2+} ions direct excitation

- **2.94 µm Q-switched Er:YAG lasers**

The Er:YAG laser was electro-optically Q-switched similarly to the Er:YLF laser. This system operates at repetition rate of 2.5 Hz at central wavelength of 2940 nm. Therefore, this laser system was used for the direct excitation of Fe^{2+} ions. The output power depends on the output beam spatial structure. It was possible to get 15–20 mJ in one ~250 ns long pulse with the Gaussian beam structure or to get higher energy in several pulses with a multimode structure. In the most cases, the laser was operated in one pulse regime with lower energy. Another similar Er:YAG laser system operated at 1 Hz repetition rate with longer rod and laser cavity, and a bit higher output energy (~45 mJ/pulse) was used for the pumping of liquid-nitrogen (LN_2) cooled Fe:ZnSe laser which was also used for further excitation of other novel Fe^{2+} ions based lasers.

- **4.05 µm gain-switched LN_2-cooled Fe:ZnSe laser**

This laser system was pumped by the Q-switched Er:YAG laser described in previous paragraph with higher output energy and was operated at cryogenic temperature of liquid nitrogen ~78 K due to longer fluorescence decay time of Fe^{2+} ions, wider and more intensive absorption band of the Fe:ZnSe crystal around this temperature. The laser was operated in the gain-switched mode due to the short Q-switched pulse excitation and a high gain of this medium. The generated wavelength was centred around ~4.05 µm with the maximum pulsed output energy in the range of typically 7–8 mJ.

Lasers used for the Fe^{2+} ions indirect excitation

$Cr^{2+} \rightarrow Fe^{2+}$ ions energy transfer excitation

In several investigated single crystal samples co-doped with Cr^{2+} and Fe^{2+} ions (Cr^{2+},Fe^{2+}:$Zn_{1-x}Mn_xSe$ or Cr^{2+},Fe^{2+}:$Zn_{1-x}Mg_xSe$), the Fe^{2+} ions were also able to be excited indirectly via the Cr^{2+} ions. In this operation mode, the Cr^{2+} ions were directly excited to their absorption peak. There is a possibility of a quick energy transfer from the Cr^{2+} ions (donor) excited energy state to the Fe^{2+} ions (acceptor) upper state resulting in the excited Fe^{2+} ions, and thus the Fe^{2+} ions laser generation can be obtained. This excitation method was demonstrated with upper mentioned pumping sources: **a)** laser diode, **b)** Er:YLF laser, and **c)** Tm:fiber laser.

5.3 Overview of the investigated single crystals

Almost all crystals were grown by high pressure Bridgman method (HPBM) in the Institute for Single Crystals at the National Academy of Sciences of Ukraine in Kharkiv in co-operation with Dr. Nazar O. Kovalenko, Dr. Igor S. Terzin, and their colleagues [53]. The properties of the furnace where these crystals by this method were grown are summarized in Tab. 5.4. Cr^{2+} active ions and or Cr^{2+},Fe^{2+} ions were (co)doped into the host materials during the synthesis process. All crystal samples had optically polished faces without any anti-reflection (AR) coatings.

Several Cr:ZnSe single crystal samples with different thicknesses were also produced at Kuban State University in Krasnodar by the group of Valery V. Badikov. Each pair of crystals with the same thickness consisted of one AR-coated and one uncoated sample.

Table 5.4: Specifications of the furnace for crystal growing by high pressure Bridgman method. Institute for Single Crystals, National Academy of Sciences of Ukraine, Kharkiv, Ukraine [215].

Parameter	Value
Maximum diameter of the growing crystal	50 mm
Height of the crystalline boule	100–150 mm
Working pressure of inert gas	1–150 atm
Maximum temperature in the crystallization zone	1900 °C
Temperature gradient on crystallization front	5–50 °C/cm
Speed of crucible moving at crystallization	0.15–15 mm/h

An overview of 17 investigated single crystals related to this work with their absorption spectra properties at most often used excitation wavelengths of ∼1.73 μm (for the Cr^{2+} ions) and ∼2.94 μm (for the Fe^{2+} ions) is summarized in Tab. 5.5. Crystals were divided into six individual sections 6.1–6.6 according to the host materials and by the active ions – single doped (Cr^{2+} or Fe^{2+} ions only) or co-doped (Cr^{2+},Fe^{2+}). The results obtained during their individual investigation can be found in the experimental Part III of this thesis in Chapter 6.

Table 5.5: Overview of the investigated single crystals and their absorption coefficients α at predominantly used excitation wavelengths of 1.73 µm (for Cr^{2+} ions), 2.94 µm, and 4.05 µm (for Fe^{2+} ions) at temperature of 78 K.

Crystal sample	**Thickness [mm]**	α **@ 1.73 µm @ 78 K [cm^{-1}]**	α **@ 2.94 µm @ 78 K [cm^{-1}]**
Section 6.1			
Cr:ZnSe (1)	6.0	3.0	—
Cr:ZnSe (2)	2, 3, 5, 10	—	—
Section 6.2			
Cr:$Zn_{1-x}Mn_xSe$ ($x \approx 0.05$)	4.2	10.2	—
Cr:$Zn_{1-x}Mn_xSe$ ($x \approx 0.10$)	4.3	4.6	—
Cr:$Zn_{1-x}Mn_xSe$ ($x \approx 0.20$)	3.9	3.9	—
Cr:$Zn_{1-x}Mn_xSe$ ($x \approx 0.30$)	3.8	4.0	—
Cr:ZnSe (3) ($x = 0$)	2.2	13.8	—
Section 6.3			
Cr,Fe:$Zn_{1-x}Mn_xSe$ ($x \approx 0.05$)	3.9	8.1	2.8
Cr,Fe:$Zn_{1-x}Mn_xSe$ ($x \approx 0.20$)	2.7	4.8	8.4
Cr,Fe:$Zn_{1-x}Mn_xSe$ ($x \approx 0.30$)	5.1	2.5	3.7
Cr,Fe:$Zn_{1-x}Mn_xSe$ ($x \approx 0.40$)	2.6	7.1	10.9
Section 6.4			
Cr:$Zn_{1-x}Mg_xSe$ ($x \approx 0.25$)	4.9	4.6	—
Cr,Fe:$Zn_{1-x}Mg_xSe$ ($x \approx 0.20$)	2.5	1.6	3.2
Cr,Fe:$Zn_{1-x}Mg_xSe$ ($x \approx 0.30$)	5.0	0.7	1.5
Cr,Fe:$Zn_{1-x}Mg_xSe$ ($x \approx 0.40$)	3.6	1.1	2.4
Fe^{2+}-only doped crystals		α **@ 2.94 µm @ 78 K [cm^{-1}]**	α **@ 4.05 µm @ 78 K [cm^{-1}]**
Section 6.5			
Fe:$Zn_{1-x}Mn_xTe$ ($x \approx 0.3$)	3.9	1.8	3.4
Section 6.6			
Fe:$Cd_{1-x}Mn_xTe$ ($x \approx 0.10$–0.76)	2–3	1.1–1.6	1.2–3.4

Part III

Experimental Part, Comparison and Summary

Chapter 6

Experimental results

This chapter describes the results of individual experiments with novel laser active media generating mid-IR laser radiation in the spectral ranges of 2–3 μm (generated by Cr^{2+} ions), 4–5 μm, and 5–6 μm (both generated by Fe^{2+} ions). Related results were published in 7 peer-reviewed (4 author, 3 co-author) papers and at 21 international conferences, and are cited in forms of [P#] ([P1–P7]) and [C#] ([C1–C21]), respectively. Papers and conference proceedings are ordered according to the date of their publishing. Corresponding references are listed at related sections in the bibliography in the end of this thesis and their full texts are enclosed in appendices 1 and 2, respectively.

The experimental part is divided into six main sections 6.1–6.6 according to the crystal host materials and active ions – Cr:ZnSe; Cr:$Zn_{1-x}Mn_xSe$; Cr,Fe-co-doped $Zn_{1-x}Mn_xSe$; Cr-only doped and Cr,Fe-co-doped $Zn_{1-x}Mg_xSe$; and Fe^{2+}-doped $Zn_{1-x}Mn_xTe$ and $Cd_{1-x}Mn_xTe$. Each section begins with the spectroscopic properties of these materials and then follow by their laser output characteristics. These are ordered in the subsections according to the wavelength of optical pumping used from the shortest up to the longest one. However, in the case of Cr,Fe co-doped samples the ordering is given by the type of excitation: **a)** Direct excitation of Cr^{2+} ions, **b)** direct excitation of Fe^{2+} ions, and **c)** indirect excitation of Fe^{2+} ions via $Cr^{2+} \rightarrow Fe^{2+}$ ions energy transfer. In the case where different excitation wavelengths for mentioned kinds of pumping were used, the results are again ordered from the shortest pumping wavelength up to the longest one.

The description of crystals and laser characteristics begins with the Sec. 6.1 investigating the Cr:ZnSe crystal samples properties, especially the temperature dependence of Cr:ZnSe (1) single crystals spectral and laser properties in the range of 78–300 K. The following optimization was performed with the second sample Cr:ZnSe (2) polished in different lengths (2, 3, 5, 10 mm) with or without anti-reflective (AR) coatings (8 samples in total). These crystals were pumped by a laser diode (LD) radiation at ∼1.7 μm (see page 64) and they could be actively cooled by water flowing through the copper holder thanks to crystals regular shapes. The influences of crystal active length, presence of AR-coatings, and pump pulse duration from 10 ms/10 Hz up to CW mode were investigated. Moreover, the spectral tunability of generated laser radiation using the intra-cavity MgF_2 birefringent Lyot plate in both modes of operation was studied and compared.

The experimental part continues with the Sec. 6.2 dealing with the influence of manganese ions of amount x presented in the host material of the $Zn_{1-x}Mn_xSe$ ($x \approx 0.05$; 0.1; 0.2; 0.3) doped with Cr^{2+} ions and their properties. The results are compared with the Cr:ZnSe (3) sample pumped under the same conditions as the manganese-host based samples. It concentrates on the temperature dependence of spectral and laser output

properties of several single crystals. It was found that increasing amount of manganese in the II-VI host material allows to increase the oscillations wavelength of generated mid-IR radiation in the 2–3 μm spectral region.

For the generation of even longer mid-IR wavelengths in the range of 4–5 μm, the Cr^{2+} and Fe^{2+} ions co-doped $Zn_{1-x}Mn_xSe$ (x ≈ 0.05; 0.2; 0.3; 0.4) single crystals were investigated and their comparison under different types and wavelengths of excitation is presented in the Sec. 6.3. Both laser active ions spectral and laser output properties and their temperature dependences were studied gradually in three different pumping methods: **a)** Direct Cr^{2+} active ions excitation into their absorption peaks at the wavelengths of ~1.53 μm, ~1.7 μm, and ~1.73 μm; **b)** Indirect Fe^{2+} ions excitation and lasing via the $Cr^{2+} \rightarrow Fe^{2+}$ ions energy transfer at the wavelengths of ~1.7 μm, ~1.73 μm, and ~1.94 μm.

The indirect excitation and lasing of Fe^{2+} ions via the $Cr^{2+} \rightarrow Fe^{2+}$ ions energy transfer was experimentally obtained for the first time. These unique results were published in [P1,P2,P4,P5,P7] and presented at [C5–C7,C9,C11–C14,C20] international conferences. In most cases, the Q-switched Er:YLF laser generating short pulses at the wavelength of ~1.73 μm was used for this purpose. However, the $Cr^{2+} \rightarrow Fe^{2+}$ ions energy transfer was also obtained and reported for longer pulse duration (in units of milliseconds) delivered by the LD at ~1.7 μm or by the Tm:fiber laser at ~1.94 μm.

However, this kind of excitation was also reached with other Cr,Fe co-doped host materials based on magnesium $Zn_{1-x}Mg_xSe$ and is reported together with their properties in the Sec. 6.4. To be specific, spectral and laser output properties of the Cr^{2+}-only doped $Zn_{1-x}Mg_xSe$ (x ≈ 0.25) and the Cr^{2+},Fe^{2+}-co-doped $Zn_{1-x}Mg_xSe$ (x ≈ 0.2; 0.3; 0.4) host materials were studied and compared in similar pumping mechanisms as the previous materials: **a)** Direct excitation of Cr^{2+} ions at the wavelength of ~1.73 μm; **b)** Direct excitation of Fe^{2+} ions at the wavelength of ~2.94 μm or ~4.05 μm; and **c)** Indirect excitation of Fe^{2+} ions via the $Cr^{2+} \rightarrow Fe^{2+}$ ions energy transfer at the wavelength of ~1.73 μm.

The Fe^{2+}-only doped novel host materials of $Zn_{1-x}Mn_xSe$ and $Cd_{1-x}Mn_xSe$ allowing the generation farther in the mid-IR part of the spectrum even beyond 5 μm were investigated in the Sec. 6.5 and 6.6, respectively. Spectral and laser output properties of the Fe:$Zn_{1-x}Mn_xTe$ (x ≈ 0.3) and the Fe:$Cd_{1-x}Mn_xTe$ (x ≈ 0.1–0.76) host materials were studied and compared under direct excitation at wavelengths of ~2.94 μm, and or ~4.05 μm. For instance, under the ~4.05 μm excitation of the $Cd_{1-x}Mn_xTe$ (x ≈ 0.76), the laser generation around the central wavelength of ~5.94 μm at RT was obtained.

It is worth to note that the optical-to-optical efficiency mentioned in the text or plots is stated with respect to the energy of the pump radiation absorbed in the crystal.

6.1 Properties of the Cr:ZnSe single crystals (1) and (2)

As the first acquaintance with the properties of investigated crystalline media the Cr:ZnSe (1) and (2) single crystals were chosen for optimization of operation conditions and parameters (see Fig. 6.1). The first aim was to find out the influence of different operation temperature of Cr:ZnSe (1) sample on its spectral and laser output properties (Sec. 6.1.1). The crystal was pumped by the Q-switched Er:YLF laser in this case.

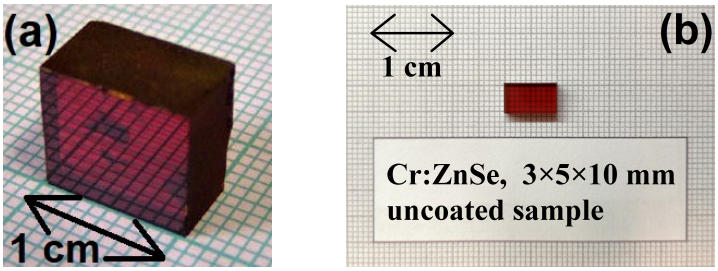

Figure 6.1: Photos of the investigated Cr:ZnSe single crystals: **(a)** Cr:ZnSe (1); **(b)** Cr:ZnSe (2).

The second sample Cr:ZnSe (2) was prepared in four different lengths with or without presence of AR-coating layers on polished facets. In this case, the aim was to investigate its optimal active length, output coupler reflectivity, pump pulse duration and a repetition rate, and also its spectral tunable range (using a MgF_2 birefringent plate). The excitation was performed by a laser diode generating radiation at the wavelength of ∼1.69 μm in the pulse mode or ∼1.71 μm in the CW mode (see Sec. 6.1.2). The results of these studies were presented at several conferences [C2, C4, C18, C21]. The summary of the absorption coefficient values of both samples at the excitation wavelength of ∼1.73 μm at 78 K and 300 K can be found in Tab. 6.1.

Table 6.1: Overview of the investigated Cr^{2+}:ZnSe (1 and 2) single crystals and their absorption coefficients α at excitation wavelength used of ∼1.73 μm at 78 K and 300 K.

Crystal	**Thickness [mm]**	α **@ 1.73 μm @ 78 K** [cm^{-1}]	α **@ 1.73 μm @ 300 K** [cm^{-1}]
Cr:ZnSe (1)	6	3	2.5
Cr:ZnSe (2)	2, 3, 5, 10	—	1.7

The absorption spectra of the Cr:ZnSe (1) and (2) (5 mm thick sample without AR-coating) single crystals at RT were measured with the Shimadzu UV-3600 spectrophotometer and are shown in Fig. 6.2. The absorption coefficient at the pumping Er:YLF laser central oscillation wavelength of ∼1.73 μm of Cr:ZnSe (1) sample was ∼2.5 cm^{-1}. The second sample Cr:ZnSe (2) was pumped by the LD at the central excitation wavelength of ∼1.7 μm where the absorption coefficient was measured as high as ∼1.5 cm^{-1}. The maximum absorption coefficients of ∼2.6 cm^{-1} and ∼1.75 cm^{-1} for the Cr:ZnSe (1) and (2) crystals, respectively, were obtained at a wavelength of ∼1775 nm typical for this crystal. The Cr^{2+} ions absorption bandwidths of Cr:ZnSe (1) and (2) samples measured at FWHM were similarly ∼0.36 μm and ∼0.37 μm, respectively.

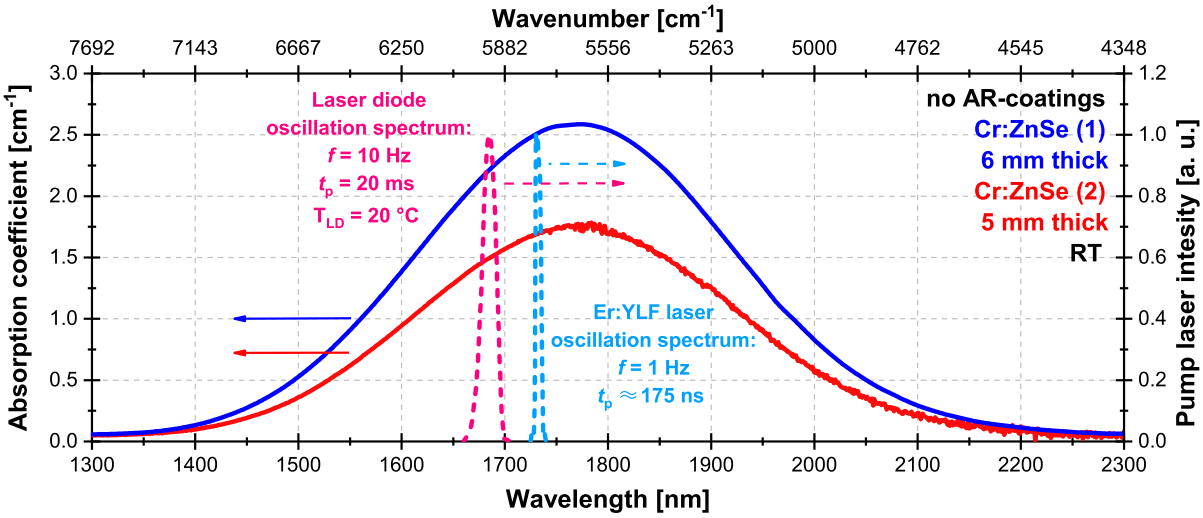

Figure 6.2: Absorption spectra of the Cr:ZnSe (1) – red curve and (2) – (dark blue curve) single crystals at RT and the oscillation spectra of pumping lasers: laser diode at ~1.7 μm – pink dashed curve; Er:YLF laser at ~1.73 μm – light blue dashed curve.

6.1.1 Temperature dependence of the Cr:ZnSe (1) spectral and laser properties pumped by the Er:YLF laser at the wavelength of ~1.73 μm

The aim of this study was to investigate the temperature dependence of absorption, fluorescence and oscillation spectra of Cr:ZnSe (1) single crystal. Dimensions of investigated crystal were $10\times9\times6\,\mathrm{mm}^3$. The temperature dependence of the laser output characteristics pumped by the Er:YLF laser at the wavelength of ~1.73 μm were also the aim of our work.

At first, the temperature dependence of the Cr:ZnSe (1) absorption spectrum was measured. The sample was fixed and thermally contacted via indium foil in the copper holder and then placed to the cryostat VPF-100 with CaF_2 windows (without AR coatings). Cryostat with the crystal was placed to the calibrated spectrophotometer UV3600 Shimadzu and was cooled using the liquid nitrogen (LN_2) to the temperature of 78 K. The step of the measurement was set to 1 nm with the slit width of 2 nm. The temperature inside the cryostat was controlled by the 325 Cryogenic Temperature Controller. The absorption spectra of the Cr:ZnSe (1) crystal were measured for chosen set of temperatures of 78, 100, 140, 180, ..., 380 K. Fresnel losses on the crystal-air/air-crystal facets of the incident probe spectrometer beam were considered and during calculation of absorption coefficient were subtracted. The temperature dependence of measured absorption spectrum is presented in Fig. 6.3a. The temperature dependence of the Cr:ZnSe (1) absorption spectrum bandwidth (FWHM) and the absorption peak central wavelength are presented in Fig. 6.3b. The Cr:ZnSe (1) crystal sample has a thermally stable absorption coefficient for wavelengths close to ~1715 nm and ~1997 nm in a wide temperature range of 78–380 K. If the pumping radiation wavelength is within the ~1715–1997 nm spectral range, it can be useful to cool down the Cr:ZnSe (1) crystal. However, if the pumping wavelength is below ~1715 nm or above ~1997 nm, it is better to keep the system at or above RT.

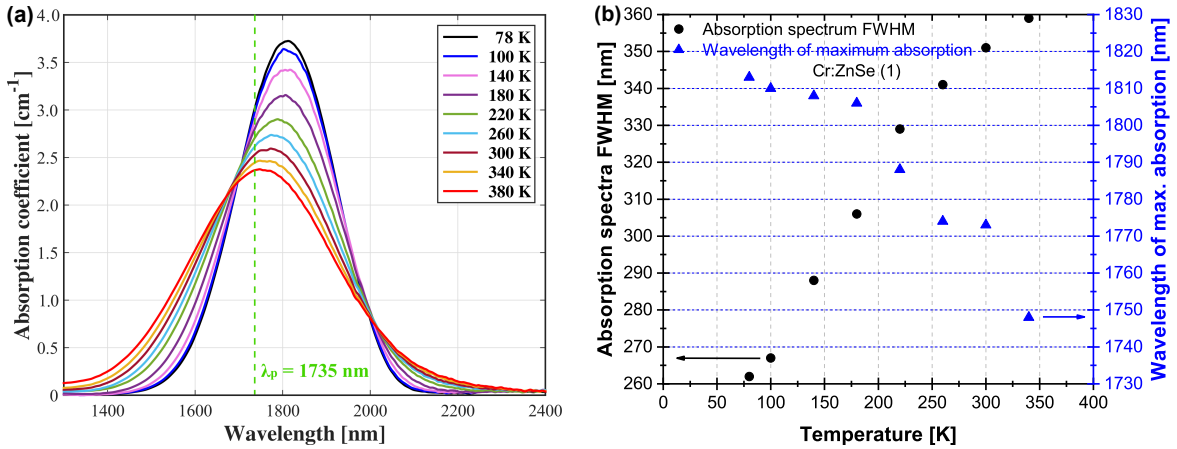

Figure 6.3: **(a)** Temperature dependence of the Cr:ZnSe (1) single crystals absorption spectra in the range of 78–380 K. Green dashed curve shows the excitation wavelength used of the Er:YLF laser. **(b)** Temperature dependence of the Cr:ZnSe (1) absorption spectrum bandwidth (black circles – left y-axis) and the absorption peak central wavelength (blue triangles – right y-axis).

The fluorescence spectrum was detected by the Thorlabs PDA-30G-EC PbS detector at the output of the Oriel 77250 monochromator with 280 μm slits on the input/output (resolution 8 nm) and diffraction grating model no. 77301 (primary wavelength region: 1.45–2.2 μm). The LP1850 longwave-pass filter was used to protect the detector from any reflected pumping radiation. The fluorescence spectra were measured for the set of temperatures of 78, 100, 140, ..., 380 K. The temperature dependence of the Cr:ZnSe (1) fluorescence spectrum is shown in Fig. 6.4a. The energy of the Er:YLF laser pumping radiation operated in the free-running (FR) mode (measured behind the pumping mirror) was set to ∼34 mJ and was stable during whole measurement at all temperatures. The temperature dependence of the Cr:ZnSe (1) single crystal fluorescence spectra bandwidth (FWHM) were analysed as well as the wavelength shift of maximum fluorescence intensity with decreasing temperature and these results are presented in Fig. 6.4b.

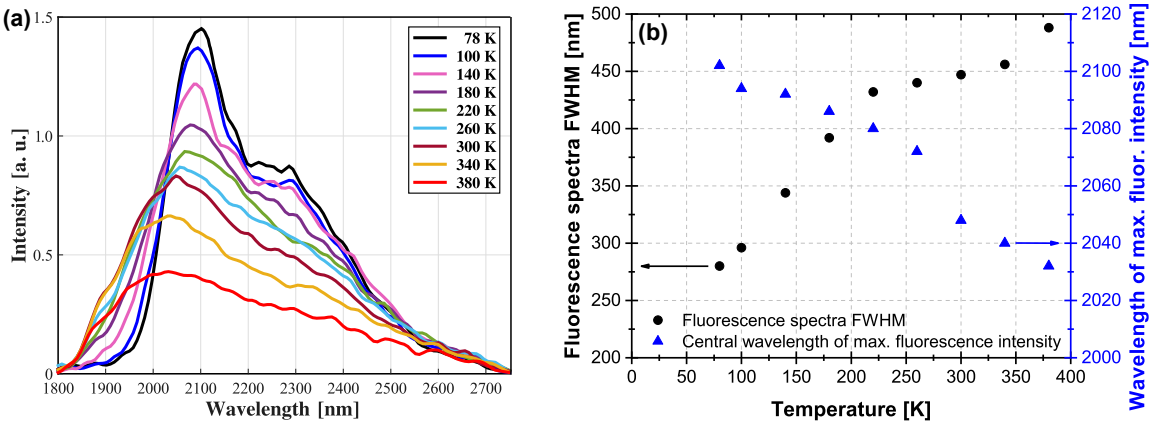

Figure 6.4: **(a)** Temperature dependence of the Cr:ZnSe (1) single crystals fluorescence spectra in the range of 78–380 K. **(b)** Temperature dependence of the Cr:ZnSe (1) fluorescence spectrum FWHM bandwidth (black circles – left y-axis) and the wavelength of maximum fluorescence intensity (blue triangles – right y-axis).

The Cr:ZnSe (1) crystal was placed in the copper holder inside the cryostat at the dis-

tance of ~130 cm from the Er:YLF output coupler. The plano-convex lens with the focal length of $f = 150$ mm was used for focusing the pumping radiation which was about 2 cm in front of focal plane (pump beam diameter ~500 μm). The Cr:ZnSe (1) optical resonator consist of a flat PM with HT of ~93 % at the wavelength of 1.73 μm and HR at typical Cr:ZnSe oscillation wavelength range. The OC with radius of curvature of $r = 150$ mm and reflectivity of $R_{OC} \approx 93$ % at ~2.4 μm was used for the measurement of the temperature dependence of the Cr:ZnSe (1) laser output energy. The resonator length was ~12 cm and the Cr:ZnSe (1) crystal was located ~4 cm from the PM.

The temporal profiles of Er:YLF laser pumping and Cr:ZnSe (1) generated laser oscillation pulses are shown in Fig. 6.5. In the case of the FR mode of pumping, the duration of both pulses (pump and generated) were ~150 μs (see Fig. 6.5a). When the electro-optically Q-switched Pockel's cell in the pumping Er:YLF laser resonator was turned on, the ~160 ns pulses were generated resulting in ~110 ns pulses of the Cr:ZnSe (1) laser (see Fig. 6.5b).

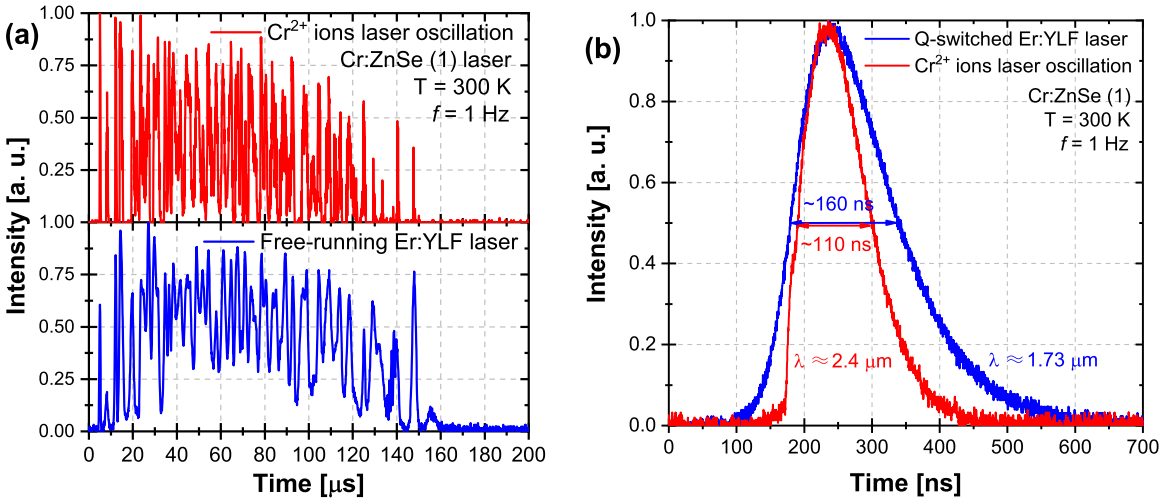

Figure 6.5: Temporal profiles of the Er:YLF laser radiation pump pulse (blue curve) and the generated Cr:ZnSe (1) laser system oscillation (red curve) in the **(a)** free-running mode and in the **(b)** Q-switched mode.

Two mirrors forming the Z-line highly reflecting the Cr:ZnSe (1) laser output beam and transparent for unabsorbed pump radiation were used at the laser output. The laser oscillation spectra were measured with the same monochromator (Oriel 77250, grating model no. 77301) as in the case of fluorescence spectra measurement. The 50 μm slits were used keeping the resolution of the measurement at 2 nm. Due to that Z-line, the monochromator was placed in the distance of ~30 cm from the Cr:ZnSe (1) laser OC. The oscillation spectrum intensity was measured by the PD36-05 InAsSbP/InAs detector. All temperature dependent measurements were performed for the same Q-switched pumping mode with the pulse energy of 11 mJ and pulse duration (FWHM) of ~160 ns (corresponding peak power of ~66,6 kW). The oscillation spectra for four different temperatures of 78, 180, 300, and 380 K are shown in Fig. 6.6a.

It was expected that the output energy will be higher for lower temperatures according to the results obtained from absorption and fluorescence spectra measurements. For instance, the absorption coefficients at the wavelength of 1.73 μm were 2.95, 2.73, 2.62, and 2.56 cm^{-1} for temperatures of 78, 180, 300, and 380 K, respectively. Due to this

fact, the temperature dependence of absorbed energy was also measured. The output energy characteristics were measured in the free-running pumping mode for the same set of temperatures. The Fresnel losses of pumping radiation on crystal facets as well as the losses caused by its passing through the AR-uncoated CaF_2 cryostat windows were considered. The output energy characteristics are shown in Fig. 6.6b.

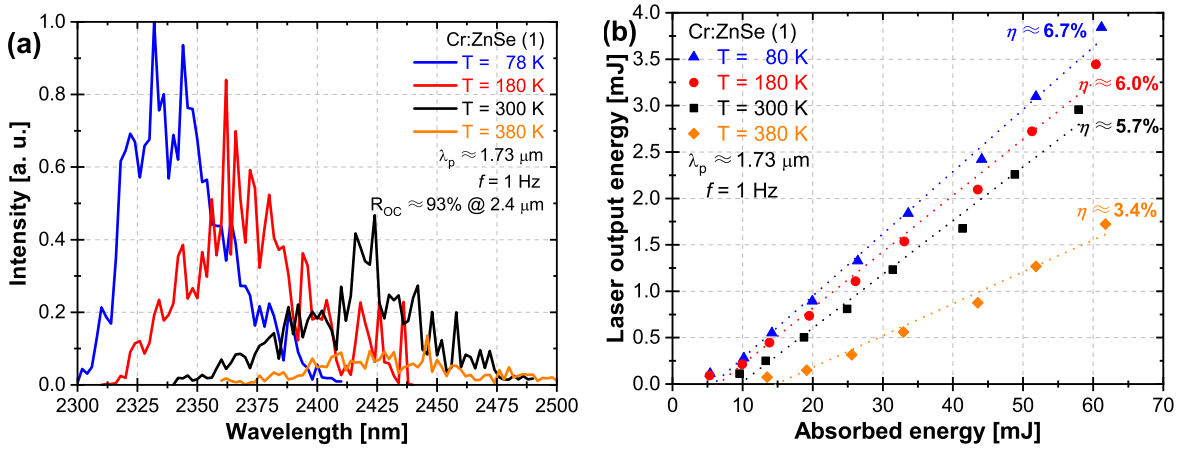

Figure 6.6: Temperature dependence of the Cr:ZnSe (1) **(a)** laser oscillation spectra and **(b)** the laser output energy on the energy absorbed in the crystal for the Q-switched pumping mode. 78 K – blue curve, 180 K – red curve, 300 K – black curve, 380 K – orange curve. Pumped by Er:YLF laser at the wavelength of ~1.73 μm.

The Cr:ZnSe (1) laser oscillation spectra for different reflectivity of output couplers of the same radius of curvature of r = -150 mm were also measured at temperature of 300 K. Three different output couplers with the reflectivity of $R_{OC} \approx 96$, 95 and 88 % at the wavelength of 2.5 μm were used. The obtained dependence can be found in Fig. 6.7. With decreasing reflectivity of the OC, the losses in the resonator were higher, and thus the generated oscillation spectrum was red shifted to shorter wavelengths, where the gain was higher.

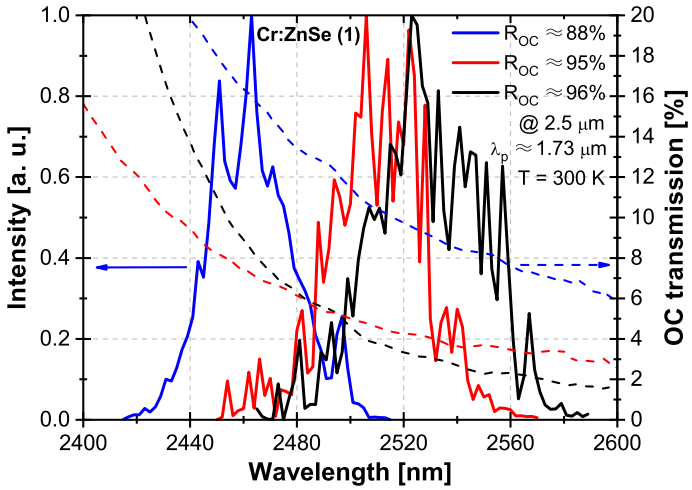

Figure 6.7: Cr:ZnSe (1) laser oscillation spectra at temperature of 300 K for different reflectivity of output couplers – full line curves. R_{OC} = 88 % at 2.5 μm – blue curve; 95 % – red curve; and 96 % – black curve. Dashed curves of same colours – transmission spectra of corresponding output couplers.

Therefore, the laser oscillation wavelength can be also tuned by the change of the losses in the resonator. This concept is also used in the case of spectral tuning by the rotation of birefringent plate placed under the Brewster angle inside the resonator cavity which selectively increasing or decreasing polarisation dependent losses. Such tunability by a 1.5 mm thick SiO_2 birefringent plate was investigated at RT under the laser diode pumping at the wavelength of ∼1.7 μm at the repetition rate of 10 Hz. The results obtained are presented in Fig. 6.8.

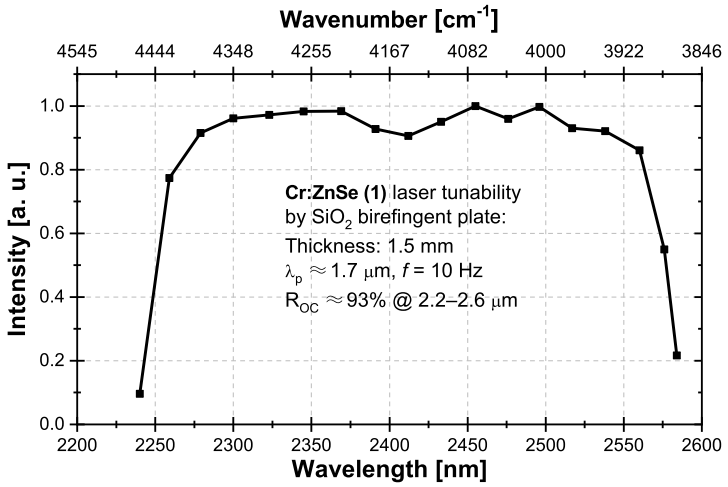

Figure 6.8: Cr:ZnSe (1) laser oscillation spectra tunability at RT by a 1.5 mm thick SiO_2 birefringent plate under excitation by the LD at the wavelength of $\lambda_p \approx 1.7$ μm with the repetition rate of $f = 10$ Hz.

To conclude, the wavelength of absorption peak maximum has shifted for 65 nm toward a longer wavelength from 1748 nm at 380 K up to 1813 nm at 78 K together with the narrowing of absorption spectrum bandwidth from 373 nm down to 262 nm. It was discovered that the absorption coefficient of the Cr:ZnSe (1) crystal remains thermally stable at wavelengths close to 1715 nm and 1997 nm in a wide temperature range of 78–380 K. The flash-lamp pumped Er:YLF laser (∼1.73 μm) in the FR mode was used for the excitation. While heating the Cr:ZnSe (1) crystal from 78 K up to 380 K, the FWHM of the fluorescence spectra broadened from 280 nm up to 488 nm with a more pronounced change in its leading edge. The highest optical-to-optical laser slope efficiency of 6.7 % was reached at the temperature of 78 K which was ∼2× higher than at the temperature of 380 K (3.4 %). It corresponds to observed dependence of the absorption coefficient increasing with decreasing crystal temperature. The output energy of 3.84 mJ at 78 K was reached which together with the FWHM pulse widths of ∼200 μs (for about 10 μs shorter than pump pulses) corresponds to the mean power of 19 mW. The central oscillation wavelength of 2.36 μm was observed for all investigated temperatures. However, there were additional peaks at ∼2.29 μm at 78 K and at ∼2.45 μm at 380 K. The mean bandwidth (FWHM) of the oscillation spectra was ∼25 nm. As a result, by cooling the Cr:ZnSe (1) system, the wavelength of maximum absorption is being shifted to the longer wavelengths as well as the wavelength of maximum intensity of fluorescence spectrum. Similar results were also observed with other investigated Cr:ZnSe (2 and 3) samples later.

6.1.2 Tunable Cr:ZnSe (2) laser excited by the laser diode at the wavelength of ~1.7 μm

The investigation of the influence of the Cr:ZnSe crystal active length on the laser output power and efficiency was performed with eight Cr:ZnSe (2) samples with thicknesses of 2, 3, 5, and 10 mm with or without AR-coatings. The LD generating radiation at the wavelength of ~1.69 μm (repetition rate of $f = 10$ Hz; pulse duration of $t_p = 20$ ms) and at ~1.7 μm in the pulse mode and in the CW mode, respectively, was used for the excitation.

The Cr:ZnSe (2) crystal fluorescence spectrum under pulsed LD radiation excitation at the wavelength of ~1.69 μm ($f = 10$ Hz/$t_p = 20$ ms) together with the absorption and LD oscillation spectrum is shown in Fig. 6.9. The fluorescence spectrum was measured using the ArcOptix Fourier-Transform Infrared (FTIR) spectrometer. The fluorescence band ranged from ~1.6 μm up to ~2.9 μm. The maximum fluorescence intensity was detected at around ~2.05 μm and the fluorescence bandwidth (FWHM) was ~0.51 μm.

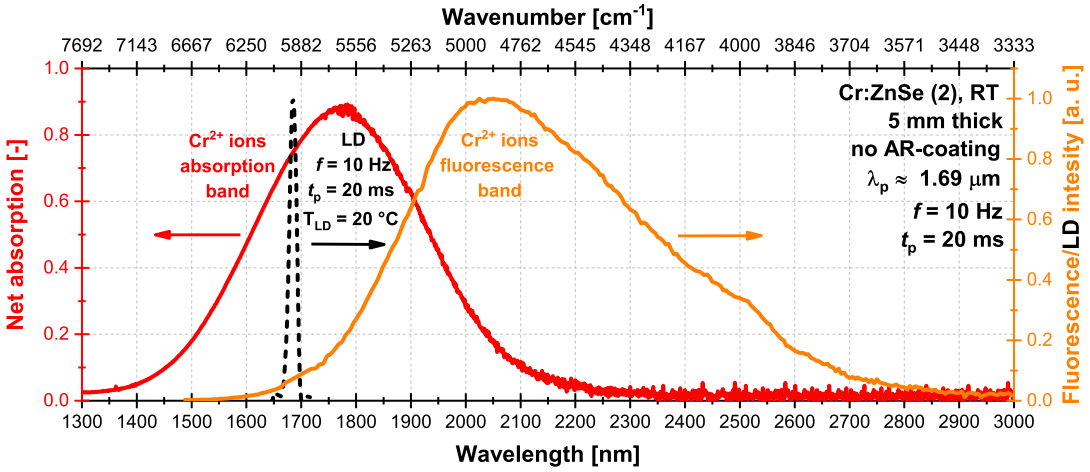

Figure 6.9: Fluorescence spectrum of the Cr:ZnSe (2) single crystal at RT (orange curve) together with the absorption spectrum (red curve) and the LD oscillation spectrum at ~1.69 μm (black dashed curve).

The Cr^{2+} ions RT fluorescence decay in the Cr:ZnSe (2) crystal was measured under excitation by the Ekspla NT252 nanosecond optical parametric oscillator (OPO) and was detected by the fast InAsSb/InAsSbP photodetector PD36-05. A typical fluorescence decay curve of the 5 mm thick Cr:ZnSe crystal at RT excited at the wavelength of $\lambda_e = 1.7$ μm with the repetition rate of $f_e = 1$ kHz and the excitation pulse duration of $t_e \approx 2.5$ ns is presented in Fig. 6.10. The measured Cr^{2+} ions fluorescence decay time at the RT was $\tau \approx 7.2 \pm 0.1$ μs. Such a long fluorescence decay time (in comparison with 5.5 μs reported in [19]) may be caused due to the fluorescence signal reabsorption and trapping. The measured Cr^{2+} ions fluorescence decay time was independent on the excitation wavelength used in a whole absorption band spectral range from 1.35 μm up to 2.25 μm (measured with the step of 50 nm).

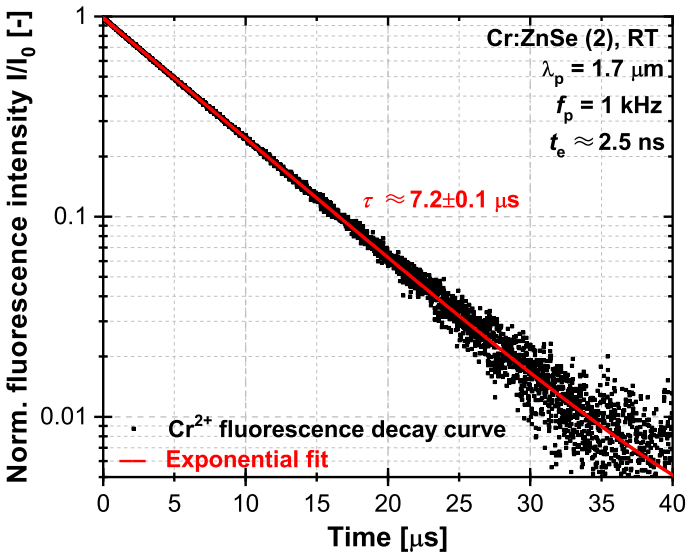

Figure 6.10: Fluorescence decay curve of the Cr:ZnSe (2) single crystal at RT (black curve) together with the exponential fit (red curve). Excitation pulse duration: $t_e \approx 2.5$ ns; excitation wavelength: $\lambda_e = 1.7\,\mu$m; repetition rate: $f_e = 1$ kHz.

The influence of the active length of the crystal was investigated in the pulse mode with only passively air-cooled crystals. The laser output properties of all samples were measured under the same conditions with the crystal located in the short optical resonator with the laser cavity length of L ≈ 1.8 cm. To optimize the maximum mean output power and slope efficiency, five different output couplers with various reflectivity in the range of 45–97 % and the same radius of curvature of -150 mm were tested. The dependence of the maximum mean output power and optical-to-optical slope efficiency is presented in Fig. 6.11.

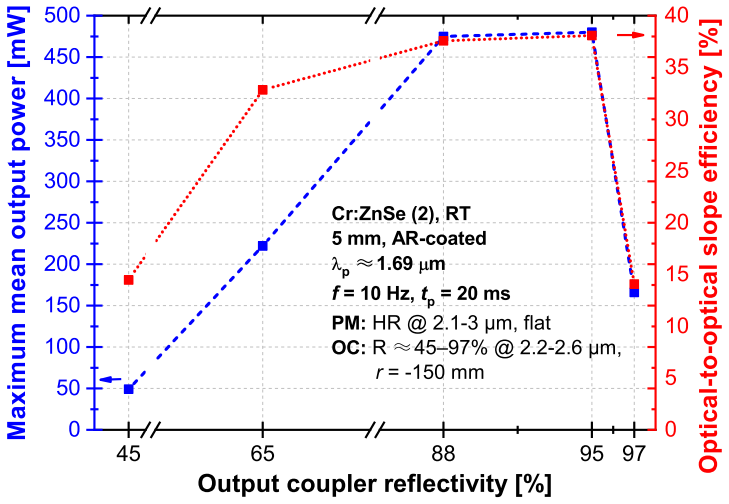

Figure 6.11: The dependence of the Cr:ZnSe (2) laser maximum mean output power (blue) and the slope efficiency (red) on the OC reflectivity. 5 mm thick AR-coated Cr:ZnSe (2) sample at RT, pump pulse repetition rate $f = 10$ Hz, pump pulse duration: $t_p = 20$ ms.

As we can see from this plot, the optimal output coupler reflectivity value ranges from

88 % to 95 %. As the optimal laser cavity output coupler was chosen concave output coupler with reflectivity of $R_{OC} \approx 88\,\%$ at 2.2–2.6 µm, r = -150 mm and a flat PM highly reflective in the spectral range of 2.1–3 µm. The comparison of maximum mean output power and corresponding slope efficiency in dependence on the crystal thickness is shown in Fig. 6.12.

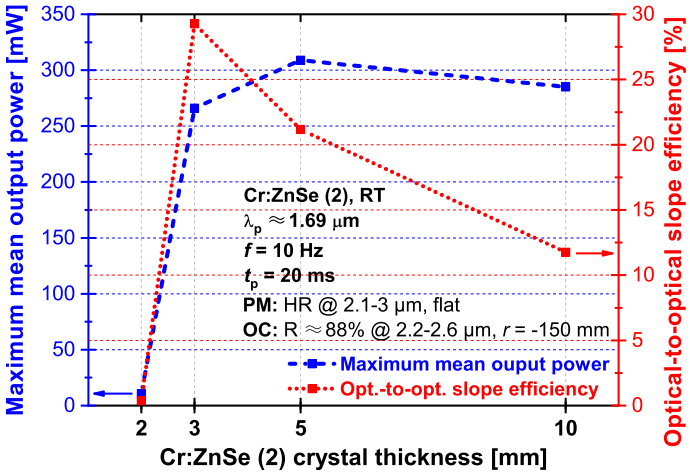

Figure 6.12: The dependence of the maximum mean output power (blue) and corresponding slope efficiency (red) on the Cr:ZnSe (2) crystal thickness. All four samples without AR-coatings at RT.

In order to select the most suitable pumping repetition rate and pulse duration for the Cr:ZnSe (2) sample with a thickness of 3 mm and no AR-coating, a series of different pump pulse configurations were gradually employed. A total of seven distinct pump pulse modes were investigated while maintaining a fixed LD current of 18 A and LD temperature of 20 °C. When the pulse duration was extended, a minor shift towards longer wavelengths in the LD central oscillation wavelength was observed. However, this shift likely had only a negligible impact on the resulting Cr:ZnSe absorption. The outcomes of this measurement are presented in Fig. 6.13.

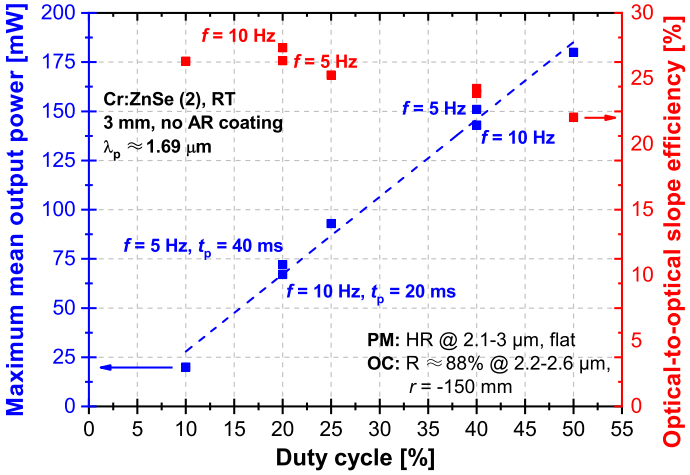

Figure 6.13: The dependence of the Cr:ZnSe (2) laser maximum mean output power (blue) and the optical-to-optical slope efficiency (red) on the duty cycle. 3 mm thick sample without AR-coatings.

When the pump pulse duty cycle was increased, the average output power of the laser also increased in line with expectations. However, a slight decrease in slope efficiency as the pump pulse duration was extended was noticed. Our aim was to achieve the highest possible efficiency for this laser system. Therefore, for subsequent measurements, a repetition rate of 10 Hz and a pulse duration of 20 ms was chosen.

The examples of two temporal profiles of the Cr:ZnSe (2) laser system generation are shown in Fig. 6.14. For increasing pump pulse duration, the drop in generated laser pulse intensity was observed (Fig. 6.14b). It corresponds to a drop in optical-to-optical slope efficiency (see Fig. 6.13).

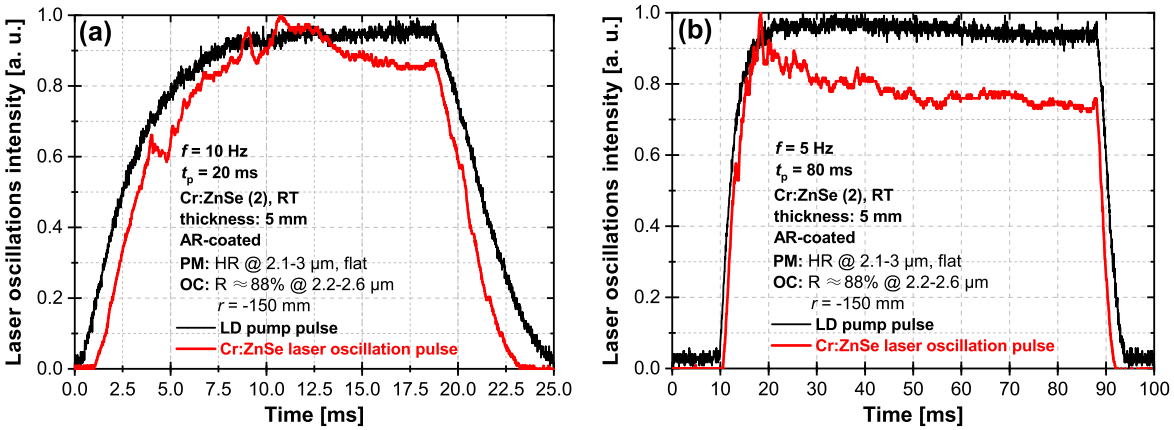

Figure 6.14: Temporal profiles of the LD pumping (black curves) and the 5 mm thick AR-coated Cr:ZnSe (2) generated laser radiation at RT (red curves) for: **(a)** $f = 10$ Hz, $t_p = 20$ ms and **(b)** $f = 5$ Hz, $t_p = 80$ ms.

The observed laser oscillation pulse temporal profiles were measured behind the monochromator at the specific wavelengths from 2.36 µm (by 20 nm step) up to 2.46 µm of the 3 mm thick Cr:ZnSe (2) sample without AR-coatings and are shown in Fig. 6.15a. Overall whole laser pulse duration followed the pump pulse and was about ∼20 ms long. As follows from Fig. 6.15a the laser oscillations at the wavelengths of 2.36 and 2.46 µm are shorter and less intensive due to much lower gain at those wavelengths as we can also see from the intensity spectral profile of laser oscillations in Fig. 6.15b.

Based on the absorption spectrum measurement, it was determined that the total losses of samples with an AR coating would be ∼4 %. This value is about 4.5× lower than the Fresnel losses of uncoated samples, which were around 18 %. The same conclusion regarding of these losses was drawn from the measurement of absorbed and unabsorbed pump power, and these losses were consistent across all samples with different thicknesses.

To compare the laser efficiencies of 3 mm and 5 mm thick samples under optimal pump pulse conditions (10 Hz/20 ms – 20 % duty cycle), the laser cavity was set to a short length of ∼1.8 cm. The cavity in both cases consisted of the same pair of mirrors used in previous experiments. The dependence of the mean output power on the absorbed pump power for both the AR-coated and the uncoated Cr:ZnSe (2) samples is depicted in Fig. 6.16.

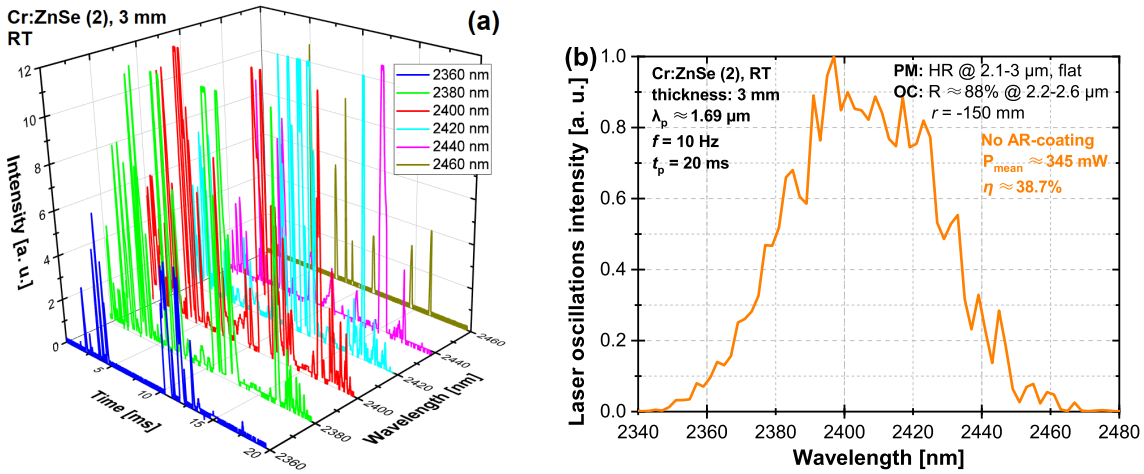

Figure 6.15: **(a)** Spectral resolved temporal profiles of the generated Cr:ZnSe (2) laser radiation at six different wavelengths of 2.36 μm (blue), 2.38 μm (green), 2.40 μm (red), 2.42 μm (cyan), 2.44 μm (violet), and 2.46 μm (olive). **(b)** The Cr:ZnSe (2) laser oscillation spectrum. 3 mm thick crystal without AR-coatings; pump pulse duration: $t_p \approx 20$ ms, repetition rate: $f = 10$ Hz, RT.

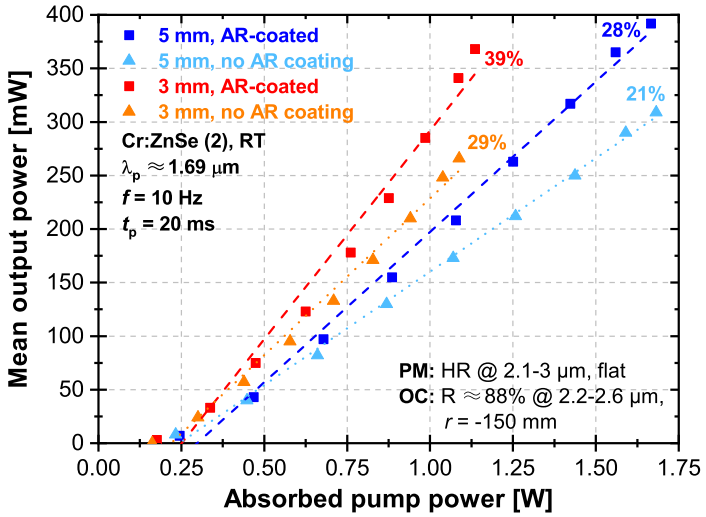

Figure 6.16: The dependence of the Cr:ZnSe (2) laser mean output power on the absorbed pump power for AR-coated (squares) and uncoated (triangles) samples of 3 mm (red/orange) and 5 mm thickness (dark/light blue) at RT.

The AR-coated samples exhibited higher mean output power and slope efficiency compared to uncoated ones at similar level of absorbed pump power. Specifically, the maximum slope efficiency achieved with the 3 mm thick AR-coated Cr:ZnSe (2) sample increased by around ~10 %, rising from ~29 % in the case of uncoated sample of the same thickness to ~39 % with the AR-coatings. Moreover, the maximum mean output power obtained with the AR-coated sample reached 368 mW, which was ~28 % higher than the output power measured for the uncoated sample (266 mW). Considering our goal of achieving maximum efficiency for the laser system, the 3 mm thick AR-coated sample was selected for further experiments with the laser oscillation wavelength tuning.

In order to improve the laser output performance, efficiency and to be able to operate the Cr:ZnSe (2) laser also in the continuous wave (CW) mode, the 3 mm and 5 mm thick AR-coated samples were placed in the copper holder actively cooled by through circulating

water (at 20 °C). For better heat transfer, the crystals were surrounded by a thin indium foil. The photo of both samples in this holder is presented in Fig. 6.17.

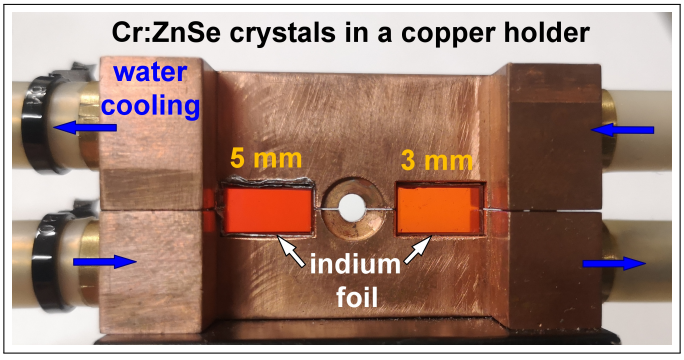

Figure 6.17: A photo of two investigated Cr:ZnSe (2) samples (thicknesses of 5 mm and 3 mm) placed in the copper holder with the schematic representation (blue arrows) of the water-cooling flow.

Thanks to the active cooling, the influence on laser output power up to CW mode could be performed. The laser output properties of the 3 mm thick, AR-coated Cr:ZnSe (2) sample were measured under in the hemispherical optical resonator with a cavity length of L ≈ 15.6 cm. The laser cavity consisted of a flat pumping mirror (PM) highly reflective in the spectral range of 2.1–3 μm and a concave (r = -150 mm) output coupler (OC) with a reflectivity of R ≈ 86–92 % in the range of 2.2–2.6 μm.

Fig. 6.18 illustrates the dependence of maximum mean laser output power on the pump pulse duration. The repetition rate was fixed at 10 Hz, and the pump pulse duration was increased with increments of 10 ms from 10 ms to the CW regime. As the pump pulse duration increased, the central radiation wavelength of the LD shifted from 1685 nm in the 10 Hz/10 ms regime up to 1707 nm in the CW mode. This wavelength shift also corresponds to a ~6.4 % increase in the absorption coefficient of the Cr:ZnSe (2) sample.

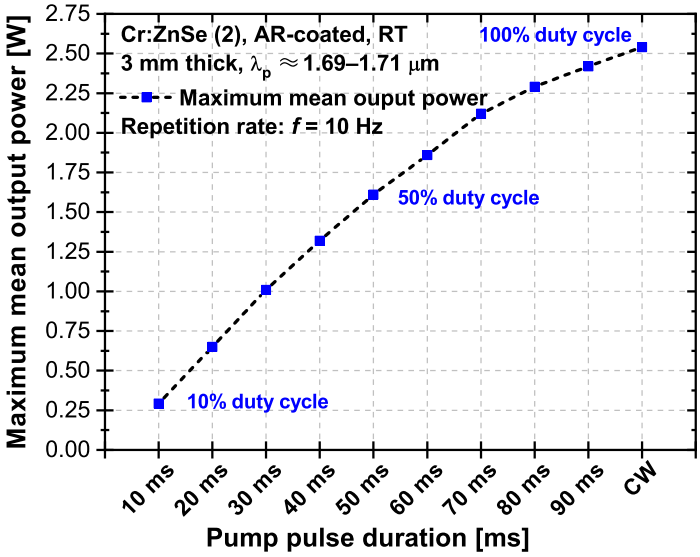

Figure 6.18: The dependence of the maximum mean output power on the increasing pump pulse duration of the Cr:ZnSe (2) laser system (3 mm thick AR-coated sample) at the RT with the step of 10 ms at the fixed repetition rate of 10 Hz.

As expected, a higher pump pulse duty cycle resulted in an increase of the mean laser output power. In Fig. 6.18, it can be seen that the maximum mean laser output power rose from ~293 mW up to ~2.54 W. However, up to a duty cycle of ~50 %, the mean output power exhibited nearly linear growth. Beyond this point, saturation was observed, leading to a decrease in the slope efficiency of the Cr:ZnSe (2) laser.

The laser cavity remained unchanged for comparison with preciously studied pulse mode. The maximum mean output power achieved for samples with thicknesses of 3 mm and 5 mm was ~2.47 W and ~2.71 W, respectively. The corresponding slope efficiencies were ~21 % and 24 %, respectively. The enhanced efficiency can be attributed to the implementation of a multi-pass pumping scheme that allows for the reuse of a significant portion of the unabsorbed pump power, as well as improved overlap between the pump and generated beams within the active medium. To further optimize efficiency, it is possible to utilize an optimal OC to reflect the unabsorbed radiation back to the crystal. This approach has the potential to enhance the overall laser performance in future experiments. In Fig. 6.19 is presented the dependence of the mean laser output power on the absorbed pump power. A lower efficiency than in the pulse mode of generation (see Fig. 6.16) could be explained by the saturation effect illustrated in Fig. 6.18.

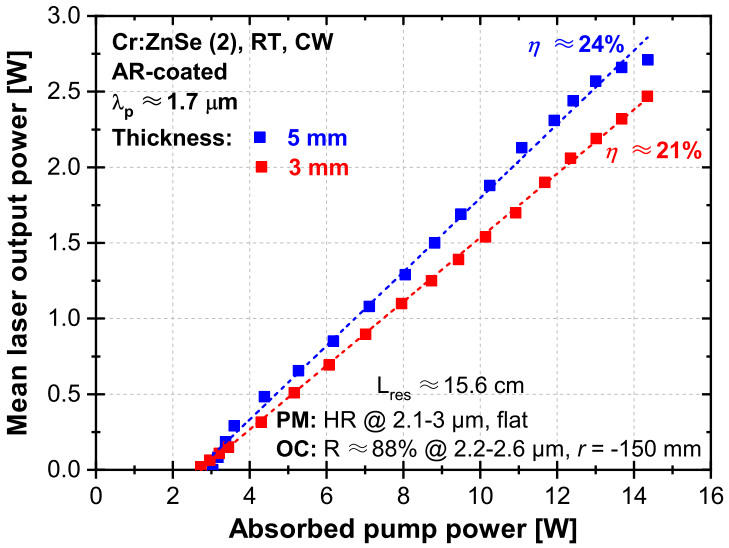

Figure 6.19: The dependence of the Cr:ZnSe (2) laser systems mean laser output power on the absorbed pump power in the CW regime at the RT (5 mm thick – blue squares; 3 mm thick – red squares).

The beam profile of the Cr:ZnSe (2) generated laser radiation was analysed by measuring it at the focal point of a curved mirror with a radius of curvature of -150 mm highly reflective at ~2.4 μm. Due to the high power of the laser output in the CW mode of operation, the beam profile was focused and measured just in the low power part of the laser beam reflected by the block made of |used silica. The knife-edge method was employed for this measurement.

The measurements were conducted under the same conditions using both 3 mm and 5 mm thick Cr:ZnSe (2) samples. The hemispheric laser cavity with a length of ~15.6 cm consisted of the same optimal pair of mirrors as in previous experiments. Fig. 6.20 presents the dependence of the beam waist diameter on the position around the focus

for both samples.

The quality of the generated laser beams was found to be quite good. The measured M^2 parameters were ~1.2±0.2 for the 3 mm thick sample and ~1.1±0.1 for the 5 mm thick sample. In the focus, the beam waist diameters were ~49±4 μm and ~42±4 μm for the 3 mm and 5 mm thick samples, respectively. This corresponds to the power densities of laser radiation in the beam waist of ~133 kW/cm^2 and ~200 kW/cm^2 for the 3 and 5 mm thick Cr:ZnSe (2) samples, respectively.

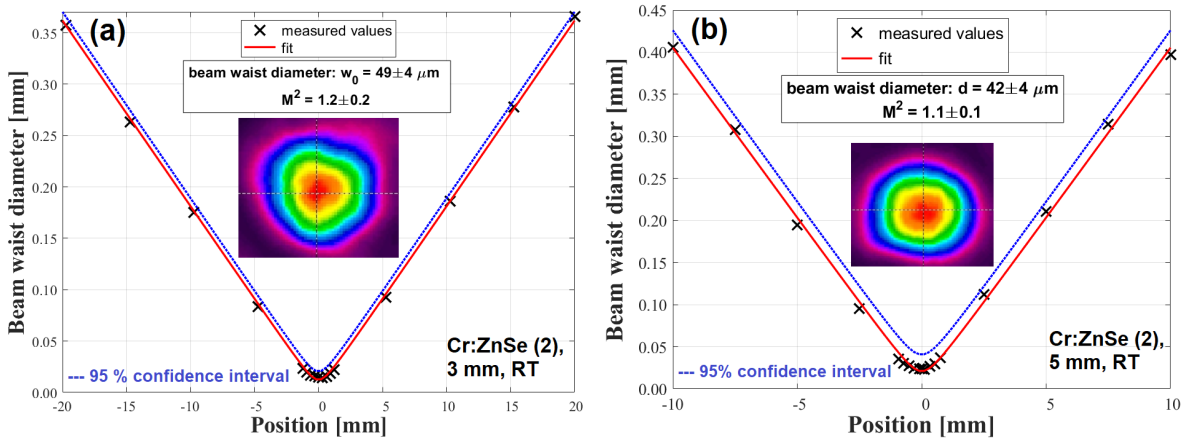

Figure 6.20: The beam waist diameter profiles of the Cr:ZnSe (2) laser systems with a crystal thickness of **(a)** 3 mm and **(b)** 5 mm at RT. Full red line curve is the fit of measured data (X) and the dotted blue curve is the upper 95 % confidence interval of this fit. The insets are photos of beam profiles in a far field (~60 cm far from the OC).

The process of central laser oscillation wavelength tunability in the Cr:ZnSe (2) laser system using a 0.8 mm thick MgF_2 birefringent plate will be discussed in following paragraphs. To incorporate the birefringent plate into the laser setup, it was positioned at a Brewster angle (of ~54°) between the crystal and the OC within the resonator cavity, which had a length of ~15.5 cm. The simplified laser system setup is shown in Fig. 5.3. The free spectral range (FSR) of this plate was calculated to be ~600 nm.

To accommodate the desired wavelength range of 2–3 μm, three different output couplers (OC1, OC2, and OC3) had to be utilized. It should be noted that an output coupler with the desired reflectivity across the entire 2–3 μm range was not present in our laboratory at the time. All three output couplers had similar reflectivity levels ~90 %. They also shared the same concave curvature with a radius of r = -150 mm. The specific reflectivity values for each output coupler were as follows: OC1 had an approximate reflectivity of R ≈ 84 % at 2.15 μm, OC2: R ≈ 92 % at 2.40 μm, and OC3: R ≈ 92 % at 2.60 μm.

The laser system's output characteristics were measured for each output coupler in the non-selective laser cavity with absence of the MgF_2 plate. The obtained laser oscillation wavelength and maximum mean output power, along with the transmission spectra of all three output couplers and the pumping mirror used, are presented in Fig. 6.21. Fig. 6.21a shows the results for the 3 mm thick AR-coated sample operated in the pulse mode (10 Hz/20 ms) and Fig. 6.21b is devoted for the 5 mm thick AR-coated sample in the CW mode for a comparison.

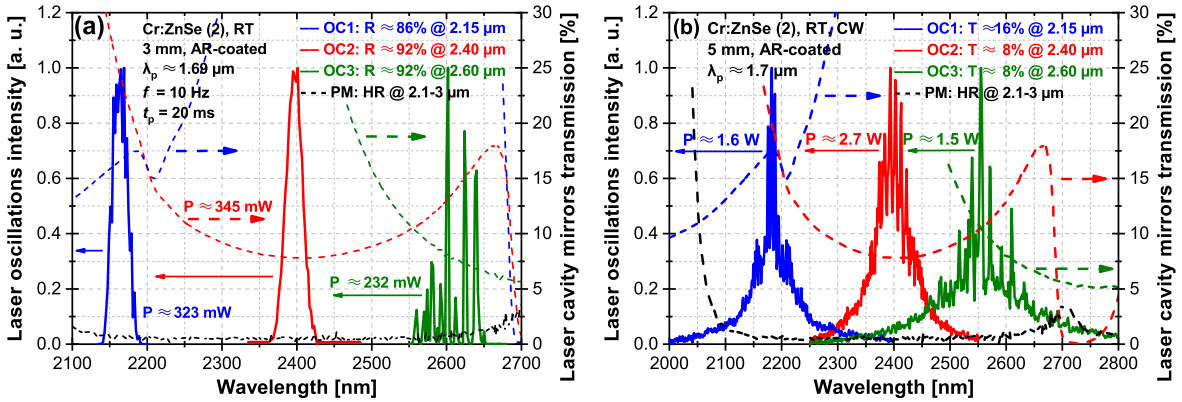

Figure 6.21: The Cr:ZnSe (2) laser oscillation spectra for three subsequently changed output couplers OC1–OC3 (without MgF_2 birefringent plate): OC1 (blue), OC2 (red), and OC3 (green). Dashed curves of the same colours represent the output couplers transmission spectra at generated wavelength range. Black dashed curve – transmission spectrum of pumping mirror. **(a)** 3 mm thick sample operated in the pulse mode (20 ms/10 Hz), **(b)** 5 mm thick sample in the CW mode.

The maximum mean output power and a central laser oscillation wavelengths for OC1–OC3 in the pulse mode (20 ms/10 Hz) with the 3 mm thick Cr:ZnSe (2) sample were gradually measured as ~323 mW at ~2.16 μm, ~345 mW at ~2.4 μm, and ~232 mW at ~2.6 μm, respectively. In the CW mode of operation with the 5 mm thick Cr:ZnSe (2) sample these results were achieved: mean output power of ~1.6 W at a central oscillation wavelength of ~2.18 μm, ~2.7 W at ~2.39 μm, and ~1.5 W at ~2.55 μm for OC1–OC3, respectively. The mean laser output power characteristics for all output couplers in both regimes are shown in Fig. 6.22.

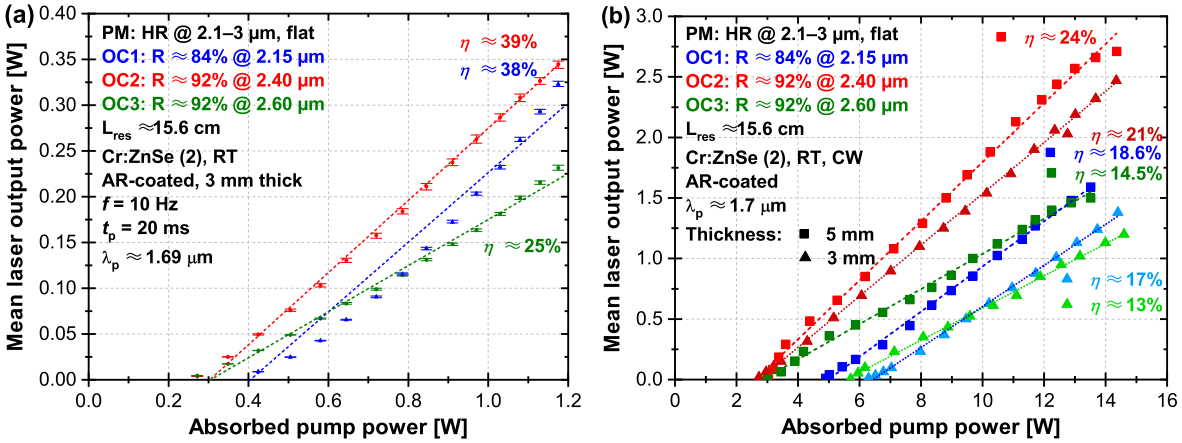

Figure 6.22: The Cr:ZnSe (2) dependence of mean laser output power on the absorbed pump power for three different output couplers OC1–OC3 (without MgF_2 birefringent plate): OC1 (blue), OC2 (red), and OC3 (green). **(a)** 3 mm thick sample operated in the pulse mode (20 ms/10 Hz), **(b)** comparison of 3 mm and 5 mm thick samples in the CW mode.

For all output couplers, a continuously tunable spectral range spanning from ~2.07 μm to ~2.67 μm was observed. Within the range of ~2.1–2.52 μm, the mean output power consistently exceeded 1 W. This corresponds to a power density of at least ~73.5 kW/cm^2 (at the focus of the -150 mm curved concave mirror), with regards to the previously

measured beam waist radius. However, the tunability beyond ∼2.7 µm appeared to be limited by the presence of water vapour absorption in that part of the spectrum [216], as well as by a low gain. The dependence of the mean laser output power on the central oscillation wavelength was measured for each OC and it is presented in Fig. 6.23.

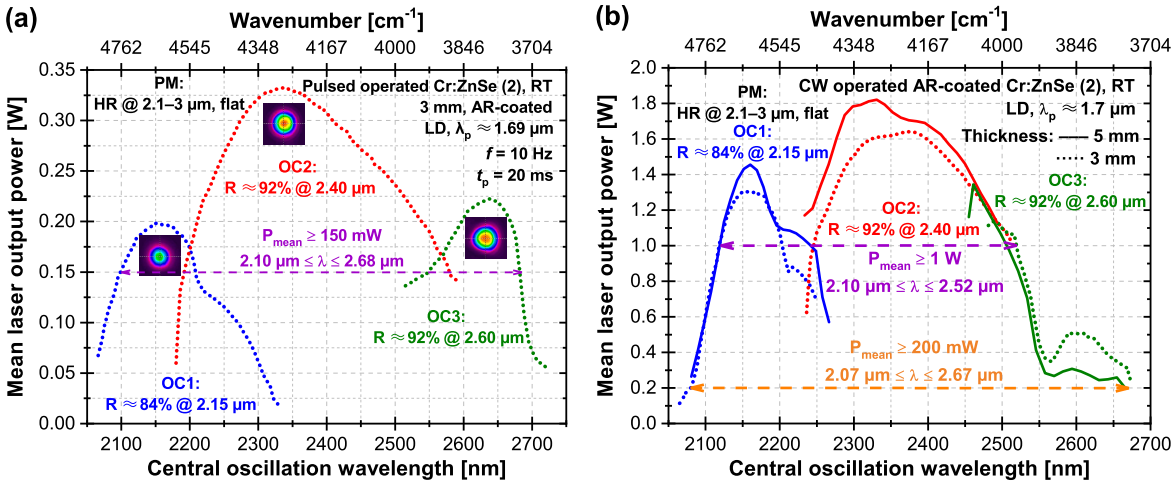

Figure 6.23: The spectral dependence of the Cr:ZnSe (2) laser systems mean output power on the tuned central laser oscillation wavelength by rotating the MgF_2 birefringent filter. **(a)** in the pulse mode (20 ms/10 Hz) with 3 mm thick crystal, **(b)** in the CW mode with 3 mm (dotted curves) and 5 mm (full line curves) thick samples.

During the wavelength tuning via MgF_2 birefringent plate of 0.8 mm thickness, the laser output exhibited narrow spectral linewidths of ∼5–10 nm (at FWHM), and the spatial profiles of the laser beam maintained a Gaussian-like shape throughout the entire tunable range. Fig. 6.24 shows these individual laser oscillation spectral lines obtained during the wavelength tuning process: Fig. 6.24a and Fig. 6.24b correspond to the pulse and CW mode of operation with 3 mm thick sample, respectively.

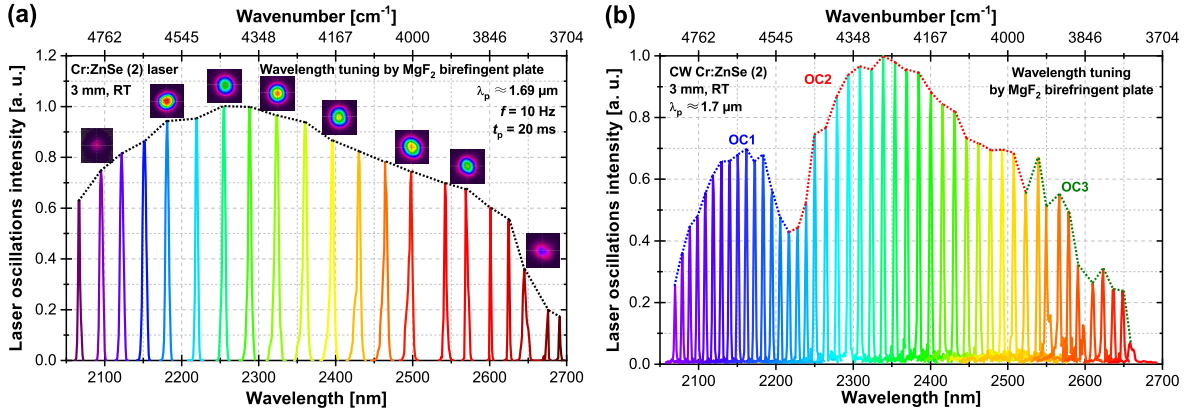

Figure 6.24: The Cr:ZnSe (2) laser system (3 mm thick sample) oscillations tunability at RT using the birefringent MgF_2 filter at Brewster angle in the resonator cavity. Examples of laser emission linewidths during the birefringent plate rotation: **(a)** in the pulse mode, **(b)** in the CW mode.

The investigated samples exhibited an absorption coefficient of ∼1.5 cm^{-1} at RT for the central excitation wavelength of ∼1.7 µm. The fluorescence band of Cr^{2+} ions

spanned from ~1.6 μm to ~2.9 μm, peaking at ~2.05 μm with a full-width at half-maximum fluorescence intensity of ~0.5 μm at RT. Additionally, the Cr^{2+} ions fluorescence decay time was measured to be ~7.2±0.1 μs at RT.

Under CW mode of operation at RT, the crystal demonstrated tunable mid-IR laser oscillations. Laser performance was examined with varying crystal thicknesses and pump pulse durations. The highest slope efficiency achieved in the pulse mode (10 Hz/20 ms) was ~39 % and in the CW mode was ~24 %, resulting in a maximum mean output powers of ~0.37 W and ~2.71 W in the pluse and CW mode, respectively. The central observed laser oscillation wavelength was ~2.4 μm. Using different output couplers and a single birefringent 0.8 mm thick MgF_2 plate, the laser radiation was continuously tunable within a wide mid-IR spectral range from 2.07 μm to 2.67 μm, with the CW mean output power exceeding 0.2 W. In the range of 2.1–2.52 μm, the CW mean output power even exceeded 1 W. The spectral linewidth of the tuned radiation was only ~5 nm (FWHM) with a Gaussian-like beam spatial profile in the whole range.

In conclusion, the LD pumped Cr:ZnSe (2) single crystal operating in the CW mode could be used as a compact, tunable, and high-power coherent mid-IR radiation source that can be effectively utilized at RT for various applications, particularly in spectroscopy.

6.2 Properties of the Cr:$Zn_{1-x}Mn_xSe$ ($x \approx 0.05$; 0.1; 0.2; 0.3) and the Cr:ZnSe (3) single crystals

To obtain the laser oscillation at longer mid-IR wavelengths in the 2–3 μm spectral region, the Cr^{2+} ions doped $Zn_{1-x}Mn_xSe$ host single crystal materials were investigated next. The aim was to investigate and compare the influence of increasing manganese amount x in the $Zn_{1-x}Mn_xSe$ host material on its spectral and laser properties. The obtained results were compared under the same conditions with the Cr:ZnSe (3) single crystal without manganese in the host (x = 0). The spectral (6.2.1) and laser output properties (6.2.2) are presented in this section.

Three conference papers [C1, C2, C19] were published to this topic. Moreover, these crystals were compared in several journals with similar materials co-doped with Cr^{2+} and Fe^{2+} ions during their future research.

The summary of the absorption coefficient values at the excitation wavelength of Er:YLF laser at ~1.73 μm at 78 K and 300 K of all five investigated single crystals can be found in Tab. 6.2 and their photos are shown in Fig. 6.25.

Table 6.2: Overview of the investigated Cr^{2+}:$Zn_{1-x}Mn_xSe$ and Cr^{2+}:ZnSe single crystals and their absorption coefficients α at excitation wavelength used of ~1.73 μm at 78 K and 300 K.

Crystal	Thickness [mm]	α @ 1.73 μm @ 78 K [cm^{-1}]	α @ 1.73 μm @ 300 K [cm^{-1}]
Cr:$Zn_{1-x}Mn_xSe$ ($x \approx 0.05$)	4.2	9.1	6.9
Cr:$Zn_{1-x}Mn_xSe$ ($x \approx 0.10$)	4.3	4.6	3.9
Cr:$Zn_{1-x}Mn_xSe$ ($x \approx 0.20$)	3.9	3.9	2.9
Cr:$Zn_{1-x}Mn_xSe$ ($x \approx 0.30$)	3.8	4.0	3.3
Cr:ZnSe (3) ($x = 0$)	2.2	13.8	11.7

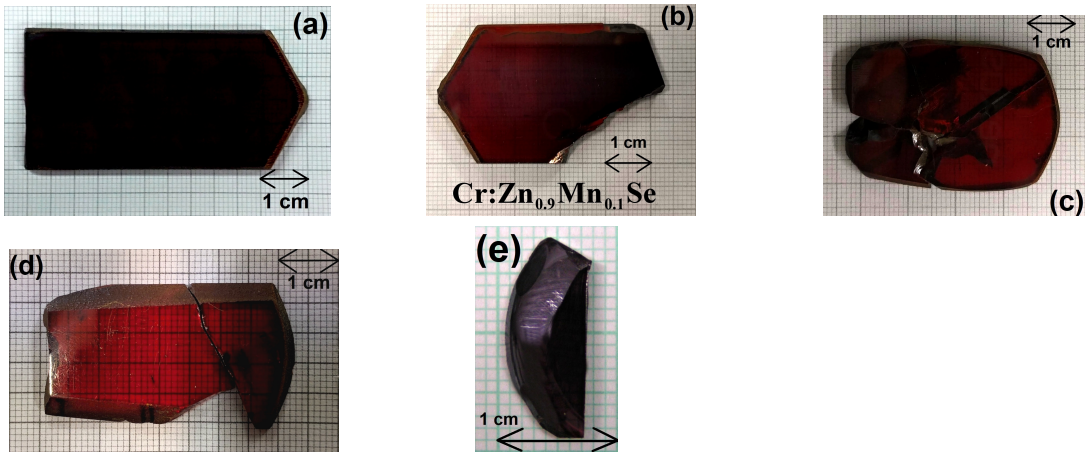

Figure 6.25: Photos of the investigated Cr:$Zn_{1-x}Mn_xSe$ and Cr:ZnSe (3) single crystals: **(a)** x ≈ 0.05, **(b)** x ≈ 0.1, **(c)** x ≈ 0.2, **(d)** x ≈ 0.3, and **(e)** Cr:ZnSe (3).

6.2.1 Spectral properties of the Cr:$Zn_{1-x}Mn_xSe$ (x ≈ 0.05; 0.1; 0.2; 0.3) and the Cr:ZnSe (3) single crystals

Besides the manganese amount (x) all crystal samples also differ in Cr^{2+} ions concentrations. It is worth to mention that Fe^{2+} ions were also presented from the production in a very small amounts in the Cr:$Zn_{1-x}Mn_xSe$ samples in some cases. The spectral width of Cr^{2+} ions absorption bands slightly increases with rising amount x of manganese in the host material. Similarly, the spectral position of maximum absorption was shifted a bit farther to the infrared spectrum. The comparison of absorption spectra of all five samples measured by the spectrophotometer Nicolet iS5 at the temperature of 78 K is presented in Fig. 6.26. The absorption coefficients of all samples slowly decreases with increasing temperature up to the RT and the absorption bandwidths narrowed slightly as well.

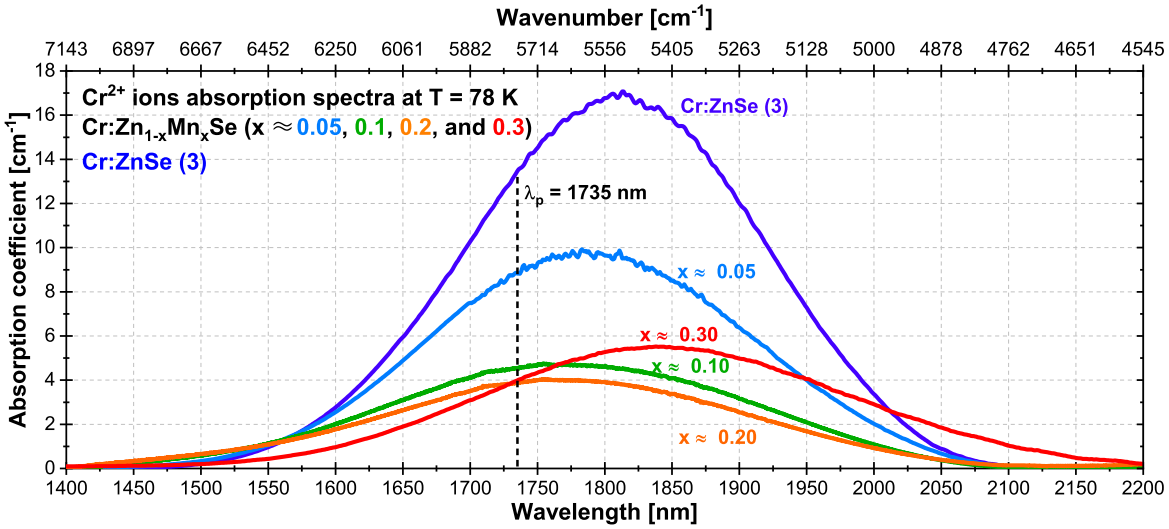

Figure 6.26: Absorption spectra of the Cr:$Zn_{1-x}Mn_xSe$ (x ≈ 0.05; 0.1; 0.2; 0.3) and the Cr:ZnSe (3) single crystals at the temperature of 78 K. Dashed line shows the spectral position of the excitation wavelength used at 1735 nm.

The Cr^{2+} ions fluorescence spectra at 78 K and 300 K are shown in Fig. 6.27. As we can see, with higher manganese amount (x) in the $Zn_{1-x}Mn_xSe$ host material, the fluorescence spectra of Cr^{2+} ions became wider and their maxima as well as whole spectra were red shifted. The fluorescence intensity maxima of the Cr:ZnSe (3) and the Cr:$Zn_{1-x}Mn_xSe$ ($x \approx 0.05$; 0.1; 0.2; 0.3) samples at the temperature of 78 K were detected at approximate wavelengths of ~2.11 µm, ~2.12 µm, ~2.15 µm, ~2.19 µm, ~2.24 µm, and ~2.27 µm, respectively. There was almost no difference in the fluorescence spectra of all samples at the temperature of 300 K as we can see in Fig. 6.27b.

The temperature dependence of the Cr^{2+} ions fluorescence decay time of the Cr:$Zn_{1-x}Mn_xSe$ ($x \approx 0.05$; 0.1; 0.2; 0.3) and the Cr:ZnSe (3) crystals are presented in Fig. 6.28. The Cr^{2+} ions fluorescence decay time remains almost the same in a wide temperature range from 78 K up to ~280 K and then slightly starts to drop.

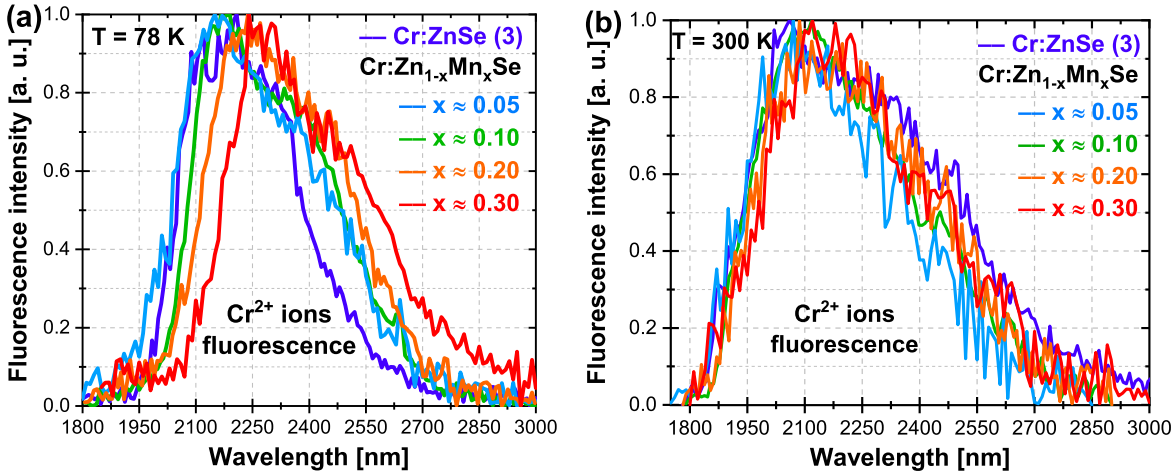

Figure 6.27: Fluorescence spectra of Cr^{2+} ions of the Cr:$Zn_{1-x}Mn_xSe$ ($x \approx 0.05$; 0.1; 0.2; 0.3) and the Cr:ZnSe (3) single crystals at the temperature of **(a)** 78 K and **(b)** 300 K.

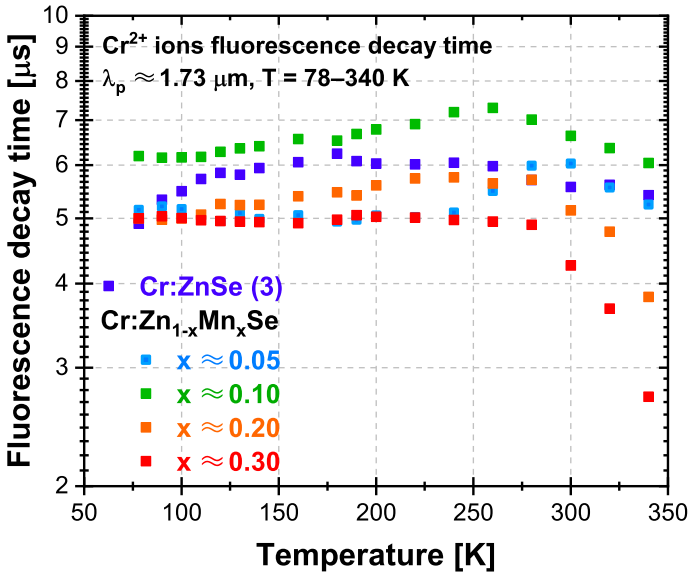

Figure 6.28: Temperature dependence of the Cr^{2+} ions fluorescence decay time of the Cr:$Zn_{1-x}Mn_xSe$ ($x \approx 0.05$; 0.1; 0.2; 0.3) and the Cr:ZnSe (3) single crystals in the temperature range of 78–340 K.

6.2.2 Laser output properties – excitation at the wavelength of ~1.73 μm

The self-lasing (gain-switched operation) of all investigated samples under the Q-switched Er:YLF laser pumping at the wavelength of ~1.73 μm was obtained. A plane-parallel resonator was formed between the planar pump mirror and one of the crystal facets. The self-lasing oscillation spectra and the corresponding pictures of output beam profiles of the Cr:$Zn_{1-x}Mn_xSe$ (x ≈ 0.05; 0.1; 0.2; 0.3) and the Cr:ZnSe (3) and laser systems with the resonator cavity without output couplers are shown in Fig. 6.29. However, in this case, the output energy was very low. The summary of their laser output properties with added output coupler with optimal reflectivity of R_{OC} ≈ 36–48 % (at generated spectral range) improving the output energy is presented in Tab. 6.3.

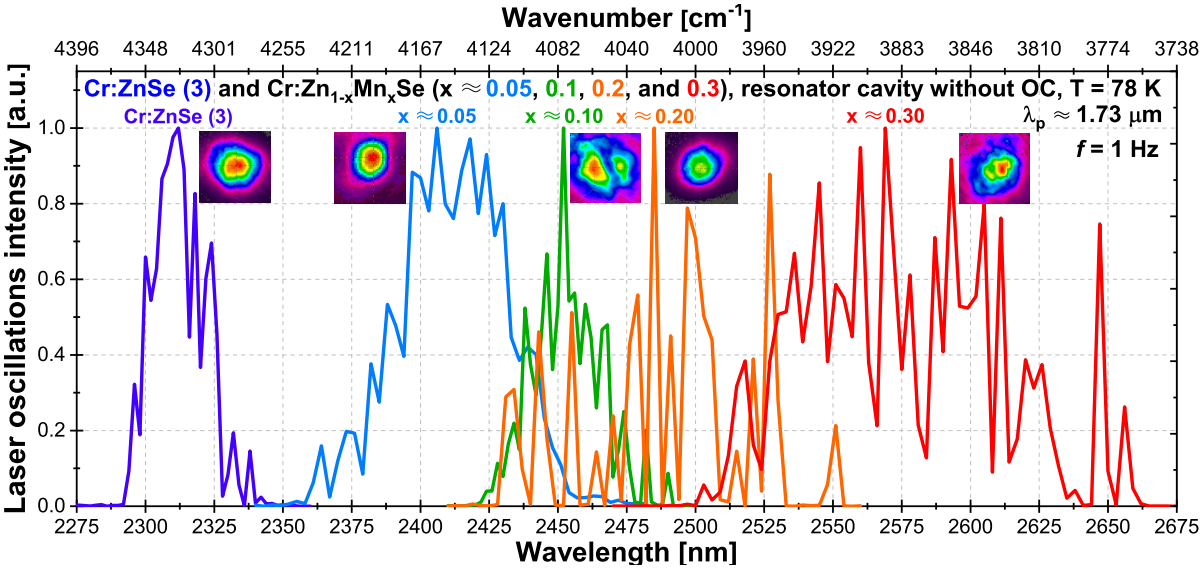

Figure 6.29: Cr^{2+} ions laser oscillation spectra of the Cr:$Zn_{1-x}Mn_xSe$ (x ≈ 0.05; 0.1; 0.2; 0.3) and the Cr:ZnSe (3) laser systems without output coupler at 78 K.

Table 6.3: Overview of the Cr^{2+} ions laser output properties of the Cr:$Zn_{1-x}Mn_xSe$ (x ≈ 0.05; 0.1; 0.2; 0.3) and the Cr:ZnSe (3) single crystals at 78 K. R_{OC} ≈ 36–48 % at generated spectral range.

Crystal	Central osc. λ @ 78 K [nm]	Maximum output energy @ 78 K [mJ]	Opt.-to-opt. efficiency [%]
Cr:$Zn_{1-x}Mn_xSe$ (x ≈ 0.05)	2406	1.63	35.2
Cr:$Zn_{1-x}Mn_xSe$ (x ≈ 0.10)	2452	2.33	43.9
Cr:$Zn_{1-x}Mn_xSe$ (x ≈ 0.20)	2485	0.98	37.2
Cr:$Zn_{1-x}Mn_xSe$ (x ≈ 0.30)	2569	1.72	28.2
Cr:ZnSe (3)	2312	1.63	31.4

Temporal profiles of the Q-switched Er:YLF laser pump pulse and the generated Cr:$Zn_{1-x}Mn_xSe$ (x ≈ 0.3) laser oscillation pulse are shown in Fig. 6.30. The pump pulse duration of ~150 ns was closely copied by the generated Cr^{2+} ions laser oscillation pulse with a bit shorter duration of ~135 ns.

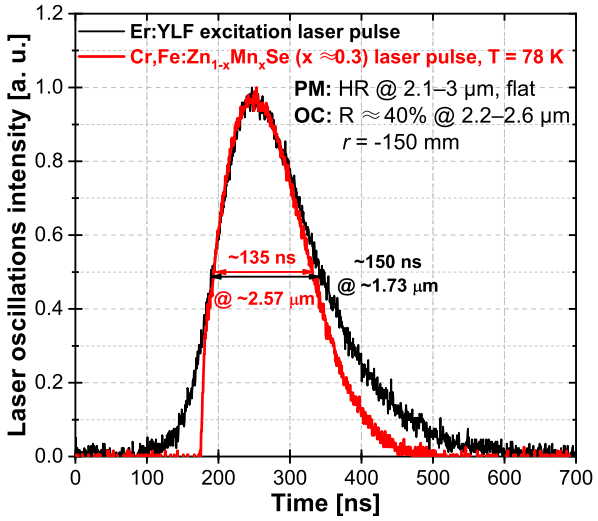

Figure 6.30: Temporal profile of the Q-switched Er:YLF laser pump pulse (black curve) and of the generated Cr:$Zn_{1-x}Mn_xSe$ (x ≈ 0.3) laser oscillation pulse at 78 K (red curve).

In conclusion, lasers based on Cr:$Zn_{1-x}Mn_xSe$ single crystals show great promise as a source of mid-IR coherent radiation in the spectral range of 2–3 µm. As the amount of manganese (x) increases in the host material, several significant effects were observed, including a red shift in the spectral wavelengths to longer mid-IR ranges, broadening of absorption, fluorescence, and oscillation spectra. Among the tested samples, Cr:$Zn_{1-x}Mn_xSe$ (x ≈ 0.1) exhibited the most favourable results, achieving a maximum laser output pulse energy of ~2.3 mJ and the highest optical-to-optical efficiency of ~44 % under a given pumping condition.

To further enhance laser performance, future efforts can focus on optimizing the active media's optical quality during crystal growth, applying AR coatings to reduce losses, and finding optimal output coupling conditions. By pursuing these measures, it is possible to improve both the laser output energy and overall efficiency of the lasers based on the Cr:$Zn_{1-x}Mn_xSe$ single crystals.

6.3 Properties of the Cr,Fe:$Zn_{1-x}Mn_xSe$ ($x \approx 0.05; 0.2; 0.3$ and 0.4) single crystals

As the next part, the comparison of Cr^{2+},Fe^{2+}:$Zn_{1-x}Mn_xSe$ single crystals has been processed. The aim of studying this material was the possibility of $Cr^{2+} \rightarrow Fe^{2+}$ ions energy transfer leading to the Fe^{2+} ions laser oscillation was investigated and laser generation in the 4–5 µm spectral region pumped via this method was obtained and published for the first time. Moreover, the comparison properties of Cr^{2+},Fe^{2+} ions co-doped with the Cr^{2+}-only doped samples studied in previous Sec. 6.2.

Up to date, several theoretical studies about this excitation method or dealing with spectroscopic measurements with similar Cr^{2+},Fe^{2+} co-doped materials were published [134,142,143,217,218]. During the investigation of these samples and working on this thesis, three author [P4,P5,P7] and two co-author papers [P1,P2] about this topic were published with the experimentally proved $Cr^{2+} \rightarrow Fe^{2+}$ ions energy transfer lasing results for the first

time. Moreover, the obtained results were presented at nine international conferences: [C5–C7, C9, C11–C14, C20]. In the following Fig. 6.31 there are the photos of these four samples. The recapitulation of the absorption spectra properties of these crystals at the excitation wavelengths used at 78 K can be found in Tab. 6.4. In Fig. 6.31e is shown the illuminated Cr,Fe:$Zn_{1-x}Mn_xSe$ (x ≈ 0.30) crystal placed between two crossed polarizing filters for the illustration of the investigated samples inhomogeneity by polarization twisting of the light passing through the crystal. All investigated samples placed between two crossed polarizing filters looked similarly as this example. The spectral (6.3.1) and laser output properties (6.3.2, 6.3.3) of both ions are presented in following subsections.

Table 6.4: Overview of the investigated Cr^{2+},Fe^{2+}:$Zn_{1-x}Mn_xSe$ single crystals and their absorption coefficients α at the excitation wavelengths used of 1.73 μm (for Cr^{2+} ions) and 2.94 μm (for Fe^{2+} ions) both at 78 K.

Crystal	Thickness [mm]	α @ 1.73 μm @ 78 K [cm^{-1}]	α @ 2.94 μm @ 78 K [cm^{-1}]
Cr,Fe:$Zn_{1-x}Mn_xSe$ (x ≈ 0.05)	3.9	8.1	2.8
Cr,Fe:$Zn_{1-x}Mn_xSe$ (x ≈ 0.20)	2.7	4.8	8.4
Cr,Fe:$Zn_{1-x}Mn_xSe$ (x ≈ 0.30)	5.1	2.5	3.7
Cr,Fe:$Zn_{1-x}Mn_xSe$ (x ≈ 0.40)	2.6	7.1	10.9

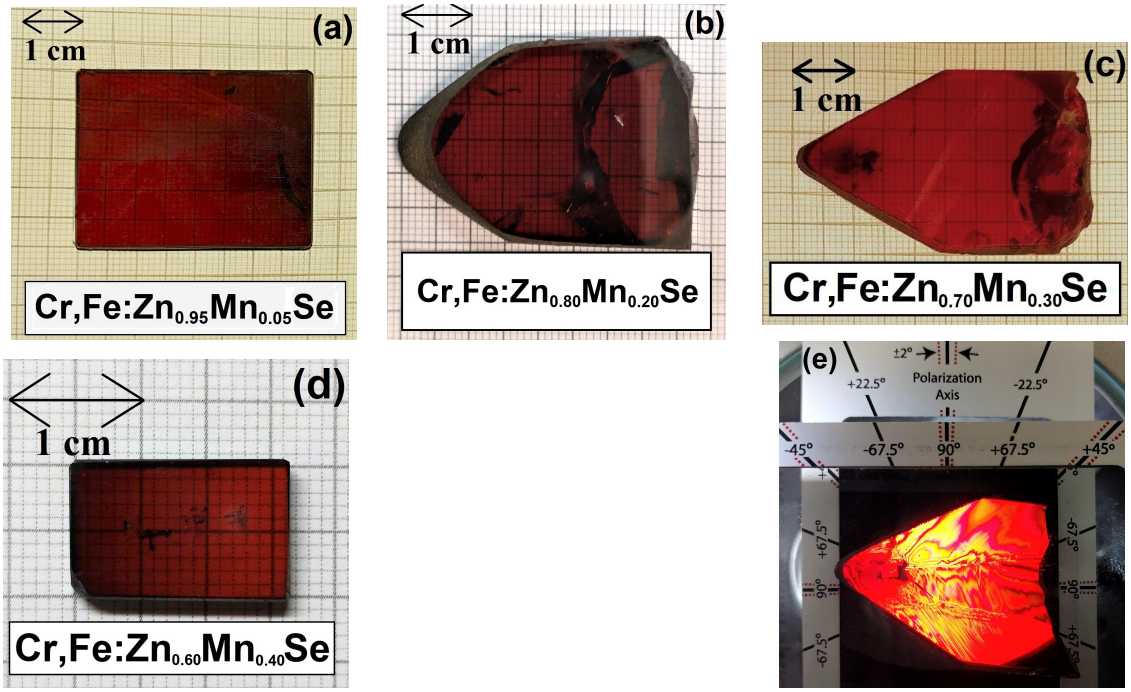

Figure 6.31: Photos of the investigated Cr,Fe:$Zn_{1-x}Mn_xSe$ single crystals: **(a)** x ≈ 0.05, **(b)** x ≈ 0.20, **(c)** x ≈ 0.30, and **(d)** x ≈ 0.40. **(e)** Cr,Fe:$Zn_{1-x}Mn_xSe$ (x ≈ 0.30) single crystal placed between two crossed polarizing filters.

6.3.1 Spectral properties of the Cr,Fe:$Zn_{1-x}Mn_xSe$ ($x \approx 0.05; 0.2; 0.3$ and 0.4) single crystals

The comparison of absorption spectra at the temperature of 78 K is presented in Fig. 6.32. The crystal samples differ in Cr^{2+} and Fe^{2+} active ions relative and absolute concentrations. The spectral width of both ions absorption bands increases with increasing amount (x) of manganese in the host material and the spectral position of maximum absorption was shifted a bit farther to the infrared part of the spectrum.

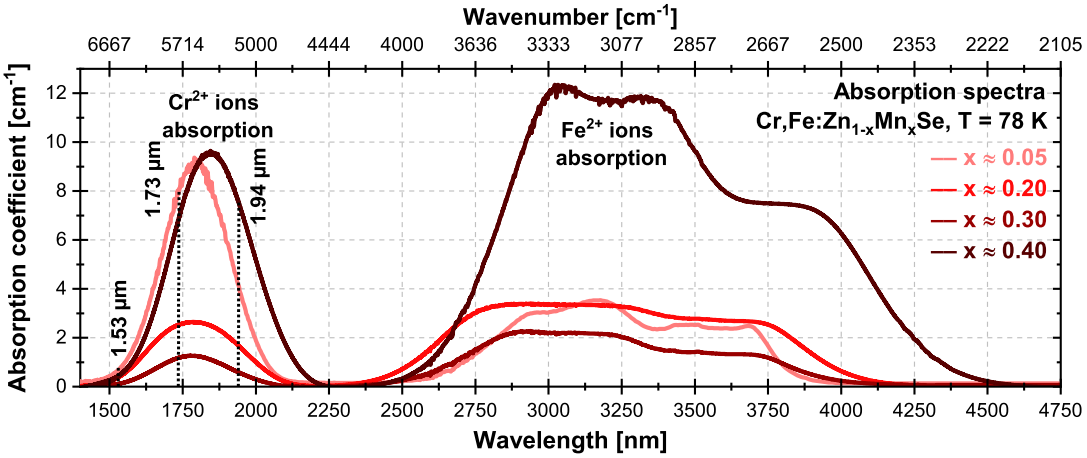

Figure 6.32: Absorption spectra of the Cr,Fe:$Zn_{1-x}Mn_xSe$ ($x \approx 0.05; 0.2; 0.3; 0.4$) single crystals at the temperature of 78 K. Dotted lines show spectral positions of central wavelengths of laser sources used for the excitation.

The Cr^{2+} and Fe^{2+} ions fluorescence spectra excited by the short pulse Q-switched Er:YLF laser at the wavelength of ~1.73 µm at 78 K are shown in Figs. 6.33a and 6.33b, respectively. As we can see, with higher manganese amount (x) present in the $Zn_{1-x}Mn_xSe$ host material, the fluorescence spectra of both ions became wider and their maxima were red shifted. In the case of Cr^{2+} ions the maxima of fluorescence intensity of $x \approx 0.05$, 0.2, 0.3 and 0.4 samples were detected at wavelengths of ~2.10 µm, ~2.18 µm, ~2.15 µm, and ~2.28 µm, respectively. In the case of Fe^{2+} ions fluorescence spectra (Fig. 6.33b), there was a drop at around ~4.25 µm caused by atmospheric absorption of CO_2 molecules.

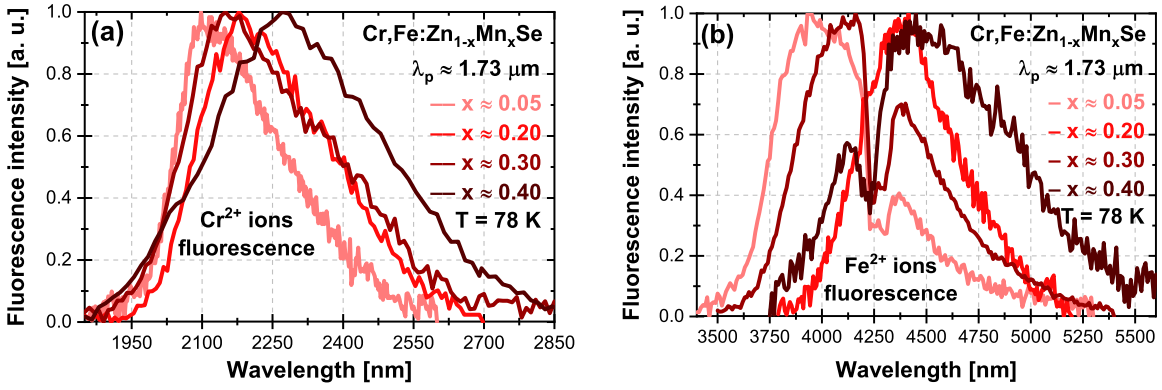

Figure 6.33: Fluorescence spectra of **(a)** Cr^{2+} ions and **(b)** Fe^{2+} ions of the Cr,Fe:$Zn_{1-x}Mn_xSe$ ($x \approx 0.05; 0.2; 0.3; 0.4$) single crystals excited at the wavelength of ~1.73 µm at the temperature of 78 K.

The temperature dependence of the Fe^{2+} ions fluorescence decay time in the Cr,Fe:$Zn_{1-x}Mn_xSe$ (x ≈ 0.05; 0.2; 0.3; 0.4) crystals excited by the Q-switched Er:YLF laser at the wavelength of ~1.73 μm is presented in Fig. 6.34. The fluorescence decay time decreases with increasing temperature from 78 K up to 300 K.

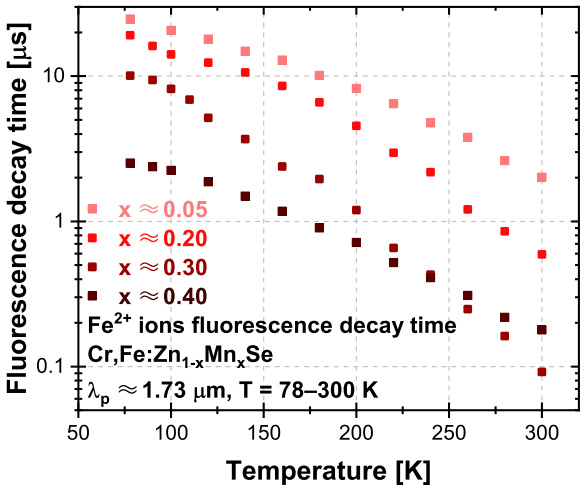

Figure 6.34: Temperature dependence of the Fe^{2+} ions fluorescence decay time of the Cr,Fe:$Zn_{1-x}Mn_xSe$ (x ≈ 0.05; 0.2; 0.3; 0.4) single crystals excited at the wavelength of ~1.73 μm in the temperature range of 78–300 K.

The temperature dependence of Cr^{2+} and Fe^{2+} ions fluorescence decay time in this host material was also measured under excitation by the Er:glass laser operated in the passive Q-switched mode using the saturable absorber Co^{2+}:$MgAl_2O_4$ (spinel) between the Er:glass active medium and the OC. The energy of one typical Er:glass laser pulse was ~8.5 mJ with the FWHM pulse duration of ~260 ns which corresponds to the peak output power of ~32.7 kW. Fluorescence decay time of Cr^{2+} and Fe^{2+} ions at RT were $\tau_{Cr^{2+}} \approx 3.5\,\mu s$ and $\tau_{Fe^{2+}} \approx 2\,\mu s$, respectively. The detailed view of Cr^{2+} fluorescence decay curves at temperatures of 78, 300 and 380 K is presented in Fig. 6.35a and the temperature dependence of the Cr^{2+} ions fluorescence decay time of the Cr,Fe:$Zn_{1-x}Mn_xSe$ (x ≈ 0.05) single crystal excited at the wavelength of ~1.53 μm is shown in Fig. 6.35b.

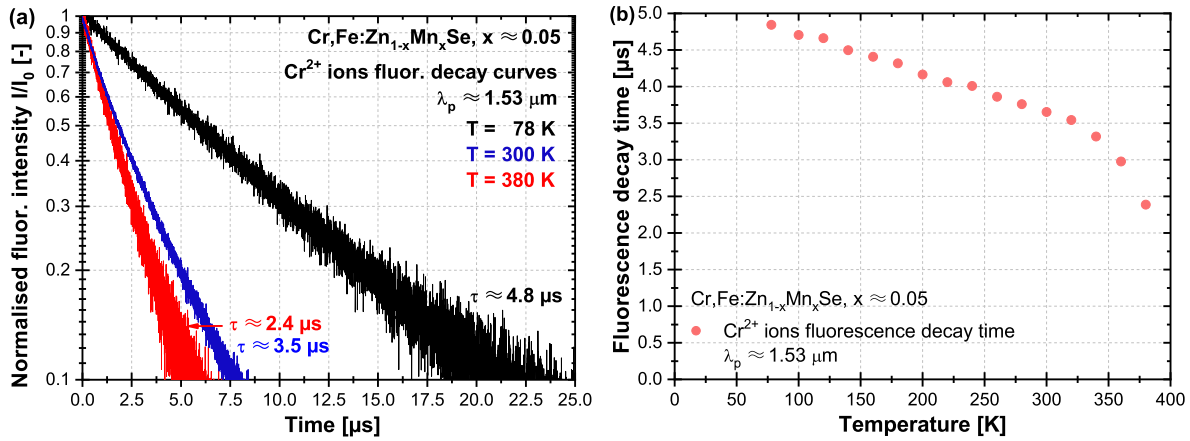

Figure 6.35: **(a)** Selected fluorescence decay curves at temperatures of 78 K (black curve), 300 K (blue curve) and 380 K (red curve) and **(b)** the temperature dependence of Cr^{2+} ions fluorescence decay time of the Cr,Fe:$Zn_{1-x}Mn_xSe$ (x ≈ 0.05) single crystal.

6.3.2 Direct Cr^{2+} ions excitation at different wavelengths

At first, the Cr^{2+} ions of the Cr,Fe:$Zn_{1-x}Mn_xSe$ crystals were excited directly by two different lasers: **a)** Er:glass laser at the wavelength of ~1.53 µm, where the absorption of Cr^{2+} ions is very weak (see Fig. 6.32), and **b)** Er:YLF laser at ~1.73 µm (see Fig. 5.5 for generated spectra of pump lasers). The obtained Cr^{2+} ions laser oscillations properties supported by adequate resonator cavity mirrors are described in two following subsections.

Cr^{2+} ions excitation by the Er:glass laser at the wavelength of ~1.53 µm

The possibility of Cr,Fe:$Zn_{1-x}Mn_xSe$ ($x \approx 0.05$) single crystal excitation at the wavelength of ~1.53 µm, where Cr^{2+} ions show a weak absorption, was demonstrated and presented at the international conference [C5]. The absorption coefficient at 1535 nm at RT was ~1.98 cm^{-1}. The laser was pumped by Er:glass laser in the free-running mode at the repetition rate of $f = 0.5$ Hz. The optical resonator consisted of the flat pumping mirror (PM) with transmittance of T ≈ 91 % at 1.53 µm together with the high reflectivity (HR) at emitted wavelength range. The curved output coupler (OC) with radius of curvature of r = -150 mm and reflectivity of R_{OC} ≈ 95 % at 2.35 µm was used. The short resonator with length of L ≈ 1.3 cm was built.

The temporal profiles of Er:glass laser pumping and generated Cr^{2+} ions laser oscillations can be found in Fig. 6.36. The generated pulse duration of ~1.5 ms for the maximum output energy was comparable to the pump pulse duration.

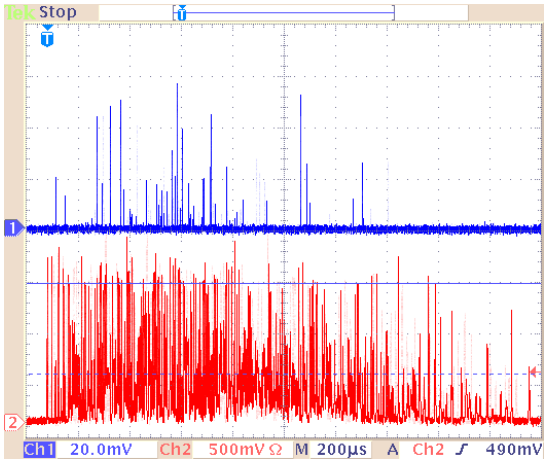

Figure 6.36: The temporal profiles of Cr^{2+} ions laser oscillations in the Cr,Fe:$Zn_{1-x}Mn_xSe$ ($x \approx 0.05$) crystal (Ch1) and Er:glass laser free-running oscillations at wavelength of 1535 nm used for the pumping (Ch2).

The dependence of the laser output energy on the energy absorbed and the laser oscillation spectrum are presented in Fig. 6.37. The maximum Cr,Fe:$Zn_{1-x}Mn_xSe$ ($x \approx 0.05$) laser system output energy was ~9 µJ. The laser oscillation spectrum was measured by photoconductive mercury cadmium telluride (MCT) detector (model no. J12D15) cooled by liquid nitrogen. The spectral width (FWHM) of generated oscillation spectrum was $\lambda_{FWHM} \approx 47$ nm in the range of 2317–2364 nm. The central laser oscillation wavelength with maximum intensity was obtained at ~2348 nm. The possibility of pumping this material at the wavelength of weak Cr^{2+} ions absorption was demonstrated.

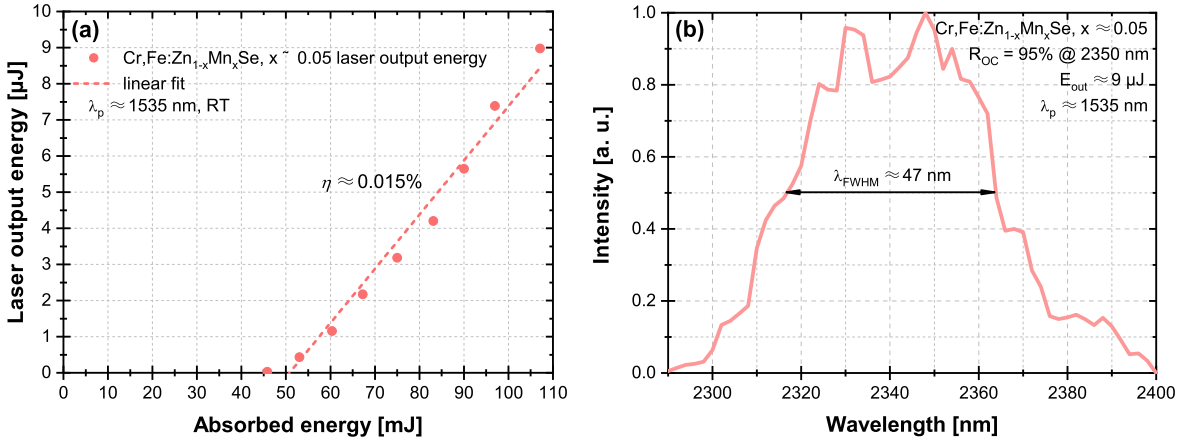

Figure 6.37: $Cr,Fe:Zn_{1-x}Mn_xSe$ ($x \approx 0.05$) laser excited by the Er:glass laser radiation at the wavelength of ~1.53 μm at the RT: **(a)** laser output energy and **(b)** laser oscillation spectrum of Cr^{2+} ions.

Cr^{2+} ions excitation by the Er:YLF laser at the wavelength of ~1.73 μm

This subsection is devoted and present the Cr^{2+} ions laser output properties of the $Cr,Fe:Zn_{1-x}Mn_xSe$ excited directly by in-laboratory built flash-lamp pumped Q-switched Er:YLF laser at the wavelength off ~1.73 μm. The Cr^{2+} ions laser oscillation spectra of the $Cr^{2+},Fe^{2+}:Zn_{1-x}Mn_xSe$ ($x \approx 0.05$; 0.2; 0.3, and 0.4) laser systems operated at temperature of 78 K directly pumped by the Er:YLF laser are shown in Fig. 6.38. The illustration pictures of two output laser beam profiles of the $Cr,Fe:Zn_{1-x}Mn_xSe$ ($x \approx 0.2$ and $x \approx 0.3$) laser systems at the temperature of 78 K are shown as insets in Fig. 6.38 as well. The overview of their laser output properties is presented in Tab. 6.5.

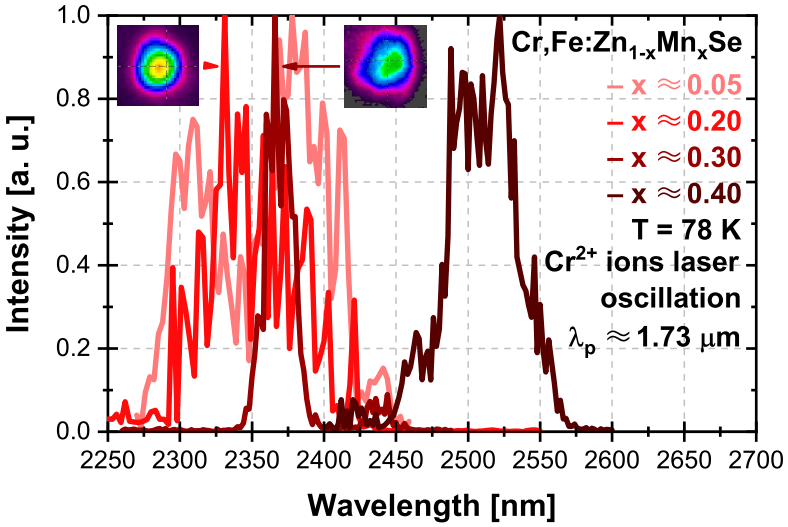

Figure 6.38: Cr^{2+} ions laser oscillation spectra of the $Cr,Fe:Zn_{1-x}Mn_xSe$ ($x \approx 0.05$; 0.2; 0.3, and 0.4) single crystals excited by the Er:YLF laser radiation at the wavelength of ~1.73 μm at 78 K. Inset: $Cr,Fe:Zn_{1-x}Mn_xSe$ ($x \approx 0.2$ and $x \approx 0.3$) laser beam profiles.

Table 6.5: Overview of the **Cr^{2+} ions** laser output properties of the **Cr**,Fe:$Zn_{1-x}Mn_xSe$ crystals at 78 K directly pumped by Er:YLF laser at the wavelength of ~1.73 µm.

Crystal	Central osc. λ @ 78 K [nm]	Maximum output energy @ 78 K [µJ]	Opt.-to-opt. efficiency [%]
Cr,Fe:$Zn_{1-x}Mn_xSe$ ($x \approx 0.05$)	2378	283	19.5
Cr,Fe:$Zn_{1-x}Mn_xSe$ ($x \approx 0.20$)	2331	156	2.6
Cr,Fe:$Zn_{1-x}Mn_xSe$ ($x \approx 0.30$)	2366	272	3.5
Cr,Fe:$Zn_{1-x}Mn_xSe$ ($x \approx 0.40$)	2522	400	8.0

To sum up, results obtained from the Cr^{2+} ions laser generation from the Cr,Fe:$Zn_{1-x}Mn_xSe$ single crystals were a bit worse compared to that previously obtained from the similar crystals doped only by Cr^{2+} ions. The increment of manganese amount (x) in the host material led to a spectral red shift to longer mid-IR wavelengths, along with broadening of absorption and fluorescence spectra was observed as well. However, the generated wavelengths from the crystals of same amount (x) of Mn were shorter compared to the Cr^{2+}-only doped crystals. This may be due to the presence of co-doped Fe^{2+} ions, which left wing absorption band partially overlaps with the right wing of Cr^{2+} ions fluorescence spectra, and thus lowering and shifting the overall Cr^{2+} ions gain to shorter wavelengths in those co-doped materials.

Among the samples tested, the highest laser output pulse energy of ~0.4 mJ was obtained with the sample with manganese content of $x \approx 0.4$. However, the best optical-to-optical efficiency (~19.5 %) under the given pumping conditions was obtained with the $x \approx 0.05$ sample. Lower Cr^{2+} ions laser oscillations output energy could be also explained due to the observed process of intra-ionic energy transfer, and thus a part of the energy from the excited Cr^{2+} ions upper laser level is transferred to Fe^{2+} ions (and the oscillations from the Fe^{2+} ions were not supported by the laser resonator cavity in this case). Therefore, the potentially transferred energy disappeared in the radiative or nonradiative spontaneous emission form and thereby lowering the Cr^{2+} ions of the maximum possible laser output energy.

6.3.3 Indirect Fe^{2+} ions excitation via $Cr^{2+} \rightarrow Fe^{2+}$ energy transfer at different wavelengths

Previously, it was demonstrated in [21] that considering solid solutions based on ZnSe with Mn or Mg ions (i.e. $Zn_{1-x}Mg_xSe$, $Zn_{1-x}Mn_xSe$, ...), the absorption and fluorescence spectra of Cr^{2+} ions exhibit a shift towards longer wavelengths compared to those of a ZnSe crystal. Simultaneously, the absorption spectrum of Fe^{2+} ions was found to have a similar shift of the long-wavelength absorption peak towards longer wavelengths as the Mn or Mg content (x) increased [219]. For instance, in the $Zn_{1-x}Mn_xSe$ ($x \approx 0.3$) crystal, an increase in the overlap between the fluorescence spectrum of Cr^{2+} ions and the absorption spectrum of Fe^{2+} ions was observed with a temperature decrease. This observation can be seen in Fig. 6.39 indicated by the green hatched overlap area.

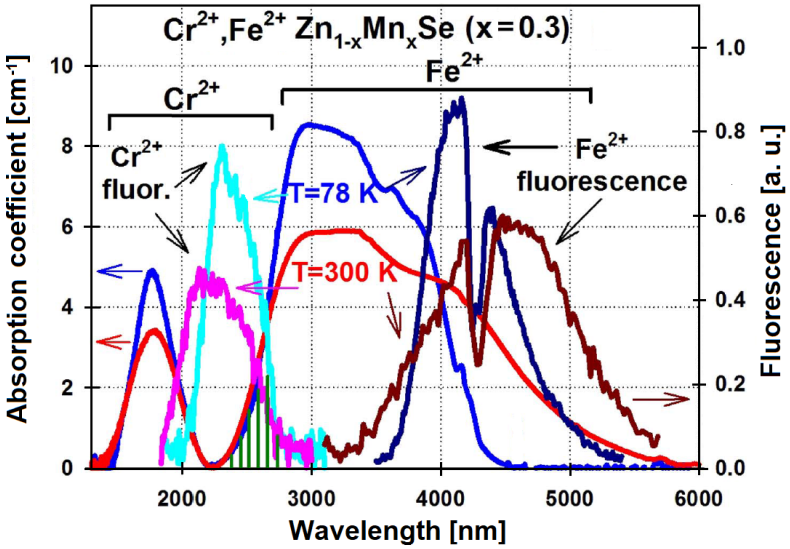

Figure 6.39: Absorption and fluorescence spectra of the Cr^{2+},Fe^{2+}:$Zn_{1-x}Mn_xSe$ (x ≈ 0.3) crystal at 78 K (blue curves) and 300 K (red curves). Green hatched area shows overlap between the Cr^{2+} ions fluorescence and Fe^{2+} ions absorption.

There is also a difference in the fluorescence decay curves of Cr^{2+} ions in Cr^{2+} only-doped and Cr^{2+},Fe^{2+} co-doped samples. In the case of Cr^{2+} ions only-doped crystal, the radiative decay curve is single exponential, and thus linear in the logarithmic scale. However, in the case of Cr^{2+},Fe^{2+} co-doped crystal, this decay curve is nonradiative (double exponential), and thus non-linear in the logarithmic scale as it is depicted in Fig. 6.40. In the presence of Fe^{2+} ions, Cr^{2+} ions nonradiative decay curve $I_N(t)$ was measured from the sample surface to avoid re-absorption effect. The decay curve was observed to be sufficiently non-exponential and approached at the tail the Cr^{2+} ions radiative decay time $I_R(t)$ in the Cr^{2+}:$Zn_{1-x}Mn_xSe$ (x ≈ 0.3) sample.

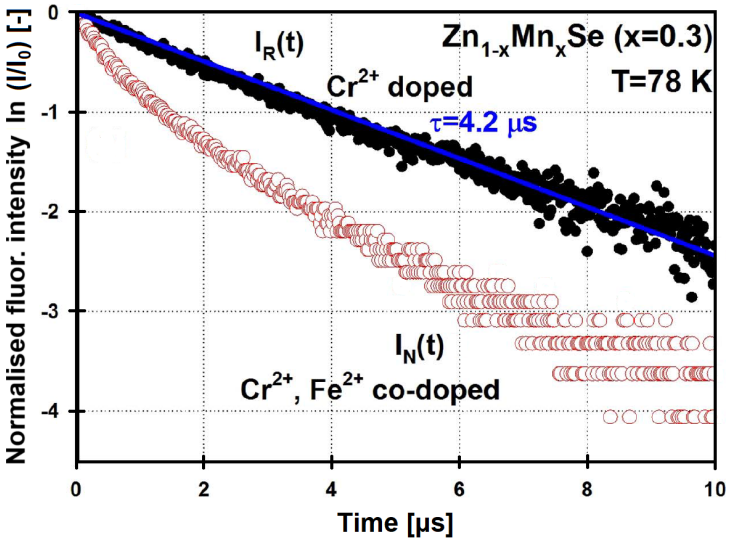

Figure 6.40: Fluorescence decay of Cr^{2+} ions in the Cr^{2+} ions only-doped $Zn_{1-x}Mn_xSe$ (x ≈ 0.3) $I_R(t)$ (black dots) and in the Cr^{2+},Fe^{2+} ions co-doped sample $I_N(t)$ (red dots) at 78 K. Blue solid line shows a single exponential approximation with the fluorescence decay time of ∼4.2 μs.

The efficiency of $Cr^{2+} \rightarrow Fe^{2+}$ ions energy transfer (donor → acceptor – η_{DA}) can be directly evaluated from Fig. 6.40 by using equation

$$\eta_{DA} = 1 - \frac{\langle \tau_{Cr,Fe} \rangle}{\tau_{Cr}}, \tag{6.1}$$

where τ_{Cr} is the Cr^{2+} ions radiative lifetime in the Cr^{2+}-only doped sample and $\langle \tau_{Cr,Fe} \rangle$ is the average Cr^{2+} ions lifetime in the Cr^{2+},Fe^{2+} co-doped sample [44]. The average lifetime can be obtained from the decay curve as

$$\langle \tau_{Cr,Fe} \rangle = \frac{\int_0^\infty I_N(t)dt}{I_0}, \tag{6.2}$$

where $I_N(t)$ is the donor (Cr^{2+}) intensity temporal profile of nonradiative lifetime (it can also be noted as $I_D(t)$) and I_0 is the initial fluorescence intensity after the excitation. With specific values it gives the efficiency value of

$$\eta_{DA} = 1 - \frac{\int_0^\infty I_N(t)dt}{\int_0^\infty I_R(t)dt} \approx 55\,\%, \tag{6.3}$$

where $I_R(t)$ is the intensity temporal profile of radiative lifetime in Cr^{2+}-only doped sample. This value seems to be high enough to have efficient $Cr^{2+} \rightarrow Fe^{2+}$ ions energy transfer in the $Zn_{1-x}Mn_xSe$ ($x \approx 0.3$) crystal under ~1.7 μm short-pulse excitation at 78 K required for Fe^{2+} ions lasing which was confirmed by a successful laser generation at 4.4 μm later.

Fe^{2+} ions indirect excitation by the laser diode at the wavelength of ~1.71 μm

The oscillation properties of the Cr,Fe:$Zn_{1-x}Mn_xSe$ ($x \approx 0.05$) crystal were examined under more intriguing conditions, involving the use of a commercial laser diode (LD) generating radiation around the wavelength of ~1.71 μm for pumping. This LD was capable of producing a maximum continuous wave (CW) output power of ~35 W. In contrast to Q-switched laser pumping, this type of optical excitation resulted in a much lower pumping rate.

The LD driver used in this setup was characterized by a relatively long excitation pulse build-up time of around ~2 ms. Consequently, there was a noticeable delay between the start of the LD pump and the onset of Fe^{2+} ions oscillation pulse. To address this issue, an optical chopper (Thorlabs MC2000B) was employed to generate pumping pulses with a duration of ~1 ms (FWHM) at a frequency of 10 Hz from the CW operation of the LD. It is important to mention that, despite the available LD pumping levels, no Cr^{2+} ions lasing was observed using the same mirror set as employed in the case of the Q-switched Er:YLF laser.

Using a power probe Coherent PM3 placed behind the LP3000 and LP3750 longwave-pass filters (Spectrogon, each filter with transmittance of $T \approx 92\,\%$ at 4.2 μm), the mean laser output power was measured. Fig. 6.41a illustrates the lasers mean output power concerning the absorbed pump power for an active medium at the temperature of 78 K.

To analyze the output beam spatial profile, a pyroelectric camera (Spiricon Pyrocam III) with a long-pass filter LP4095 (Spectrogon) was employed. The output beam shape exhibited distortion compared to the fundamental Gaussian mode, likely due to the active crystal experiencing high thermal loading as a consequence of significant Cr^{2+} ions absorption. The beam profile can be seen as an inset of Fig. 6.41a.

Oscillation pulse of Fe^{2+} ions was measured by the MCT photodetector behind the band-pass filter (Thorlabs FB4250-250). Typical temporal profiles of the pump and Fe^{2+} ions laser oscillation pulses at 78 K are shown in Fig. 6.41b.

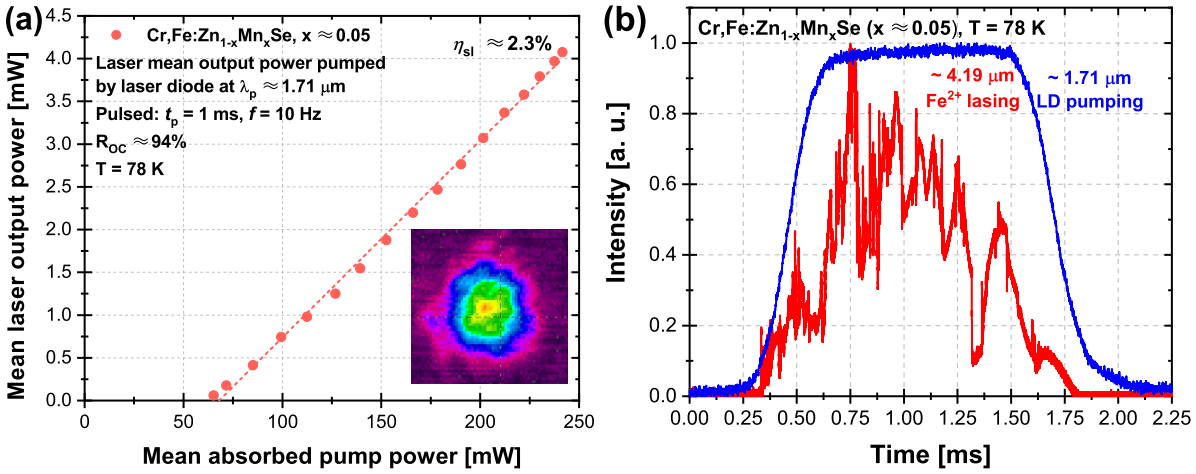

Figure 6.41: $Cr,Fe:Zn_{1-x}Mn_xSe$ ($x \approx 0.05$) **(a)** mean laser output power as a function of the mean absorbed LD pump power in the case of $Cr^{2+} \rightarrow Fe^{2+}$ ions energy transfer at 78 K. Inset presents the laser beam spatial profile for the maximum obtained output power of ~4.1 mW. **(b)** The oscillograms of the ~1.71 μm LD pump pulse (blue curve) and the generated Fe^{2+} ions laser oscillation pulse at 78 K (red curve).

By utilizing a ~1.71 μm commercial laser diode with 1 ms pulse duration and a repetition rate of 10 Hz, the excitation of Fe^{2+} ions through $Cr^{2+} \rightarrow Fe^{2+}$ ions energy transfer mode was successfully achieved. This was the first demonstration, to our best knowledge, of Fe^{2+} ions laser generation under this type of compact excitation. At a low temperature of the sample of 78 K, the laser system exhibited a maximum mean output power of ~4.1 mW in this pulse mode of operation. The slope efficiency of ~2.3 % concerning the absorbed power was obtained. The laser operation was observed within a temperature range from 78 K up to 110 K, resulting in a central oscillation wavelength shift from ~4.19 μm to ~4.23 μm.

These findings present a promising demonstration of the potential to develop a compact diode-pumped mid-IR coherent laser source that operates in (and may be even wider) range of ~4.1–4.3 μm. To further enhance the efficiency of Fe^{2+} ions oscillations, future efforts should focus on optimizing the absolute concentrations of Cr^{2+} and Fe^{2+} ions, as well as the Cr^{2+} to Fe^{2+} ions concentration ratio, to fine-tune the energy transfer process. Such optimization holds the potential to significantly improve the Fe^{2+} ions oscillation efficiency.

Fe^{2+} ions indirect excitation by the Er:YLF laser at the wavelength of ~1.73 μm

In this subsection, the obtained results with Fe^{2+} ions laser oscillations pumped via the $Cr^{2+} \rightarrow Fe^{2+}$ ions energy transfer at the wavelength of ~1.73 μm are described. The Fe^{2+} ions laser oscillation spectra of the $Cr,Fe:Zn_{1-x}Mn_xSe$ ($x \approx 0.05$; 0.2; 0.3, and 0.4) laser systems together with the corresponding laser beam spatial profiles are presented in Fig. 6.42.

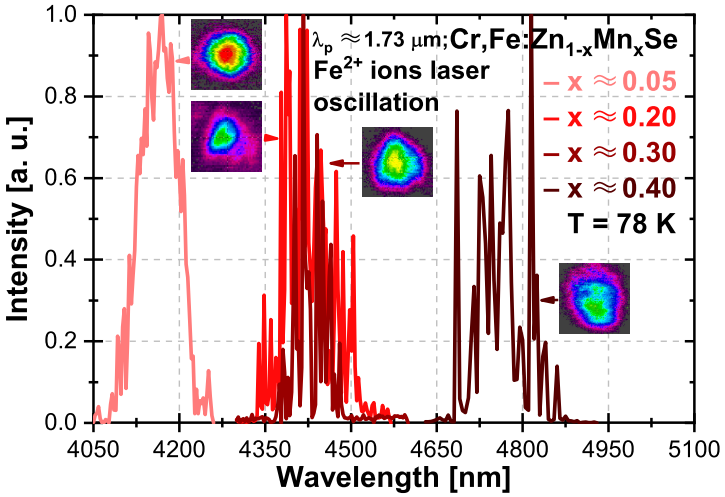

Figure 6.42: Fe^{2+} ions laser oscillation spectra of the Cr,Fe:$Zn_{1-x}Mn_xSe$ ($x \approx 0.05$; 0.2; 0.3, and 0.4) single crystals at the temperature of 78 K pumped via the $Cr^{2+} \rightarrow Fe^{2+}$ ions energy transfer at the wavelength of ~1.73 μm. Inset: corresponding laser beam profiles.

The Cr^{2+} and Fe^{2+} ions oscillations were observed under currently maximum pumping pulse energy of the Er:YLF laser (~12 mJ). Examples of typical oscillograms are shown in Fig. 6.43. As could be seen in Fig. 6.43a, both ions oscillations started with a minimal delay behind the pumping pulse. This mode was classified as the intra-cavity pumping process. The output energy of Cr^{2+} ions lasing at ~2.36 μm was measured up to 900 μJ while the energy at Fe^{2+} ions lasing wavelength at ~4.45 μm reached up to 60 μJ. Therefore, a simultaneous dual wavelength laser generation can be reached with this material.

After applying certain filters to decrease the energy of the pumping pulses, the oscillation of Cr^{2+} ions ceased. Only oscillation from Fe^{2+} ions persisted, but it occurred approximately delayed by ~700 ns after the pump pulse peak intensity. This oscillation mode was identified as the $Cr^{2+} \rightarrow Fe^{2+}$ ions energy transfer. Fig. 6.43b displays the oscillograms of the pumping pulse and the oscillation of Fe^{2+} ions in this mode for comparison.

Under temperatures of the crystal below 100 K, using ~5.5 mJ of absorbed pump energy at ~1.73 μm, the maximum output energy achieved in this mode was 20 μJ at ~4.4 μm. As the temperature increased, the wavelength of Fe^{2+} ions oscillation in the Cr,Fe:$Zn_{1-x}Mn_xSe$ ($x \approx 0.3$) crystal exhibited a slight shift towards longer wavelengths. It changed from approximately ~4.42 μm at 78 K to about ~4.44 μm at 150 K. This small shift towards longer wavelengths could be attributed to the absorption influence of the atmosphere (particularly by CO_2 molecules) on the oscillation spectrum, as the laser cavity mirrors were located outside the evacuated cryostat chamber.

The overview of the Fe^{2+} ions lasing properties of all four samples in the case of pumping via the $Cr^{2+} \rightarrow Fe^{2+}$ ions energy transfer is presented in Tab. 6.6.

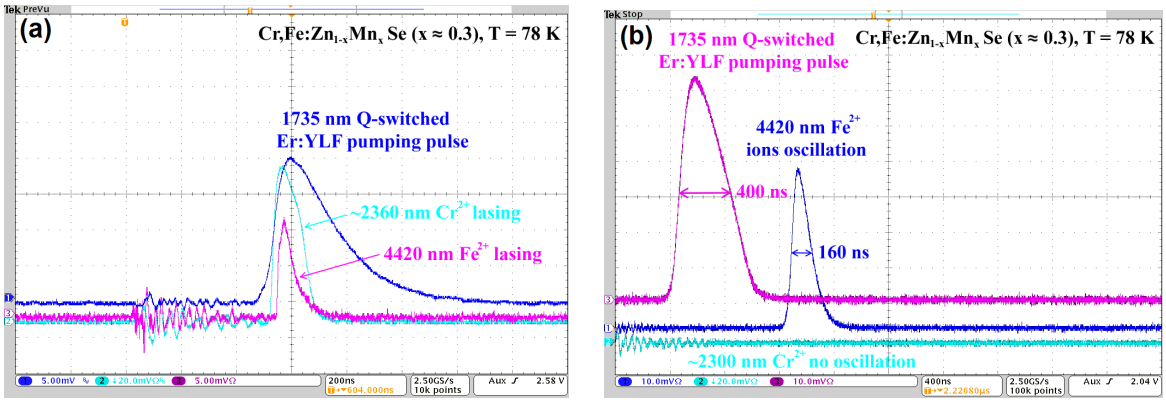

Figure 6.43: Oscillograms of the Q-switched Er:YLF laser pumping pulse (dark blue curve) to Cr^{2+} ions absorption band in the Cr,Fe:$Zn_{1-x}Mn_xSe$ (x ≈ 0.3) crystal followed by Cr^{2+} ions oscillations (cyan curve) and Fe^{2+} ions lasing at ~4.42 µm at 78 K (pink curve) **(a)** in the intra-cavity pumping mode and only Fe^{2+} ions lasing in the **(b)** energy transfer mode.

Table 6.6: Overview of the **Fe^{2+} ions** laser output properties of the Cr,**Fe**:$Zn_{1-x}Mn_xSe$ crystals at the temperature of 78 K pumped via the $Cr^{2+} \rightarrow Fe^{2+}$ ions energy transfer at the wavelength of ~1.73 µm.

Crystal	Central osc. λ @ 78 K [nm]	Maximum output energy @ 78 K [µJ]	Opt.-to-opt. efficiency [%]
Cr,**Fe**:$Zn_{1-x}Mn_xSe$ (x ≈ 0.05)	4167	83	1.2
Cr,**Fe**:$Zn_{1-x}Mn_xSe$ (x ≈ 0.20)	4378	127	1.6
Cr,**Fe**:$Zn_{1-x}Mn_xSe$ (x ≈ 0.30)	4417	20	0.4
Cr,**Fe**:$Zn_{1-x}Mn_xSe$ (x ≈ 0.40)	4815	100	1.9

Using the Q-switched Er:YLF laser with a wavelength of ~1.73 µm, pulse duration of ~200 ns, and a frequency of 1 Hz, short pulse excitation was employed. This excitation method specifically led to the intra-cavity pumping mode of $Cr^{2+} \rightarrow Fe^{2+}$ ions, with a possibility of subsequent $Cr^{2+} \rightarrow Fe^{2+}$ ions energy transfer, resulting in laser oscillations of Fe^{2+} ions. The achieved Fe^{2+} ions laser oscillations via this excitation process were observed within a temperature range from 78 K up to 200 K, causing the central oscillation wavelength to vary from ~4.1 µm to ~4.45 µm with increasing temperature of the active medium. At a temperature of 78 K, the highest output energy reached ~83 µJ, and an optical-to-optical efficiency of ~1 % was attained.

Fe^{2+} ions indirect excitation by the Tm:fiber laser at the wavelength of ~1.94 µm

Initially, oscillations of Fe^{2+} ions were achieved using a pump pulse duration of 1 ms. Throughout the experiments, the oscillations of Cr^{2+} ions were carefully controlled but were not observed even with the maximum pump energies. Fig. 6.44 displays the oscillograms of the pump and Fe^{2+} ions oscillation pulses at 78 K. As depicted in this figure, the intensity of Fe^{2+} ions oscillations closely tracks the intensity of the Tm:fiber laser pump oscillation, and no termination of laser oscillation was observed up to repetition rate of 20 Hz (see Fig. 6.44b). It is worth mentioning that increasing the repetition rate to 20 Hz resulted in a shorter duration of the Fe^{2+} ions oscillation pulse, as shown in Fig. 6.44b. This reduction in pulse duration is likely caused by localized heating of the Cr,Fe:$Zn_{1-x}Mn_xSe$ (x ≈ 0.3) crystal, leading to a decrease in the quantum yield

of Fe^{2+} ions due to a strong non-radiative quenching of fluorescence decay time with increasing temperature [219].

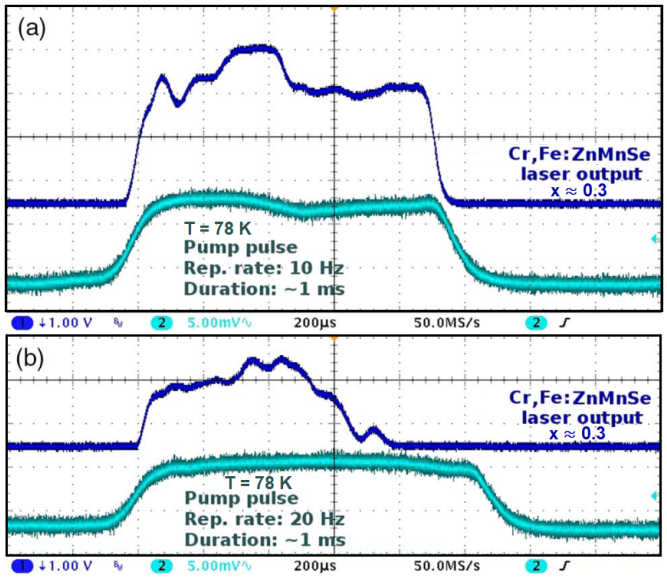

Figure 6.44: Oscillograms of pump (channel 2 – cyan curve) and Fe^{2+} ions oscillation (channel 1 – blue curve) pulses of the Cr,Fe:$Zn_{1-x}Mn_xSe$ (x ≈ 0.3) laser at 78 K for the repetition rates of **(a)** 10 Hz and **(b)** 20 Hz.

To enhance the laser output energy, a lower reflectivity OC with $R_{OC} \approx 95\,\%$ was employed. Fig. 6.45 illustrates the measured relationship between the absorbed energy from the Tm:fiber and the resulting output energy of the Cr,Fe:$Zn_{1-x}Mn_xSe$ (x ≈ 0.3) laser under these conditions. It is evident that the slope efficiency for pumping Fe^{2+} ions via Cr^{2+} ions at ~1.94 µm was ~1 %. The spatial beam profile of the laser output radiation was assessed using a pyroelectric camera (Spiricon Pyrocam III) and is displayed in the inset of Fig. 6.45. The shape did not exhibit an ideal Gaussian distribution, which can be attributed to the localized heating of the active crystal.

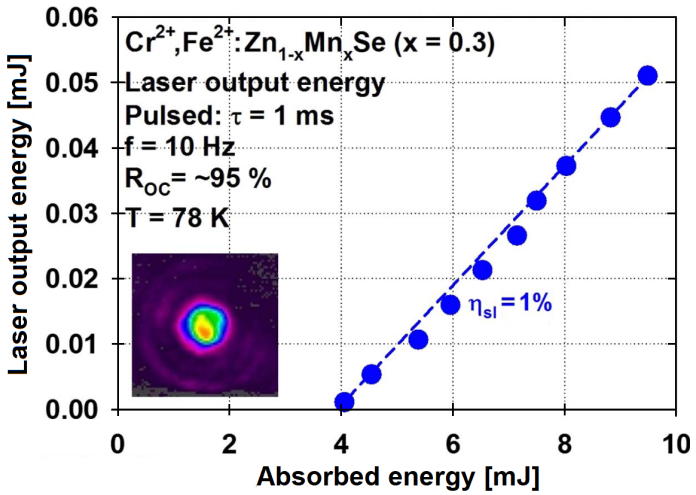

Figure 6.45: Input-output characteristics of the Cr,Fe:$Zn_{1-x}Mn_xSe$ (x ≈ 0.3) laser under ~1.94 µm Tm:fiber laser pumping at 78 K. Inset, the laser output beam spatial profile at the maximum output energy.

The tunability of Fe^{2+} ions in the Cr,Fe:$Zn_{1-x}Mn_xSe$ (x ≈ 0.3) crystal was explored using an OC with $R_{OC} > 99\,\%$. To introduce tunability, a 2 mm thick MgF_2 birefringent plate was inserted as a tuning element at the Brewster angle between the active medium placed in the cryostat (with pumping mirror inside) and the OC outside the cryostat. In order to prevent excessive heating of the active medium, the pump pulse duration was reduced by a factor of five to ∼200 µs. The tuning curve of the Cr,Fe:$Zn_{1-x}Mn_xSe$ (x ≈ 0.3) crystal is summarized in Fig. 6.46a. It is worth mentioning that the tuning range at shorter wavelengths around and bellow ∼4.3 µm may have been constrained by strong CO_2 absorption centred at ∼4.3 µm. Fig. 6.46b presents examples of the oscillation spectra for various rotation angles of the intra-cavity birefringent filter. The output spectra exhibit significant width of around 50 nm, which can be attributed to the high gain of Fe^{2+} ions and the low spectral selectivity of the MgF_2 plate employed.

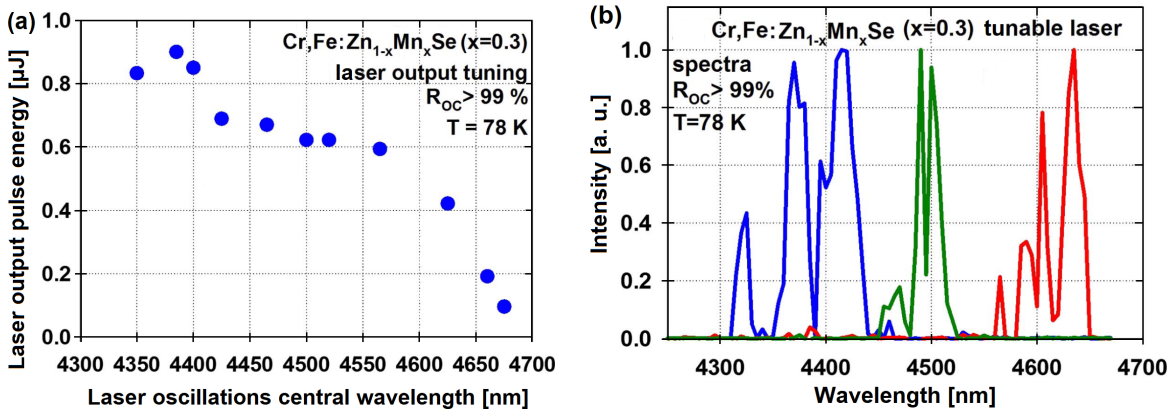

Figure 6.46: The Cr,Fe:$Zn_{1-x}Mn_xSe$ (x ≈ 0.3) laser tunability at 78 K using the MgF_2 birefringent plate; **(a)** tuning curve of Fe^{2+} ions oscillations and **(b)** examples of some selected oscillation spectra while tuning.

In summary, the novel long-pulse (∼1 ms) laser operation of Fe^{2+} ions in the Cr,Fe:$Zn_{1-x}Mn_xSe$ (x ≈ 0.3) crystal, which was pumped by a ∼1.94 µm Tm:fiber laser through Cr^{2+} ions, was demonstrated. This was the first instance of such laser operation, to the best of our knowledge. The lasing was achieved within the temperature range of 78 to 110 K, with the central oscillation wavelength shifting by 60 nm from ∼4.45 µm at 78 K to ∼4.51 µm at 110 K. By using an intra-cavity tuning element, a wide tuning range of over 300 nm (from ∼4.35 µm to ∼4.67 µm at 78 K) was obtained.

However, it was observed that the long-pulse operation suffered from crystal heating, which in turn led to the undesirable quenching of Fe^{2+} ions fluorescence decay time. To enhance the efficiency of Fe^{2+} ions lasing, improved thermal management of the active crystal and further optimization of its optical quality are necessary.

Previous research has shown a decrease in Fe^{2+} output when Cr^{2+} ions are present in the ZnSe crystal. Hence, the absolute and relative concentrations of Cr^{2+} and Fe^{2+} ions are crucial factors to enhance lasing efficiency through the $Cr^{2+} \rightarrow Fe^{2+}$ ions energy transfer. Additionally, optimizing the Mn content in the Cr,Fe:$Zn_{1-x}Mn_xSe$ solid solution is essential to reduce the Fe^{2+} ions fluorescence decay time quenching effect while maintaining a reasonable $Cr^{2+} \rightarrow Fe^{2+}$ overlap integral.

6.4 Properties of the Cr:$Zn_{1-x}Mg_xSe$ ($x \approx 0.25$) and the Cr,Fe:$Zn_{1-x}Mg_xSe$ ($x \approx 0.2; 0.3; 0.4$) single crystals

Next studied materials were Cr^{2+},Fe^{2+} co-doped and Cr^{2+}-only doped $Zn_{1-x}Mg_xSe$ single crystals. The investigation of these materials was performed to compare their properties with previously studied $Zn_{1-x}Mn_xSe$ host materials (Sec. 6.3). The overview of the spectroscopic properties of both active ions can be found in subsection 6.4.1. The direct excitation of Cr^{2+} (subsection 6.4.2) and Fe^{2+} (subsection 6.4.3) ions at two different wavelengths of ~2.94 μm (Er:YAG laser) and ~4.05 μm (Fe:ZnSe laser operated at 78 K pumped by Er:YAG laser) was performed and compared. Similarly as in the previous case, the possibility of Fe^{2+} ions excitation via the $Cr^{2+} \rightarrow Fe^{2+}$ ions energy transfer was also investigated and successfully obtained (subsection 6.4.4).

Two author peer reviewed papers [P6, P7] about these materials were published confirming the Fe^{2+} ions laser oscillations via the $Cr^{2+} \rightarrow Fe^{2+}$ ions energy transfer for the first time. Moreover, the results were also published at these international conferences [C1, C10, C12, C13, C16, C17]. The review of absorption spectra properties at the excitation wavelengths used is summarized in Tab. 6.7. The photos of chosen single crystals are presented in the following Fig. 6.47.

Table 6.7: Overview of the investigated Cr^{2+}:$Zn_{1-x}Mg_xSe$ ($x \approx 0.25$) and Cr^{2+},Fe^{2+}:$Zn_{1-x}Mg_xSe$ ($x \approx 0.2$; 0.3; 0.4) single crystals and their absorption coefficients α at 78 K at excitation wavelengths used of ~1.73 μm (for Cr^{2+} ions), and ~2.94 μm and ~4.05 μm (for Fe^{2+} ions).

Crystal	Thickness [mm]	α @ 1.73 μm @ 78 K [cm^{-1}]	α @ 2.94 μm @ 78 K [cm^{-1}]	α @ 4.05 μm @ 78 K [cm^{-1}]
Cr:$Zn_{1-x}Mg_xSe$ ($x \approx 0.25$)	4.9	4.6	—	—
Cr,Fe:$Zn_{1-x}Mg_xSe$ ($x \approx 0.20$)	2.5	1.6	3.2	2.5
Cr,Fe:$Zn_{1-x}Mg_xSe$ ($x \approx 0.30$)	5.0	0.7	1.5	1.7
Cr,Fe:$Zn_{1-x}Mg_xSe$ ($x \approx 0.40$)	3.6	1.1	2.4	2.9

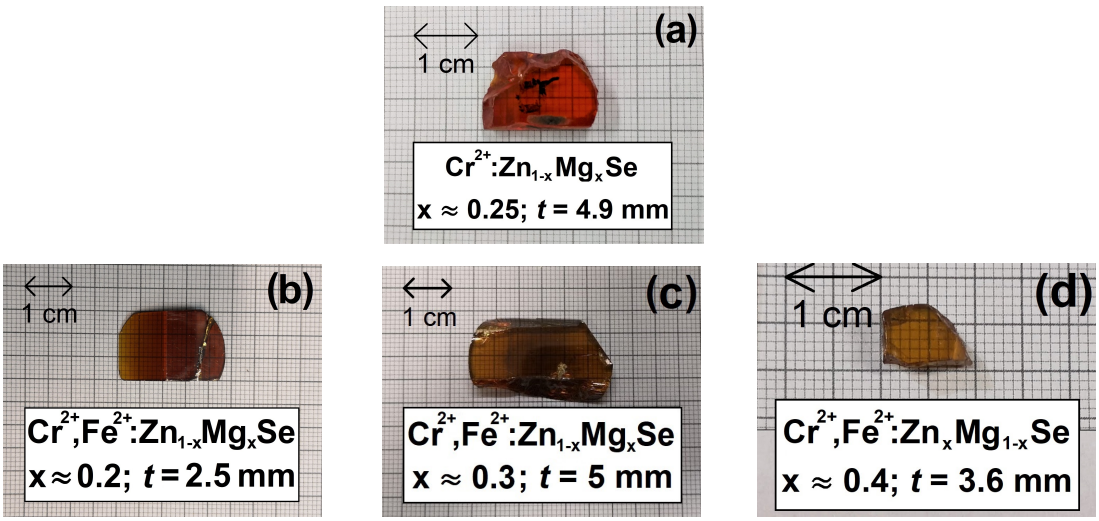

Figure 6.47: Photos of the **(a)** **Cr**:$Zn_{1-x}Mg_xSe$ ($x \approx 0.25$), and the **Cr,Fe**:$Zn_{1-x}Mg_xSe$: **(b)** $x \approx 0.2$, **(c)** $x \approx 0.3$, and **(d)** $x \approx 0.4$ single crystals.

6.4.1 Spectral properties of the Cr:$Zn_{1-x}Mg_xSe$ (x ≈ 0.25) and the Cr,Fe:$Zn_{1-x}Mg_xSe$ (x ≈ 0.2; 0.3; 0.4) single crystals

The comparison of absorption spectra of all four samples at temperatures of 78 K (full line curves) and also 300 K (dashed curves) is presented in Fig. 6.48. As we can see from this figure, the Cr:$Zn_{1-x}Mg_xSe$ (x ≈ 0.25) sample contained a small amount of Fe^{2+} ions as well. We observed this phenomena several times that during the crystal growth and their doping with Cr^{2+} ions, a contamination by small amount of Fe^{2+} ions occurred. The crystal samples differ in Cr^{2+} and Fe^{2+} active ions relative and absolute concentrations. The spectral width of both ions absorption bands slightly increases with increasing amount (x) of magnesium in the host material and the spectral position of maximum absorption was shifted a bit farther to the mid-infrared part of the spectrum. The overview of the absorption spectra properties at excitation wavelengths used can be found in Tab. 6.7.

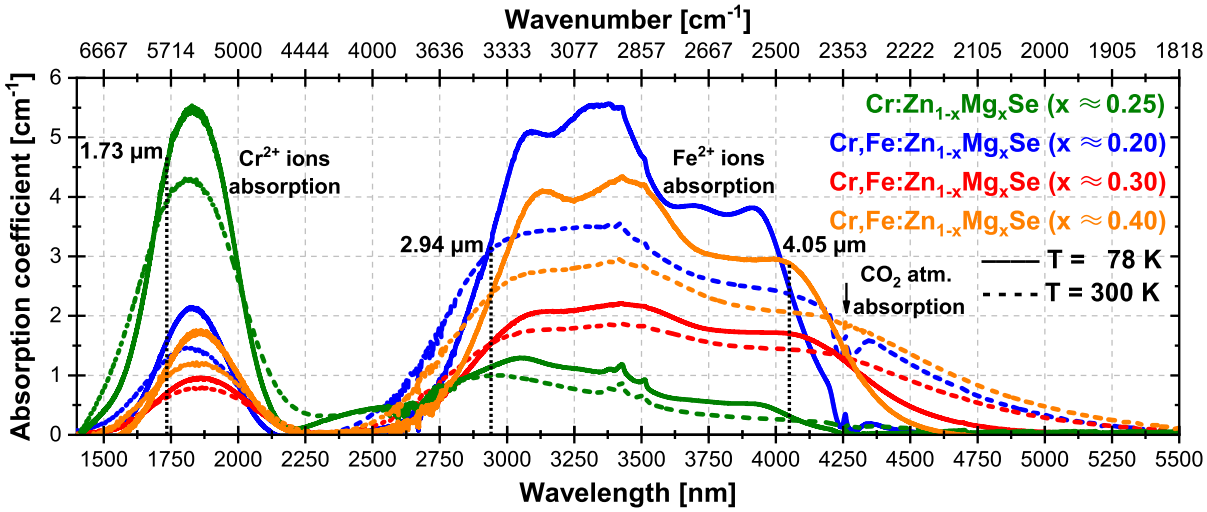

Figure 6.48: Absorption spectra of the Cr:$Zn_{1-x}Mg_xSe$ (x ≈ 0.25 – green curves) and the Cr,Fe:$Zn_{1-x}Mg_xSe$ (x ≈ 0.2 – blue curves, 0.3 – red curves, and 0.4 – orange curves) single crystals at the temperature of 78 K (dashed curves) and 300 K (full line curves). Black dotted lines show spectral positions of pump sources used at the wavelengths of 1.73 µm, 2.94 µm, and 4.05 µm.

The Cr^{2+} and Fe^{2+} ions fluorescence spectra at 78 K are shown in Figs. 6.49a and 6.49b, respectively. As we can see, with higher magnesium amount (x) in the $Zn_{1-x}Mg_xSe$ host material, the fluorescence spectra of both ions became wider and their maxima were shifted farther to the mid-IR part of the spectrum. Intensity maxima of Cr^{2+} ions fluorescence of the Cr^{2+}-only doped sample with magnesium content of x ≈ 0.25, and Cr^{2+},Fe^{2+} co-doped samples with Mg amounts of x ≈ 0.2 and x ≈ 0.3 were detected at wavelengths of ~2.21 µm, ~2.19 µm, and ~2.26 µm, respectively. The Fe^{2+} ions were excited both directly by Er:YAG laser at the wavelength of ~2.94 µm, and indirectly by Er:YLF laser at ~1.73 µm via the $Cr^{2+} \rightarrow Fe^{2+}$ ions energy transfer. A typical drop in the Fe^{2+} ions fluorescence spectra around ~4.2 µm caused by the atmospheric absorption of CO_2 molecules was observed as in previous cases. Fluorescence intensity maxima of Fe^{2+} ions of Cr^{2+},Fe^{2+} ions co-doped samples with Mg amounts of x ≈ 0.2, x ≈ 0.3, and x ≈ 0.4 for direct excitation at the wavelength of ~2.94 µm were detected at ~4.42 µm, ~4.54 µm, and ~4.68 µm, respectively. A fluorescence spectral shift of ~160 nm with rising amount of magnesium in the matrix by every Δx ≈ 0.1 was observed. As we can

see from the Fig. 6.49 there was almost no difference in fluorescence spectra between indirect (~1.73 µm) and direct (~2.94 µm) excitation of Fe^{2+} ions in the case of $x \approx 0.2$ and $x \approx 0.3$ samples.

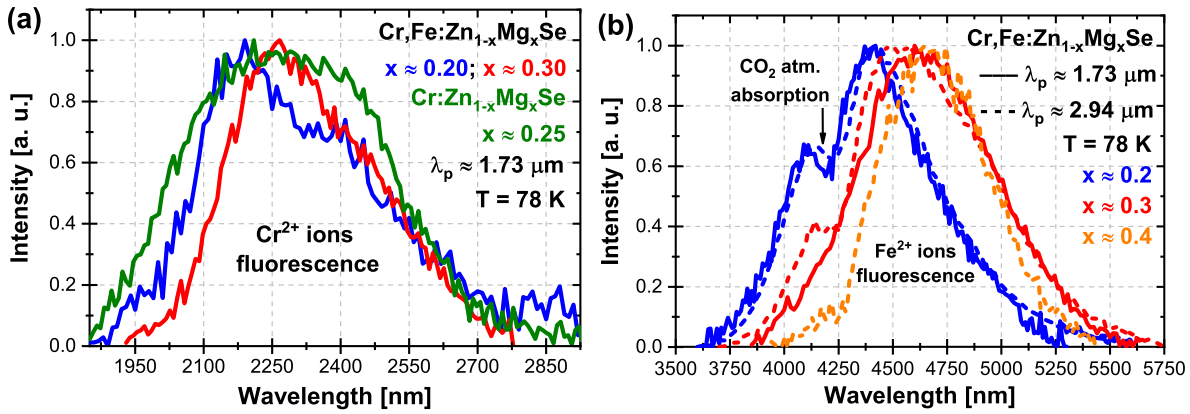

Figure 6.49: Fluorescence spectra of **(a)** Cr^{2+} ions and **(b)** Fe^{2+} ions of the Cr:$Zn_{1-x}Mg_xSe$ ($x \approx 0.25$ – green curve) and the Cr,Fe:$Zn_{1-x}Mg_xSe$ ($x \approx 0.2$ – blue curves; $x \approx 0.3$ – red curves; $x \approx 0.4$ – orange curve) single crystals at the temperature of 78 K. Pumping wavelengths: $\lambda_p \approx 1.73$ µm – full lines, $\lambda_p \approx 2.94$ µm – dashed lines.

The temperature dependence of the Cr^{2+} ions fluorescence decay times of the Cr:$Zn_{1-x}Mg_xSe$ ($x \approx 0.25$) crystal excited by the Q-switched Er:YLF laser radiation at the wavelength of ~1.73 µm and Fe^{2+} ions fluorescence decay times of the Cr,Fe:$Zn_{1-x}Mg_xSe$ ($x \approx 0.2$; 0.3; 0.4) crystals excited by the Q-switched Er:YAG laser radiation at the wavelength of ~2.94 µm are presented in Fig. 6.50. Fe^{2+} ions fluorescence decay time rapidly decreases with increasing temperature in the investigated range from 78 K up to 300 K.

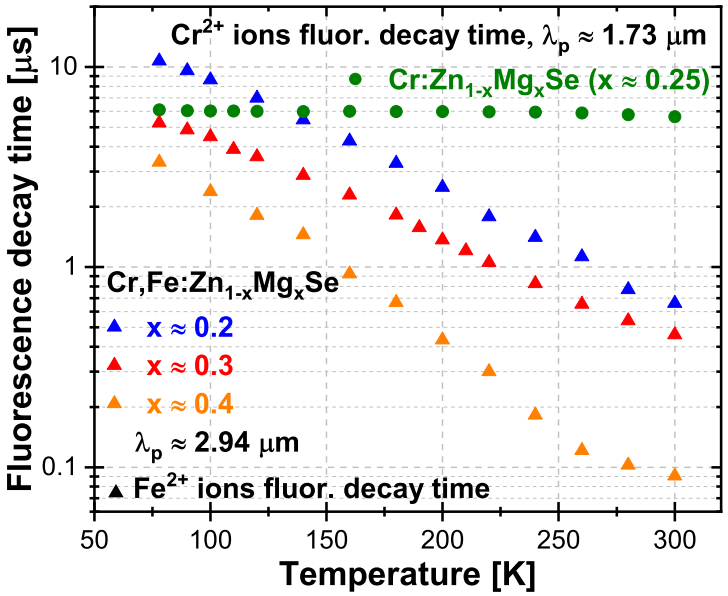

Figure 6.50: Temperature dependence of the Cr^{2+} (pumped at wavelength of $\lambda_p \approx 1.73$ µm) and Fe^{2+} ions (pumped at $\lambda_p \approx 2.94$ µm) fluorescence decay time of the Cr:$Zn_{1-x}Mg_xSe$ ($x \approx 0.25$ – green points) and the Cr,Fe:$Zn_{1-x}Mg_xSe$ ($x \approx 0.2$ – blue; $x \approx 0.3$ – red; $x \approx 0.4$ – orange triangles) single crystals in the temperature range of 78–300 K.

6.4.2 Direct Cr^{2+} ions excitation by the Er:YLF laser at the wavelength of ~1.73 μm

For Cr^{2+} ions excitation only, proper mirrors of the resonator were chosen and the obtained Cr^{2+} ions laser oscillation spectra of the Cr:$Zn_{1-x}Mg_xSe$ (x ≈ 0.25) and the Cr,Fe:$Zn_{1-x}Mg_xSe$ (x ≈ 0.2; 0.3) laser systems together with the illustration pictures of corresponding generated laser beam profiles are shown in Fig. 6.51.

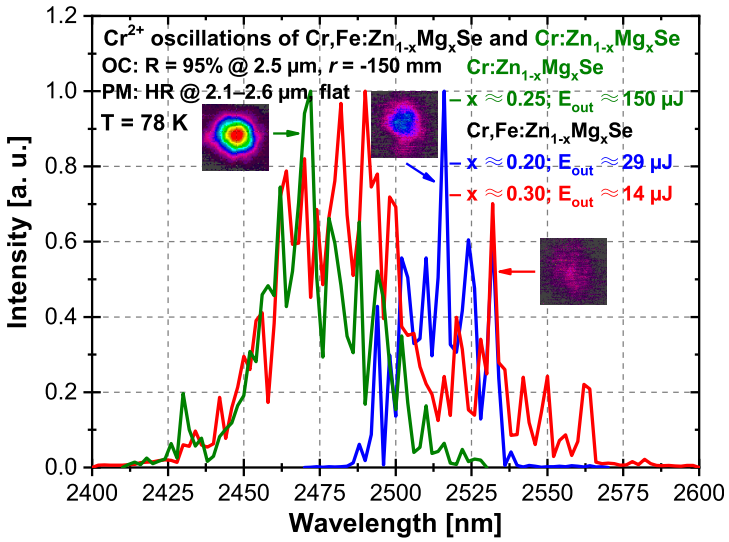

Figure 6.51: Cr^{2+} ions laser oscillation spectra of the Cr:$Zn_{1-x}Mg_xSe$ (x ≈ 0.25) – green curve, and the Cr,Fe:$Zn_{1-x}Mg_xSe$ (x ≈ 0.2 – blue curve; x ≈ 0.3 – red curve) single crystals at the temperature of 78 K. Inset: corresponding laser beam profiles.

The direct excitation of Cr^{2+} ions led to laser oscillations at central wavelengths of ~2.47, ~2.52, and ~2.49 μm with energies of ~150 μJ, ~29 μJ, and ~14 μJ (all at 78 K) for the Cr:$Zn_{1-x}Mg_xSe$ (x ≈ 0.25) and Cr,Fe:$Zn_{1-x}Mg_xSe$ (x ≈ 0.2 and 0.3) crystals, respectively. The overview of the Cr^{2+} ions lasing properties is presented in Tab. 6.8.

Table 6.8: Overview of the **Cr^{2+} ions** laser output properties of the Cr:$Zn_{1-x}Mg_xSe$ (x ≈ 0.25) and the **Cr**,Fe:$Zn_{1-x}Mg_xSe$ (x ≈ 0.2; 0.3) crystals at 78 K directly excited at the wavelength of λ ≈ **1.73 μm**.

Crystal	Central osc. λ @ 78 K [nm]	Maximum output energy @ 78 K [μJ]
Cr:$Zn_{1-x}Mg_xSe$ (x ≈ 0.25)	2472	150
Cr,Fe:$Zn_{1-x}Mg_xSe$ (x ≈ 0.20)	2517	29
Cr,Fe:$Zn_{1-x}Mg_xSe$ (x ≈ 0.30)	2489	14

6.4.3 Direct Fe^{2+} ions excitation at wavelengths of ~2.94 μm and ~4.05 μm

The Fe^{2+} ions of the Cr,Fe:$Zn_{1-x}Mg_xSe$ crystals were excited directly by two different laser: **a)** Q-switched Er:YAG laser at the wavelength of ~2.94 μm and **b)** gain-switched Fe:ZnSe laser at ~4.05 μm operated at 78 K (pumped by Q-switched Er:YAG laser). The absorption

and fluorescence spectra related to these samples are mentioned in 6.4.1. The obtained Fe^{2+} ions laser oscillations properties are described in two following subsections.

Fe^{2+} ions direct excitation by the Er:YAG laser at the wavelength of ~2.94 μm

The direct optical excitation of Fe^{2+} ions was realized by the radiation at the wavelength of ~2.94 μm with Q-switched Er:YLF laser pulses with energy of ~9 mJ and FWHM pulse duration of ~150 ns. The resonator cavity used consisted of a flat pumping mirror HR in the 3.9–5 μm range and a concave OC with reflectivity of $R_{OC} \approx 88\,\%$ at 3.6–5.4 μm. These parameters were the same for all three samples for the comparison. The maximum output energies of the laser systems were ~0.87, ~0.43, and ~0.22 mJ for the x ≈ 0.2, 0.3, and 0.4 crystals, respectively. It corresponds to the conversion efficiencies (with respect to energy absorbed in the crystal) of ~15.7, ~7.3, and ~4.0 % respectively. This direct pumping led to laser oscillations at ~4.53, ~4.81, and ~4.97 μm for the x ≈ 0.2, 0.3, and 0.4, respectively. These central laser oscillation wavelengths of Fe^{2+} ions were comparable with oscillations obtained later via the $Cr^{2+} \rightarrow Fe^{2+}$ ions energy transfer excited at the wavelength of ~1.73 μm (see subsection 6.4.4). The Cr,Fe:$Zn_{1-x}Mg_xSe$ laser oscillation spectra together with corresponding laser beam profiles at the temperature of 78 K directly pumped by the Er:YAG laser radiation at the wavelength of ~2.94 μm are presented in Fig. 6.52.

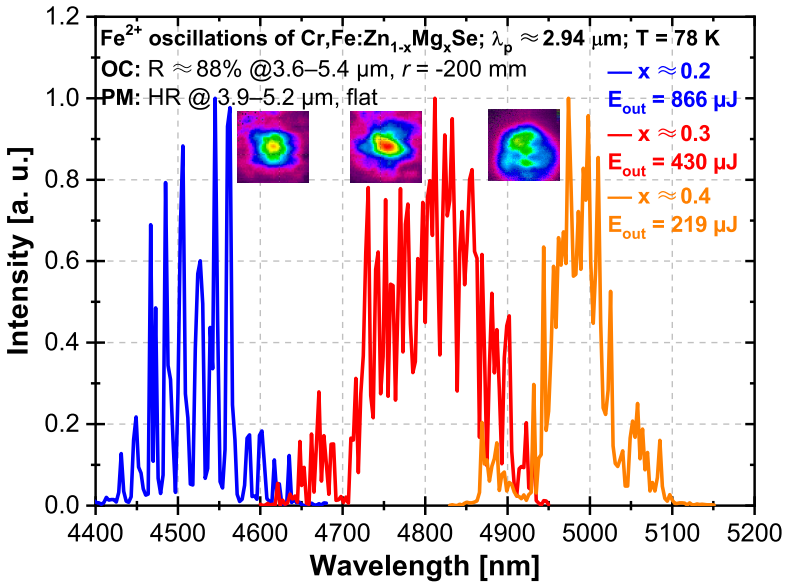

Figure 6.52: Fe^{2+} ions laser oscillation spectra of the Cr,Fe:$Zn_{1-x}Mg_xSe$ (x ≈ 0.2 – blue curve, x ≈ 0.3 – red curve, x ≈ 0.4 – orange curve) single crystals at the temperature of 78 K excited directly at the wavelength of ~2.94 μm. Inset: corresponding laser beam profiles.

The corresponding oscillograms of pumping and Fe^{2+} ions generated laser pulses of two samples with magnesium amount in the host material of x ≈ 0.2 and 0.3 are shown in Fig. 6.53. The overview of measured laser output properties is presented in Tab. 6.9.

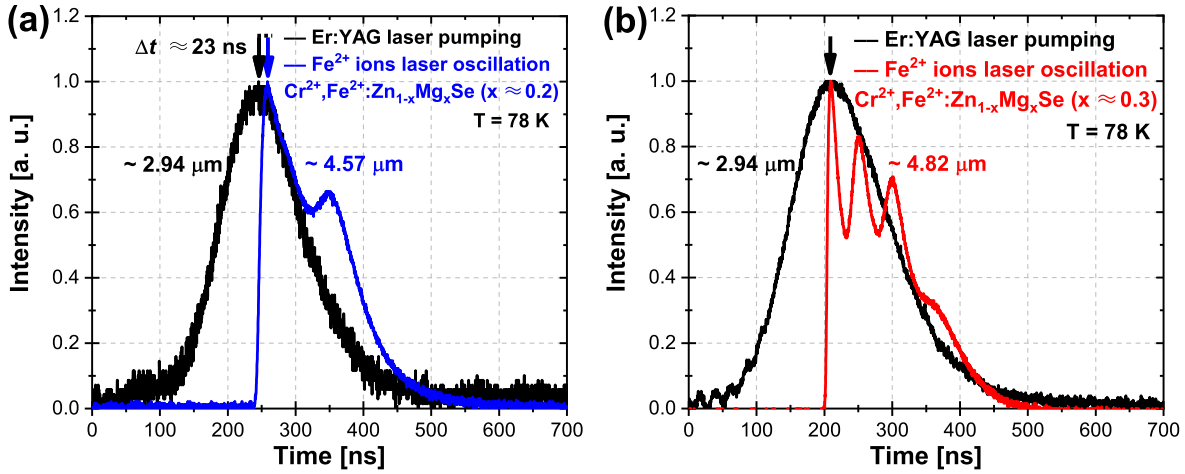

Figure 6.53: Oscillograms of the Fe^{2+} ions laser oscillation of Cr,Fe:$Zn_{1-x}Mg_xSe$ laser systems at the temperature of 78 K pumped directly at the wavelength of ~2.94 μm (black curves): **(a)** x ≈ 0.2 – blue curve; **(b)** x ≈ 0.3 – red curve. Arrows indicate the temporal positions of generated pulses maximum intensity.

Table 6.9: Overview of the **Fe^{2+} ions** laser output properties of the Cr,**Fe**:$Zn_{1-x}Mg_xSe$ single crystals at 78 K directly excited at the wavelength of λ ≈ **2.94 μm**.

Crystal	Central osc. λ @ 78 K [μm]	Maximum output energy @ 78 K [μJ]	Opt.-to-opt. efficiency [%]
Cr,**Fe**:$Zn_{1-x}Mg_xSe$ (x ≈ 0.2)	4.53	866	15.7
Cr,**Fe**:$Zn_{1-x}Mg_xSe$ (x ≈ 0.3)	4.81	430	7.3
Cr,**Fe**:$Zn_{1-x}Mg_xSe$ (x ≈ 0.4)	4.97	219	4.0

Fe^{2+} ions direct excitation by the Fe:ZnSe laser at 78 K (pumped by Er:YAG laser radiation) at the wavelength of ~4.05 μm

Another direct Fe^{2+} ions optical excitation was realized at the wavelength of ~4.05 μm by the gain-switched Fe:ZnSe laser (described in detail in previous Sec. 5.2) operated at 78 K with the output pulse energy of ~9 mJ in ~120 ns pulses (FWHM). The Cr,Fe:$Zn_{1-x}Mg_xSe$ (x ≈ 0.2; 0.3; 0.4) laser systems were realized within the similar resonator cavity conditions as in previous cases (R_{OC} ≈ 88 %, r = -200 mm). The Fe^{2+} ions laser oscillation spectra of the Cr,Fe:$Zn_{1-x}Mg_xSe$ together with corresponding laser beam profiles at the temperature of 78 K directly excited by the gain-switched Fe:ZnSe laser radiation at the wavelength of ~4.05 μm and the oscillogram of the pumping and generated pulses of the Cr,Fe:$Zn_{1-x}Mg_xSe$ (x ≈ 0.4) are presented in Fig. 6.54. The overview of measured laser output properties is summarized in Tab. 6.10.

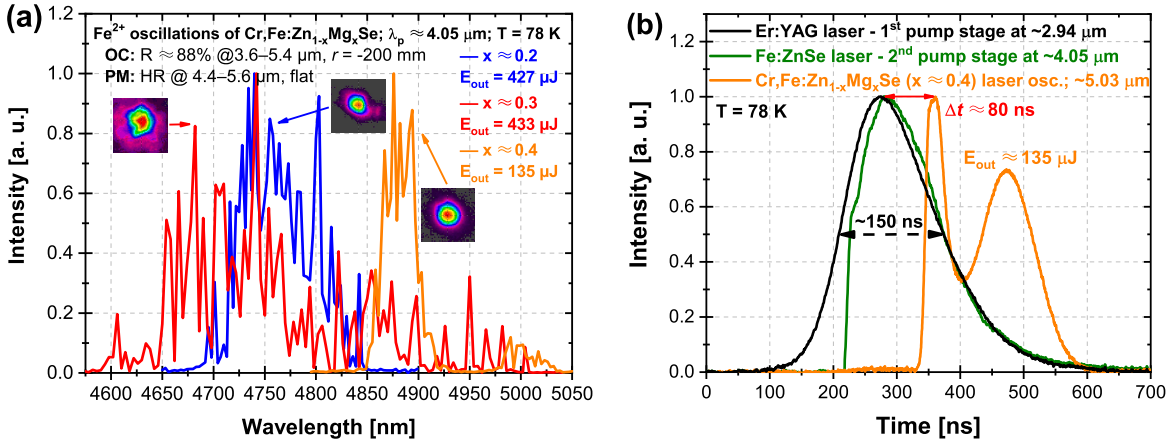

Figure 6.54: **(a)** Fe^{2+} ions laser oscillation spectra of the Cr,Fe:$Zn_{1-x}Mg_xSe$ ($x \approx 0.2$ – blue curve, $x \approx 0.3$ – red curve, $x \approx 0.4$ – orange curve) single crystals at the temperature of 78 K excited directly at the wavelength of ~4.05 μm. Inset: corresponding laser beam profiles. **(b)** Oscillogram of the Cr,Fe:$Zn_{1-x}Mg_xSe$ ($x \approx 0.4$) – Er:YAG laser oscillation (black curve) exciting the Fe:ZnSe laser at 78 K (green curve) and generated Cr,Fe:$Zn_{1-x}Mg_xSe$ ($x \approx 0.4$) laser oscillation (orange curve).

Table 6.10: Overview of the **Fe^{2+} ions** laser output properties of the Cr,**Fe**:$Zn_{1-x}Mg_xSe$ single crystals at 78 K directly excited at the wavelength of $\lambda \approx$ **4.05 μm**.

Crystal	Central osc. λ @ 78 K [μm]	Maximum output energy @ 78 K [μJ]	Opt.-to-opt. efficiency [%]
Cr,**Fe**:$Zn_{1-x}Mg_xSe$ ($x \approx 0.2$)	4.76	427	30.5
Cr,**Fe**:$Zn_{1-x}Mg_xSe$ ($x \approx 0.3$)	4.80	433	9.1
Cr,**Fe**:$Zn_{1-x}Mg_xSe$ ($x \approx 0.4$)	4.86	135	2.6

It is seen that for the excitation by ~4.05 μm the resulted Fe^{2+} ions oscillations are in similar spectral range as for the ~2.94 μm pumping. Central oscillation wavelengths of the Cr,Fe:$Zn_{1-x}Mg_xSe$ ($x \approx 0.2$, 0.3, and 0.4) crystals were ~4.76, ~4.80, and ~4.86 μm with the corresponding maximum output energies of ~0.43, ~0.43 and ~0.14 μJ, respectively. Optical-to-optical efficiencies were measured as high as 30.5, 9.1, and 2.6 %, for $x \approx 0.2$, 0.3, and 0.4 samples, respectively. In contrast to ~2.94 μm excitation of the Cr,Fe:$Zn_{1-x}Mg_xSe$ ($x \approx 0.4$), where the generated pulses started almost immediately after the pumping radiation maximum, the generated pulses in the case of ~4.05 μm were delayed by about ~80 ns.

6.4.4 Indirect Fe^{2+} ions excitation via $Cr^{2+} \rightarrow Fe^{2+}$ energy transfer by the Er:YLF laser at the wavelength of ~1.73 μm

The Fe^{2+} ions excitation via the $Cr^{2+} \rightarrow Fe^{2+}$ ions energy transfer was obtained only for the Cr,Fe:$Zn_{1-x}Mg_xSe$ ($x \approx 0.2$ and $x \approx 0.3$) samples and the laser oscillation spectra are shown in Fig. 6.55. The laser output energies of ~0.7 μJ and ~4 μJ generated at central wavelengths of ~4.55 μm and ~4.8 μm for the magnesium amount in the host material of $x \approx 0.2$ and 0.3, respectively, were obtained. The overview of their laser output properties is presented in Tab. 6.11.

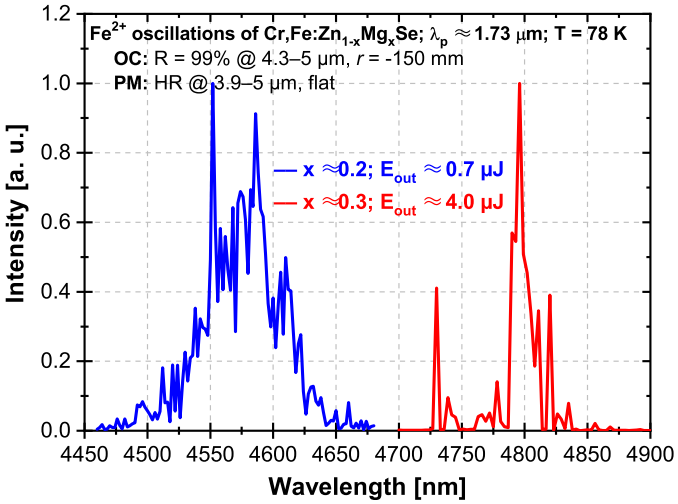

Figure 6.55: Fe^{2+} ions laser oscillation spectra of the Cr,Fe:$Zn_{1-x}Mg_xSe$ ($x \approx 0.2$ – blue curve and $x \approx 0.3$ – red curve) single crystals excited via the $Cr^{2+} \rightarrow Fe^{2+}$ ions energy transfer at 78 K.

Fig. 6.56 presents oscillograms illustrating the typical pumping and laser pulses for the $Cr^{2+} \rightarrow Fe^{2+}$ energy transfer mode. In the case of the energy transfer the generated pulse was delayed after the pump pulse compared to the direct Fe^{2+} ions excitation where the generated pulse was built up almost immediately. These delays were measured as ~1.1 μs and ~0.4 μs for crystals with $x \approx 0.2$ (Fig. 6.56a) and $x \approx 0.3$ (Fig. 6.56b), respectively. It is important to notice here that laser oscillations from the Cr^{2+} ions under these conditions were not observed.

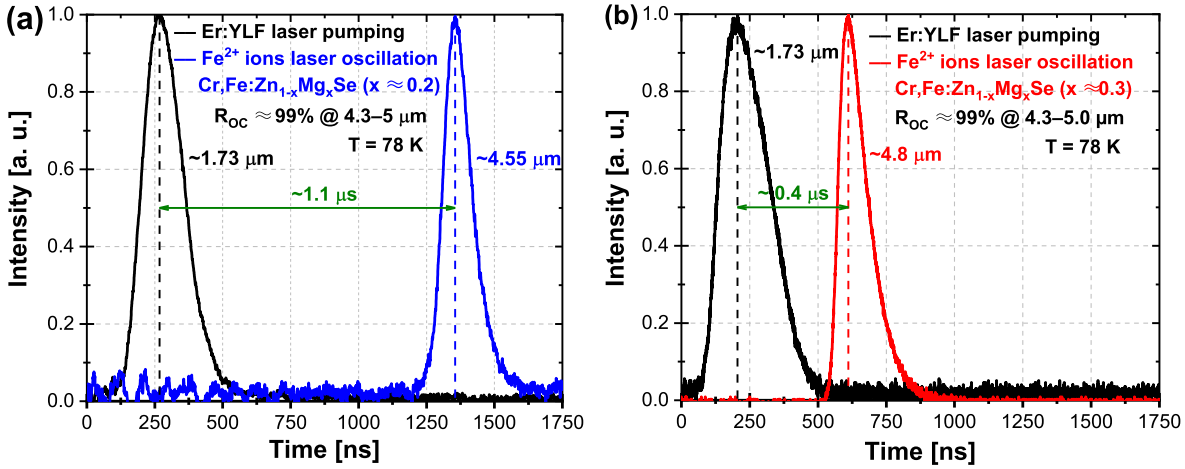

Figure 6.56: Oscillograms of the Fe^{2+} ions laser oscillation of Cr,Fe:$Zn_{1-x}Mg_xSe$ laser systems at the temperature of 78 K pumped via the $Cr^{2+} \rightarrow Fe^{2+}$ energy transfer at the wavelength of ~1.73 μm (black curves): **(a)** $x \approx 0.2$ – blue curve; **(b)** $x \approx 0.3$ – red curve. Dashed lines indicate the temporal position of generated pulses maximum intensity.

Table 6.11: Overview of the indirectly pumped $\mathbf{Fe^{2+}}$ ions laser output properties of the Cr,**Fe**:$Zn_{1-x}Mg_xSe$ single crystals at the temperature of 78 K excited through the $Cr^{2+} \rightarrow Fe^{2+}$ ions energy transfer at the wavelength of $\lambda \approx$ **1.73 μm**.

Crystal	Central osc. λ @ 78 K [μm]	Maximum output energy @ 78 K [μJ]
Cr,**Fe**:$Zn_{1-x}Mg_xSe$ ($x \approx 0.2$)	4.55	0.7
Cr,**Fe**:$Zn_{1-x}Mg_xSe$ ($x \approx 0.3$)	4.80	4.0

The findings open up possibilities for construction of a new coherent laser source based on Cr,Fe:$Zn_{1-x}Mg_xSe$ crystal generating in the mid-IR range (4.5–4.9 μm). The Fe^{2+} ions laser operation (based on wurtzite $A^{II}B^{VI}$ matrices) can be achieved through three methods: **a)** compact pumping of Fe^{2+} ions indirectly using co-doped Cr^{2+} ions at ~1.73 μm, **b)** direct excitation of Fe^{2+} ions at ~2.94 μm, or **c)** direct excitation of Fe^{2+} ions at ~4.05 μm.

6.5 Properties of the Fe:$Zn_{1-x}Mn_xTe$ ($x \approx 0.3$) single crystal

As the last materials with the laser oscillation wavelength farthest in the mid-IR from all investigated samples, the Fe^{2+}-only doped samples in new host materials were studied. This section is devoted to the Fe:$Zn_{1-x}Mn_xTe$ ($x \approx 0.3$) single crystal. The direct excitation of Fe^{2+} ions at two different wavelengths of ~2.94 μm and ~4.05 μm was realized and compared. The overview of its spectroscopic and laser output characteristics can be found in subsections 6.5.1 and 6.5.2, respectively.

The results obtained with the Fe:$Zn_{1-x}Mn_xTe$ ($x \approx 0.3$) single crystal were published in one peer reviewed paper [P3] and were presented at international conference [C8]. Based on the measured laser output properties, it was confirmed that Fe^{2+} ions laser oscillations reached the far mid-IR part of spectrum even beyond 5 μm. The review of absorption spectra characteristics at both excitation wavelengths used is summarized in Tab. 6.12. The photo of investigated single crystal is presented in Fig. 6.57.

Table 6.12: Overview of the investigated Fe^{2+}:$Zn_{1-x}Mn_xTe$ ($x \approx 0.3$) single crystal and its absorption coefficient α at temperature of 78 K at excitation wavelengths used of ~2.94 μm and ~4.05 μm.

Crystal	Thickness [mm]	α @ 2.94 μm @ 78 K [cm^{-1}]	α @ 4.05 μm @ 78 K [cm^{-1}]
Fe:$Zn_{1-x}Mn_xTe$ ($x \approx 0.3$)	3.9	1.8	3.4

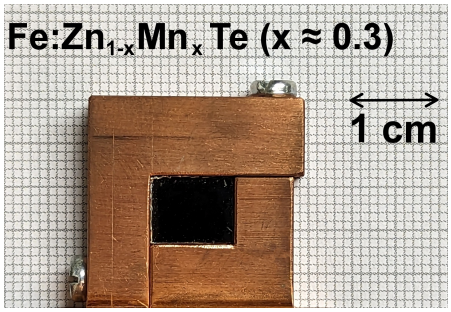

Figure 6.57: Photo of the Fe:$Zn_{1-x}Mn_xTe$ ($x \approx 0.3$) single crystal in the copper holder.

6.5.1 Spectral properties of the Fe:$Zn_{1-x}Mn_xTe$ ($x \approx 0.3$) single crystal

The absorption spectra of the Fe:$Zn_{1-x}Mn_xTe$ ($x \approx 0.3$) single crystal were examined across a temperature range spanning from 78 K to 300 K. For these measurements the Fresnel reflection losses were taking into account. The resulting absorption together with the fluorescence spectra excited at wavelengths of ~2.94 and ~4.05 μm, respectively, are depicted in Fig. 6.58. The investigation revealed that with rising temperature, the spectral

linewidth primarily expanded in the long-wavelength part of the spectrum. Additionally, from this graph, it becomes evident that the potential pumping radiation covers a broad spectral range of 3–4 μm which was tested under pumping by both radiation at wavelengths of ~2.94 μm and ~4.05 μm delivered by Q-switched Er:YAG and gain switched Fe:ZnSe laser at 78 K, respectively.

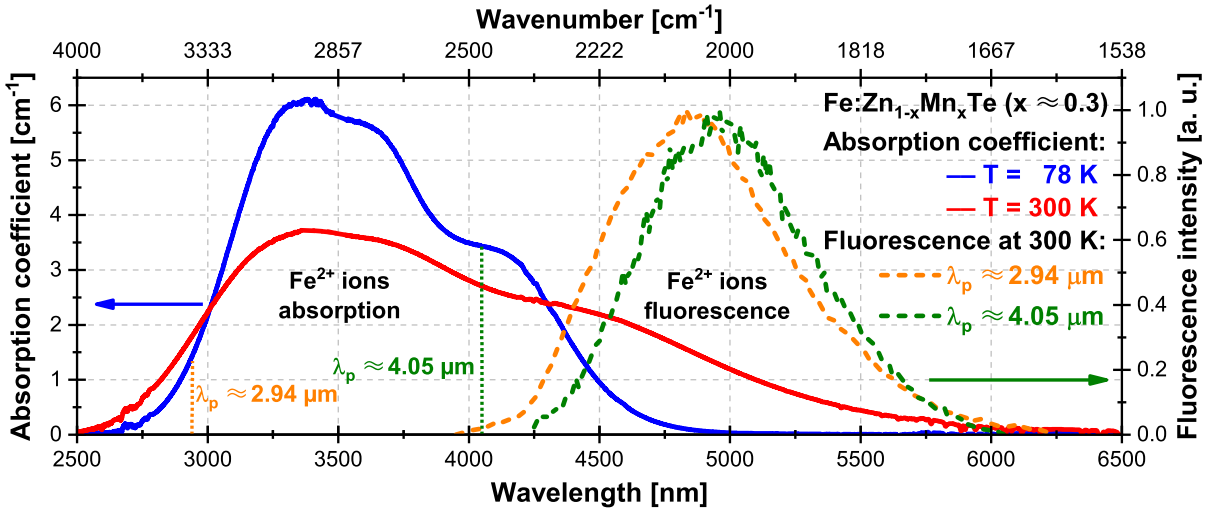

Figure 6.58: The absorption and fluorescence spectra of the Fe:$Zn_{1-x}Mn_xTe$ (x ≈ 0.3) single crystal: absorption at 78 K – full line blue curve and at 300 K – full line red curve. Fluorescence spectra at 300 K excited at the wavelength of ~2.94 μm – orange dashed curve and at ~4.05 μm – green dashed curve.

Fluorescence spectra were recorded using the ~2.94 μm (Er:YAG) and ~4.05 μm (Fe:ZnSe) laser radiation, at temperature of 300 K. The outcomes are also illustrated in Fig. 6.58.

The duration of fluorescence decay was assessed while using the ~2.94 μm Q-switched Er:YAG laser with short pulses. The sample under investigation was positioned within a cryostat cooled with liquid nitrogen, and the decay patterns were recorded using a Vigo PVI-6 photodetector. As the temperature increased, the decay time decreased, going from ~40 μs at 78 K down to ~2.3 μs at 240 K (see Fig. 6.59).

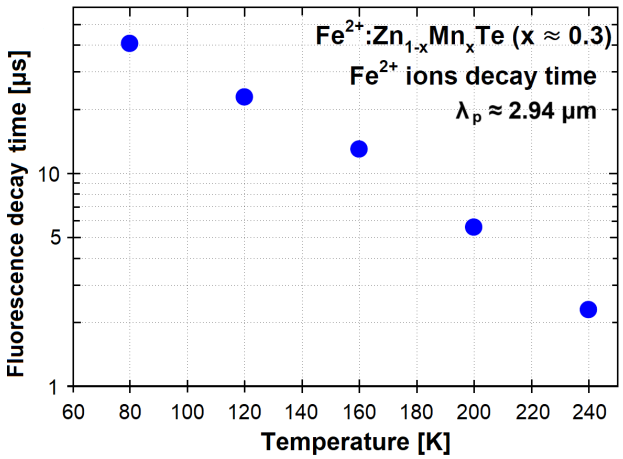

Figure 6.59: Temperature dependence of the Fe^{2+} ions fluorescence decay time of the Fe:$Zn_{1-x}Mn_xTe$ (x ≈ 0.3) single crystal. Excitation wavelength: $\lambda_p \approx 2.94$ μm.

6.5.2 Laser output properties of the Fe:$Zn_{1-x}Mn_xTe$ ($x \approx 0.3$) single crystal pumped at the wavelengths of ~2.94 μm and ~4.05 μm

The Fe:$Zn_{1-x}Mn_xTe$ ($x \approx 0.3$) laser was operated within a temperature range of 78 K to 160 K. Comparison of the laser oscillation spectra can be seen in Fig. 6.60a, where the laser was pumped at wavelengths of ~2.94 μm and ~4.05 μm. It is worth noting that certain reductions in the oscillation spectra could be attributed to the absorption of atmospheric gases in this spectral range. It may occurred due to the fact that part of the resonator was located in the air (the cavity mirrors were outside the evacuated cryostat). Fig. 6.60b provides a dependence of the central oscillation wavelengths on the increasing temperature in the range of 78–160 K. An approximate red shift of 3 nm/K was detected, consistent with earlier findings involving various solid solutions [219].

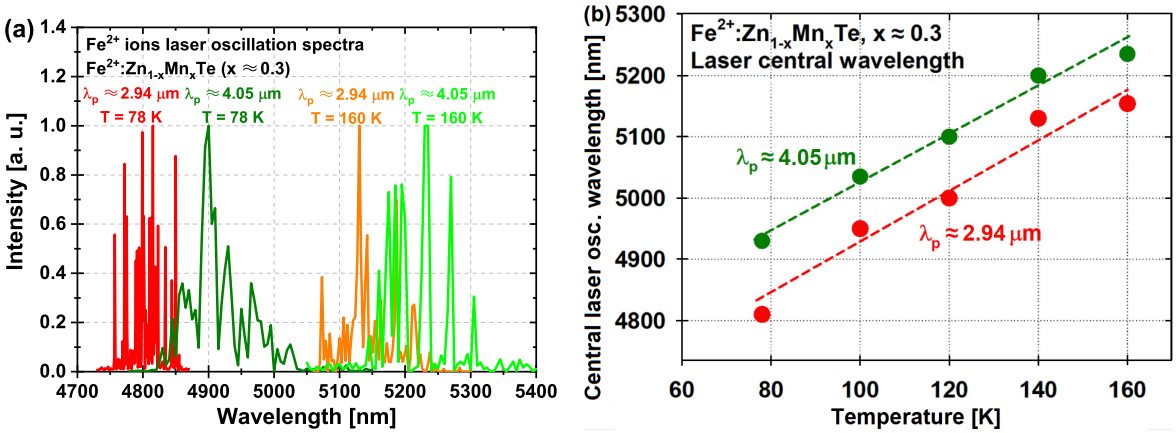

Figure 6.60: **(a)** Examples of the Fe:$Zn_{1-x}Mn_xTe$ ($x \approx 0.3$) laser oscillation spectra pumped by ~2.94 μm (red and orange curves) or ~4.05 μm radiation (dark green and light green curves) for temperatures of 78 K and 160 K, respectively. **(b)** Fe:$Zn_{1-x}Mn_xTe$ ($x \approx 0.3$) laser central oscillation wavelength shift with temperature under ~2.94 μm (red circles) or ~4.05 μm (green circles) laser pumping in the temperature range of 78–160 K. Dashed line – linear trend ~3 nm/K.

Output energy of the Fe:$Zn_{1-x}Mn_xTe$ ($x \approx 0.3$) laser pumped by the Er:YAG laser at the wavelength of ~2.94 μm with the OC reflectivity of $R_{OC} \approx 97\,\%$ was 2 μJ. Changing the OC to lower reflectivity of 88 % led to output energy increase up to ~10 μJ. Though the overall efficiency (~1 %) even in this case was quite low due to non-perfect optical quality of the investigated crystals. In the case of ~4.05 μm pumping, the maximum obtained Fe:$Zn_{1-x}Mn_xTe$ ($x \approx 0.3$) laser output energy was ~1.5 μJ.

Temporal profiles for both pumping methods were measured using photodetectors Vigo PVI-6. The outcomes are displayed in Fig. 6.61a for Er:YAG pumping and in Fig. 6.61b for Fe:ZnSe pumping. For the Er:YAG excitation (~2.94 μm), the laser pulse from Fe:$Zn_{1-x}Mn_xTe$ ($x \approx 0.3$) lasted ~180 ns (at FWHM) and experienced delay of ~100 ns after the rising edge of the Er:YAG pumping pulse. As for the Fe:ZnSe excitation (~4.05 μm), the laser pulse from Fe:$Zn_{1-x}Mn_xTe$ ($x \approx 0.3$) lasted ~60 ns (FWHM) and encountered an ~80 ns delay after the rising edge of the FeZnSe pumping pulse.

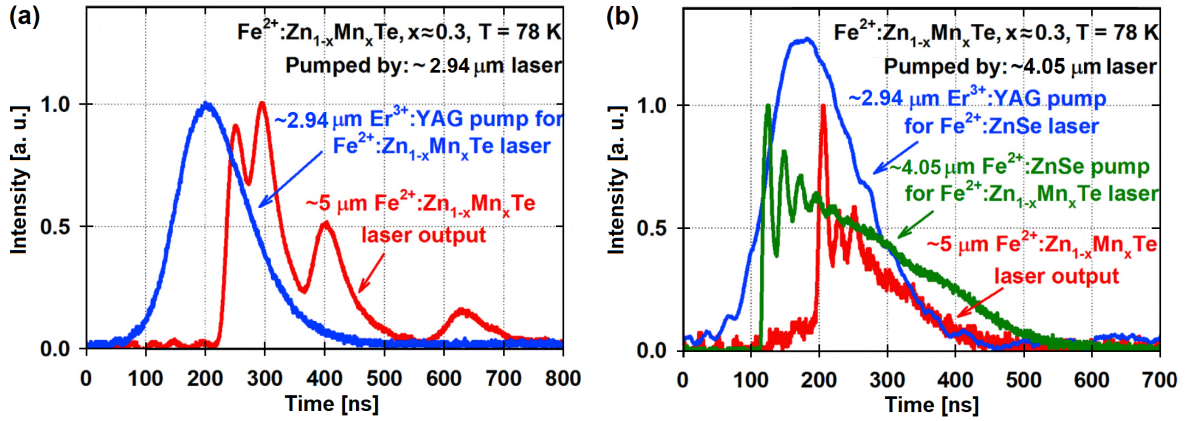

Figure 6.61: **(a)** Temporal profiles of the Er:YAG pumping pulse at ~2.94 μm (blue curve) and the Fe:$Zn_{1-x}Mn_xTe$ (x ≈ 0.3) ~5 μm laser oscillations at 78 K (red curve); **(b)** temporal profiles of the Er:YAG pumping pulse (blue curve) for the Fe:ZnSe laser, Fe:ZnSe laser oscillations at ~4.05 μm (green curve) used for the Fe:$Zn_{1-x}Mn_xTe$ (x ≈ 0.3) laser pumping and its laser oscillations at 78 K (red curve).

An investigation of the Fe:$Zn_{1-x}Mn_xTe$ (x ≈ 0.3) crystal revealed highly promising spectroscopic characteristics and laser output characteristics. This active material demonstrated successful lasing when pumped by the Er:YAG laser at ~2.94 μm and the Fe:ZnSe laser (at 78 K) at ~4.05 μm. The study encompassed a temperature range from 78 K up to 290 K, and the differences in spectroscopic and laser output properties were observed and documented. Under ~2.94 μm laser excitation, the central oscillation wavelength was ~4.8 μm at 78 K, and it shifted to ~5.15 μm at 160 K. When pumped by ~4.05 μm laser radiation, the central oscillation wavelength experienced a red shift to ~4.9 μm at 78 K, and it further shifted to 5.25 μm at 160 K.

6.6 Properties of the Fe:$Cd_{1-x}Mn_xTe$ (x ≈ 0.1–0.76) single crystals

As the last materials with the laser oscillation wavelength farthest in the mid-IR from all investigated samples, the Fe^{2+}-doped $Cd_{1-x}Mn_xTe$ (x ≈ 0.1–0.76) single crystals were studied. The details about the Fe:$Cd_{1-x}Mn_xTe$ crystal growth were described by Kovalenko et al. in [53]. Crystals were only possible to pump by the radiation at the wavelength of ~4.05 μm. The overview of spectroscopic and laser output properties of investigated samples can be found in subsections 6.6.1 and 6.6.2, respectively.

The results obtained with the Fe:$Cd_{1-x}Mn_xTe$ (x ≈ 0.1–0.76) single crystals were presented at international conference [C3]. With the Fe:$Cd_{1-x}Mn_xTe$ (x ≈ 0.76) sample, the Fe^{2+} ions laser oscillations close to 6 μm were reached. The review of absorption spectra characteristics at the excitation wavelengths used is summarized in Tab. 6.13. The illustration photo of one of studied single crystal samples is presented in Fig. 6.62.

Table 6.13: Overview of the investigated Fe^{2+}:$Cd_{1-x}Mn_xTe$ (x ≈ 0.1–0.76) single crystals and their absorption coefficients α at temperature of 78 K at excitation wavelength used of ~4.05 μm.

Crystal	Thickness [mm]	α @ 2.94 μm @ 78 K [cm^{-1}]	α @ 4.05 μm @ 78 K [cm^{-1}]
Fe:$Cd_{1-x}Mn_xTe$ (x ≈ 0.1–0.76)	2–3	1.1–1.6	1.2–3.4

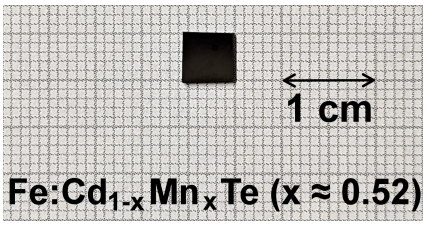

Figure 6.62: Photo of the studied Fe:$Cd_{1-x}Mn_xTe$ (x ≈ 0.52) single crystal.

6.6.1 Spectral properties of the Fe:$Cd_{1-x}Mn_xTe$ ($x \approx 0.1$–0.76) single crystals

In following experiments, a set of five Fe^{2+}:$Cd_{1-x}Mn_xTe$ crystals with different Cd/Mn ratios (x ≈ 0.1; 0.52; 0.56; 0.68; and 0.76) with thicknesses ranging from 2 up to 3 mm were utilized. Their surfaces were polished without any AR coatings. The crystals were synthesized using the Bridgman technique, and during the process, the concentration of iron in the melt was maintained at ~10^{17} cm^{-3}.

However, it should be noted that due to an additional iron content present in the manganese raw material, the actual concentration of Fe^{2+} ions in the solid-solution was higher than intended. Furthermore, this iron concentration increased consistently with the manganese content. The estimated values for Fe^{2+} ions concentration in the solid-solution were as follows: $2.1 \cdot 10^{18}$ cm^{-3} (x ≈ 0.1); $2.5 \cdot 10^{18}$ cm^{-3} (x ≈ 0.52); $2.6 \cdot 10^{18}$ cm^{-3} (x ≈ 0.56); $3.1 \cdot 10^{18}$ cm^{-3} (x ≈ 0.68); and $3.7 \cdot 10^{18}$ cm^{-3} (x ≈ 0.76). The absorption spectra of selected samples are shown in Fig. 6.63.

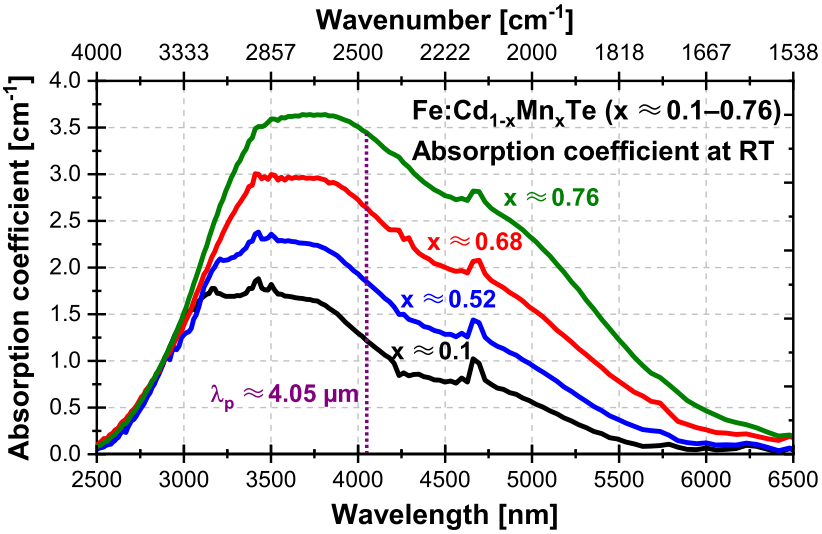

Figure 6.63: The absorption spectra of the Fe:$Cd_{1-x}Mn_xTe$ (x ≈ 0.1; 0.52; 0.68; and 0.76) single crystals at RT. Purple dotted curve shows the spectral position of excitation wavelength used at ~4.05 μm.

The spectroscopic characteristics measurement demonstrated a clear dependence on the crystal composition (Mn content) and its temperature. It was observed that as the Mn content (x) increased, the absorption cross-section of Fe^{2+} ions at temperature of 300 K also increased, particularly in the long-wavelength part of the spectrum, as depicted in Fig. 6.64a. Fig. 6.64b presents the temperature dependence of the spectral position of maximum absorption.

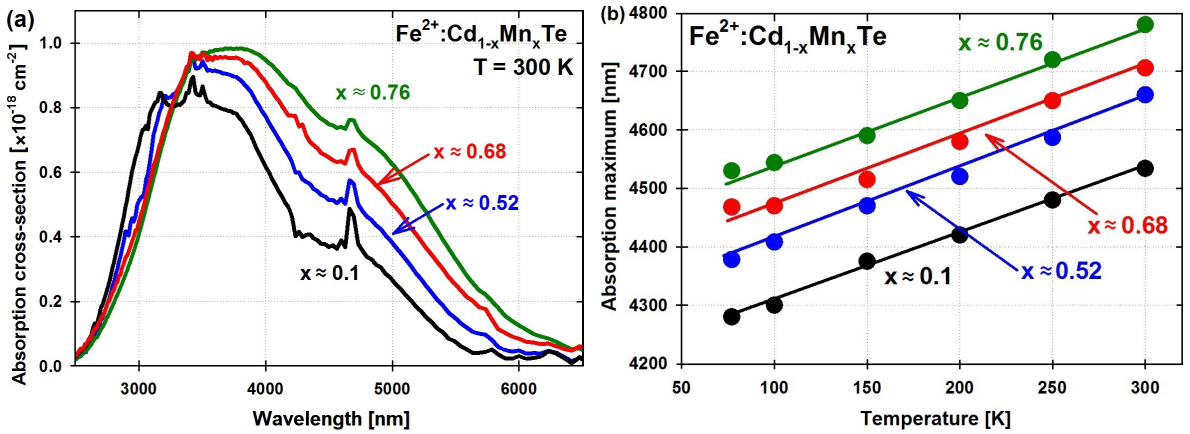

Figure 6.64: **(a)** Fe:$Cd_{1-x}Mn_xTe$ (x ≈ 0.1; 0.52; 0.68; and 0.76) absorption cross sections; **(b)** temperature dependence of spectral positions of absorption spectrum maximum.

A similar trend was noticed in the emission cross-section spectra at temperature of 300 K, as shown in Fig. 6.65. Moreover, the fluorescence spectrum underwent changes on both sides of the fluorescence curves as the Mn content (x) increased. Fig. 6.65a illustrates examples of emission cross section for three crystals (x ≈ 0.1; 0.52; 0.68) at temperature of 300 K. It was also observed that the fluorescence spectra maxima shifted towards longer wavelengths with the increase in Mn content (x), accompanied by significant nonradiative quenching of fluorescence decay time. Fig. 6.65b shows overall gain coefficient together with laser oscillations spectra at temperature of 300 K.

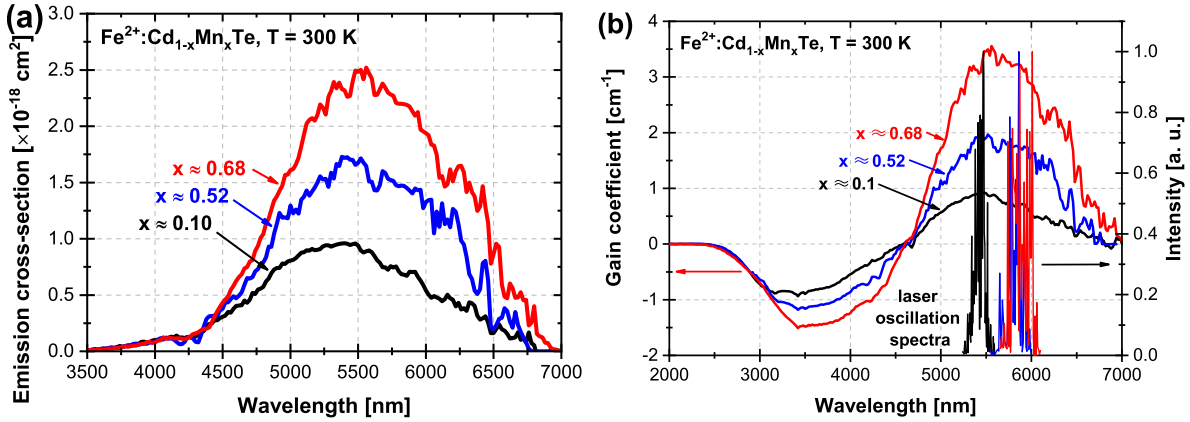

Figure 6.65: Fe:$Cd_{1-x}Mn_xTe$ (x ≈ 0.1; 0.52; and 0.68) **(a)** emission cross section and **(b)** gain coefficient together with laser oscillations spectra at temperature of 300 K.

From the results of measuring of the Fe:$Cd_{1-x}Mn_xTe$ (x ≈ 0.1 and 0.76) fluorescence decay curves (at two temperatures of 80 and 200 K) follows strong nonradiative quenching. It may be caused by a low Stokes shift between the absorption and fluorescence spectra maxima, poses a challenge for achieving effective lasing at RT with these crystals.

6.6.2 Laser output properties of the Fe:$Cd_{1-x}Mn_xTe$ ($x \approx 0.1$–0.76) single crystals under ~4.05 μm pumping

The Fe:$Cd_{1-x}Mn_xTe$ laser was pumped by the Fe:ZnSe. The Fe:ZnSe resonator cavity consisted of a flat pumping mirror with high transmission at 2.94 μm and high reflectivity at ~4 μm, along with a flat OC with the reflectivity of $R_{OC} \approx 88\,\%$ at 4 μm. The Fe:ZnSe laser was operated in the cryostat at temperature of 78 K exhibited the following output characteristics: an oscillation wavelength of ~4.05 μm, a maximum output energy of ~3 mJ, a pulse duration of ~200 ns (FWHM), and a repetition rate of 1 Hz.

Fig. 6.66 illustrates the Fe:$Cd_{1-x}Mn_xTe$ ($x \approx 0.52$; 0.56; 0.76) laser output energy results for the OC with the reflectivity of $R_{OC} \approx 95\,\%$ at 5.8 μm. However, the highest output energy of ~30 μJ and a slope efficiency of ~2.3 % concerning the absorbed pump energy was obtained with the most optimal sample with Mn content of $x \approx 0.52$ using a more opened OC with the reflectivity of $R_{OC} \approx 90\,\%$ at 5.8 μm. Additionally, the laser output beam profile for all samples closely resembled a Gaussian shape, as exemplified in the inset of Fig. 6.66, using optimal sample with Mn content of $x \approx 0.52$ as an example.

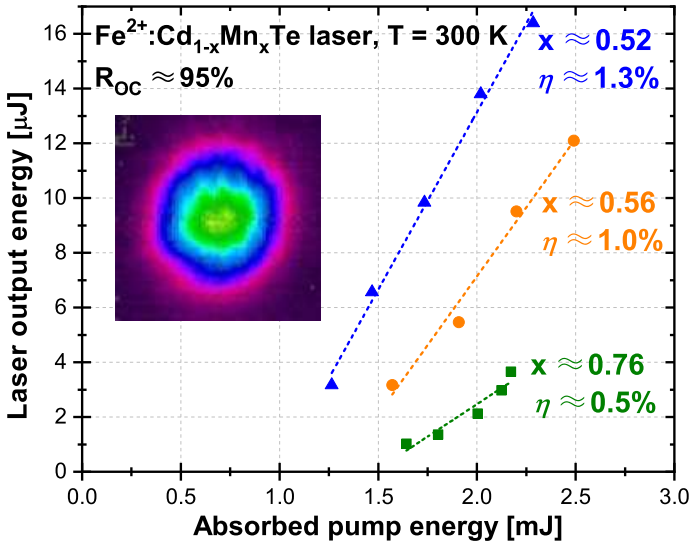

Figure 6.66: Fe:$Cd_{1-x}Mn_xTe$ ($x \approx 0.52$, 0.56 and 0.76) laser output energy characteristics at temperature of 300 K with OC reflectivity of $R_{OC} \approx 95\,\%$ at 5.8 μm. Inset: Fe:$Cd_{1-x}Mn_xTe$ ($x \approx 0.52$) laser beam spatial profile.

Laser radiation generation was achieved for all samples tested at RT. The position of the central laser oscillation wavelength depended on the Mn content (x) in a consistent manner, even at lower temperatures. Fig. 6.67a presents an example of measured oscillation spectra for three samples with varying Mn content ($x \approx 0.1$; 0.52; 0.76), all measured in the same non-selective cavity configuration. However, due to the strong absorption of various molecular gases present in the atmosphere, the oscillation spectra were significantly influenced.

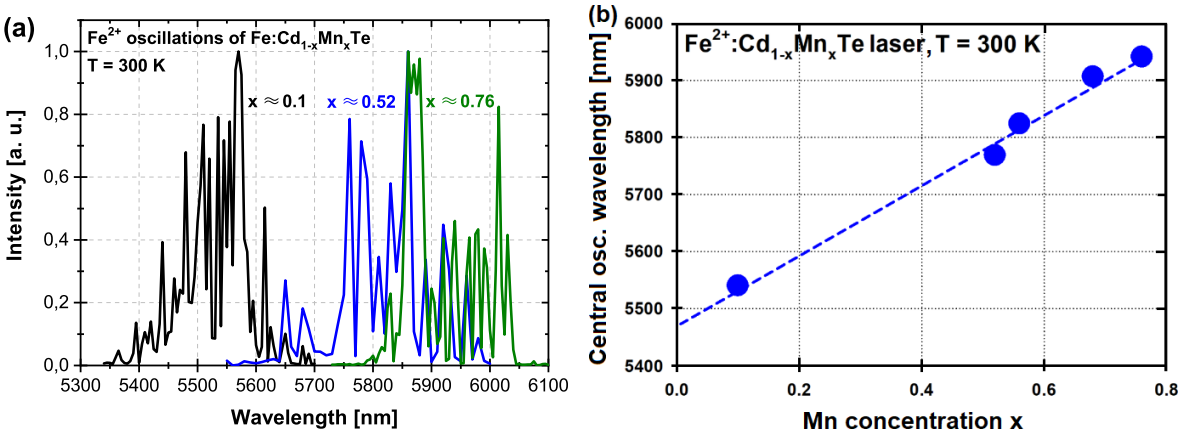

Figure 6.67: **(a)** Oscillation spectra of three Fe:$Cd_{1-x}Mn_xTe$ crystals with various Mn content (x ≈ 0.1; 0.52; and 0.76) obtained in the air at RT measured all in the same setup; **(b)** Fe:$Cd_{1-x}Mn_xTe$ central oscillation wavelengths dependence on Mn content x ≈ 0.1; 0.52; 0.56; 0.68; and 0.76 measured in the air at RT.

To accurately determine the oscillation spectrum's maximum position, all spectra were approximated using a Gaussian-shaped curve. The findings from this fitting indicate that spectral position of the central laser oscillation wavelength shifts towards longer wavelengths with an increase in Mn content (x) at RT. These oscillation spectra for all tested Fe:$Cd_{1-x}Mn_xTe$ samples are summarized in Fig. 6.67b, demonstrating a linear relationship between the spectral position of the central laser oscillation wavelength and the Mn content of x. Specifically, the oscillation spectrum maximum shifts from ~5.54 μm for the sample with x ≈ 0.1 up to ~5.94 μm for the sample with x ≈ 0.76, corresponding to ~60 nm shift per each 10 % increase in Mn content in the solid solution. This was the longest laser oscillation wavelength obtained during this research.

Temperature dependence of the spectral positions of central oscillation wavelength of the Fe:$Cd_{1-x}Mn_xTe$ laser systems for different Mn content of x ≈ 0.1; 0.56; 0.68; and 0.76 can be seen in Fig. 6.68.

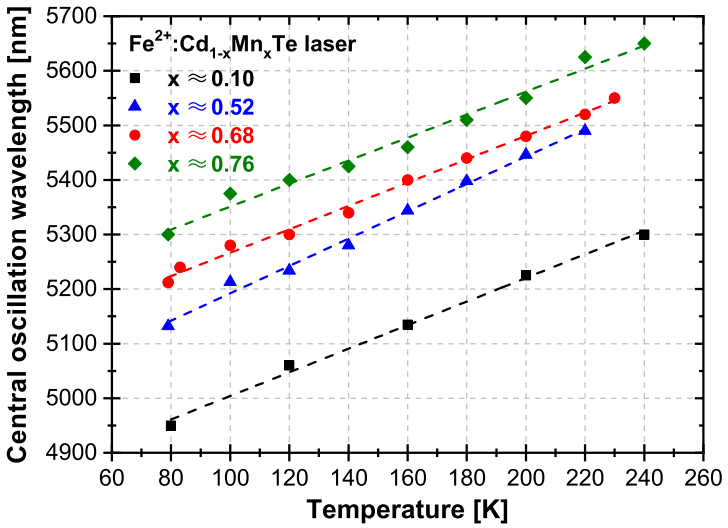

Figure 6.68: Temperature dependence of the Fe:$Cd_{1-x}Mn_xTe$ (x ≈ 0.1; 0.52; 0.68; 0.76) lasers output central oscillation wavelength.

In conclusion, the RT lasing from a group of new laser active materials of Fe:$Cd_{1-x}Mn_xTe$ was achieved. The crystals were optically pumped using a $\sim$4.05 µm LN_2-cooled Fe:ZnSe laser. The oscillation wavelength maxima increased almost linearly as the Mn content (x) in the sample increased, with a rate of $\sim$60 nm per each 10 % increment in Mn content.

With the sample of the highest Mn content ($x \approx 0.76$) was able to obtain generation of laser radiation at the central oscillation wavelength at an impressive $\sim$5.94 µm. However, as the Mn content increased further, a decrease in the output energy due to intense nonradiative quenching was noticed. Nevertheless, an output energy of up to $\sim$30 µJ, corresponding to about $\sim$2.3 % slope efficiency concerning the absorbed pump energy was demonstrated. These results indicate exciting possibilities for constructing compact solid-state lasers that generate radiation in the desirable wavelength range of 5–6 µm.

Part IV

Conclusions

Chapter 7

Discussion and conclusion

To conclude, the influence of presence and amount (x) of manganese or magnesium ions in several novel laser active materials of $Zn_{1-x}Mn_xSe$, $Zn_{1-x}Mg_xSe$, $Zn_{1-x}Mn_xTe$ and $Cd_{1-x}Mn_xTe$ singly doped by Cr^{2+} and or Fe^{2+} ions, or co-doped by both Cr^{2+},Fe^{2+} ions was studied and obtained results were compared with spectroscopic and laser properties of previously known Cr:ZnSe or Fe:ZnSe crystals. The temperature dependences of these characteristics were also investigated. The crystal samples involved in this research were the results of a long-term cooperation with Dr. Maxim E. Doroshenko from the Prokhorov General Physics Institute at Russian Academy of Sciences and the crystal samples producer team leaded by Dr. Nazar O. Kovalenko from the Institute for Single Crystals, National Academy of Sciences of Ukraine. Recapitulation of main obtained results and observed dependences can be found in following Sec. 7.1. The chapter continues with the brief overview of conclusions for practice and further development of science in Sec. 7.2.

7.1 Summary of achieved results

This work presents the results of the study of novel laser active media singly doped with Cr^{2+} or Fe^{2+} ions, or co-doped with Cr^{2+},Fe^{2+} ions. The spectroscopic properties of the single crystals and the laser output characteristics of the designed and experimentally built laser systems were investigated. Emphasis was mainly focused on temperature dependence and also the influence of the amount (x) of manganese (Mn) and magnesium (Mg) ions in $Zn_{1-x}Mn_xSe$, $Zn_{1-x}Mg_xSe$, $Zn_{1-x}Mn_xTe$, and $Cd_{1-x}Mn_xTe$ host materials.

The excitation of laser active ions was investigated for different wavelengths of pump radiation: (optionally Q-switched) Er:glass laser, laser diode, Q-switched Er:YLF laser or thulium fiber laser generating radiation at the wavelengths of ~1.53, ~1.69–1.71, ~1.73, and ~1.94 μm, respectively, for the Cr^{2+} ions direct optical excitation. Q-switched Er:YAG or gain-switched Fe:ZnSe laser operated at 78 K generating radiation at the wavelengths of ~2.94 and ~4.05 μm, respectively, were used in the case of Fe^{2+} ions direct optical excitation. In addition, with the Cr^{2+},Fe^{2+} ions co-doped samples, the Fe^{2+} ions laser generation in different modes of excitation was achieved via: a) direct or b) indirect excitation realized through the $Cr^{2+} \rightarrow Fe^{2+}$ inter-ionic energy transfer.

Due to the various factors affecting, among other things, the wavelength of the generated radiation, the overall laser oscillations could have been achieved in wide ranges of mid-infrared spectral region, which is demonstrated in Fig. 7.1 and Fig. 7.2 for Cr^{2+}-doped, and Fe^{2+}-doped or Cr^{2+},Fe^{2+} co-doped materials, respectively. These

graphs show how matrix composition, temperature and different wavelengths of excitation radiation may influence the spectrum of generated laser oscillation. The presence of manganese or magnesium ions in the host material shifts the generated laser oscillations spectra towards longer wavelength. With temperature rising from low temperatures around 78 K, the fluorescence and spectrum of generated radiation are being red shifted to longer mid-infrared wavelengths as well as by using a longer excitation wavelength.

In the case of Cr^{2+} ions, the laser oscillations were obtained in a wide (tunable) range from ~2.1 up to ~2.7 μm. The laser oscillations obtained with Fe^{2+} doped or Cr^{2+},Fe^{2+} co-doped crystals ranged from ~3.95 up to ~6.05 μm with the exception of some atmospheric gas absorption lines.

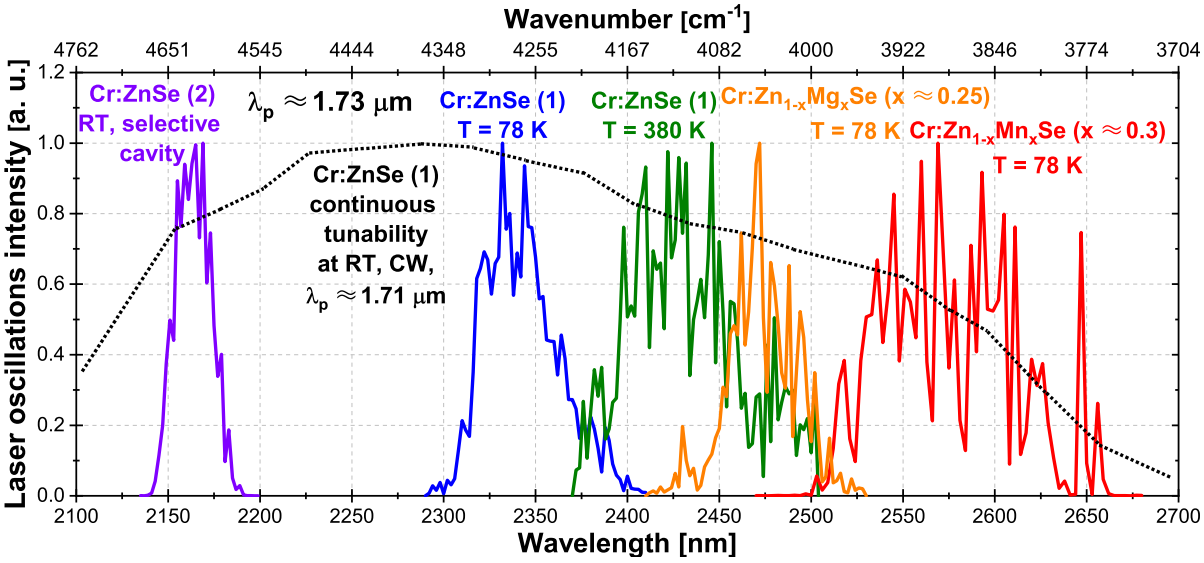

Figure 7.1: Overview of obtained Cr^{2+}-doped lasers oscillation wavelengths at different temperatures directly pumped by Er:YLF laser at the wavelength of ~1.73 μm or by laser diode at ~1.71 μm (black dotted curve).

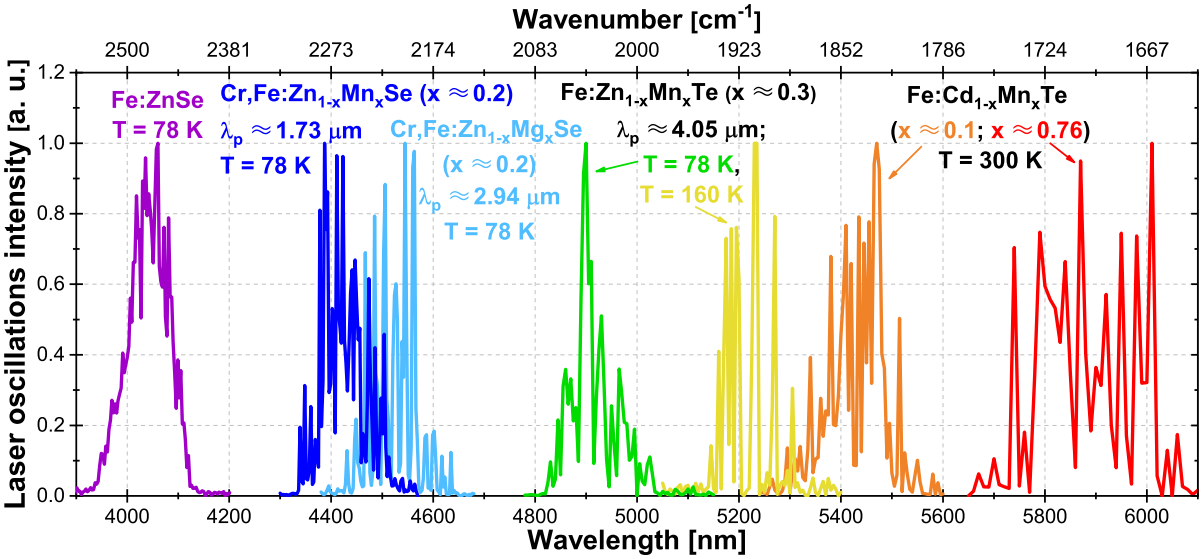

Figure 7.2: Overview of obtained Fe^{2+}-doped or Cr^{2+},Fe^{2+} co-doped lasers oscillation wavelengths at various temperatures and for different excitation wavelengths λ_p.

It is important to mention that the generation of radiation far in the mid-infrared was a part of basic research focused on completely novel laser active materials. Because the studied crystal samples were cut and polished from firstly grown crystal boules, the performance and obtained laser output power/energy of the generated radiation as well as the efficiency of the experimentally built laser systems were limited. Especially due to low optical quality of the tested samples and the absence of anti-reflective coatings and therefore high Fresnel reflection losses on the crystal-air interfaces. The goal of this work was not to obtain high output powers, but above all to expand and demonstrate the novel possibilities of the generation of radiation of unique wavelengths in the mid-infrared spectral region directly from the solid-state laser media that were previously only achievable by non-linear phenomena (OPG, OPO, etc.) or with the help of gas laser (CO laser: 5–6 μm). From this point of view, these systems have a simpler design, they may be more compact and have lower acquisition costs for their implementation.

Compared to Cr:ZnSe or Fe:ZnSe, the presence of manganese or magnesium amount (x) in the host materials of Cr-doped or Cr,Fe co-doped $Zn_{1-x}Mn(Mg)_xSe$ causes broadening of both the absorption and fluorescence spectra. Therefore, the wavelength of generated radiation is thus longer compared to pure ($x = 0$) Cr/Fe:ZnSe. Moreover, with increasing amount of manganese or magnesium in the host, the more pronounced the spectral red shift is. Comparing the $Zn_{1-x}Mn_xSe$ and $Zn_{1-x}Mg_xSe$ host materials, the greater red shift of absorption, fluorescence and generated laser oscillation spectra was observed with the $Zn_{1-x}Mg_xSe$ media for the same amount (x) of Mn and Mg. This can be illustrated as a comparison of the Cr^{2+} ions fluorescence spectra and Fe^{2+} ions laser oscillations spectra of the Cr,Fe:$Zn_{1-x}Mn_xSe$ and Cr,Fe:$Zn_{1-x}Mg_xSe$ ($x \approx 0.3$) at temperature of 78 K presented in Fig. 7.3a and Fig. 7.3b, respectively. In the case of Cr^{2+} ions fluorescence, the spectra of the Cr,Fe:$Zn_{1-x}Mg_xSe$ ($x \approx 0.3$) were shifted farther to infrared part of the spectrum by ~115 nm compared to the Cr,Fe:$Zn_{1-x}Mn_xSe$ ($x \approx 0.3$). It was even more obvious in terms of generated laser oscillations where the shift by ~300 nm was observed. As well as in the case of other investigated materials, the generated spectrum is being shifted even farther to mid-infrared part of the spectrum with increasing temperature of the laser active materials. On the other hand, the Fe^{2+} ions decay time is being quenched with rising temperature, and thus the more efficient laser generation is obtained for shorter (Q-switched) pump pulses.

During the experiments with Cr^{2+} and Fe^{2+} ions co-doped single crystals, the Fe^{2+} ions laser radiation under Cr^{2+} ions excitation was obtained for the first time. This was an evidence of the possibility of inter-ionic energy transfer from excited Cr^{2+} ions to Fe^{2+} ions with subsequent laser generation in the spectral region of 4–5 μm. This $Cr^{2+} \rightarrow Fe^{2+}$ energy transfer excitation method was observed and reported in both Cr^{2+},Fe^{2+} ions co-doped $Zn_{1-x}Mn_xSe$ and $Zn_{1-x}Mg_xSe$ crystalline samples. Although there were already published some theoretical studies on the possibility of such energy transfer before (see research about this topic in Sec. 2.1.4), previously published experimental works were predominantly based on spectroscopic characterisation. The only case of successful laser generation was achieved with the Co^{2+},Fe^{2+}:ZnS(Se) materials. However, the lasing was obtained only for very low temperatures of 14–23 K [132].

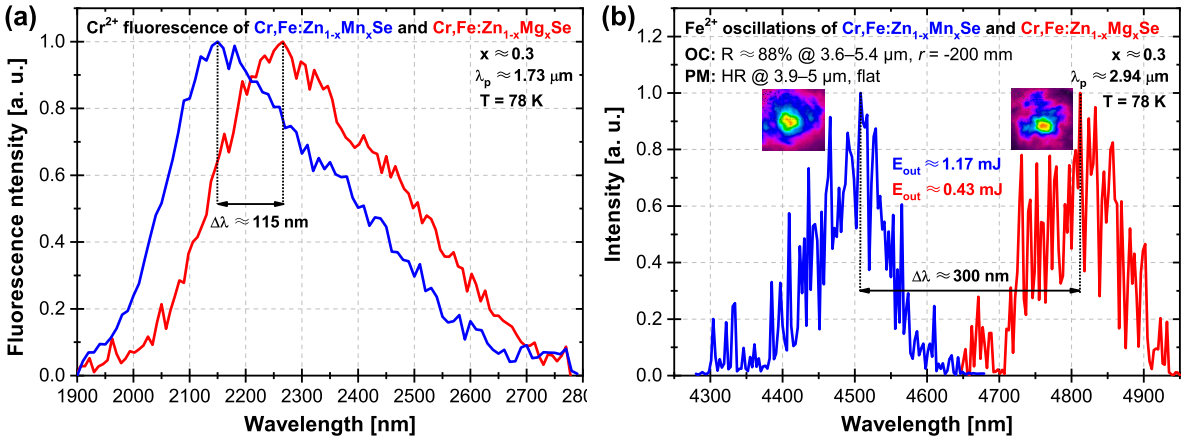

Figure 7.3: The comparison of the **(a)** Cr^{2+} ions fluorescence spectral and **(b)** Fe^{2+} ions laser oscillations spectra of the Cr,Fe:$Zn_{1-x}Mn_xSe$ – blue curve and Cr,Fe:$Zn_{1-x}Mg_xSe$ – red curve ($x \approx 0.3$) single crystals directly excited at wavelengths of $\lambda_p \approx 1.73$ and 2.94 μm at 78 K, respectively. Inset are the output laser beam profile structures.

In this work, the Fe^{2+} ions laser generation via this energy transfer mechanism was obtained for various set of laser active media temperatures and for different excitation wavelengths (laser diode at ~1.71 μm, Q-switched Er:YLF laser at ~1.73 μm, and Tm:fiber laser at ~1.94 μm). Moreover, different pump pulse durations (~150 ns long Q-switched pulses of Er:YLF laser or units of milliseconds in the case of the laser diode or Tm:fiber laser pumping) were applied and subsequent comparably long laser radiation pulses were successfully generated. Thanks to available various set of testing samples differing in manganese and magnesium amount (x) as well as in the Cr^{2+} and Fe^{2+} ions relative and absolute concentrations, the study of these factors influencing the energy transfer efficiency could be done. It was discovered, that this excitation mechanism may be quite efficient under certain conditions (temperature, active ions concentrations, optimal amount of Mn or Mg in the host material, etc.). Except the laser oscillations from Fe^{2+} ions, it was also possible to achieve simultaneous laser generation from Cr^{2+} ions in a single laser cavity as well. Therefore, it was possible to generate simultaneously laser radiation at dual wavelength of ~2.5 and ~4.5 μm.

Another investigated novel laser material was the Fe^{2+}:$Zn_{1-x}Mn_xTe$ ($x \approx 0.3$) single crystal. Based on the spectroscopic measurements, it was found that for this crystal it is more appropriate to use excitation radiation with a wavelength of ~4 μm, which was also subsequently experimentally confirmed. For comparison, the Fe^{2+} ions were also pumped at a wavelength of ~2.94 μm and the expected red shift of obtained generated laser oscillations was observed for longer ~4.05 μm pump wavelength used. It can be seen in Fig. 7.2 as well.

The last investigated novel host materials were $Cd_{1-x}Mn_xTe$ ($x \approx 0.1$–0.76) doped by the Fe^{2+} ions. From measured absorption spectra it was found that it is again more advantageous to excite the Fe^{2+} ions in this matrix with radiation at a wavelength of ~4.05 μm, where the absorption coefficient is more than twice as high as at a wavelength of ~2.94 μm. Apart from that, the laser generation was even not obtained for ~2.94 μm pumping. The longest generated wavelength from all tested samples reaching ~6 μm was also obtained with these crystals. Specifically, the central oscillation wavelength of ~5.94 μm was achieved with the crystal with manganese content of $x \approx 0.76$

(see Fig. 7.2). This spectral part brings us to the CO laser generation area, where these novel solid-state laser systems could replace this complex and expensive system with dangerous handling in some applications in future.

To conclude, there exist many factors that may influence the efficiency and lasing results such as manganese or magnesium ions amount in the host material, both active ions concentration (absolute values as well as relative ratio between them), temperature of the active medium, etc. Our results obtained were mainly limited because of a low optical quality of the firstly grown crystal samples and limitations in pumping energy scaling. Hopefully, we assume that with a sufficient amount of newly produced samples prepared with a higher quality and after the optimization of concentrations of Cr^{2+}, Fe^{2+}, Mn^{2+} and Mg^{2+} ions the future laser output results improvement may be available. Moreover, placing the resonator laser cavity mirrors inside the cryostat in the case of generation of radiation from Fe^{2+} ions, where the atmospheric absorption is not negligible, may also improve the output parameters in future.

In terms of generated wavelengths, the gap in the direct generation of laser radiation in the area between 3 µm (Er:YAG laser) and 4 µm (Fe:ZnSe laser) remains to be filled. This radiation may be partially obtained from Fe^{2+} ions doped in other matrices or from laser systems based on Dy^{3+} ions. This spectral range will be the subject of our next investigations.

7.2 Conclusions for practice and further development of science

A research of novel laser active media generally contributes to the future development of laser systems design and their subsequent applications. In this work, wide ranges of generated laser oscillations covering ~2.1–2.7 µm and ~3.95–6.05 µm spectral regions in the mid-infrared part of the spectrum were obtained with various laser active media. The achieved results related to the topic of this work were published in 7 peer-reviewed papers after recognition by the scientific community in the field. The experimental results were also presented at 21 international scientific conferences as a poster or an oral presentation. All these works are enclosed in form of appendices 1 and 2 to this thesis.

The main conclusions for practice and further development of science are as follows. The inter-ionic energy transfer between Cr^{2+} and Fe^{2+} laser active ions co-doped in single host materials was experimentally investigated and successfully obtained. Specifically, the $Cr^{2+} \rightarrow Fe^{2+}$ ions energy transfer was achieved with the Cr^{2+},Fe^{2+}:$Zn_{1-x}Mn_xSe$ and the Cr^{2+},Fe^{2+}:$Zn_{1-x}Mg_xSe$ single crystals for the first time. Moreover, different Cr^{2+} ions optical excitation sources, various chosen temperatures of active media, and different pump pulse durations were successfully tested. The radiation in the 4–5 µm spectral range is usually being generated by Fe^{2+} doped lasers which are pumped by another, usually solid-state laser, as for instance Er:YAG. The principle of the excitation via energy transfer has been proven and it was confirmed that such pumped laser systems may be compact and efficient while using commercially available lasers (laser diodes or a thulium-doped fiber laser) for the Cr^{2+} ions excitation. More details related to this topic can be found in published papers in [P1, P2, P4–P7]. Overall, these findings are an important initial step towards developing compact, cost-effective, and efficient directly diode-pumped broadband mid-IR Fe^{2+}-based laser sources and amplifiers. Moreover, the obtained simultaneous dual laser oscillation wavelengths of ~2.5 µm from Cr^{2+} ions

and ∼4.5 µm from Fe^{2+} ions generated in one single crystal sample could be possibly used for difference frequency generation (DFG) or optical parametric oscillation (OPO) in appropriate non-linear optical material in future.

The other significant contribution for practice was the achieved laser radiation in the spectral range of 5–6 µm generated using the novel Fe:CdMnTe laser. Such radiation may be used for excitation of some future solid-state laser materials enabling to reach even longer mid-infrared laser oscillation wavelengths. It is also possible to consider replacing the complex CO gas laser in some applications of the radiation in this spectral region in future.

Bibliography

Related peer-reviewed papers

[P1] Doroshenko, M. E., Jelínková, H., **Říha, A.**, Jelínek, M., Němec, M., Kovalenko, N. O., Gerasimenko, A. S.: Mid-IR (4.4 µm) $Zn_{1-x}Mn_xSe:Cr^{2+},Fe^{2+}$ ($x \approx 0.3$) laser pumped by 1.7 µm laser using $Cr^{2+} \rightarrow Fe^{2+}$ energy transfer, *Optics Letters*, Jun. 2019, **vol. 44(11)**, p. 2724–2727.

[P2] Doroshenko, M., Jelínek, M., **Říha, A.**, Šulc, J., Jelínková, H., Kubeček, V., Kovalenko, N. O., Gerasimenko, A. S.: Long-pulse 4.4–4.6 µm laser oscillations of Fe^{2+} ions in a $Zn_{1-x}Mn_xSe$ ($x \approx 0.3$) crystal pumped by a 1940 nm Tm fiber laser through $Cr^{2+} \rightarrow Fe^{2+}$ energy transfer, *Optics Letters*, Nov. 2019, **vol. 44(21)**, p. 5334–5337.

[P3] Doroshenko, M. E., Jelínková, H., Jelínek, M., **Říha, A.**, Šulc, J., Kovalenko, N. O., Terzin, I. S.: Comparison of novel $Fe^{2+}:Zn_{1-x}Mn_xTe$ ($x \approx 0.3$) laser crystal operating near 5 µm at 78 K with other known Mn co-doped A^{II}-B^{VI} solid solutions, *Optical Materials*, Oct. 2020, **vol. 108**, p. 110392.

[P4] **Říha, A.**, Jelínková, H., Doroshenko, M. E., Jelínek, M., Němec, M., Kovalenko, N. O., Terzin, I. S.: Mid-IR lasing of Fe^{2+} ions via $Cr^{2+} \rightarrow Fe^{2+}$ energy transfer process with YLF:Er or laser diode pumping at 1.7 µm, *Optical Materials Express*, Feb. 2020, **vol. 10(2)**, p. 662.

[P5] **Říha, A.**, Doroshenko, M. E., Jelínková, H., Němec, M., Jelínek, M., Šulc, J., Vyhlídal, D., Kovalenko, N. O., Terzin, I. S.: 2.3- and 4.4-µm lasing in $Cr,Fe:Zn_{1-x}Mn_xSe$ ($x \approx 0.3$) single crystal pumped by Q-switched Er:YLF laser at 1.73 µm, *Physics of Wave Phenomena*, Jul. 2020, **vol. 28(3)**, p. 231–235.

[P6] **Říha, A.**, Jelínková, H., Doroshenko, M. E., Jelínek, M., Šulc, J., Němec, M., Čech, M., Vyhlídal, D., Kovalenko, N. O.: Gain-switched laser operation of $Cr^{2+},Fe^{2+}:Zn_{1-x}Mg_xSe$ ($x \approx 0.2$; $x \approx 0.3$) single crystals under $Cr^{2+} \rightarrow Fe^{2+}$ energy transfer at 1.73 µm and direct Fe^{2+} ions excitation at 2.94 µm, *Journal of Luminescence*, Aug. 2021, p. 118375.

[P7] **Říha, A.**, Jelínková, H., Doroshenko, M. E., Jelínek, M., Šulc, J., Němec, M., Vyhlídal, D., Kovalenko, N. O.: Mid-infrared laser generation of $Zn_{1-x}Mn_xSe$ and $Zn_{1-x}Mg_xSe$ ($x \approx 0.3$) single crystals co-doped by Cr^{2+} and Fe^{2+} ions – comparison of different excitation wavelengths, *Materials*, Jul. 2022, **vol. 15(15)**, p. 5277.

Related conference proceedings

[C1] **Říha, A.**, Němec, M., Jelínková, H., Čech, M., Vyhlídal, D., Doroshenko, M. E., Komar, V. K., Gerasimenko, A. S.: Diode-pumped Cr-doped ZnMnSe and ZnMgSe lasers, in: *Photonics, Devices, and Systems VII*, **vol. 10603**, Dec. 2017, p. 1060312, International Society for Optics and Photonics.

[C2] **Říha, A.**, Jelínková, H., Němec, M., Švejkar, R., Doroshenko, M. E., Osiko, V. V., Kovalenko, N. O., Gerasimenko, A. S.: Cr:ZnMnSe diode-pumped laser, in: *2018 International Conference Laser Optics (ICLO)*, Jun. 2018, p. 5–5.

[C3] Jelínková, H., Doroshenko, M. E., Jelínek, M., Šulc, J., Vyhlídal, D., **Říha, A.**, Kovalenko, N. O., Gerasimenko, A. S.: Fe:CdMnTe laser generating 5.4–6 µm radiation, in: *Solid State Lasers XXVIII: Technology and Devices*, **vol. 10896**, Mar. 2019, p. 108961V, International Society for Optics and Photonics.

[C4] **Říha, A.**, Jelínková, H., Němec, M., Čech, M., Vyhlídal, D., Doroshenko, M. E., Badikov, V. V.: Temperature dependence of Cr:ZnSe active medium spectral and laser properties, in: *High-Power, High-Energy, and High-Intensity Laser Technology IV*, **vol. 11033**, Apr. 2019, p. 110330Y, International Society for Optics and Photonics.

[C5] **Říha, A.**, Jelínková, H., Němec, M., Čech, M., Doroshenko, M. E., Kovalenko, N. O.: Cr,Fe:ZnMnSe laser excited by flash-lamp pumped Er:glass laser, in: *2019 Conference on Lasers and Electro-Optics Europe European Quantum Electronics Conference (CLEO/Europe-EQEC)*, Jun. 2019, p. 1–1.

[C6] **Říha, A.**, Doroshenko, M. E., Jelínková, H., Němec, M., Šulc, J., Vyhlídal, D., Jelínek, M., Papashvili, A. G., Kovalenko, N. O., Gerasimenko, A. S.: $Cr^{2+} \rightarrow Fe^{2+}$ energy transfer parameters in $Zn_{1-x}Mn_xSe:Cr^{2+},Fe^{2+}$ ($x \approx 0.3$) crystal and 4.4 µm Fe^{2+} lasing under 1.7 µm pumping, in: *Laser Congress 2019 (ASSL, LAC, LS\&C) (2019), paper JM5A.26*, Sep. 2019, p. JM5A.26, Optical Society of America.

[C7] **Říha, A.**, Doroshenko, M. E., Jelínková, H., Jelínek, M., Němec, M., Kubeček, V., Čech, M., Kovalenko, N. O., Terzin, I. S.: Tunable $Cr^{2+},Fe^{2+}:Zn_{1-x}Mn_xSe$ ($x \approx 0.05$) and ($x \approx 0.3$) lasers around 4.4 µm at 78 K pumped

by a 1.94 µm Tm:fiber laser via $Cr^{2+} \rightarrow Fe^{2+}$ energy transfer, in: *Solid State Lasers XXIX: Technology and Devices*, **vol. 11259**, Feb. 2020, p. 1125919, International Society for Optics and Photonics.

[C8] Jelínková, H., Doroshenko, M. E., Jelínek, M., Šulc, J., Vyhlídal, D., **Říha, A.**, Kovalenko, N. O., Terzin, I. S.: Fe:ZnMnTe laser generating around 5 µm at 78 K, in: *Solid State Lasers XXIX: Technology and Devices*, **vol. 11259**, Feb. 2020, p. 1125923, International Society for Optics and Photonics.

[C9] **Říha, A.**, Doroshenko, M. E., Jelínková, H., Němec, M., Jelínek, M., Kovalenko, N. O., Terzin, I. S.: Mid-IR simultaneous lasing of Cr^{2+} and Fe^{2+} Ions at 2.4 and 4.2 µm in Cr^{2+},Fe^{2+}:$Zn_{1-x}Mn_xSe$ (x ≈ 0.05) crystal pumped by Er:YLF laser at 1.73 µm, in: *2020 International Conference Laser Optics (ICLO)*, Nov. 2020, p. 1–1, IEEE, Saint Petersburg, Russia.

[C10] **Říha, A.**, Doroshenko, M. E., Jelínková, H., Němec, M., Jel9nek, M., Kovalenko, N. O., Terzin, I. S.: 2.5 µm and 4.5 µm lasing in Cr^{2+},Fe^{2+}:$Zn_{0.81}Mg_{0.19}Se$ single crystal under 1.73 µm Q-switched pumping via $Cr^{2+} \rightarrow Fe^{2+}$ energy transfer, in: *Europhysics Conference Abstracts*, **vol. 44A**, Sep. 2020, p. 22, Mulhouse: European Physical Society.

[C11] **Říha, A.**, Doroshenko, M. E., Jelínková, H., Němec, M., Vyhlídal, D., Jelínek, M., Šulc, J., Papashvili, A. G., Kovalenko, N. O., Terzin, I. S.: 4.19 µm Fe^{2+} ions lasing in $Zn_{1-x}Mn_xSe$:Cr^{2+},Fe^{2+} (x ≈ 0.05) single crystal under 1.71 µm laser diode pumping via $Cr^{2+} \rightarrow Fe^{2+}$ ions energy transfer, in: *OSA High-brightness Sources and Light-driven Interactions Congress 2020 (EUVXRAY, HILAS, MICS) (2020), paper JM3A.27*, Nov. 2020, p. JM3A.27, Optica Publishing Group.

[C12] **Říha, A.**, Jelínková, H., Doroshenko, M. E., Šulc, J., Jelínek, M., Čech, M., Vyhlídal, D., Kovalenko, N. O.: Low temperature gain-switched operation of non-cubic Cr^{2+},Fe^{2+}:$Zn_{1-x}Mg_xSe$ (x ≈ 0.2 and x ≈ 0.3) single crystals in mid-infrared under different excitation wavelengths, in: *Solid State Lasers XXX: Technology and Devices*, Clarkson, W. A., Shori, R. K., editors, Mar. 2021, p. 31, SPIE, Online Only, United States.

[C13] **Říha, A.**, Jelínková, H., Doroshenko, M. E., Jelínek, M., Šulc, J., Vyhlidal, D., Kovalenko, N. O., Terzin, I. S.: Comparison of gain-switched operated Cr^{2+} and Fe^{2+} ions co-doped $Zn_{1-x}Mn_xSe$ and $Zn_{1-x}Mg_xSe$ (x ≈ 0.3) lasers in mid-IR under different excitation wavelengths, in: *High Power Lasers and Applications*, Butcher, T. J., Hein, J., Bakule, P., Haefner, C. L., Korn, G., Silva, L. O., editors, Apr. 2021, p. 25, SPIE, Online Only, Czech Republic.

[C14] **Říha, A.**, Doroshenko, M. E., Jelínková, H., Němec, M., Jelínek, M., Čech, M., Kovalenko, N. O., Terzin, I. S.: 4.7–5.1 µm lasing in Cr^{2+},Fe^{2+}:$Zn_{1-x}Mn_xSe$ (x ≈ 0.4) single crystal under 1.73 µm and 2.94 µm pumping, in: *2021 Conference on Lasers and Electro-Optics Europe European Quantum Electronics Conference (CLEO/Europe-EQEC)*, Jun. 2021, p. 1–1.

[C15] **Říha, A.**, Jelínková, H., Doroshenko, M. E., Jelínek, M., Šulc, J., Němec, M., Čech, M., Kovalenko, N. O.: Comparison of spectroscopic and laser properties of Cr^{2+},Fe^{2+}:$Zn_{1-x}Mn_xSe$ (x ≈ 0.2 and x ≈ 0.4) single crystals under Er:YLF laser excitation at 1.73 µm, in: *Advanced Solid State Lasers (2021), paper ATu4A.3*, Oct. 2021, p. ATu4A.3, Optical Society of America.

[C16] **Říha, A.**, Jelínková, H., Doroshenko, M. E., Jelínek, M., Němec, M., Čech, M., Vyhlídal, D., Kovalenko, N. O.: Mid-infrared laser generation at 4.7–5.1 µm of the Cr,Fe:$Zn_{1-x}Mg_xSe$ (x ≈ 0.4) single crystal under various excitation wavelengths, in: *Solid State Lasers XXXI: Technology and Devices*, Clarkson, W. A., Shori, R. K., editors, Mar. 2022, p. 54, SPIE, San Francisco, United States.

[C17] **Říha, A.**, Jelínková, H., Doroshenko, M. E., Jelínek, M., Němec, M., Šulc, J., Kovalenko, N. O.: Excitation of the Cr^{2+},Fe^{2+}:$Zn_{1-x}Mg_xSe$ (x ≈ 0.2, 0.3, and 0.4) single crystals by 2.94 µm and 4.05 µm radiation resulting in 4.4–5.1 µm mid-infrared laser generation, in: *Optica High-brightness Sources and Light-driven Interactions Congress 2022 (2022), paper JW5A.12*, Mar. 2022, p. JW5A.12, Optica Publishing Group.

[C18] **Říha, A.**, Jelínková, H., Doroshenko, M. E., Šulc, J., Veselský, K., Němec, M., Čech, M., Badikov, V. V.: Mid-infrared diode pumped Cr:ZnSe laser continuously tunable from 2.1 µm up to 2.7 µm operated at room temperature, in: *22nd Polish-Slovak-Czech Optical Conference on Wave and Quantum Aspects of Contemporary Optics*, **vol. 12502**, Dec. 2022, p. 1250202, SPIE.

[C19] **Říha, A.**, Jelínková, H., Doroshenko, M. E., Němec, M., Šulc, J., Vyhlídal, D., Čech, M., Kovalenko, N. O.: Mid-IR spectral and laser properties comparison of Cr:ZnSe and Cr:$Zn_{1-x}Mn_xSe$ (x ≈ 0.05, 0.1, 0.2, 0.3) single crystals, in: *Optica Advanced Photonics Congress 2022 (2022), paper JTu6B.13*, Dec. 2022, p. JTu6B.13, Optica Publishing Group.

[C20] **Říha, A.**, Jelínková, H., Doroshenko, M. E., Němec, M., Šulc, J., Vyhlídal, D., Kovalenko, N. O.: The influence of Cr^{2+} to Fe^{2+} ions concentration ratio on the Cr,Fe:$Zn_{1-x}Mn_xSe$ (x ≈ 0.15) laser properties excited via $Cr^{2+} \rightarrow Fe^{2+}$ energy transfer, in: *Solid State Lasers XXXII: Technology and Devices*, **vol. 12399**, Mar. 2023, p. 172–180, SPIE.

[C21] **Říha, A.**, Jelínková, H., Doroshenko, M. E., Němec, M., Šulc, J., Čech, M., Badikov, V. V.: Laser-diode-pumped Cr:ZnSe CW laser tunable in mid-IR range of 2.05–2.65 µm, in: *High-power, High-energy Lasers and Ultrafast Optical Technologies*, **vol. 12577**, Jun. 2023, p. 82–92, SPIE.

Other publications and conference proceedings

[O1] Švejkar, R., Šulc, J., **Říha, A.**, Jelínková, H., Doroshenko, M. E., Kovalenko, N. O., Gerasimenko, A. S.: Er:YAG pumped compact Fe:ZnMnSe laser tunable in spectral range 3950–4500 nm at 80 K, in: *2018 International Conference Laser Optics (ICLO)*, Jun. 2018, p. 56–56, IEEE, St. Petersburg.

[O2] Dostálová, T., Jelínková, H., Kratochvíl, J., **Říha, A.**, Šulc, J., Němec, M., Nocar, A., Bradna, P., Pečenka, J.: Diode activated home bleaching techniques with stereolithographic models and trays, in: *Lasers in Dentistry XXVI*, **vol. 11217**, Feb. 2020, p. 1121704, International Society for Optics and Photonics.

Bibliography

[1] Maiman, T. H.: Stimulated optical radiation in ruby, *Nature*, Aug. 1960, **vol. 187(4736)**, p. 493–494.

[2] Šulc, J., Jelínková, H.: Solid-state lasers for medical applications, in: *Lasers for Medical Applications*, Jelínková, H., editor, Woodhead Publishing Series in Electronic and Optical Materials, p. 127–176, Woodhead Publishing, Jan. 2013.

[3] Duarte, F. J., editor: *Tunable lasers handbook*, Optics and photonics, Academic Press, San Diego, 1995.

[4] McNaught, A. D., Wilkinson, A.: *Compendium of chemical terminology*, Wiley, Oxford England; Malden, MA, USA, 2nd edition edition, Sep. 1997.

[5] Mirov, S. B., Fedorov, V. V., Moskalev, I. S., Martyshkin, D. V.: Recent progress in transition-metal-doped II–VI mid-IR lasers, *IEEE Journal of Selected Topics in Quantum Electronics*, May 2007, **vol. 13(3)**, p. 810–822.

[6] Orgel, L. E.: The effects of crystal fields on the properties of transition-metal ions, *Journal of the Chemical Society (Resumed)*, Jan. 1952, p. 4756–4761.

[7] Renk, K. F.: *Basics of laser physics: For students of science and engineering*, Graduate Texts in Physics, Springer International Publishing, Cham, 2017.

[8] Paschotta, R., Society of Photo-optical Instrumentation Engineers: *Field guide to lasers*, SPIE, Bellingham, Wash., 2008.

[9] Krebs, R. E.: *The history and use of our Earth's chemical elements: a reference guide*, Greenwood Press, Westport, Conn., 2006.

[10] Greenwood, N. N., Earnshaw, A.: *Chemistry of the elements*, Butterworth-Heinemann, Oxford ; Boston, 2nd ed edition, 1997.

[11] Reddy, S. L., Endo, T., Reddy, G. S.: Electronic (absorption) spectra of 3d transition metal complexes, *Advanced Aspects of Spectroscopy*, Aug. 2012.

[12] Sennaroglu, A.: *Solid-state lasers and applications*, CRC PRESS, S.l., 2019.

[13] Ebrahim-Zadeh, M., Sorokina, I. T., editors: *Mid-infrared coherent sources and applications*, NATO Science for Peace and Security Series B: Physics and Biophysics, Springer Netherlands, Dordrecht, 2008.

[14] Grebe, G., Schulz, H.-J.: Interpretation of excitation spectra of ZnS:Cr^{2+} by fitting the eigenvalues of the tanabe-sugano matrices, *physica status solidi (b)*, 1972, **vol. 54(1)**, p. K69–K72.

[15] Grebe, G., Schulz, H.-J.: Luminescence of Cr^{2+} centres and related optical interactions involving crystal field levels of chromium ions in zinc sulfide, *Zeitschrift für Naturforschung A*, Dec. 1974, **vol. 29(12)**, p. 1803–1819.

[16] Grebe, G., Roussos, G., Schulz, H.-J.: Cr^{2+} excitation levels in ZnSe and ZnS, *Journal of Physics C: Solid State Physics*, Dec. 1976, **vol. 9(24)**, p. 4511–4516.

[17] Graham, K., Mirov, S. B., Fedorov, V. V., Zvanut, M. E., Avanesov, A., Badikov, V., Ignat'ev, B., Panutin, V., Shevirdyaeva, G.: Spectroscopic characterization and laser performance of diffusion doped Cr^{2+}:ZnS, in: *Advanced Solid-State Lasers (2001), paper WB12*, Jan. 2001, p. WB12, Optical Society of America.

[18] Grebe, G., Roussos, G., Schulz, H. J.: Infrared luminescence of ZnSe:Cr crystals, *Journal of Luminescence*, Mar. 1976, **vol. 12-13**, p. 701–705.

[19] Sorokina, I. T.: Cr^{2+}-doped II–VI materials for lasers and nonlinear optics, *Optical Materials*, Sep. 2004, **vol. 26(4)**, p. 395–412.

[20] Sadofyev, Y. G., Pevtsov, V. F., Dianov, E. M., Trubenko, P. A., Korshkov, M. V.: Molecular beam epitaxy growth and characterization of ZnTe:Cr^{2+} layers on GaAs(100), *Journal of Vacuum Science & Technology B: Microelectronics and Nanometer Structures*, 2001, **vol. 19(4)**, p. 1483.

[21] Doroshenko, M. E., Osiko, V. V., Jelínková, H., Jelínek, M., Němec, M., Šulc, J., Kovalenko, N. O., Gerasimenko, A. S., Puzikov, V. M.: Spectroscopic and laser properties of Cr^{2+} ions in $Zn_{1-x}Mg_xSe$ solid solutions, *Optical Materials*, Sep. 2015, **vol. 47**, p. 185–189.

[22] Klokishner, S. I., Tsukerblat, B. S., Reu, O. S., Palii, A. V., Ostrovsky, S. M.: Jahn-Teller vibronic coupling in CdSe doped with Cr^{2+} ions, *Optical Materials*, May 2005, **vol. 27(8)**, p. 1445–1450.

[23] Klokishner, S., Reu, O., Ostrovsky, S., Palii, A., Towe, E.: A vibronic model for the absorption spectra of Cr^{2+} ions in $CdSe_xS_{1-x}$, *Journal of Physics: Condensed Matter*, Nov. 2007, **vol. 19(48)**, p. 486213.

[24] Kück, S.: Spectroscopy and laser characteristics of Cr^{2+}-doped chalcogenide crystals – overview and recent results, *Journal of Alloys and Compounds*, Jul. 2002, **vol. 341(1)**, p. 28–33.

[25] Vallin, J. T., Watkins, G. D.: EPR of Cr^{2+} in II–VI lattices, *Physical Review B*, Mar. 1974, **vol. 9(5)**, p. 2051–2072.

[26] Chen, M., Hu, C., Li, W., Kou, H., Li, J., Pan, Y., Jiang, B.: Cr^{3+} in diffusion doped Cr^{2+}:ZnS, *Ceramics International*, Jun. 2014, **vol. 40(5)**, p. 7573–7577.

[27] Vallin, J. T., Slack, G. A., Roberts, S., Hughes, A. E.: Infrared absorption in some II–VI compounds doped with Cr, *Physical Review B*, Dec. 1970, **vol. 2(11)**, p. 4313–4333.

[28] Demirbas, U., Sennaroglu, A.: Intracavity-pumped Cr^{2+}:ZnSe laser with ultra-broad tuning range between 1880 and 3100 nm, *Optics Letters*, Aug. 2006, **vol. 31(15)**, p. 2293–2295.

[29] Nagl, N., Gröbmeyer, S., Pervak, V., Pronin, O., Mak, K. F., Krausz, F.: Directly diode-pumped, Kerr-lens mode-locked Cr:ZnSe oscillator, in: *2019 Conference on Lasers and Electro-Optics Europe European Quantum Electronics Conference (CLEO/Europe-EQEC)*, Jun. 2019, p. 1–1.

[30] Mualin, O., Vogel, E. E., de Orúe, M. A., Martinelli, L., Bevilacqua, G., Schulz, H.-J.: Two-mode Jahn-Teller effect in the absorption spectra of Fe^{2+} in II–VI and III–V semiconductors, *Physical Review B*, Dec. 2001, **vol. 65(3)**, p. 035211.

[31] Goetz, G., Zimmermann, H., Schulz, H. J.: Jahn-Teller interaction at Cr^{2+} (d^4) centres in tetrahedrally coordinated II–VI lattices studied by optical spectroscopy, *Zeitschrift für Physik B Condensed Matter*, Dec. 1993, **vol. 91(4)**, p. 429–436.

[32] Klokishner, S. I., Tsukerblat, B. S., Reu, O. S., Palii, A. V., Ostrovsky, S. M.: Jahn-Teller vibronic coupling in II–VI compounds with Cr^{2+} ion, *Chemical Physics*, Sep. 2005, **vol. 316(1)**, p. 83–92.

[33] Malguth, E., Hoffmann, A., Phillips, M. R.: Fe in III–V and II–VI semiconductors, *physica status solidi (b)*, 2008, **vol. 245(3)**, p. 455–480.

[34] Mitra, S. S.: Phonon assignments in ZnSe and GaSb and some regularities in the phonon frequencies of zincblende-type semiconductors, *Physical Review*, Nov. 1963, **vol. 132(3)**, p. 986–991.

[35] Fedorov, V., Martyshkin, D., Karki, K., Mirov, S.: Q-switched and gain-switched Fe:ZnSe lasers tunable over 3.60–5.15 µm, *Optics Express*, May 2019, **vol. 27(10)**, p. 13934.

[36] Myoung, N., Fedorov, V. V., Mirov, S. B., Wenger, L. E.: Temperature and concentration quenching of mid-IR photoluminescence in iron doped ZnSe and ZnS laser crystals, *Journal of Luminescence*, Mar. 2012, **vol. 132(3)**, p. 600–606.

[37] Adams, J. J., Bibeau, C., Page, R. H., Krol, D. M., Furu, L. H., Payne, S. A.: 4.0–4.5 µm lasing of Fe:ZnSe below 180 K, a new mid-infrared laser material, *Optics Letters*, Dec. 1999, **vol. 24(23)**, p. 1720.

[38] Denker, B., Shklovsky, E., editors: *Handbook of solid-state lasers: materials, systems and applications*, no. number 35 in Woodhead Publishing series in electronic and optical materials, Woodhead Publishing, Cambridge, UK ; Philadelphia, PA, 2013.

[39] Evans, J. W., Harris, T. R., Reddy, B. R., Schepler, K. L., Berry, P. A.: Optical spectroscopy and modeling of Fe^{2+} ions in zinc selenide, *Journal of Luminescence*, Aug. 2017, **vol. 188**, p. 541–550.

[40] DeLoach, L., Page, R., Wilke, G., Payne, S., Krupke, W.: Transition metal-doped zinc chalcogenides: spectroscopy and laser demonstration of a new class of gain media, *IEEE Journal of Quantum Electronics*, Jun. 1996, **vol. 32(6)**, p. 885–895.

[41] Paschotta, R.: *Encyclopedia of laser physics and technology*, Wiley-VCH, Weinheim, 2008.

[42] Adachi, S.: *Optical constants of crystalline and amorphous semiconductors*, Springer US, Boston, MA, 1999.

[43] Sorokina, I. T., Sorokin, E., Lieto, A. D., Tonelli, M., Vinogradov, E. A.: Spectroscopy and room-temperature continuous-wave lasing from a new gain material Cr^{2+}:ZnS_xSe_{1-x}, in: *Conference on Lasers and Electro-Optics/International Quantum Electronics Conference and Photonic Applications Systems Technologies (2004), paper CThE1*, May 2004, p. CThE1, Optical Society of America.

[44] Mirov, S. B., Fedorov, V. V., Martyshkin, D., Moskalev, I. S., Mirov, M., Vasilyev, S.: Progress in mid-IR lasers based on Cr and Fe-doped II–VI chalcogenides, *IEEE Journal of Selected Topics in Quantum Electronics*, Jan. 2015, **vol. 21(1)**, p. 292–310.

[45] Mirov, S. B., Moskalev, I. S., Vasilyev, S., Smolski, V., Fedorov, V. V., Martyshkin, D., Peppers, J., Mirov, M., Dergachev, A., Gapontsev, V.: Frontiers of mid-IR lasers based on transition metal doped chalcogenides, *IEEE Journal of Selected Topics in Quantum Electronics*, Sep. 2018, **vol. 24(5)**, p. 1–29.

[46] Isshiki, M., Wang, J.: Wide-bandgap II–VI semiconductors: growth and properties, in: *Springer Handbook of Electronic and Photonic Materials*, Kasap, S., Capper, P., editors, Springer Handbooks, p. 1–1, Springer International Publishing, Cham, 2017.

[47] Gallian, A., Fedorov, V. V., Kernal, J., Mirov, S. B., Badikov, V. V.: Laser oscillation at 2.4 μm from Cr^{2+} in ZnSe optically pumped over Cr ionization transitions, in: *Advanced Solid-State Photonics (TOPS) (2005), paper 241*, Feb. 2005, p. 241, Optical Society of America.

[48] Kovalenko, N. O.: Comparative characterization of technology for ZnSe crystal growth, Sep. 2014.
URL https://agenda.infn.it/event/8606/?print=1&view=event

[49] Piper, W. W., Polich, S. J.: Vapor-phase growth of single crystals of II–VI compounds, *Journal of Applied Physics*, Jul. 1961, **vol. 32(7)**, p. 1278–1279.

[50] Prior, A. C.: Growth from the vapor of large single crystals of lead selenide of controlled composition, *Journal of the Electrochemical Society*, Jan. 1961, **vol. 108(1)**, p. 82.

[51] Bridgman, P. W.: The thermal conductivity of liquids under pressure, *Proceedings of the American Academy of Arts and Sciences*, 1923, **vol. 59(7)**, p. 141–169.

[52] Fukuda, T., Umetsu, K., Rudolph, P., Koh, H. J., Iida, S., Uchiki, H., Tsuboi, N.: Growth and characterization of twin-free ZnSe single crystals by the vertical Bridgman method, *Journal of Crystal Growth*, Apr. 1996, **vol. 161(1)**, p. 45–50.

[53] Kovalenko, N. O., Terzin, I. S., Sulima, S. V., Poluboiarov, O. O., Kapustnik, A. K., Sofronov, D. S., Mateichenko, P. F., Dubina, N. G., Abashin, S. L., Fedorov, A. G.: High-pressure Bridgman growth and characterization of $Cd_{1-x}Mn_xTe$:Fe crystals, *Crystal Research and Technology*, 2017, **vol. 52(8)**, p. 1600378.

[54] Mirov, S., Fedorov, V., Graham, K., Moskalev, I., Sorokina, I., Sorokin, E., Gapontsev, V., Gapontsev, D., Badikov, V., Panyutin, V.: Diode and fibre pumped Cr^{2+}:ZnS mid-infrared external cavity and microchip lasers, *IEE Proceedings - Optoelectronics*, Aug. 2003, **vol. 150(4)**, p. 340–345.

[55] Su, C.-H.: *Vapor crystal growth and characterization: ZnSe and related II–VI compound semiconductors*, Springer International Publishing, Cham, 2020.

[56] Vanmil, B. L., Ptak, A. J., Bai, L., Wang, L., Chirila, M., Giles, N. C., Myers, T. H., Wang, L.: Heavy Cr doping of ZnSe by molecular beam epitaxy, *Journal of Electronic Materials*, Jul. 2002, **vol. 31(7)**, p. 770–775.

[57] Zhang, Y., Yang, C., Feng, G.: Doping non-uniformity influence on the electrical and optical properties of chromium doped zinc selenide, *Materials Today Communications*, Dec. 2020, p. 101946.

[58] Schliesser, A., Picqué, N., Hänsch, T. W.: Mid-infrared frequency combs, *Nature Photonics*, Jul. 2012, **vol. 6(7)**, p. 440–449.

[59] Hammerling, P., Budgor, A. B., Pinto, A.: *Tunable solid state lasers: Proceedings of the first international conference*, Springer Berlin Heidelberg, Berlin, Heidelberg, 1985.

[60] Fazzio, A., Caldas, M. J., Zunger, A.: Many-electron multiplet effects in the spectra of 3d impurities in heteropolar semiconductors, *Physical Review B*, Sep. 1984, **vol. 30(6)**, p. 3430–3455.

[61] Kaminskii, A. A.: Laser crystals and ceramics: recent advances, *Laser & Photonics Reviews*, 2007, **vol. 1(2)**, p. 93–177.

[62] Johnson, L. F., Guggenheim, H. J.: Phonon-terminated coherent emission from V^{2+} ions in MgF_2, *Journal of Applied Physics*, Nov. 1967, **vol. 38(12)**, p. 4837–4839.

[63] Brauch, U., Dürr, U.: Vibronic laser action of V^{2+}:$CsCaF_3$, *Optics Communications*, Aug. 1985, **vol. 55(1)**, p. 35–40.

[64] Knierim, W., Honold, A., Brauch, U., Dürr, U.: Optical and lasing properties of V^{2+}-doped halide crystals, *JOSA B*, Jan. 1986, **vol. 3(1)**, p. 119–124.

[65] Clausen, R., Petermann, K.: Mn^{2+} and Fe^{3+} doped oxides for short wavelength solid state lasers, *Journal of Luminescence*, Feb. 1988, **vol. 40-41**, p. 185–186.

[66] Clausen, R., Petermann, K.: Mn^{2+} as a potential solid-state laser ion, *IEEE Journal of Quantum Electronics*, Jun. 1988, **vol. 24(6)**, p. 1114–1117.

[67] Singh, V., Chakradhar, R. P. S., Rao, J. L., Kwak, H.-Y.: Investigations on green-emitting, Mn^{2+}:$BaAl_{12}O_{19}$ phosphors obtained by solution combustion process, *Journal of Materials Science*, Jun. 2011, **vol. 46(11)**, p. 3928–3934.

[68] Qian, J., Li, P., Huang, Y., Wang, C., Zhang, Y., Bai, F., Fan, W., Li, Y., Li, H., Peng, M., Dai, Y., Zhao, Q.-Z.: Long persistent luminescence in Mn^{2+}-activated sodium gallium germanate glass and glass ceramics induced by infrared femtosecond laser pulses, *Optical Materials Express*, Jul. 2016, **vol. 6(7)**, p. 2380–2388.

[69] Danilkin, M. I., Vereschagina, N. Y., Vainer, Y. G., Kochiev, M. V., Ambrozevich, S. A., Romet, I., Mändar, H., Morozov, A. N., Repeev, Y. A., Spassky, D. A., Shutov, A. V., Seleznev, L. V., Mokrousova, D. V., Selyukov, A. S.: Ultrafast and slow Mn^{2+} luminescence in lithium tetraborate, *Journal of Alloys and Compounds*, Nov. 2021, **vol. 883**, p. 160852.

[70] Johnson, L. F., Dietz, R. E., Guggenheim, H. J.: Optical maser oscillation from Ni^{2+} in MgF_2 involving simultaneous emission of phonons, *Physical Review Letters*, Oct. 1963, **vol. 11(7)**, p. 318–320.

[71] Johnson, L. F., Dietz, R. E., Guggenheim, H. J.: Spontanrous and stimulated emission from Co^{2+} ions in MgF_2 and ZnF_2, *Applied Physics Letters*, Jul. 1964, **vol. 5(2)**, p. 21–22.

[72] Johnson, L. F., Guggenheim, H. J., Thomas, R. A.: Phonon-terminated optical masers, *Physical Review*, Sep. 1966, **vol. 149(1)**, p. 179–185.

[73] Moulton, P. F., Mooradian, A.: Broadly tunable cw operation of Ni:MgF_2 and Co:MgF_2 lasers, *Applied Physics Letters*, Dec. 1979, **vol. 35(11)**, p. 838–840.

[74] Johnson, B. C., Moulton, P. F., Mooradian, A.: Mode-locked operation of Co:MgF_2 and Ni:MgF_2 lasers, *Optics Letters*, Apr. 1984, **vol. 9(4)**, p. 116–118.

[75] Løvold, S., Moulton, P., Killinger, D., Menyuk, N.: Frequency tuning characteristics of a Q-switched Co:MgF_2 laser, *IEEE Journal of Quantum Electronics*, Mar. 1985, **vol. 21(3)**, p. 202–208.

[76] Moulton, P.: An investigation of the Co:MgF_2 laser system, *IEEE Journal of Quantum Electronics*, Oct. 1985, **vol. 21(10)**, p. 1582–1595.

[77] Walling, J. C.: Tunable paramagnetic-ion solid-state lasers, in: *Tunable Lasers*, Mollenauer, L. F., White, J. C., editors, Topics in Applied Physics, p. 331–398, Springer, Berlin, Heidelberg, 1987.

[78] Di Lieto, A.: Development of a cw Co:MgF_2 laser, *Optics and Lasers in Engineering*, Mar. 2003, **vol. 39(3)**, p. 309–315.

[79] German, K. R., Dürr, U., Künzel, W.: Tunable single-frequency continuous-wave laser action in Co^{2+}:$KZnF_3$, *Optics Letters*, Jan. 1986, **vol. 11(1)**, p. 12–14.

[80] Moulton, P. F., Mooradian, A., Reed, T. B.: Efficient cw optically pumped Ni:MgF_2 laser, *Optics Letters*, Nov. 1978, **vol. 3(5)**, p. 164–166.

[81] Fox, A. M., Maciel, A. C., Ryan, J. F.: Efficient cw performance of a Co:MgF_2 laser operating at 1.5–2.0 μm, *Optics Communications*, Aug. 1986, **vol. 59(2)**, p. 142–144.

[82] Rines, D. M., Moulton, P. F., Welford, D., Rines, G. A.: High-energy operation of a Co:MgF_2 laser, *Optics Letters*, May 1994, **vol. 19(9)**, p. 628–630.

[83] Mollenauer, L. F., White, J. C., Pollock, C. R., editors: *Tunable lasers*, *Topics in Applied Physics*, vol. 59, Springer Berlin Heidelberg, Berlin, Heidelberg, 1992.

[84] Moulton, P. F.: Recent advances in solid-state lasers, in: *Conference on Lasers and Electro-Optics (1984), paper WA2*, Jun. 1984, p. WA2, Optica Publishing Group.

[85] Ferguson, J., Masui, H.: Emission from Ni-Ni and Ni-Co pairs in $KMgF_3$ crystals, *Journal of Luminescence*, Jan. 1979, **vol. 18-19**, p. 224–226.

[86] Feuerhelm, L. N., Sibley, W. A.: Optical transitions of Ni^{2+} and radiation defects in MgF_2 and MnF_2, *Journal of Physics C: Solid State Physics*, Feb. 1983, **vol. 16(4)**, p. 799.

[87] Moulton, P.: Pulse-pumped operation of divalent transition-metal lasers, *IEEE Journal of Quantum Electronics*, Aug. 1982, **vol. 18(8)**, p. 1185–1188.

[88] Kück, S.: Laser-related spectroscopy of ion-doped crystals for tunable solid-state lasers, *Applied Physics B*, Apr. 2001, **vol. 72(5)**, p. 515–562.

[89] Sorokin, E., Naumov, S., Sorokina, I.: Ultrabroadband infrared solid-state lasers, *IEEE Journal of Selected Topics in Quantum Electronics*, May 2005, **vol. 11(3)**, p. 690–712.

[90] Kernal, J., Fedorov, V. V., Gallian, A., Mirov, S. B., Badikov, V. V.: 3.9–4.8 μm gain-switched lasing of Fe:ZnSe at room temperature, *Optics Express*, 2005, **vol. 13(26)**, p. 10608.

[91] Fedorov, V., Mirov, S., Gallian, A., Badikov, D., Frolov, M., Korostelin, Y., Kozlovsky, V., Landman, A., Podmar'kov, Y., Akimov, V., Voronov, A.: 3.77–5.05 μm tunable solid-state lasers based on Fe^{2+}-doped ZnSe crystals operating at low and room temperatures, *IEEE Journal of Quantum Electronics*, Sep. 2006, **vol. 42(9)**, p. 907–917.

[92] Fedorov, V. V., Mirov, M. S., Mirov, S. B., Gapontsev, V. P., Erofeev, A. V., Smirnov, M. Z., Altshuler, G. B.: Compact 1J mid-IR Cr:ZnSe Laser, in: *Frontiers in Optics 2012/Laser Science XXVIII (2012), paper FW6B.9*, Oct. 2012, p. FW6B.9, Optica Publishing Group.

[93] Mond, M., Albrecht, D., Kretschmann, H., Heumann, E., Huber, G., Kück, S., Levchenko, V., Yakimovich, V., Shcherbitsky, V., Kisel, V.,

Kuleshov, N.: Erbium doped fibre amplifier pumped Cr^{2+}:ZnSe laser, *physica status solidi (a)*, 2001, **vol. 188(4)**, p. R3–R5.

[94] Mirov, S. B., Fedorov, V. V., Graham, K., Moskalev, I. S., Badikov, V. V., Panyutin, V.: Erbium fiber laser-pumped continuous-wave microchip Cr^{2+}:ZnS and Cr^{2+}:ZnSe lasers, *Optics Letters*, Jun. 2002, **vol. 27(11)**, p. 909–911.

[95] Podlipensky, A. V., Shcherbitsky, V. G., Kuleshov, N. V., Mikhailov, V. P., Levchenko, V. I., Yakimovich, V. N., Postnova, L. I., Konstantinov, V. I.: Pulsed laser operation of diffusion-doped Cr^{2+}:ZnSe, *Optics Communications*, Aug. 1999, **vol. 167(1)**, p. 129–132.

[96] Nagl, N., Grobmeyer, S., Potzlberger, M., Pervak, V., Krausz, F., Krausz, F., Mak, K. F.: Directly diode-pumped few-optical-cycle Cr:ZnS laser at 800 mW of average power, in: *Conference on Lasers and Electro-Optics (2020), paper SF3H.5*, May 2020, p. SF3H.5, Optica Publishing Group.

[97] Jelínková, H., Koranda, P., Doroshenko, M. E., Basiev, T. T., Šulc, J., Němec, M., Černý, P., Komar, V. K., Kosmyna, M. B.: Cr^{2+}:ZnSe laser pumped by 1.66 μm or 1.97 μm radiations, *Laser Physics Letters*, Sep. 2006, **vol. 4(1)**, p. 23.

[98] Mond, M., Albrecht, D., Heumann, E., Huber, G., Kück, S., Levchenko, V. I., Yakimovich, V. N., Shcherbitsky, V. G., Kisel, V. E., Kuleshov, N. V., Rattunde, M., Schmitz, J., Kiefer, R., Wagner, J.: 1.9-μm and 2.0-μm laser diode pumping of Cr^{2+}:ZnSe and Cr^{2+}:CdMnTe, *Optics Letters*, Jun. 2002, **vol. 27(12)**, p. 1034–1036.

[99] Dai, Y. F., Li, Y. Y., Zou, X., Dong, Y. J., Leng, Y. X.: High-efficiency broadly tunable Cr:ZnSe single crystal laser pumped by Tm:YLF laser, *Laser Physics Letters*, Sep. 2013, **vol. 10(10)**, p. 105816.

[100] Albrecht, D., Mond, M., Heumann, E., Huber, G., Kuck, S., Levchenko, V., Yakimovich, V., Shcherbitsky, V., Kisel, V., Kuleshov, N., Rattunde, M., Schmitz, J., Kiefer, R., Wagner, J.: Efficient 100 mW Cr^{2+}:ZnSe laser pumped by a 1.9 μm laser diode, in: *Summaries of Papers Presented at the Lasers and Electro-Optics. CLEO '02. Technical Diges*, May 2002, p. 121–122 vol.1.

[101] Podlipensky, A., Shcherbitsky, V., Kuleshov, N., Levchenko, V., Yakimovich, V., Mond, M., Heumann, E., Huber, G., Kretschmann, H., Kück, S.: Efficient laser operation and continuous-wave diode pumping of Cr^{2+}:ZnSe single crystals, *Applied Physics B*, Jan. 2001, **vol. 72(2)**, p. 253–255.

[102] Wagner, G. J., Carrig, T. J., Page, R. H., Schaffers, K. I., Ndap, J.-O., Ma, X., Burger, A.: Continuous-wave broadly tunable Cr^{2+}:ZnSe laser, *Optics Letters*, Jan. 1999, **vol. 24(1)**, p. 19–21.

[103] Zakel, A., Wagner, G. J., Sullivan, A. C., Wenzel, J. F., Alford, W. J., Carrig, T. J.: High-brightness, rapidly-tunable Cr:ZnSe lasers, in: *Advanced Solid-State Photonics (TOPS) (2005), paper 723*, Feb. 2005, p. 723, Optical Society of America.

[104] Yumoto, M., Saito, N., Takagi, U., Wada, S.: Electronically tuned Cr:ZnSe laser pumped with Q-switched Tm:YAG laser, *Optics Express*, Sep. 2015, **vol. 23(19)**, p. 25009–25016.

[105] Fedorov, V. V., Moskalev, I. S., Mirov, M. S., Mirov, S. B., Wagner, T. J., Bohn, M. J., Berry, P. A., Schepler, K. L.: Energy scaling of nanosecond gain-switched Cr^{2+}:ZnSe lasers, in: *Solid State Lasers XX: Technology and Devices*, vol. 7912, Feb. 2011, p. 333–339, SPIE.

[106] Gallian, A., Camata, R., Stanishevsky, A., Watkins, C. L., Zvanut, M. E., Gallian, A.: *Optical and electrical characteristics of Cr and Fe doped ZnSe thin film and bulk materials for optically and electrically pumped lasers*, Dissertation thesis, The University of Alabama at Birmingham, 2006.

[107] Velikanov, S. D., Danilov, V. P., Zakharov, N. G., Il'ichev, N. N., Kazantsev, S. Y., Kalinushkin, V. P., Kononov, I. G., Nasibov, A. S., Studenikin, M. I., Pashinin, P. P., Firsov, K. N., Shapkin, P. V., Shchurov, V. V.: Fe^{2+}:ZnSe laser pumped by a nonchain electric-discharge HF laser at room temperature, *Quantum Electronics*, Feb. 2014, **vol. 44(2)**, p. 141–144.

[108] Ke, C., Wang, R., Li, Z., Hang, Y.: Room temperature high energy high efficient Fe^{2+}:ZnSe laser, in: *2015 Conference on Lasers and Electro-Optics Pacific Rim (2015), paper 27A2_4*, Aug. 2015, p. 27A2_4, Optica Publishing Group.

[109] Velikanov, S. D., Zaretsky, N. A., Zotov, E. A., Kazantsev, S. Y., Kononov, I. G., Korostelin, Y. V., Maneshkin, A. A., Firsov, K. N., Frolov, M. P., Yutkin, I. M.: Room-temperature 1.2-J Fe^{2+}:ZnSe laser, *Quantum Electronics*, Jan. 2016, **vol. 46(1)**, p. 11.

[110] Firsov, K. N., Frolov, M. P., Gavrishchuk, E. M., Kazantsev, S. Y., Kononov, I. G., Korostelin, Y. V., Maneshkin, A. A., Velikanov, S. D., Yutkin, I. M., Zaretsky, N. A., Zotov, E. A.: Laser on single-crystal ZnSe:Fe^{2+} with high pulse radiation energy at room temperature, *Laser Physics Letters*, Jan. 2016, **vol. 13(1)**, p. 015002.

[111] Antonov, V. A., Firsov, K. N., Gavrishchuk, E. M., Kononov, I. G., Kurashkin, S. V., Podlesnykh, S. V., Raspopov, N. A., Sirotkin, A. A., Zhavoronkov, N. V.: Energy and spectral-temporal characteristics of a Fe:ZnSe laser on heavily doped single crystals, *Applied Physics B*, Oct. 2020, **vol. 126(11)**, p. 179.

[112] Ruan, P., Pan, Q., Alekseev, E. E., Kazantsev, S. Y., Mashkovtseva, L. S., Mironov, Y. B., Podlesnikh, S. V.: Performance improvement of a Fe^{2+}:ZnSe laser pumped by non-chain pulsed HF laser, *Optik*, Sep. 2021, **vol. 242**, p. 167005.

[113] Kozlovsky, V. I., Frolov, M. P., Korostelin, Y. V., Skasyrsky, Y. K.: Nanosecond-pulsed RT-operating at 4 μm Fe:ZnSe laser pumped inside the cavity of a LD side-pumped Er:YLF laser, *Optics Express*, Sep. 2018, **vol. 26(19)**, p. 24497–24505.

[114] Fedorov, V. V., Fedorov, V. V., Martyshkin, D. V., Martyshkin, D. V., Mirov, M. S., Mirov, M. S., Moskalev, I. S., Vasyliev, S., Peppers, J., Mirov, S. B., Mirov, S. B., Gapontsev, V. P.: Fe-doped II-VI mid-Infrared laser materials for the 3 to 8 μm region, in: *CLEO: 2013 (2013), paper JM4K.2*, Jun. 2013, p. JM4K.2, Optica Publishing Group.

[115] Evans, J. W., Sanamyan, T., Berry, P. A.: A continuous wave Fe:ZnSe laser pumped by efficient Er:Y_2O_3 laser, in: *Solid State Lasers XXIV: Technology and Devices*, vol. 9342, Feb. 2015, p. 74–79, SPIE.

[116] Jelínková, H., Doroshenko, M. E., Jelínek, M., Šulc, J., Němec, M., Kubeček, V., Zagoruiko, Y. A., Kovalenko, N. O., Gerasimenko, A. S., Puzikov, V. M., Komar, V. K.: Fe:ZnSe and Fe:ZnMgSe lasers pumped by Er:YSGG radiation, in: *Solid State Lasers XXIV: Technology and Devices*, vol. 9342, Feb. 2015, p. 367–372, SPIE.

[117] Leonov, S., Frolov, M., Korostelin, Y., Skasyrsky, Y., Kozlovsky, V.: Gain-switched Fe:ZnSe laser pumped by a coupled-cavity Q-switched Er:ZrF_4 fiber laser, *Optics Letters*, Jun. 2023, **vol. 48(11)**, p. 2957–2960.

[118] Myoung, N., Martyshkin, D. V., Fedorov, V. V., Mirov, S. B.: Energy scaling of 4.3 μm room temperature Fe:ZnSe laser, *Optics Letters*, Jan. 2011, **vol. 36(1)**, p. 94–96.

[119] Pushkin, A. V., Migal, E. A., Uehara, H., Goya, K., Tokita, S., Frolov, M. P., Korostelin, Y. V., Kozlovsky, V. I., Skasyrsky, Y. K., Potemkin, F. V.: Compact, highly efficient, 2.1-W continuous-wave mid-infrared Fe:ZnSe coherent source, pumped by an Er:ZBLAN fiber laser, *Optics Letters*, Dec. 2018, **vol. 43(24)**, p. 5941.

[120] Pushkin, A. V., Migal, E. A., Tokita, S., Korostelin, Y. V., Potemkin, F. V.: Femtosecond graphene mode-locked Fe:ZnSe laser at 4.4 μm, *Optics Letters*, Feb. 2020, **vol. 45(3)**, p. 738–741.

[121] Akimov, V. A., Voronov, A. A., Kozlovskii, V. I., Korostelin, Y. V., Landman, A. I., Podmar'kov, Y. P., Frolov, M. P.: Efficient IR Fe:ZnSe laser continuously tunable in the spectral range from 3.77 to 4.40 μm, *Quantum Electronics*, Oct. 2004, **vol. 34(10)**, p. 912–914.

[122] Voronov, A. A., Kozlovskii, V. I., Korostelin, Y. V., Landman, A. I., Podmar'kov, Y. P., Frolov, M. P.: Laser parameters of a Fe:ZnSe crystal in the 85–255 K temperature range, *Quantum Electronics*, Sep. 2005, **vol. 35(9)**, p. 809.

[123] Karki, K., Karki, K., Yu, S., Fedorov, V., Martyshkin, D., Subedi, S., Wu, Y., Wu, Y., Mirov, S.: Hot-pressed ceramic Fe:ZnSe gain-switched laser, *Optical Materials Express*, Dec. 2020, **vol. 10(12)**, p. 3417–3423.

[124] Dai, T., Guo, C., Li, Y., Ju, Y., Yao, B., Duan, X.: A room temperature operation mid-IR Fe:ZnSe laser pumped by Ho,Pr:$LiLuF_4$ laser at 2.9-μm, *Optics & Laser Technology*, Oct. 2019, **vol. 118**, p. 179–182.

[125] Voronov, A. A., Kozlovskii, V. I., Korostelin, Y. V., Landman, A. I., Podmar'kov, Y. P., Skasyrskii, Y. K., Frolov, M. P.: A continuous-wave Fe^{2+}:ZnSe laser, *Quantum Electronics*, Dec. 2008, **vol. 38(12)**, p. 1113.

[126] Kozlovsky, V. I., Akimov, V. A., Frolov, M. P., Korostelin, Y. V., Landman, A. I., Martovitsky, V. P., Mislavskii, V. V., Podmar'kov, Y. P., Skasyrsky, Y. K., Voronov, A. A.: Room-temperature tunable mid-infrared lasers on transition-metal doped II–VI compound crystals grown from vapor phase, *physica status solidi (b)*, 2010, **vol. 247(6)**, p. 1553–1556.

[127] Doroshenko, M. E., Jelínková, H., Jelínek, M., Vyhlídal, D., Šulc, J., Kovalenko, N. O., Terzin, I. S.: Influence of the pumping wavelength on laser properties of Fe^{2+} ions in ZnSe crystal, *Optics Letters*, Apr. 2019, **vol. 44(7)**, p. 1686.

[128] Djeu, N., Hartwell, V. E., Kaminskii, A. A., Butashin, A. V.: Room-temperature 3.4-μm Dy:$BaYb_2F_8$ laser, *Optics Letters*, Jul. 1997, **vol. 22(13)**, p. 997–999.

[129] Woodward, R. I., Majewski, M. R., Bharathan, G., Hudson, D. D., Fuerbach, A., Jackson, S. D.: Watt-level dysprosium fiber laser at 3.15 μm with 73 % slope efficiency, *Optics Letters*, Apr. 2018, **vol. 43(7)**, p. 1471–1474.

[130] Karipidou, A.: Energy transfer processes in ZnSe:Ni,Fe, in: *Energy Transfer Processes in Condensed Matter*, Di Bartolo, B., editor, NATO ASI Series, p. 687–687, Springer US, Boston, MA, 1984.

[131] Peppers, J., Myoung, N., Fedorov, V. V., Mirov, S. B.: Mid-IR laser oscillation via energy transfer in the Co:Fe:ZnS/Se co-doped crystals, in: *Solid State Lasers XXI: Technology and Devices*, Clarkson, W. A., Shori, R. K., editors, Feb. 2012, p. 8235, San Francisco, California, USA.

[132] Myoung, N., Martyshkin, D. V., Fedorov, V. V., Mirov, S. B.: Mid-IR lasing of iron-cobalt co-doped ZnS(Se) crystals via Co-Fe energy transfer, *Journal of Luminescence*, Jan. 2013, **vol. 133**, p. 257–261.

[133] Peppers, J., Martyshkin, D. V., Fedorov, V. V., Mirov, S. B.: Spectroscopic characterization and energy transfer process in cobalt and cobalt-iron co-doped ZnSe/ZnS crystals, in: *Solid State Lasers XXIII: Technology and Devices*, vol. 8959, Feb. 2014, p. 282–288, SPIE.

[134] Antonov, V. A., Firsov, K. N., Gavrishchuk, E. M., Ikonnikov, V. B., Kononov, I. G., Kotereva, T. V., Kurashkin, S. V., Podlesnykh, S. V., Rodin, S. A., Savin, D. V., Sirotkin, A. A., Titirenko, A. M., Zhavoronkov, N. V.: Luminescent and lasing characteristics of polycrystalline Cr:Fe:ZnSe exited at 2.09 and 2.94 μm wavelengths, *Laser Physics Letters*, Aug. 2019, **vol. 16(9)**, p. 095002.

[135] Ivanov, V. Y., Shagov, A. A., Szczerbakow, A., Godlewski, M.: Excitation mechanism of blue anti-Stokes and 2.4 μm infrared emission in ZnSe:Cr, *Physica B: Condensed Matter*, Dec. 2001, **vol. 308-310**, p. 942–944.

[136] Ivanov, V. Y., Godlewski, M., Surkova, T. P., Zhavoronkov, N., Omelchuk, A. R.: Blue anti-stokes emission in chromium and iron doped wide band gap II–VI compounds, *physica status solidi (b)*, 2002, **vol. 229(1)**, p. 355–359.

[137] Ivanov, V., Godlewski, M., Szczerbakow, A., Omel'chuk, A., Davydov, A., Zhavoronkov, N., Raciukaitis, G.: Optically pumped mid-infrared stimulated emission of ZnSe:Cr crystals, *Acta Physica Polonica A*, Jun. 2004, **vol. 105(6)**, p. 553–558.

[138] Jaeck, J., Haidar, R., Pardo, F., Pelouard, J.-L., Rosencher, E.: Electrically enhanced infrared photoluminescence in Cr:ZnSe, *Applied Physics Letters*, May 2010, **vol. 96(21)**, p. 211107.

[139] Klein, P. B., Furneaux, J. E., Henry, R. L.: Laser oscillation at 3.53 μm from Fe^{2+} in n-InP:Fe, *Applied Physics Letters*, Apr. 1983, **vol. 42(8)**, p. 638–640.

[140] Tomm, J. W., Steinmeyer, G., Fürtjes, P., Griebner, U., Elsaesser, T.: Excitation transfer from Cr^{2+} to Fe^{2+} ions in co-doped ZnSe as a pumping scheme for infrared solid-state lasers, *Journal of Electronic Materials*, May 2023.

[141] Steinmeyer, G., Tomm, J. W., Fuertjes, P., Griebner, U., Balabanov, S. S., Elsaesser, T.: Efficient electronic excitation transfer via phonon-assisted dipole-dipole coupling in Fe^{2+}:Cr^{2+}:ZnSe, *Physical Review Applied*, May 2023, **vol. 19(5)**, p. 054043.

[142] Wang, X., Chen, Z., Zhang, L., Jiang, B., Xu, M., Hong, J., Wang, Y., Zhang, P., Zhang, L., Hang, Y.: Preparation, spectroscopic characterization and energy transfer investigation of iron-chromium diffusion co-doped ZnSe for mid-IR laser applications, *Optical Materials*, Apr. 2016, **vol. 54**, p. 234–237.

[143] Wang, X., Chen, Z., Zhang, L., Xu, M., Chen, G., Jiang, B., Ke, C., Zhang, L., Hang, Y.: Charge state and energy transfer investigation of iron-chromium co-doped ZnS polycrystalline prepared by step-temperature diffusion for mid-infrared laser applications, *Journal of Alloys and Compounds*, Feb. 2017, **vol. 695**, p. 3767–3771.

[144] Fedorov, V., Carlson, T., Mirov, S.: Energy transfer in iron-chromium co-doped ZnSe middle-infrared laser crystals, *Optical Materials Express*, May 2019, **vol. 9(5)**, p. 2340–2347.

[145] Page, R. H., Skidmore, J. A., Schaffers, K. I., Beach, R. J., Payne, S. A., Krupke, W. F.: Demonstrations of diode - pumped and grating - tuned ZnSe:Cr^{2+} lasers, in: *Advanced Solid State Lasers (1997), paper LS6*, Jan. 1997, p. LS6, Optica Publishing Group.

[146] Fedorov, V. V., Gallian, A., Moskalev, I., Mirov, S. B.: En route to electrically pumped broadly tunable middle infrared lasers based on transition metal doped II–VI semiconductors, *Journal of Luminescence*, Jul. 2007, **vol. 125(1)**, p. 184–195.

[147] Sorokina, I. T.: Broadband Mid-Infrared Solid-State Lasers, in: *Mid-Infrared Coherent Sources and Applications*, Ebrahim-Zadeh, M., Sorokina, I. T., editors, NATO Science for Peace and Security Series B: Physics and Biophysics, p. 225–260, Springer Netherlands, Dordrecht, 2008.

[148] Koranda, P., Jelínková, H., Šulc, J., Němec, M., Doroshenko, M. E., Basiev, T. T., Komar, V. K., Gerasimenko, A. S., Puzikov, V. M.: Cr:ZnSe laser crystal grown by Bridgeman technique: characteristics and laser performance, in: *Solid State Lasers XVI: Technology and Devices*, vol. 6451, Feb. 2007, p. 64510M, International Society for Optics and Photonics.

[149] Godard, A.: Infrared (2–12 μm) solid-state laser sources: a review, *Comptes Rendus Physique*, Dec. 2007, **vol. 8(10)**, p. 1100–1128.

[150] Akimov, V. A., Kozlovskii, V. I., Korostelin, Y. V., Landman, A. I., Podmar'kov, Y. P., Skasyrskii, Y. K., Frolov, M. P.: Efficient pulsed Cr^{2+}:CdSe laser continuously tunable in the spectral range from 2.26 to 3.61 μm, *Quantum Electronics*, Mar. 2008, **vol. 38(3)**, p. 205.

[151] Sparks, J. R., Aro, S. C., He, R., Goetz, M. L., Krug, J. P., McDaniel, S. A., Berry, P. A., Cook, G., Schepler, K. L., Sazio, P. J., Gopalan, V., Badding, J. V.: Chromium doped zinc selenide optical fiber lasers, *Optical Materials Express*, Aug. 2020, **vol. 10(8)**, p. 1843–1852.

[152] Carrig, T. J., Wagner, G. J., Sennaroglu, A., Jeong, J. Y., Pollock, C. R.: Mode-locked Cr^{2+}:ZnSe laser, *Optics Letters*, Feb. 2000, **vol. 25(3)**, p. 168.

[153] Sorokin, E., Sorokina, I. T.: Ultrashort-pulsed Kerr-lens modelocked Cr:ZnSe laser, in: *CLEO/Europe and EQEC 2009 Conference Digest (2009), paper CF1_3*, Jun. 2009, p. CF1_3, Optical Society of America.

[154] Cizmeciyan, M. N., Kim, J. W., Bae, S., Hong, B. H., Rotermund, F., Sennaroglu, A.: Graphene mode-locked Cr:ZnSe laser, in: *Advanced Solid-State Lasers Congress (2013), paper MW1C.4*, Oct. 2013, p. MW1C.4, Optica Publishing Group.

[155] Leshchenko, V. E., Talbert, B. K., Lai, Y. H., Li, S., Tang, Y., Hageman, S. J., Smith, G., Agostini, P., DiMauro, L. F., Blaga, C. I.: High-power few-cycle Cr:ZnSe mid-infrared source for attosecond soft x-ray physics, *Optica*, Aug. 2020, **vol. 7(8)**, p. 981–988.

[156] Gallian, A., Fedorov, V. V., Mirov, S. B., Badikov, V. V., Galkin, S. N., Voronkin, E. F., Lalayants, A. I.: Hot-pressed ceramic Cr^{2+}:ZnSe gain-switched laser, *Optics Express*, Nov. 2006, **vol. 14(24)**, p. 11694–11701.

[157] Alford, W. J., Wagner, G. J., Sullivan, A. C., Keene, J. A., Carrig, T. J.: High-Power and Q-Switched Cr:ZnSe Lasers, in: *Advanced Solid-State Photonics*, 2003, p. 13, OSA, San Antonio, Texas.

[158] Pollock, C. R., Pollock, C. R., Brilliant, N. A., Gwin, D., Carrig, T. J., Alford, W. J., Heroux, J. B., Wang, W. I., Vurgaftman, I., Meyer, J. R.: Mode locked and Q-switched Cr:ZnSe laser using a Semiconductor Saturable Absorbing Mirror (SESAM), in: *Advanced Solid-State Photonics (TOPS) (2005), paper 252*, Feb. 2005, p. 252, Optica Publishing Group.

[159] Wang, Z.-W., Chen, X.-F., He, J.-L., Xu, X.-G., Zhang, B.-T., Yang, K.-J., Wang, R.-H., Liu, X.-M.: Graphene Q-switched Cr:ZnSe laser, *IEEE Journal of Quantum Electronics*, May 2015, **vol. 51(5)**, p. 1–5.

[160] Wang, Y., Fernandez, T. T., Coluccelli, N., Gambetta, A., Laporta, P., Galzerano, G.: 47-fs Kerr-lens mode-locked Cr:ZnSe laser with high spectral purity, *Optics Express*, Oct. 2017, **vol. 25(21)**, p. 25193–25200.

[161] Sorokina, I. T., Sorokin, E., Lieto, A. D., Tonelli, M., Page, R. H., Schaffers, K. I.: Active and passive mode-locking of the Cr^{2+}:ZnSe laser, in: *Advanced Solid-State Lasers (2001), paper MC2*, Jan. 2001, p. MC2, Optical Society of America.

[162] Sorokina, I. T., Sorokin, E.: Femtosecond Cr^{2+}-based lasers, *IEEE Journal of Selected Topics in Quantum Electronics*, Jan. 2015, **vol. 21(1)**, p. 273–291.

[163] Vasilyev, S., Moskalev, I., Mirov, M., Smolski, V., Mirov, S., Gapontsev, V.: Ultrafast middle-IR lasers and amplifiers based on polycrystalline Cr:ZnS and Cr:ZnSe, *Optical Materials Express*, Jul. 2017, **vol. 7(7)**, p. 2636–2650.

[164] Sorokina, I. T., Sorokin, E., Carrig, T. J.: Femtosecond pulse generation from a SESAM mode-locked Cr:ZnSe laser, in: *Conference on Lasers and Electro-Optics/Quantum Electronics and Laser Science Conference and Photonic Applications Systems Technologies (2006), paper CMQ2*, May 2006, p. CMQ2, Optical Society of America.

[165] Sorokina, I. T., Sorokin, E.: Chirped-mirror dispersion controlled femtosecond Cr:ZnSe laser, in: *Advanced Solid-State Photonics (2007), paper WA7*, Jan. 2007, p. WA7, Optical Society of America.

[166] Cizmeciyan, M. N., Cankaya, H., Kurt, A., Sennaroglu, A.: Kerr-lens mode-locked femtosecond Cr^{2+}:ZnSe laser at 2420 nm, *Optics Letters*, Oct. 2009, **vol. 34(20)**, p. 3056.

[167] Slobodchikov, E., Moulton, P. F.: 1-GW-peak-power, Cr:ZnSe laser, in: *CLEO:2011 - Laser Applications to Photonic Applications*, 2011, p. PDPA10, OSA, Baltimore, Maryland.

[168] Cizmeciyan, M. N., Cankaya, H., Kurt, A., Sennaroglu, A.: Operation of femtosecond Kerr-lens mode-locked Cr:ZnSe lasers with different dispersion compensation methods, *Applied Physics B*, Mar. 2012, **vol. 106(4)**, p. 887–892.

[169] Vasilyev, S., Mirov, M., Gapontsev, V.: Kerr-lens mode-locked femtosecond polycrystalline Cr^{2+}:ZnS and Cr^{2+}:ZnSe lasers, *Optics Express*, 2014, **vol. 22(5)**, p. 5118–5123.

[170] Nagl, N., Gröbmeyer, S., Pervak, V., Krausz, F., Pronin, O., Mak, K. F.: Directly diode-pumped, Kerr-lens mode-locked, few-cycle Cr:ZnSe oscillator, *Optics Express*, Aug. 2019, **vol. 27(17)**, p. 24445.

[171] Pires, H., Baudisch, M., Sanchez, D., Hemmer, M., Biegert, J.: Ultrashort pulse generation in the mid-IR, *Progress in Quantum Electronics*, Sep. 2015, **vol. 43**, p. 1–30.

[172] Cizmeciyan, M. N., Kim, J. W., Bae, S., Hong, B. H., Rotermund, F., Sennaroglu, A.: Graphene mode-locked femtosecond Cr:ZnSe laser at 2500 nm, *Optics Letters*, Feb. 2013, **vol. 38(3)**, p. 341–343.

[173] Wang, Y., Fleming, F., McCracken, R. A., Liebig, C., McDaniel, S., Cook, G., Laporta, P., Kar, A. K., Galzerano, G.: Hot-isostatic-pressed Cr:ZnSe ultrafast laser at 2.4 μm, *Optics & Laser Technology*, Oct. 2022, **vol. 154**, p. 108300.

[174] Nagl, N.: *A new generation of ultrafast oscillators for mid-infrared applications*, Springer Theses, 2021.

[175] Wagner, G. J., Carrig, T. J., Jarman, R. H., Page, R. H., Schaffers, K. I., Ndap, J.-O., Ma, X., Burger, A.: High-efficiency, broadly tunable continuous-wave Cr^{2+}:ZnSe laser, in: *Advanced Solid State Lasers (1999), paper WD2*, Jan. 1999, p. WD2, Optica Publishing Group.

[176] Sorokin, E., Sorokina, I., Di Lieto, A., Tonelli, M., Page, R.: Tunable diode-pumped continuous-wave single crystal and ceramic Cr^{2+}:ZnSe lasers, in: *Technical Digest. CLEO/Pacific Rim 2001. 4th Pacific Rim Conference on Lasers and Electro-Optics (Cat. No.01TH8557)*, vol. Supplement, Jul. 2001, p. 26–27 suppl.

[177] Sorokin, E., Sorokina, I. T., Page, R. H.: Room-temperature CW diode-pumped Cr^{2+}:ZnSe laser, in: *Advanced Solid-State Lasers (2001), paper MB11*, Jan. 2001, p. MB11, Optica Publishing Group.

[178] Sorokin, E., Sorokina, I. T.: Tunable diode-pumped continuous-wave Cr^{2+}:ZnSe laser, *Applied Physics Letters*, May 2002, **vol. 80(18)**, p. 3289–3291.

[179] Moskalev, I. S., Fedorov, V. V., Mirov, S. B.: InP diode-pumped Cr:ZnS and Cr:ZnSe highly efficient, widely tunable, mid-IR lasers, in: *Solid State Lasers XIX: Technology and Devices*, vol. 7578, Feb. 2010, p. 75781K, International Society for Optics and Photonics.

[180] Renz, G., Speiser, J., Giesen, A., Sorokina, I. T., Sorokin, E.: Cr:ZnSe bulk and Cr:ZnSe thin disk CW lasers, in: *Lasers, Sources, and Related Photonic Devices (2012), paper AT4A.3*, Jan. 2012, p. AT4A.3, Optica Publishing Group.

[181] Renz, G., Speiser, J., Giesen, A., Sorokina, I. T., Sorokin, E.: Cr:ZnSe thin disk cw laser, in: *Solid State Lasers XXII: Technology and Devices*, vol. 8599, Mar. 2013, p. 310–316, SPIE.

[182] Stites, R. W., Cook, G., Berry, P. A., Schepler, K. L.: Power scaling a Cr:ZnSe thin disk laser by increasing pump diameter, in: *CLEO: 2014 (2014), paper JTu4A.124*, Jun. 2014, p. JTu4A.124, Optica Publishing Group.

[183] Moskalev, I., Mirov, S., Mirov, M., Vasilyev, S., Smolski, V., Zakrevskiy, A., Gapontsev, V.: 140 W Cr:ZnSe laser system, *Optics Express*, Sep. 2016, **vol. 24(18)**, p. 21090–21104.

[184] Kozlovsky, V. I., Korostelin, Y. V., Landman, A. I., Mislavskii, V. V., Podmar'kov, Y. P., Skasyrsky, Y. K., Frolov, M. P.: Pulsed Fe^{2+}:ZnS laser continuously tunable in the wavelength range of 3.49–4.65 μm, *Quantum Electronics*, Jan. 2011, **vol. 41(1)**, p. 1.

[185] Frolov, M. P., Korostelin, Y. V., Kozlovsky, V. I., Skasyrsky, Y. K.: 2 mJ room temperature Fe:CdTe laser tunable from 5.1 to 6.3 μm, *Optics Letters*, Nov. 2019, **vol. 44(22)**, p. 5453.

[186] Frolov, M. P., Korostelin, Y. V., Kozlovsky, V. I., Leonov, S. O., Skasyrsky, Y. K.: Tunable in the range of 4.5–6.8 μm room temperature single-crystal Fe:CdTe laser pumped by Fe:ZnSe laser, *Optics Express*, Jun. 2020, **vol. 28(12)**, p. 17449.

[187] Frolov, M. P., Korostelin, Y. V., Kozlovsky, V. I., Podmar'kov, Y. P., Skasyrsky, Y. K.: High-energy thermoelectrically cooled Fe:ZnSe laser tunable over 3.75–4.82 μm, *Optics Letters*, Feb. 2018, **vol. 43(3)**, p. 623–626.

[188] Coco, M. G., Aro, S. C., McDaniel, S. A., Hendrickson, A., Krug, J. P., Sazio, P. J., Cook, G., Gopalan, V., Badding, J. V.: Continuous wave Fe^{2+}:ZnSe mid-IR optical fiber lasers, *Optics Express*, Sep. 2020, **vol. 28(20)**, p. 30263–30274.

[189] Migal, E., Pushkin, A., Bravy, B., Gordienko, V., Minaev, N., Sirotkin, A., Potemkin, F.: 3.5-mJ 150-fs Fe:ZnSe hybrid mid-IR femtosecond laser at 4.4 μm for driving extreme nonlinear optics, *Optics Letters*, May 2019, **vol. 44(10)**, p. 2550–2553.

[190] Akimov, V. A., Frolov, M. P., Korostelin, Y. V., Kozlovsky, V. I., Landman, A. I., Podmar'kov, Y. P., Voronov, A. A.: Room-temperature operation of a Fe^{2+}:ZnSe laser, in: *Laser Optics 2006: Solid State Lasers and Nonlinear Frequency Conversion*, vol. 6610, Apr. 2007, p. 50–55, SPIE.

[191] Evans, J. W., Berry, P. A., Schepler, K. L.: A passively Q-switched, CW-pumped Fe:ZnSe laser, *IEEE Journal of Quantum Electronics*, Mar. 2014, **vol. 50(3)**, p. 204–209.

[192] Xu, F., Pan, Q., Zhang, Y., Zhang, R., Chen, Y., Yu, D., Chen, F.: Pulse high energy Fe:ZnSe laser pumped by Q-switched Er:YAG laser, *Optics Express*, Jul. 2023, **vol. 31(16)**, p. 26807–26814.

[193] Ongstad, A., Evan, L., Hoeffner, E., Lucero, A., Evans, J., Schmitt-Sody, A.: A 4.1 micron mode-locked Fe:ZnSe laser, in: *Laser Congress 2018 (ASSL)*, 2018, Boston, Massachusetts, USA.

[194] Frolov, M. P., Gordienko, V. M., Korostelin, Y. V., Kozlovsky, V. I., Podmar'kov, Y. P., Potemkin, F. V., Skasyrsky, Y. K.: Fe^{2+}-doped CdSe single crystal: growth, spectroscopic and laser properties, potential use as a 6 µm broadband amplifier, *Laser Physics Letters*, Dec. 2016, **vol. 14(2)**, p. 025001.

[195] Evans, J. W., Berry, P. A., Schepler, K. L.: A broadly tunable continuous-wave Fe:ZnSe laser, in: *Solid State Lasers XXII: Technology and Devices*, vol. 8599, Mar. 2013, p. 60–67, SPIE.

[196] Martyshkin, D. V., Fedorov, V. V., Mirov, M., Moskalev, I., Vasilyev, S., Smolski, V., Zakrevskiy, A., Mirov, S. B.: High power (9.2 W) CW 4.15 µm Fe:ZnSe laser, in: *Conference on Lasers and Electro-Optics (2017), paper STh1L.6*, May 2017, p. STh1L.6, Optical Society of America.

[197] Li, E., Uehara, H., Uehara, H., Yao, W., Tokita, S., Potemkin, F., Yasuhara, R., Yasuhara, R.: High-efficiency, continuous-wave Fe:ZnSe mid-IR laser end pumped by an Er:YAP laser, *Optics Express*, Dec. 2021, **vol. 29(26)**, p. 44118–44128.

[198] Koechner, W.: *Solid-state laser engineering*, Springer Series in Optical Sciences, Springer-Verlag, New York, 6 edition, 2006.

[199] Yang, R. Q.: Infrared laser based on intersubband transitions in quantum wells, *Superlattices and Microstructures*, Jan. 1995, **vol. 17(1)**, p. 77–83.

[200] Dormidonov, A. E., Firsov, K. N., Gavrishchuk, E. M., Ikonnikov, V. B., Kazantsev, S. Y., Kononov, I. G., Kotereva, T. V., Savin, D. V., Timofeeva, N. A.: High-efficiency room-temperature ZnSe:Fe^{2+} laser with a high pulsed radiation energy, *Applied Physics B*, Jul. 2016, **vol. 122(8)**, p. 211.

[201] Grishin, M.: *Advances in solid state lasers development and applications*, IntechOpen, Feb. 2010.

[202] Tittel, F. K., Richter, D., Fried, A.: Mid-Infrared Laser Applications in Spectroscopy, in: *Solid-State Mid-Infrared Laser Sources*, Sorokina, I. T., Vodopyanov, K. L., editors, Topics in Applied Physics, p. 458–529, Springer, Berlin, Heidelberg, 2003.

[203] Bernhardt, B., Sorokin, E., Jacquet, P., Thon, R., Becker, T., Sorokina, I. T., Picqué, N., Hänsch, T. W.: Mid-infrared dual-comb spectroscopy with 2.4-µm Cr^{2+}:ZnSe femtosecond lasers, *Applied Physics B*, Jul. 2010, **vol. 100(1)**, p. 3–8.

[204] Vodopyanov, K. L.: *Laser-based mid-infrared sources and applications*, Wiley, 1 edition, Jun. 2020.

[205] Hesse, M., Meier, H., Zeeh, B., editors: *Spectroscopic methods in organic chemistry*, Thieme, Stuttgart, 2. ed edition, 2008.

[206] Fischer, C., Sorokin, E., Sorokina, I. T., Sigrist, M. W.: Photoacoustic monitoring of gases using a novel laser source tunable around 2.5 μm, *Optics and Lasers in Engineering*, Mar. 2005, **vol. 43(3)**, p. 573–582.

[207] Rudy, C. W.: Mid-IR lasers: Power and pulse capability ramp up for mid-IR lasers, May 2014.
URL https://www.laserfocusworld.com/lasers-sources/article/16550254/midir-lasers-power-and-pulse-capability-ramp-up-for-midir-lasers

[208] Henderson, B., Khodabakhsh, A., Metsälä, M., Ventrillard, I., Schmidt, F. M., Romanini, D., Ritchie, G. A. D., Te Lintel Hekkert, S., Briot, R., Risby, T., Marczin, N., Harren, F. J. M., Cristescu, S. M.: Laser spectroscopy for breath analysis: towards clinical implementation, *Applied Physics. B, Lasers and Optics*, 2018, **vol. 124(8)**, p. 161.

[209] Čech, D.: *Obrábění paprskem laseru*, Dissertation thesis, Czech Technical University in Prague, Aug. 2020, accepted: 2020-09-04T13:50:44Z Publisher: České vysoké učení technické v Praze. Vypočetní a informační centrum.
URL https://dspace.cvut.cz/handle/10467/89916

[210] Urban, W.: Physics and spectroscopic applications of carbon monoxide lasers, a review, *Infrared Physics & Technology*, Jan. 1995, **vol. 36(1)**, p. 465–473.

[211] Pushkin, A., Migal, E., Suleimanova, D., Mareev, E., Potemkin, F.: High-power solid-state near- and mid-IR ultrafast laser sources for strong-field science, *Photonics*, Feb. 2022, **vol. 9(2)**, p. 90.

[212] Soibel, A., Wright, M., Farr, W., Keo, S., Hill, C., Yang, R. Q., Liu, H. C.: Free space optical communication utilizing mid-infrared interband cascade laser, in: *Free-Space Laser Communication Technologies XXII*, vol. 7587, Feb. 2010, p. 241–250, SPIE.

[213] Tovey, D., Pigeon, J., Tochitsky, S., Louwrens, G., Ben-Zvi, I., Martyshkin, D., Fedorov, V., Karki, K., Mirov, S., Joshi, C.: Lasing in 15 atm CO_2 cell optically pumped by a Fe:ZnSe laser, *arXiv:2106.12143 [physics]*, Jun. 2021.

[214] Querry, M., R.: Optical constants of minerals and other materials from the millimeter to the ultraviolet, online, University of Missouri - Kansas City, University of Missouri - Kansas City, Nov. 1987, section: Technical Reports.
URL https://apps.dtic.mil/sti/citations/ADA192210

[215] Institute for Single Crystals - Engineering service - Bridgman method.
URL https://web.archive.org/web/20201029051925/http://iscrystals.com/page-details.html?cat_id=86&id=101

[216] Ptashnik, I. V., Klimeshina, T. E., Petrova, T. M., Solodov, A. A., Solodov, A. M.: Water vapor continuum absorption in the 2.7 and 6.25 μm bands

at decreased temperatures, *Atmospheric and Oceanic Optics*, May 2016, **vol. 29(3)**, p. 211–215.

[217] Peppers, J., Fedorov, V. V., Mirov, S. B.: Mid-IR photoluminescence of Fe^{2+} and Cr^{2+} ions in ZnSe crystal under excitation in charge transfer bands, *Optics Express*, Feb. 2015, **vol. 23(4)**, p. 4406.

[218] Watkins, R., Gafarov, O., Bernard, C., Fedorov, V., Mirov, S.: Thermally-induced optical bistability in Cr and Fe doped ZnSe mid-IR laser materials, in: *2017 Conference on Lasers and Electro-Optics (CLEO)*, May 2017, p. 1–2.

[219] Doroshenko, M., Jelínková, H., Osiko, V., Jelínek, M., Vyhlídal, D., Šulc, J., Němec, M., Kovalenko, N., Gerasimenko, A.: Fe:ZnMnSe laser active material at 78–300 K: Spectroscopic properties and laser generation at 4.2–5.0 µm, *Journal of Luminescence*, Dec. 2017, **vol. 192**, p. 1300–1307.